Penman, Gary (2025) *A new measurement of the neutron electric form factor with the Super Bigbite Spectrometer apparatus*. PhD thesis.

https://theses.gla.ac.uk/85150/

A New Measurement of the Neutron Electric Form Factor with the Super Bigbite Spectrometer Apparatus

Gary Penman

Submitted in fulfilment of the requirements for the
Degree of Doctor of Philosophy

School of Physics and Astronomy
College of Science and Engineering
University of Glasgow

April 2025

Abstract

Protons and neutrons, collectively known as nucleons, make up the nuclei at the core of atoms which form our world. The nucleon has been under intensive study for over 100 years, and yet we still do not fully understand the internal dynamics which govern properties like its spin or its mass - which contributes to almost all of the visible mass in the universe. These dynamics are governed by quantum chromodynamics (QCD), the predictions of which are experimentally tested at high energy accelerator facilities such as Jefferson Lab. The GEN-II experiment (E12-09-016) is one such experiment.

GEN-II is part of the Super Bigbite Spectrometer (SBS) experimental form factor programme taking place in Hall A at Jefferson Lab, which aims to make precision measurements of the nucleon electromagnetic form factors (EMFFs) at record high values of squared four-momentum transfer Q^2. EMFFs describe the electric and magnetic moment distributions within the nucleon. They can be measured through elastic electron scattering off the nucleon, and describe the recoil response of the target nucleon at a given energy scale.

GEN-II is a double polarised semi-exclusive beam target asymmetry (BTA) experiment, seeking to measure the electric form factor of the neutron, G_E^n, at three new values of squared four-momentum transfer $Q^2 = 2.92, 6.74$ and 9.82 GeV^2. The latter two points being at record high Q^2. The form factor is determined through measuring the BTA of quasielastic scattering of a neutron from a polarised nuclear target. The experiment utilised the CEBAF accelerator to produce longitudinally polarised electrons up to ~85% polarisation, which were scattered off neutrons within a novel polarised helium-3 (^{3}He) target. This new polarised ^{3}He target was employed by building on the technology of its precursors which existed in similar preceding experiments. This target was designed to operate at the high luminosities typical of Hall A, and reached a record breaking combination of polarisation and beam intensity known as figure of merit, three times larger than those predecessors.

The SBS collaboration designed and constructed two brand new high acceptance spectrometers for these experiments, an electron arm named Bigbite (BB) and a hadron arm named Super Bigbite. Both spectrometers featured a large acceptance EM dipole magnet, and complementary detector systems. The electron arm contained gaseous electron multipliers (GEMs) which were used for high precision tracking of the scattered electrons, a heavy gas cherenkov (GRINCH) which was used for PID between electrons and pions, a plastic scintillator timing hodoscope to provide high resolution timing of the start of events, and a pair of EM calorimeters (BBCal) which provided energy measurements of detected particles, and provided the experimental trigger. The hadron arm also contained a system of GEMs which will be utilised for future SBS experiments, and a hadron calorimeter designed to provide position, timing and energy measurements of the recoiling nucleon.

The calibration of all detector subsystems, beam and target data is discussed, with a focus on novel timing calibrations to the hodoscope and hadron calorimeter. An analysis of selecting quasielastic events and suppressing background contributions from a number of sources which contaminate the final event sample is given. The largest irreducible backgrounds are found to be from misidentified protons, timing accidentals and inelastic events. The physical asymmetry is measured and used to extract a value for the form factor ratio G_E^n/G_M^n. High precision Q^2 data for G_M^n is used to then extract G_E^n. This work finds at $Q^2 = 2.92\ \mathrm{GeV}^2$ that $G_E^n = 0.0129^{+0.0019}_{-0.0020}$. This result is in statistical agreement with existing fits to world data, and predictions from the constituent quark model and Dyson–Schwinger equations, in this region of Q^2.

Declaration

The work in this thesis is based on research carried out within the Nuclear and Hadron Physics Research Group, School of Physics and Astronomy, University of Glasgow, Scotland and in collaboration with Thomas Jefferson National Accelerator Facility, Virginia, United States. The work contained herein is all my own work unless referenced to the contrary in this deceleration or within the main text of the thesis as appropriate.

The GEN-II experiment was carried out by the SBS and Hall A collaborations of Jefferson Lab. The experimental setup of all of the detectors, target and monitoring equipment was achieved by the collective effort of the entire collaboration. Similarly the CEBAF accelerator which is utilised for its electron beam takes the continuous work of the entirety of Jefferson Lab personnel to operate. Software specific to this experiment is a collaborative effort, which I contributed to in the SBS-offline and SBS-replay GitHub repositories, as well as maintenance of offline utility and monitoring scripts in the counting house during experimental data taking.

I was stationed at Jefferson Lab for periods of time before and during experimental running. I worked as part of the target team to install the infrastructure for the polarised helium-3 target system, and built, installed and commissioned the first target cells setups. I contributed to the collection of data through shift work and run coordinator work, ultimately covering the second highest number of weighted shifts in the collaboration, and performed online analysis and data checks during experimental running.

As described in chapter 4, the original detector calibrations for most systems used values out of the GMN experiment which ran before GEN-II. These were performed by the GMN student analysis team. Further GEN specific calibrations were carried out by the GEN student analysis team. I originally calibrated the timing hodoscope, and then eventually recalibrated it along with the HCal and coincidence timing data. The beam position monitoring as well as Bigbite optics, momentum reconstruction and GEM calibrations were performed by Sean Jeffas (University of Virginia). Energy calibration for BBCal and HCal was done by Kate Evans (College of William and Mary) and Hunter Presley (University of Virginia) respectively. The GRINCH timing alignment and PID performance has been studied and calibrated by myself and Jack Jackson (College of William and Mary). Additionally, an analysis of the background contamination arising from nitrogen gas in the target cell was performed by

Sean Jeffas, and the values are used in the final analysis. All other work regarding the final G_E^n analysis in chapter 5, and results presented in chapter 6 are my own. No part of this thesis has been submitted elsewhere for any other degree or qualification.

“Getting an education was a bit like a communicable sexual disease. It made you unsuitable for a lot of jobs and then you had the urge to pass it on.”

- Terry Pratchett, Hogfather

Acknowledgements

First and foremost, I would like to express my deepest gratitude to my supervisors, Rachel Montgomery and David Hamilton, for their invaluable guidance, support, and encouragement throughout the course of my PhD. Their expertise and advice have been instrumental in shaping this work and my growth as a researcher. It has been a pleasure to work with you both.

I am also sincerely grateful to my colleagues in the Nuclear and Hadron Physics research group for fostering such a stimulating and supportive environment. Working alongside such talented and driven individuals has been a privilege. I would like to especially thank Derek Glazier and Peter Hurck for their patience and guidance, even with the most trivial questions and problems, and Bryan McKinnon for his continual aid, as well as for keeping the group systems afloat. I would also like to extend my thanks to my friends and fellow PhD students in office 414 — Dave, Kayleigh, Richard, and Ryan. Your camaraderie, advice, and often absurd humour made the daily challenges of research far more manageable. To all those who have not been specifically named, of which there are many, thank you for adding to this fantastic experience. It would not be right to leave unmentioned our friends and colleagues in York, in particular Stuart Fegan, for many nights spent scheming the future of hadron physics in Curlers — here's to many more.

Special thanks go to my colleagues at Jefferson Lab, whose collaboration and insightful discussions significantly contributed to this work. In particular, I would like to acknowledge Arun Tadepalli for his exceptional support, expertise, and willingness to always offer help and advice whenever needed. I would also like to express my thanks and fondness to the GEN students — Sean, Kate, Hunter, Jack, and Vimukthi — who have endured this long path alongside me. I wish you all success in the future. Thanks also to the spokespeople of the experiment, Gordon Cates, Bogdan Wojtsekhowski, and Todd Averett, for planning and coordinating the experiment and allowing me to undertake this project. Furthermore, I wish to thank Andrew Puckett and Eric Fuchey, whose efforts made the multiple SBS analyses possible.

Beyond academia, I am deeply thankful to all of my friends and family at home for their unwavering belief in me, their understanding, and their endless encouragement, especially during the more challenging moments of this journey. I would like to specifically thank my

dad, Michael, for his continuous and enduring support throughout my life. Our weekend catch-ups at the pub always provided much-needed time to de-stress away from work.

Finally, and most importantly, to my loving girlfriend, Zoe. Thank you for your unconditional love, patience, and support throughout this entire process. You have shared my stresses, put up with my hectic schedule, and endured my often long absences from home. Your strength and encouragement have been a constant source of motivation, and this accomplishment would not have been possible without you by my side.

This thesis is dedicated to my mum, Caroline, and my gran, Sarah, whom I wish could have been here to see its completion.

“QCD nowadays has a split personality. It embodies “hard” and “soft” physics, both being hard subjects, and the softer the harder.”

- Yuri Dokshitzer[1]

Contents

List of Figures

List of Tables

Chapter 1

Introduction

Nuclear physics is an ever-evolving field that has contributed significantly to our understanding of the fundamental laws of nature. The quest to unravel the mysteries of the universe at the subatomic level has led to significant advancements in our understanding of the fundamental particles and the forces that govern their interactions.

In the last one hundred years or so, incredible advances have been made in understanding the subatomic world. Nuclear and atomic physics experiments in the early 1900s which were fairly simple a posteriori, had surprising results at the time. In 1911 Ernest Rutherford demonstrated that matter consists of atoms on the scale of 10^{-10} m with a central positive charge and a surrounding cloud of negatively charged electrons [2], superseding the earlier Thompson plum pudding model. He named this central charge the nucleus, which we now know has dimensions less than 10^{-13} m, but contains 99.95% of the atomic mass. Then, in 1919 Rutherford went further, discovering that this "nucleus" contains positively charged particles, by extracting hydrogen nuclei from collisions with nitrogen. He coined these charged particles "protons", the Greek word for "first" [3]. This presented a problem of mass, as the number of these protons required to balance the charge of a given nucleus, would not account for all of the measured mass, and visa versa. This problem was solved over a decade later by James Chadwick while experimenting with proton ejection in light nuclei collisions, wherein he measured a mass defect [4]. The conclusion was that these results would follow directly, if the emitted particle were close to the proton mass, but with a net zero charge. He termed this particle the neutron. Collectively, protons and neutrons have become known as "nucleons". Combined with electrons, this provided an elegant and simple model of the atom as a set of three elementary particles.

However, soon after the discovery of the neutron, Frisch and Stern measured the proton magnetic moment as 2.79 nuclear magnetons ($\mu_N = e\hbar/2M$) [5]. This was larger than the prediction of 1 from Relativistic Quantum Field Theory (RQFT) for a spin-$\frac{1}{2}$ particle

$$\mu = g\left(\frac{e}{2m}\right)\frac{\hbar}{2}, \tag{1.1}$$

where g is the g-factor which is approximately 2 for a spin-$\frac{1}{2}$ point particle, e and m are the charge and mass of the particle respectively and $\hbar$ is Planck's (reduced) constant. This was the first indirect evidence of structure below the nucleon level. Around the same time, Hideki Yukawa proposed a new force and associated quanta, required to balance the electromagnetic repulsion between the protons within an atom [6]. This became known as the strong force, with the quanta the meson. Several years later, Alvarez and Bloch published a measurement of the magnetic moment of the neutron, reporting a value of μ_n = -1.93 ± 0.02 μ_N [7], again drastically different from the prediction of 0 from Eqn. 1.1. It was becoming clear that there was more to matter than the simple three particle picture, and that nucleons likely had some internal structure.

A quantum theory of atomic emissions had been presented by Dirac in the 1920s [8], however there were various discrepancies with experimental data, until 1947 when Hans Bethe performed the first quantum computation via a novel technique, renormalisation [9]. This was the first step towards Quantum Electrodynamics as it would become known.

These mysteries and innovations around the subatomic structure fuelled decades of technological and theoretical progress, which started with the first electron beam experiments in the 1950s. Early scattering experiments between 1953-1956 at Stanford HEP Lab by Hofstadter et al [10–12], revealed the nucleon substructure which we now attribute to quarks and gluons, and made the first measurement of the proton size. It was demonstrated that electron-proton (ep) scattering could be described by a scattering cross section σ, which was the product of the scattering cross section for a point particle, and a form factor - an effective distribution function of the charge and momentum currents within the proton. The cross section as a function of scattering angle θ_e has the form

$$\sigma(\theta_e) = \sigma_M \left| \int \rho(r) e^{iq.r} d^3 r \right|^2 = \sigma_M |F(q)|^2 \tag{1.2}$$

where $\rho(r)$ is the effective electromagnetic charge distribution, F is the form factor which evolves as a function of the four-momentum transfer between the electron and proton, q, and σ_M is the scattering cross section for a point particle. This work confirmed Rosenbluth's theory of elastic scattering of electrons on protons [13]. However at this point very little was understood about the proton's internal structure until 1964, when Murray Gell-Mann and George Zweig independently introduced the idea of constituent particles of the nucleon.

Gell-Mann had earlier realised that these multiplets were the representations of a mathematical group of three identical objects under a flavour SU(3) symmetry, starting with an isospin doublet and a strange singlet. He called this representation the "Eightfold Way" in a reference to the Buddhist eightfold path to enlightenment. Gell-Mann and Zweig both realised that three objects that encompassed separately the up isospin, the down isospin, and the strangeness could form all the known baryons by combining three of them, and the mesons by combining the object and its anti-object, provided these particles had fractional electric charge. Gell-Mann called these “quarks” after the phrase in the work Finnegan’s Wake by James Joyce: “Three Quarks for Muster Mark” [14]. The first experimental evidence for quarks came from deep inelastic scattering (DIS) experiments at the Stanford Linear Accelerator Center (SLAC) in 1968 [15]. Since then, six quark flavours have been discovered, the most recent being the heaviest, the top quark, at Fermilab in 1995 [16, 17].

Gell-Mann’s quark model was able to explain the various multiplets of known particles at the time, as well as those discovered since. However another problem had at this point become apparent. The spin-$\frac{3}{2}$ Δ^{++} baryon is composed of three apparently identical quarks with zero angular momentum, which seemed to violate the well supported Pauli exclusion principle. The solution to this problem, was the addition of a new quantum number under an SU(3) symmetry, which was called colour charge: red, green and blue. Along with his student at the time, Harold Fritzsch, Gell-Mann considered that this colour group could be interpreted as a gauge group, where the interaction of the quarks is generated by an octet of some massless colour gauge bosons, which they called gluons. The resultant gauge theory they developed is Quantum Chromodynamics (QCD).

Equipped with a gauge theory of electric- and colour-charge interactions, in addition to Weinberg and Salam’s recent proposal of electroweak theory [18, 19], and Higgs’ gauge symmetry breaking [20], physics was closer than ever to a complete theory of the universe. In 1974, John Iliopoulos presented the combined progress in gauge theories in full for the first time [21]. Modestly termed the “Standard Model” this theory has lived up to its name for the last 50 years, notably being “completed” in 2012 with the monumental discovery of the Higgs boson at the Large Hadron Collider (LHC) and confirmation of the existence of the corresponding Higgs field [22]. The Standard Model is considered an elegant theory which appears to accurately model most of our observations of the universe. The Standard Model Lagrangian describes three of the four fundamental forces and classifies all of the known particles - 16 fermions, four gauge bosons and the Higgs scaler boson.

Despite its successes, there are large unsolved problems. The Standard Model fails to describe the baryon asymmetry in the universe, as well as neutrino oscillations and their non-zero masses. It does not explain the acceleration of the universe via any type of dark energy nor does it provide a dark matter candidate as required by observational cosmology. Perhaps most notably, Quantum Mechanics and General Relativity, which perfectly describe the micro and macroscopic realms respectively, are currently totally incompatible with each other, leading to the absence of a theory of gravity in the Standard Model.

Decades of work trying to further understand the interactions of matter under the SM regime, as well as find new beyond the standard model physics, have lead us to this modern era of high energy and hadron physics. One topic that is particularly important to understand is the non-perturbative limits of QCD, which describe how low momentum interactions occur, such as the dynamics inside of the nucleon that Hofstadter began to probe all the way back in 1954.

The work of this thesis in particular, is an investigation of the electric form factor of the neutron in such an electron scattering experiment. Elastic form factors are a mathematical representation of the way in which a target particle (such as a nucleus or proton) responds to the electromagnetic field of an incoming particle (such as an electron or photon). Specifically, they describe the elastic scattering of the incoming particle off the target particle, and the resulting change in the momentum and energy of the incoming particle. The scattering of electrons off nuclei or nucleons is elastic when there is total conservation of kinetic energy between the initial and final states. The electron simply scatters off the target, changing direction and momentum. In a fixed target experiment, the target nucleus which begins at rest, gains some momentum in a direction parallel to the momentum transfer. In this regard, form factors provide information about the internal structure of nuclei and nucleons. Form factors are typically expressed as functions of the squared four-momentum transfer Q^2, which is defined as the difference between the initial and final four-momenta of the electron squared. This is often referred to in shorthand as the "momentum transfer". The form factors describe the distribution of charge and current density within the target particle, and how they respond to the incoming electromagnetic field. In particular, the form factors determine the angular distribution and polarisation of the scattered electrons, which can be measured in experiments. The study of elastic form factors has provided important insights into the structure of nuclei and nucleons, including their distribution of charge and magnetic moments. This information is critical for understanding the behaviour of matter at the subatomic level, and in fully understanding QCD.

This thesis presents an analysis of one kinematic setting of the E12-09-016 (GEN-II) experiment undertaken at Thomas Jefferson National Accelerator Facility. GEN-II was a double polarised fixed target electron scattering experiment on helium-3, which aimed to extract the electric form factor of the neutron, G_E^n, at three new kinematic points. Of these, two are at higher momentum transfer than current world data, and present an unprecedented opportunity to explore the structure of the nucleon in a new regime. This thesis will present an analysis of kinematic setting 2, which was the first production setting, and corresponds to elastic scattering at momentum transfer $Q^2 = 2.92$ GeV².

In chapter 2 we will lay the mathematical foundation for scattering between point particles and particles with structure, and the underlying formalism of the form factors. In chapter 3 a detailed account of the experimental setup will be given and the calibrations applied to each subsystem will be discussed in chapter 4. In chapter 5 we will describe the analysis framework and techniques employed in extracting the form factor G_n^E from the data, and the final results will be discussed in chapter 6.

Chapter 2

Electron Scattering and Nucleon Structure

Experiment E12-09-016 aimed to measure the electric form factor of the neutron at three new kinematics points, two of which were at larger values of squared four-momentum transfer (Q^2) than explored in previous experiments. This was done by impinging a longitudinally polarised beam of electrons on a transversely polarised fixed target of gaseous helium-3 (^{3}He), and measuring the resulting beam-target asymmetry between positive and negative helicity states of the incoming electron. The purpose of this chapter is to present the scattering formalism of E12-09-016, and the underlying theoretical ideas necessary for studying nucleon structure. This is by no means a full pedagogical review of the early scattering literature, neither is it intended as a full derivation of the appropriate quantum field theories from first principles. Rather, this section aims to outline the necessary building blocks required to describe polarised scattering off spin-$\frac{1}{2}$ targets with (non point-particle) structure appropriate for the scope of this thesis. A more complete picture can be found in Refs. [23, 24] from which much of the following information is found or inspired.

This chapter will concern itself with building a theoretical framework with the goal in mind of an expression for the beam-target asymmetry which is the observable measured in the extraction of G_E^n. As such, we will outline the basic ideas behind the relevant quantum field theories, and begin constructing our expressions on the basis of Rutherford scattering between point particles, building up to the relativistic regime of Mott scattering, then introducing formalism for target structure, and then the Rosenbluth theory of elastic scattering of electrons off protons. Finally we will look at the status of world data on nucleon form factors from previous Rosenbluth technique measurements, as well as modern disagreements borne out of novel experiments exploiting polarisation degrees of freedom which offer new sensitivities to the form factors.

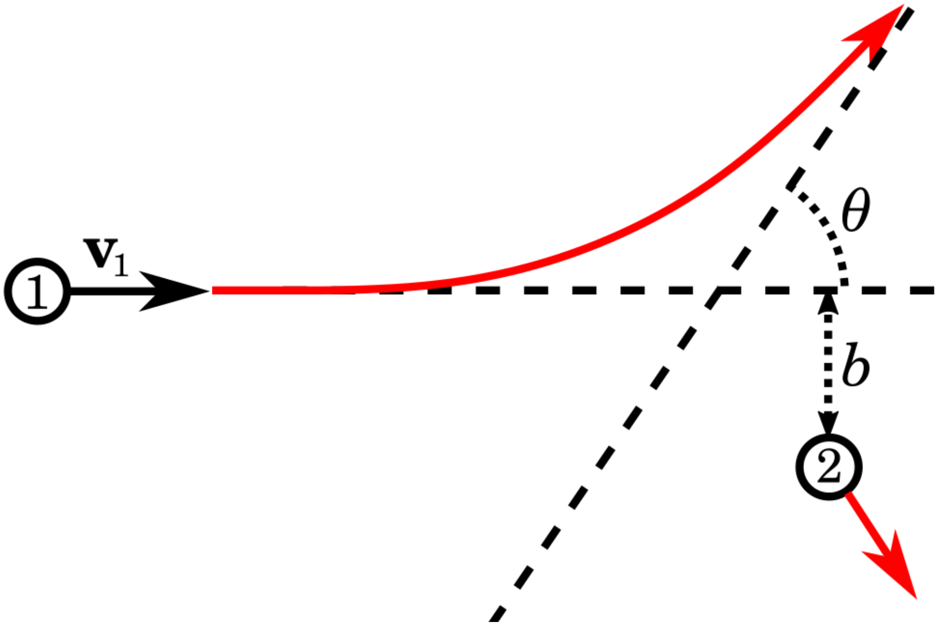

Figure 2.1: Classical Rutherford scattering between an incoming charge with velocity v_1 and a stationary charge, at angle θ parameterised by the impact parameter b. Figure amended from [25].

2.1 Classical Rutherford scattering

Rutherford (Coulomb) scattering, formalised at the same time as the discovery of the nucleus, is the scattering of two spinless particles in the limit in which the target recoil is neglected and the scattered particle is non-relativistic. Consider two particles with charges $q_1 = Z_1 e$ with velocity v_1 and $q_2 = Z_2 e$ at rest, where Z_1, Z_2 are integer multiples of the electron charge e. Fig. 2.1 shows these particles interacting classically via the Coulomb potential

$$V(r) = \frac{Z_1 Z_2 e^2}{4\pi\epsilon_0 r^2}, \tag{2.1}$$

where r is the distance between the particles. The repulsive Coulomb force results in the incoming electron being scattered at an angle θ. Considering a head-on collision, then by equating the potential energy at the point of closest approach $r = d_0$, to the initial kinetic energy $E_k = 1/2 m_1 v_1^2$, it can be shown that [26]

$$d_0 = \frac{Z_1 Z_2 e^2}{4\pi\epsilon_0 E_k}. \tag{2.2}$$

If the collision is no longer head-on, rather the line of incidence between the particles is separated by a distance b (which we will call the impact parameter) as demonstrated in

Fig. 2.1, then the scattering angle will decrease. The relationship between b and d_0 is [26]

$$\tan\left(\frac{\theta}{2}\right) = \frac{d_0}{2b}. \tag{2.3}$$

Then by simple rearrangement the impact parameter is given as

$$b = \frac{Z_1 Z_2 e^2}{4\pi\epsilon_0 m v_0^2} \cot\frac{\theta}{2}. \tag{2.4}$$

From classical mechanics, the differential cross section is defined as [27]

$$\frac{d\sigma}{d\Omega} = \frac{b}{\sin\theta}\left|\frac{db}{d\theta}\right|, \tag{2.5}$$

where $d\Omega = d\phi d\theta \sin\theta$ represents the differential solid angle, with ϕ the azimuthal scattering angle around the beam axis. By direct substitution and taking $Z_1 = Z_2 = 1$ (since electrons and protons each have magnitude of charge 1e) the Rutherford cross section can therefore be expressed as

$$\left(\frac{d\sigma}{d\Omega}\right)_{\text{Rutherford}} = \frac{\alpha^2}{16E_k^2 \sin^4\frac{\theta}{2}} \tag{2.6}$$

where $\alpha \approx 1/137$ is the fine structure constant and E_k is the kinetic energy of the incoming electron.

2.2 Quantum Electrodynamics and Relativistic Scattering

Interactions at the energy scales of GEN-II are not classical, and the particles have non-zero spins, so adjustments to theories are required to account for relativity and spin. Quantum Electrodynamics (QED) stands as the relativistic quantum field theory describing the fundamental interaction between charged particles and electromagnetic fields. At its heart lies the concept of gauge symmetry, where the theory exhibits local symmetry under transformations of the electromagnetic potential. This symmetry dictates the interactions between charged particles and photons, the quanta of the electromagnetic field. Through the formalism of second quantisation, QED treats particles as excitations of underlying quantum fields, leading to the notion of creation and annihilation operators that govern particle dynamics. QED encounters challenges in dealing with divergent integrals arising from loop diagrams, a phenomenon known as ultraviolet divergences. To address this issue, renormalisation techniques are employed, whereby divergent terms are absorbed into redefinitions of physical parameters, preserving the theory's predictive capacity while maintaining agreement with experimental observations.

In QED charged particles are considered to be surrounded by clouds of virtual photons and e^+e^- pairs continuously being created and annihilated. The attraction of opposite electric charges causes the virtual positrons on average to be closer to the electron, which creates a screening effect on the charge known as vacuum polarisation. This gives rise to an effective charge $e(r)$ that becomes smaller at a larger distance r, described by the beta function

$$\beta(r) = -\frac{de(r)}{d\ln r}. \tag{2.7}$$

Processes at the lowest order of perturbation theory are often referred to as leading-order or tree-level. Corrections to tree-level processes arise at higher orders of perturbation theory, known as loop corrections. The QED beta function is known to four-loop approximation, and at one loop approximation is positive and equal to

$$\beta(\alpha) = \frac{2\alpha^2}{3\pi}. \tag{2.8}$$

The strength of electromagnetic interactions is governed by the fine structure constant $\alpha = e^2/4\pi\epsilon_0\hbar c$. The effect of a changing effective charge on the coupling is known as running coupling, and for QED the effect is relatively small. At low energies relevant to many physics processes (and every day life) $\alpha \approx 1/137$, whereas at the scale of the electroweak bosons (order 100 GeV) α is closer to $1/127$. At some incredibly high energy QED becomes strongly coupled and in fact at a finite large energy α is predicted to become infinite at the Landau Pole [28]. Since α is much less than unity at effectively all physically relevant energy scales, the QED Lagrangian can be treated perturbatively, and as a result QED has been a tremendously successful calculative tool with some of the the most accurate physical predictions to date [29].

2.2.1 Scattering in QED

Scattering in QED is described via Feynman diagrams such as that of Fig. 2.2. These diagrams have associated rules from which we can translate pictorial representations of particle interactions for complex scattering processes into mathematical expressions for scattering amplitudes and resultant reaction cross sections. Consider the simple case of a point-like spin 1/2 charged particle off an arbitrary target. Neglecting any external effects, and working in natural units where $\hbar = c = 1$, the wavefunction ψ of the particle is governed by the Dirac equation for a free particle,

$$(i\gamma^\mu\partial_\mu - m)\psi = 0. \tag{2.9}$$

Here m is the mass of the particle, ψ the Dirac spinor / four-component wavefunction, μ runs from 0→3, and γ^μ are the 4x4 Dirac γ-matrices which satisfy the anti-commutation

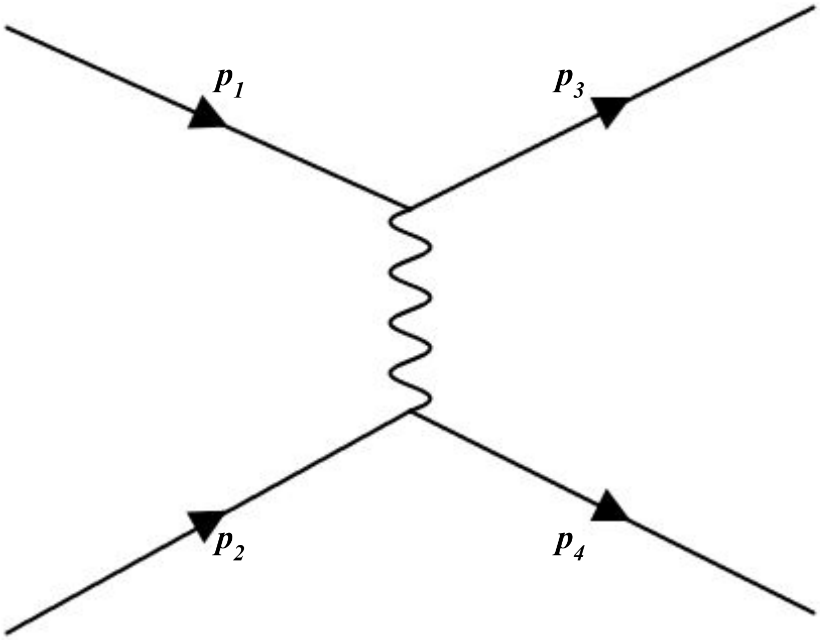

Figure 2.2: Scattering between two spin-1/2 particles with four-momenta p_1 and p_2, resulting in scattered particles with four-momenta p_3 and p_4 through the exchange of a virtual photon.

relationship

$$\gamma^{\mu}\gamma^{\nu}+\gamma^{\nu}\gamma^{\mu}=2g^{\mu\nu} \tag{2.10}$$

where $g_{\mu\nu}$ is the Minkowski metric tensor. The Dirac γ-matrices are defined as

$$\begin{aligned}\gamma^{0}&=\begin{pmatrix} I & 0 \\ 0 & -I \end{pmatrix}\\ \vec{\gamma}&=\begin{pmatrix} 0 & \vec{\sigma} \\ -\vec{\sigma} & 0 \end{pmatrix}\end{aligned} \tag{2.11}$$

where the components of $\vec{\sigma}$ are the Pauli matrices with the forms

$$\begin{aligned}\sigma_1=\sigma_x&=\begin{pmatrix} 0 & 1 \\ 1 & 0 \end{pmatrix}\\ \sigma_2=\sigma_y&=\begin{pmatrix} 0 & -i \\ i & 0 \end{pmatrix}\\ \sigma_3=\sigma_z&=\begin{pmatrix} 1 & 0 \\ 0 & -1 \end{pmatrix}.\end{aligned} \tag{2.12}$$

Introducing Feynman (or Dirac) slash notation, $\not{\delta} = \gamma^\mu \delta_\mu$, the free QED Lagrangian is then simply

$$\mathscr{L}_{\text{free}} = \bar{\psi}(i\not{\delta} - m)\psi. \tag{2.13}$$

We can begin describing the evolution of the system by constructing a charge current density

$$j^\mu = -e\bar{\psi}\gamma^\mu\psi \tag{2.14}$$

where $\bar{\psi}$ is the adjoint of the Dirac spinor which follows the relationship

$$\bar{\psi} \equiv \psi^\dagger\gamma^0. \tag{2.15}$$

Then, we can represent the free wavefunction of a particle with four momentum p as

$$\psi = u(p)e^{-p\cdot x} \tag{2.16}$$

for some four component spinor u. Substituting the wavefunction of Eqn. 2.16 into the Dirac equation, Eqn. 2.9, yields the result

$$(\gamma^\mu p^\mu - m)\psi = 0. \tag{2.17}$$

For an electron in an electromagnetic field represented by the four-potential A^μ we can perform gauge transformations which make the Dirac equation Lorentz invariant,

$$\begin{aligned} p^\mu &\rightarrow p^\mu + eA^\mu \\ \delta^\mu &\rightarrow D^\mu = \delta^\mu + ieA^\mu. \end{aligned} \tag{2.18}$$

We can also construct a kinetic term for the photon gauge field, $F_{\mu\nu}F^{\mu\nu}$, for $F_{\mu\nu} = \delta_\mu A_\nu - \delta_\nu A_\mu$, which is invariant under local gauge transformations. The resultant full QED Lagrangian for an interacting theory is now

$$\mathscr{L}_{\text{QED}} = \bar{\psi}(i\not{D} - m)\psi = \bar{\psi}(i\not{\delta} - m)\psi - e\bar{\psi}\not{A}\psi = \mathscr{L}_{\text{free}} - j^\mu A_\mu - \frac{1}{4}F_{\mu\nu}F^{\mu\nu}. \tag{2.19}$$

Substituting this into the Euler-Lagrange equations provides the equations of motion for a particle in a potential,

$$\delta_\nu\left(\frac{\delta\mathscr{L}}{\delta(\delta_\nu A_\mu)}\right) - \frac{\delta\mathscr{L}}{\delta A_\mu} = 0. \tag{2.20}$$

Each partial differential term in Eqn. 2.20 can be solved to give

$$\begin{aligned}\frac{\delta\mathscr{L}}{\delta(\delta_\nu A_\mu)} &= -F^{\mu\nu}\\ \frac{\delta\mathscr{L}}{\delta A_\mu} &= -e\bar{\psi}\gamma^\mu\psi,\end{aligned}\tag{2.21}$$

and by equating both parts and rearranging we acquire the equations of motion,

$$\delta_\nu F^{\mu\nu} = -e\bar{\psi}\gamma^\mu\psi. \tag{2.22}$$

We can expand the second term in A_μ and apply the derivative across both terms in F through the linearity of partial derivatives. Furthermore, applying the commutation of partial derivatives ($\delta_\nu\delta^\mu A^\nu = \delta_\mu\delta^\nu A^\nu$) and the Lorentz gauge condition ($\delta_\nu A^\nu = 0$) achieves the result

$$\delta_\nu F^{\mu\nu} = \delta_\nu\delta^\nu A^\mu = \Box A^\mu = -e\bar{\psi}\gamma^\mu\psi \tag{2.23}$$

where $\Box = \delta_\nu\delta^\nu$ is the d'Alembert operator. We can immediately recognise that the four-potential and associated charge current distribution are related through Maxwell's equations

$$\Box A^\mu = j^\mu. \tag{2.24}$$

For a transition of our particle between an initial state i with momentum p_i and final state f with momentum p_f, the transition current can be written as

$$j_\mu^{fi} = \bar{u}_f\gamma_\mu u_i e^{i(p_f-p_i)\cdot x} \tag{2.25}$$

and it is simple to show thereafter that the solution to Maxwell's equations, Eqn. 2.24 for A^μ is

$$A^\mu = -\frac{j_\mu^{fi}}{(p_i-p_f)^2} = -\frac{j_\mu^{fi}}{q^2} \tag{2.26}$$

where $q = p_i - p_f$ is the four momentum transfer.

To achieve the transition amplitude, we require the Hamiltonian density. The canonical momenta conjugates to the fermion and gauge fields respectively are

$$\begin{aligned}\pi_\psi &= \frac{\delta\mathscr{L}}{\delta(\delta_0\psi)} = \frac{\delta(\bar{\psi}i\gamma^\mu\delta_\mu\psi)}{\delta(\delta_0\psi)} = \bar{\psi}i\gamma^0\\ \pi_{\bar{\psi}} &= \frac{\delta\mathscr{L}}{\delta(\delta_0\bar{\psi})} = 0\\ \pi^i &= \frac{\delta\mathscr{L}}{\delta(\delta_0 A_i)} = \frac{\delta(-F_{\mu\nu}F^{\mu\nu})}{\delta(\delta_0 A_i)} = \frac{\delta((\delta_0 A_i - \delta_i A_0)F^{0i})}{\delta(\delta_0 A_i)} = F^{0i}.\end{aligned}\tag{2.27}$$

We can use the fact that $F^{0i} = -F_{0i}$ to conclude that $\pi^i = -F_{0i}$, and also since the photon field has no time derivative that $\pi^0 = 0$, and write the Hamiltonian density as

$$\mathscr{H} = \pi_\psi \delta_0 \psi + \pi_{\bar{\psi}} \delta_0 \bar{\psi} + \pi^\mu \delta_0 A_\mu - \mathscr{L} = \bar{\psi} i \gamma^0 \delta_0 \psi + \pi^i \delta_0 A_i - \mathscr{L}_{\text{QED}}. \tag{2.28}$$

With some rearrangement, re-expression in terms of the Euler-Lagrange equations, and substituting $\delta_0 \psi$ and $\delta_0 A_i$ where required, we can write the Hamiltonian density as

$$\mathscr{H}_{\text{QED}} = \bar{\psi}(-i\gamma^0\gamma^i\delta_i + m)\psi + (\pi^i\pi^i + (\nabla \times \vec{A})^2) - e\bar{\psi}\gamma^\mu\psi A_\mu \tag{2.29}$$

where the last term is the interacting term which forms the interaction Hamiltonian density $\mathscr{H}_{\text{int}}$. For completion, the full Hamiltonian, which is not required further, is

$$H = \int d^3x \mathscr{H}_{\text{QED}}. \tag{2.30}$$

Now, the transition between initial and final states is described by the S matrix

$$S = T \exp\left(-i \int d^4x \mathscr{H}_{\text{int}}(x)\right) \tag{2.31}$$

where T is the time ordering operator. For a small coupling constant, which is true as discussed for QED (generally), we can perform a power expansion of S,

$$S = 1 + (-i)\int d^4x \mathscr{H}_{\text{int}}(x) + \frac{(-i)^2}{2!}\int d^4x d^4y T[\mathscr{H}_{\text{int}}(x)\mathscr{H}_{\text{int}}(y)] + \dots . \tag{2.32}$$

We can simplify this as $S = 1 + T_{fi}$ where T_{fi} is the transition amplitude. The transition between states is then described by

$$\langle i|S|f\rangle = \delta_{fi} + \langle i|T_{fi}|f\rangle = (2\pi)^4\delta^4(p_f - p_i)M_{fi} \tag{2.33}$$

where M_{fi} is the invariant matrix element calculable from Feynman diagrams. To leading-order in the perturbation theory then, the transition amplitude from initial state i to final state f for a transition current j_μ^{fi} is

$$T_{fi} = \int \bar{\psi}_f \gamma_\mu A^\mu \psi_i d^4x = -e\int j_\mu^{fi} A^\mu d^4x. \tag{2.34}$$

We need to extend this from a particle scattering from a fixed potential, to two particles scattering from one another. Assuming both particles are spin 1/2, then the transition amplitude for scattering between two currents j_1^μ and j_2^μ is

$$T_{fi} = -i\int j_1^\mu \frac{1}{q^2} j_{\mu,2} d^4x = -ie^2\int \bar{\psi}_{f,1}\gamma_\mu\psi_{i,1}\frac{1}{q^2}\bar{\psi}_{f,2}\gamma^\mu\psi_{i,2}d^4x \tag{2.35}$$

Finally, while the derivation is outside the scope of this work, Feynman's functional integral method allows us to read the Feynman rules for vertices directly from the Lagrangian of an interacting theory. The two terms in the free Lagrangian of Eqn. 2.13 yield the Dirac and EM propagators for the electrons and photons respectively.

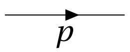

$$= \int \frac{d^4p}{(2\pi)^4}\frac{ie^{-ip\cdot(x-y)}}{\not{p} - m + i\epsilon}$$

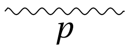

$$= \int \frac{d^4q}{(2\pi)^4}\frac{-ig_{\mu\nu}e^{-iq\cdot(x-y)}}{q^2 + i\epsilon}. \tag{2.36}$$

The interaction term in the QED Lagrangian of Eqn. 2.19 provides the QED vertex,

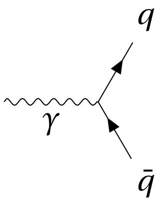

$$= ie\gamma^{\mu}\int d^4x. \tag{2.37}$$

Elastic scattering of electrons from nucleons is mediated by an exchange of a photon via QED. As such this is the first step towards describing the reaction of interest. In the next section we will derive the relativistic scattering cross section for spin 1/2 point particles off a fixed target, which reflects the GEN-II experimental setup.

2.2.2 Mott Scattering

Mott, or spin-coupled Coulomb scattering, is the relativistic scattering of two particles with spin. Consider again the two body reaction drawn in Fig. 2.2, where a spin-1/2 electron with four-momentum p_1 strikes an arbitrary spin-1/2 particle with four-momentum p_2, resulting in a scattered electron with four-momentum p_3 and a recoiling target particle with four-momentum p_4. Neglecting the nucleon structure for now, we can use this to approximate the electron-proton scattering cross section. The transition rate from initial to final states W_{fi} gives the probability of transition per unit time per target particle through Fermi's second Golden Rule

$$W_{fi} = \frac{|T_{fi}|^2}{tV} = \frac{2\pi}{\hbar}\left|M_{fi}\right|^2\rho_f, \tag{2.38}$$

where t is the time interval, V is the interaction volume, ρ_f is the resultant density of final states, T_{fi} is the transition amplitude and M_{fi} is the matrix element. The differential cross section can be expressed as

$$d\sigma = \frac{W_{fi}}{\Phi}dQ^2 \tag{2.39}$$

for the flux of initial beam particles Φ and the Lorentz invariant phase space dQ^2. It can be shown that working in the centre of mass frame, the differential cross section can be expressed as

$$\frac{d\sigma}{d\Omega} = \frac{1}{64\pi^2 s}\langle |M_{fi}|^2 \rangle \tag{2.40}$$

where s is the centre-of-mass energy squared, which is equal to $M^2 + 2ME + 2m_e$ for a fixed target, where E is the energy of the incoming electron, m_e is the electron mass and M is the mass of the target. For $M \gg m_e, E$, s can be approximated as M^2, as was the case in the original derivation by Mott.

The matrix element can be simply written down from the Feynman diagram using the Feynman rules, and the complex square can be taken,

$$\begin{aligned} M_{fi} &= -\frac{e^2}{(p_1 - p_3)^2}[\bar{u}_3 \gamma^\mu u_1][\bar{u}_4 \gamma_\mu u_2] \\ \langle |M_{fi}|^2 \rangle &= \frac{8e^4}{(p_1 - p_3)^4}[(p_1 \cdot p_2)(p_3 \cdot p_4) + (p_1 \cdot p_4)(p_2 \cdot p_3) \\ &\quad - m_e^2 (p_2 \cdot p_4) - M^2 (p_1 \cdot p_3) + 2m_e^2 M^2], \end{aligned} \tag{2.41}$$

where e is the electric charge of the electron. From Fig. 2.2, if we neglect the target particle recoil for now, then the four-vectors can be constructed as

$$\begin{aligned} p_1 &= (E_1, \vec{p}_1) = (E, 0, 0, E), \\ p_2 &= (M, 0), \\ p_3 &= (E_3, \vec{p}_3) = (E, E\cos\theta, 0, E\sin\theta), \\ p_4 &= (M, 0), \end{aligned} \tag{2.42}$$

where E' is the energy of the scattered electron and we have neglected the electron mass, since $m_e \ll M, E$. We can now explicitly calculate the individual components of the matrix element,

$$\begin{aligned} (p_1 - p_3)^2 &= -4E^2 \sin^2 \frac{\theta}{2} \\ p_1 \cdot p_3 &= 2E^2 \sin^2 \frac{\theta}{2} \\ p_2 \cdot p_4 &= M^2 \\ p_1 \cdot p_2 = p_3 \cdot p_4 = p_1 \cdot p_4 &= p_2 \cdot p_3 = ME, \end{aligned} \tag{2.43}$$

where θ is the scattering angle of the electron, with respect to the incoming beam. Putting all of this into Eqn. 2.40 and substituting $\alpha = e^2/4\pi$, yields the Mott differential cross section

$$\left(\frac{d\sigma}{d\Omega}\right)_{\text{MOTT}} = \frac{\alpha^2}{4E^2\sin^4\frac{\theta}{2}}\cos^2\frac{\theta}{2} \tag{2.44}$$

where we recognise the first term as the Rutherford differential cross section with $E_k = E(E_k \gg m_e)$, and the second term is the overlap between initial/final state wavefunctions of the electron, arising from the quantum mechanics of spin-$\frac{1}{2}$ particles.

In the limit that the recoil is no longer considered negligible, the electron loses energy in the collision and the cross section must be modified. The scattered electron and target four-vectors become

$$\begin{aligned} p_3 &= (E', E'\cos\theta, 0, E'\sin\theta) \\ p_4 &= (E_4, \vec{p}_4). \end{aligned} \tag{2.45}$$

We can simplify the terms involving p_4 in the matrix element by momentum conservation, $p_4 = p_1 + p_2 - p_3$. Re-solving each of the matrix element components and performing the substitution again now yields

$$\begin{aligned} \frac{d\sigma}{d\Omega} &= \frac{\alpha^2}{4E^2\sin^4\frac{\theta}{2}}\frac{E'}{E}\left(\cos^2\frac{\theta}{2} - \frac{q^2}{2M^2}\sin^2\frac{\theta}{2}\right) \\ &= \left(\frac{d\sigma}{d\Omega}\right)_{\text{MOTT}}\frac{E'}{E}\left(1 - \frac{q^2}{2M^2}\tan^2\frac{\theta}{2}\right). \end{aligned} \tag{2.46}$$

where the fraction E'/E represents the necessary recoil correction and the new sine term arises from the magnetic interaction between the two spins. Note that we are still only considering the case of relativistic spin-1/2 point particle scattering. In the next section we will fully encapsulate the nucleon structure of our real world target particle.

2.3 Quantum Chromodynamics and the Nucleon

We have described the relativistic scattering of two spin-1/2 point particles in the fixed target frame, with the target mass and recoil taken into consideration. The final requirement, and ultimately the motivation of all of our efforts, is to describe the structure of the interacting nucleon. This structure arises from Quantum Chromodynamics (QCD). QCD is the theory of the strong force which binds colour charged quarks and gluons into composite colourless mesons and baryons. Described by the SU(3) group, QCD is a non-Abelian gauge theory in which the corresponding bosons (8 gluons) are themselves charged under the group, so exhibit self interactions. Similarly to the QED case, virtual gluon and quark-antiquark pairs permeate the QCD vacuum. However now the gluon self coupling results in additional virtual gluons. If QCD were Abelian, then the beta function would take the same form as that of QED. However, the additional virtual gluon components, which are negative, complicate the situation. The calculation of the QCD vacuum polarisation is non-trivial and outside the scope of this work, however a detailed calculation is provided in Ref. [30]. At one-loop approximation the beta function is

$$\beta(\alpha_s) = -\left(11 - \frac{2n_f}{3}\right)\frac{\alpha_s^2}{2\pi} \tag{2.47}$$

where n_f is the number of quark flavours. It is clear that for $n_f < \frac{33}{2} \approx 16$ the ensuing beta function is overall negative resulting in an "anti-screening" effect. As such with six quark flavours the coupling constant $\alpha_s \equiv \alpha_s(Q^2)$ decreases with the energy scale.

Above the characteristic energy scale of QCD, Λ_{QCD}, perturbative approaches to the theory are possible. However, the scaling nature of α results in large enough values at low energies, that perturbative cutoffs no longer work since subsequent power of α are no longer negligible, i.e. $\alpha_s = \alpha_s^2 = \alpha_s^3 = ... = 1$. Fundamentally understanding the nature of QCD requires characterising behaviour at both low and high Q^2. While pQCD is probed at ever increasing energies by collaborations such as those at CERN with the Large Hadron Collider (LHC) [31], non-perturbative studies such as lattice QCD [32] and hadron spectroscopy [33] seek to understand the structure of hadrons, and validate the plethora of multiplet resonance states predicted by QCD. Of this zoo of hadrons, only two stable particles are formed; the proton and neutron (nucleons). Together, these constitute the majority of the visible matter in our universe.

We still need to understand confinement and the dynamics of QCD which are responsible for our observed properties of the nucleon which are traditionally used to classify a particle. This is the focus of many modern experiments including those at JLab. A key objective of modern physics is answering three seemingly simple questions: Why do only nucleons exist in stable states? How do their masses and spin emerge from QCD? And how is their internal structure characterised?

2.3.1 Particles with Structure

To adequately describe experimental data we need to extend our formalism to scattering of an electron from a target with arbitrary structure in order to properly parameterise the cross section of nucleon scattering. Consider once again the transition amplitude for two interacting currents with a momentum transfer of q, where we take $j_2^\mu \to J^\mu$ to be the nucleonic current and again j_μ represents the electron current,

$$T_{fi} = -i\int j^\mu \frac{1}{q^2} J_\mu d^4x. \tag{2.48}$$

The most general form for J_μ is a Lorentz 4-vector, therefore we must list all linearly independent 4-vector quantities which can describe the interaction. All possible 4x4 matrices can be constructed from the 16 linearly independent matrices

$$I, \gamma^\mu, \gamma^5, \sigma^{\mu\nu}, \gamma^\mu\gamma^5 \tag{2.49}$$

where we have constructed

$$\gamma^5 = i\gamma^0\gamma^1\gamma^2\gamma^3 \tag{2.50}$$

$$\sigma^{\mu\nu} = \frac{i}{2}(\gamma^\mu\gamma^\nu - \gamma^\nu\gamma^\mu) \tag{2.51}$$

with the final remaining available four-vectors being the incoming and outgoing momenta, p, p' respectively. γ^5 is a pseudoscalar which is anti commuting with the parity operator, and since parity is conserved in the electromagnetic interaction then γ^5 can be removed from consideration. The most general form for the hadronic current then is

$$\begin{aligned} J^\mu =& e\bar{u}(p')\Big[\gamma^\mu K_1(q^2) + i\sigma^{\mu\nu}(p'-p)_\nu K_2(q^2) + i\sigma^{\mu\nu}(p'+p)_\nu K_3(q^2) \\ &+ (p'-p)^\mu K_4(q^2) + (p'+p)^\mu K_5(q^2)\Big] u(p) e^{i(p-p')\cdot x}. \end{aligned} \tag{2.52}$$

for arbitrary functions $K(q^2)$ [23]. A useful tool in simplifying this expression is the Gordon decomposition identity,

$$\bar{u}\gamma^\mu u = \frac{1}{2M}\bar{u}(p^\mu + p'^\mu + i\sigma^{\mu\nu}(p'_\nu - p_\nu))u. \tag{2.53}$$

By applying this, the $(p'+p)^\mu$ terms can be rewritten as linear combinations of the γ^μ and $\sigma^{\mu\nu}$ terms. So the general form reduces to

$$J^\mu = e\bar{u}(p')\Big[\gamma^\mu K_1(q^2) + \frac{i\kappa}{2M}\sigma^{\mu\nu}q_\nu K_2(q^2) + q^\mu K_3(q^2)\Big] u(p) e^{i(p-p')\cdot x}. \tag{2.54}$$

Furthermore we must enforce current conservation $\partial_\mu J^\mu = q_\mu J^\mu = 0$, and any terms which do not vanish for arbitrary K must have $K = 0$. The K_1 term vanishes via the Dirac equation

$$\gamma^\mu q_\mu = \gamma^\mu(p^\mu - p'^\mu) = (m - m) = 0. \tag{2.55}$$

The K_2 term also vanishes after some algebraic manipulation due to the antisymmetric nature of $\sigma^{\mu\nu}$, leaving only an K_3 term in q^2. Hence K_3 must be zero. Rewriting the remaining K terms as F, the resultant hadronic current is

$$J^\mu = e\bar{u}(p')\Big[\gamma^\mu F_1(q^2) + \frac{i\kappa}{2M}\sigma^{\mu\nu}q_\nu F_2(q^2)\Big] u(p) e^{i(p-p')\cdot x}. \tag{2.56}$$

2.3.2 Elastic Scattering in OPEX

A crucial ingredient in the theoretical formalism for elastic electron-nucleon (eN) scattering is the one-photon-exchange approximation (OPEX), the assumption that scattering via exchange of a single photon is the dominant process, since higher-order diagrams should be smaller by a factor $\alpha = 1/137$. The OPEX is often interchangeably called the Born approximation, since the resultant scattering properties are analogous with the First Born Approximation that second order terms in the Lippmann-Schwinger equation for scattering of a wave-vector in a potential can be neglected [34]. In this work we will assume the First Born Approximation is a good and valid approximation, i.e. that the scattering is relatively weak. Efforts to measure the effects of higher order terms (two-photon exchange or TPE) exist in the literature [35, 36], and this idea is discussed in Sec 2.5.1. In the OPEX, the electron-nucleon elastic scattering amplitude is described at a first order by the product of the leptonic and hadronic tensor currents, l_μ and J_μ.

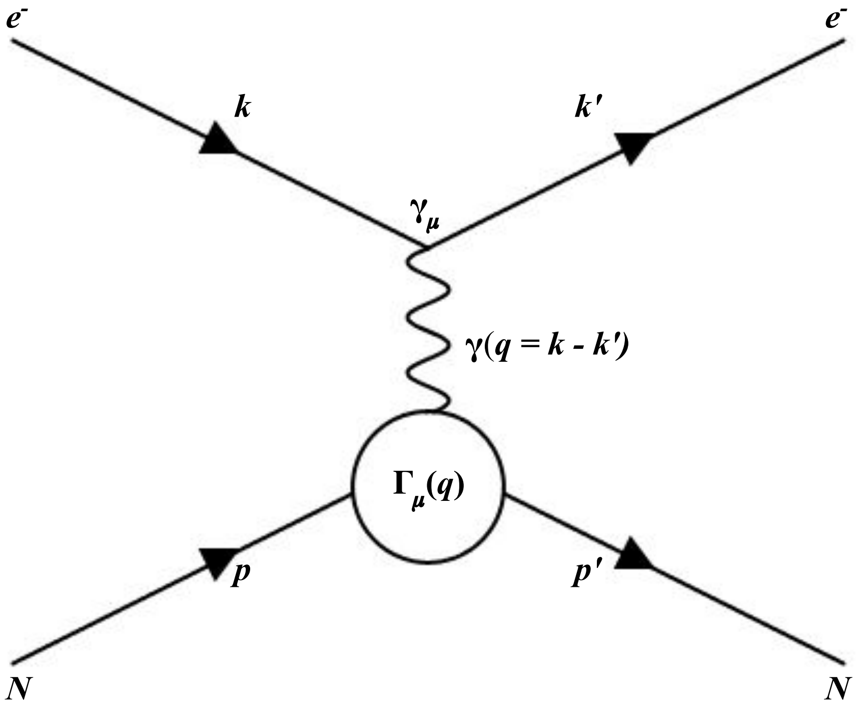

Figure 2.3: Diagram of elastic scattering between an electron and nucleon. The structure is encoded in the born term Γ_μ of the nucleon vertex.

Consider the scattering shown in Fig. 2.3 of an incident electron with four-momentum $k \equiv (E, \mathbf{k})$ off a nucleon of mass M which is taken to be initially at rest in the lab frame, therefore having four-momentum $p \equiv (E_n, \mathbf{p}) = (M, \mathbf{0})$. The electron scatters with four-momentum $k' \equiv (E'_e, \mathbf{k}')$ and the nucleon recoils correspondingly with a four-momentum $p' \equiv (E'_n, \mathbf{p}')$ having absorbed the virtual photon which carries four-momentum transfer

$q \equiv k - k'$. The Lorentz invariant OPEX amplitude can be written as

$$iM_{fi} = \frac{-i}{q_\mu^2} l_\mu J^\mu = \frac{-i}{q_\mu^2} [ie\bar{u}(k')\gamma^\nu u(k)][-ie\bar{v}(p')\Gamma^\mu(p',p)v(p)]. \tag{2.57}$$

Here the most general form for J_μ which satisfies relativistic invariance and current conservation, and also includes an internal structure is applied. We demonstrated the form of this in Eqn. 2.56. As such Γ^μ represents the photon-nucleon vertex function (or Born term) which contains the nucleon structure information. It has the form

$$\Gamma^\mu = \gamma^\mu F_1(Q^2) + \frac{i\sigma^{\mu\nu} q_\nu}{2M} \kappa_j F_2(Q^2) \tag{2.58}$$

where M is the nucleon mass, κ is the anomalous magnetic moment in units of nuclear magnetons $\mu_N = e\hbar/(2M_p)$, and $Q^2 \equiv -q^2 = -(k-k')^2 > 0$, is the four-momentum transfer squared. The Dirac and Pauli form factors are the only structure functions allowed in the Born term by relativistic invariance [37]. The Dirac form factor F_1 describes elastic scattering where the spin state of the nucleon is the same in the initial and final states (helicity conserving). The Pauli form factor F_2 describes the case in which the initial and final spin states are flipped (helicity non-conserving). The Dirac and Pauli form factors are analytically expressible in the limit $Q^2 \to 0$, where Q^2 represents the virtuality of the photon mediator in the scattering reaction,

$$\begin{aligned} F_{1p}(0) &= 1, \quad F_{2p}(0) = \kappa_p \\ F_{1n}(0) &= 0, \quad F_{2n}(0) = \kappa_n \end{aligned} \tag{2.59}$$

for the proton (subscript p) and neutron (subscript n) respectively. Here $\kappa_p = \mu_p - 1$ and $\kappa_n = \mu_n$ are the proton and neutron anomalous magnetic moments respectively with $\mu_p =$ 2.7928 μ_N and μ_n = -1.9130 μ_N.

In the lab frame, the differential cross section for eN scattering is then expressible as

$$\frac{d\sigma}{d\Omega} = \left(\frac{d\sigma}{d\Omega}\right)_{\text{MOTT}} \frac{E'}{E} \left(F_1^2(Q^2) + \tau \left[F_2^2(Q^2) + 2[F_1(Q^2) + F_2(Q^2)]^2 \tan^2\frac{\theta}{2} \right] \right) \tag{2.60}$$

with $\tau = \frac{Q^2}{4M^2}$, sometimes referred to as the threshold. This cross section is immediately fairly complicated, in particular containing an interference term between F_1 and F_2. It is common and more convenient to express the experimental cross section in terms of the Sachs electric and magnetic form factors G_E and G_M [38], linear combinations of F_1 and F_2 given as

$$\begin{aligned} G_E &= F_1 - \tau F_2 \\ G_M &= F_1 + F_2. \end{aligned} \tag{2.61}$$

The experimental differential scattering cross section can then be written as

$$\frac{d\sigma}{d\Omega} = \left(\frac{d\sigma}{d\Omega}\right)_{\mathrm{MOTT}} \frac{E'}{E} \left[\frac{G_E^2 + \frac{\tau}{\epsilon} G_M^2}{1+\tau}\right] \tag{2.62}$$

where $\epsilon = \left[1 + 2(1+\tau)\tan^2\frac{\theta}{2}\right]^{-1}$. In the OPEX ϵ can be interpreted as the polarisation of the virtual photon. Eqn. 2.62 is referred to as the Rosenbluth differential cross section, which describes the unpolarised scattering of electrons off nucleons with extended structure.

2.4 Physical Interpretation of Nucleon Form Factors

The electromagnetic form factors describe the spatial distributions of electric charge and current inside nucleons. In the Breit frame, G_E and G_M are the Fourier transforms of the electric and magnetic moment distributions respectively. This is a transformation between the conjugate momentum and position spaces.

2.4.1 Charge Distributions, Dipoles and Fourier Transforms

The general form of the Fourier transform for a charge distribution ρ is

$$F(q) = \int d^3r \rho(\vec{r}) e^{i\vec{q}\cdot\vec{r}}. \tag{2.63}$$

For a distribution with spherical symmetry this can be expanded as

$$\begin{aligned} F(q^2) &= \int dr r^2 \rho(r) \int\int d\phi \sin\theta d\theta e^{iqx\cos\theta} \\ &= 2\pi \int dr r^2 \rho(r) \int \sin\theta d\theta \\ &= \frac{4\pi}{q} \int dr r \rho(r) \sin(qr) \end{aligned} \tag{2.64}$$

where the physics is encoded purely in the radial part of the distribution, r.

Fig. 2.4 shows the shape of various common charge distributions associated with particles, and the resultant Fourier transformation in the Born approximation which yields a form factor distribution. In particular a charge distribution with an exponential form results in a form factor which takes the the shape of a dipole of the form

$$F(q^2) = \frac{F(0)}{\left(A + \frac{|q^2|}{B}\right)^2} \tag{2.65}$$

for arbitrary constants A, B. An exponential form is a natural anzatz for a charge distribution and early measurements of proton form factors followed this giving rise to the dipole form

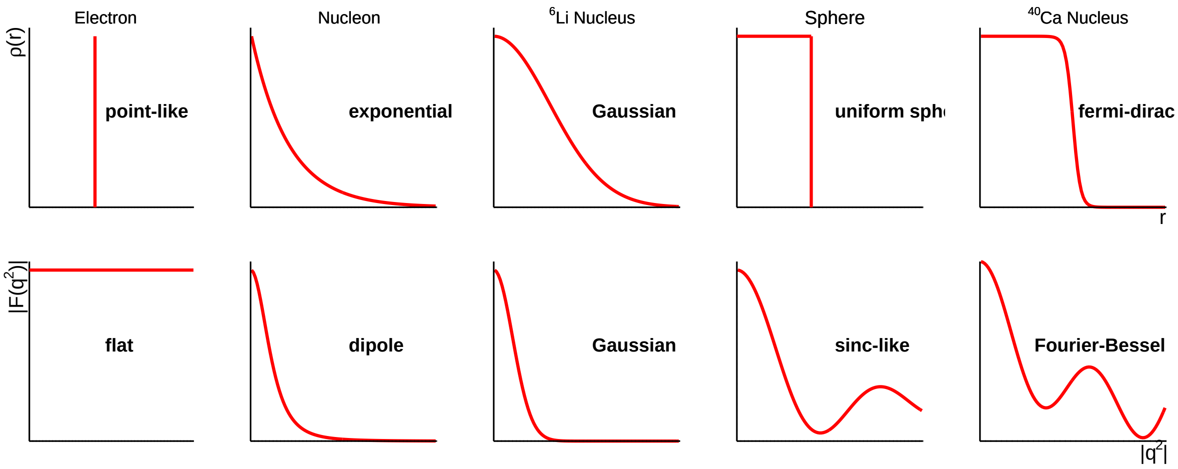

Figure 2.4: The relationships between various charge distributions and their corresponding form factors out of Fourier transformations in the Born approximation.

factor,

$$G_D(Q^2) = \left(1 + \frac{Q^2}{0.71}\right)^{-2}. \tag{2.66}$$

It will be seen that the dipole form factor parameterisation described both the electric and magnetic charge distributions of the proton well, up to around 5 GeV^2. This suggests then that at large distances, the proton appears to behave as a dipole charge. It will also be seen that deviations from this relationship begin to appear at large momentum transfer, suggesting that the intricate substructure of the nucleons manifests at relatively small scales.

2.4.2 Nucleon Size

In the low q limit, the sine part of the expression can be expanded in a Taylor series such that

$$\begin{aligned} F(q^2) &= \frac{4\pi}{q}\int dr\, r\rho(r)\left(qr - \frac{(qr)^2}{3!} + ...\right) \\ &= 4\pi\int dr\, r^2\rho(r) - \frac{q^2}{6}4\pi\int dr\, r^4\rho(r) + ... \\ &= Z\left(1 - \frac{q^2}{6}\langle r^2\rangle + ...\right) \end{aligned} \tag{2.67}$$

where $\langle r^2\rangle = \int d^3r\, r^2\rho(r) = 4\pi\int dr\, r^4\rho(r)$ is the RMS charge radius of the nucleon. We can see then that to zeroth order the form factor is purely the charge, and the first order correction is proportional to the RMS radius. This allows the RMS radius to be extracted from data by measuring the form factors at low q and deriving it via

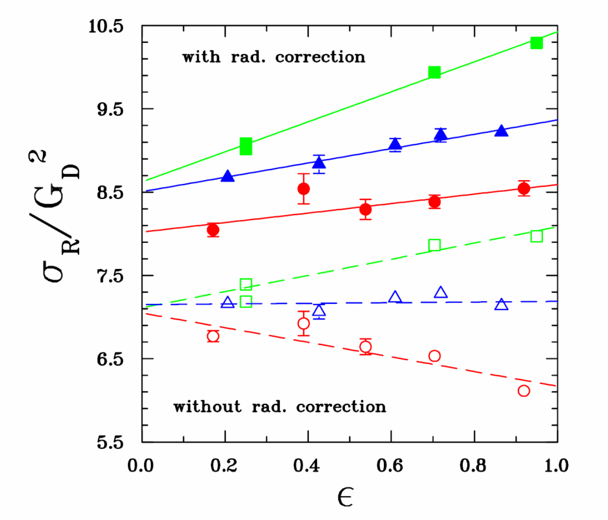

Figure 2.5: Cross section data points from the analysis of [39] with and without radiative corrections.

$$\langle r^2 \rangle = -\frac{6}{F(0)} \frac{dF(q^2)}{dq^2}\bigg|_{q=0}. \tag{2.68}$$

2.5 Rosenbluth Separation

Until the early 1990s, Rosenbluth separation was the only method available to obtain separated values of G_E^2 and G_M^2 for both the proton and neutron. Rosenbluth separation exploits the linear nature of ϵ in the form factor term of the differential cross section in Eqn. 2.40. A reduced cross section can be defined as

$$\sigma_R = \frac{\left(\frac{d\sigma}{d\Omega}\right)_{\text{EXP}}}{\left(\frac{d\sigma}{d\Omega}\right)_{\text{MOTT}} \frac{E'}{E}} \frac{\epsilon(1+\tau)}{\tau} = \frac{\epsilon}{\tau} G_E^2 + G_M^2, \tag{2.69}$$

where $(d\sigma/d\Omega)_{\text{EXP}}$ is the cross section measured experimentally. By using different beam energies and scattering angles, σ_{R} could be measured a fixed Q^2 and varying ϵ as shown by the data from Ref. [39] in Fig. 2.5. From multiple measurements of the cross section at varying ϵ, values for G_E^p and G_M^p can be directly obtained from the slope and intercept of the fit respectively. As already mentioned and will be seen, early low Q^2 proton form factor data showed that the dipole was a very good approximation for G_E^p in particular. As such it has become a common practice to report the form factor values as a ratio to G_D, namely G_E/G_D and $G_M/\mu G_D$; and then as a result the ratio is reported as $\mu G_E/G_M$.

2.5.1 Radiative Corrections

As previously discussed, the interpretation of cross section data in terms of Eqn. 2.62 (the Rosenbluth differential cross section), relies on the concept of single photon exchange (OPEX). In reality, measurements of form factors via Rosenbluth separation must be corrected for radiative effects which introduce multiple photon contributions. At first order, there are several mechanisms which required correction: bremsstrahlung from incident or scattered electron; vertex photon exchange; vacuum polarisation and self-energy, shown in Fig. 2.6. The first realisation of the required calculative techniques was by Mo and Tsai in 1969 [40] and was refined in 2000 by Maximon and Tjon [41]. These calculative tools have allowed for scattering cross section measurements beyond an accessible region of $Q^2 = 10$ GeV², using the Rosenbluth separation method. The effect on the magnitude of cross section measurements as a result of two-photon radiative corrections is illustrated in Fig. 2.5. However, these corrective procedures can typically only evaluated in the phase space region in which one of the two photons has a very small momentum relative to the total momentum transfer [42]. As will be seen, measurements exploiting polarisation degrees of freedom in the early 2000's were found to have large disagreements with existing Rosenbluth form factor data. This observed discrepancy between cross-section and polarisation data at high-Q^2 is now believed to be due to explicitly "hard" two-photon exchange in which both photons can carry large momentum. This is impossible to calculate model-independently and has therefore been neglected in standard radiative correction prescriptions [35, 36]. Radiative corrections have a much smaller impact in double polarisation experiments however, as much of their effect cancels out in the asymmetry.

2.5.2 Nuclear Corrections

Extracting the proton form factors via ep scattering is fairly straightforward since hydrogen is a free proton target (while H_2 exists as a diatomic molecule, the separation between each hydrogen nucleus (proton) is on the order of 1 pm and as such they can be considered "free" on the nuclear scale of 1 fm). Measurements utilising nuclear targets require corrections to account for nuclear effects which arise as a result of the target being a bound multi-nucleon system. As will be seen early unpolarised G_n^E extractions from ed scattering in particular suffered from large systematic errors as a result of the model dependence on the choice of deuteron wavefunction. Additionally electron-nucleon scattering from a nucleus is often modelled in the plane-wave impulse approximation (PWIA or IA) in which both the initial and final state electrons can be considered plane-wave states [44].

In the case of this experiment we are dealing with a semi-exclusive electro-disintegration reaction of the form $^3\text{He}(e, e'N)X$ where N is the scattered nucleon and X is the undetected spectator system. This nuclear break up may be modelled by several processes [45]:

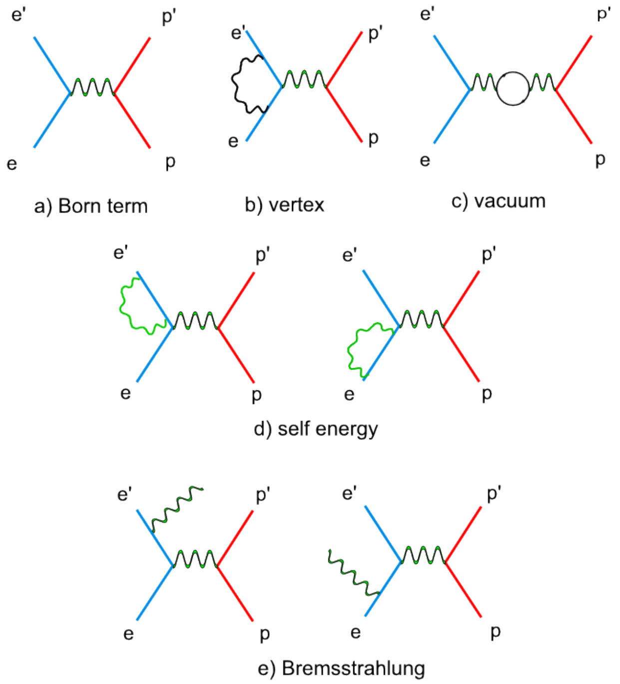

Figure 2.6: The Born term and first order radiative correction diagrams for the electron in ep scattering. Figure from [43].

1. single nucleon knock-out with no further interaction, i.e. PWIA;
2. (single or multiple) rescattering of the struck nucleon off spectator nucleon(s), known as final state interactions (FSI);
3. coupling of the virtual photon to a virtual meson which is exchanged between two nucleons, often called meson exchange currents (MEC);
4. coupling of the virtual photon to the nucleon which has first gone into an excited state, known as an isobar configuration (IC).

These processes are illustrated in Fig. 2.7. Scattering in the PWIA ignores contributions from FIS, MEC and IC, and also has to be corrected for relativistic distortion to the wavefunction at $Q^2 > 1$. A nuclear model of electro-disintegration is used to correct the data for this, and is discussed in Sec. 5.10

2.6 Polarisation Degrees of Freedom and the E12-09-016 Technique

The aim of this experiment is to extend the small data set for G_E^n up to the as of yet unexplored region of 10 GeV^2 in a series of three double polarisation measurements. Double polarisation experiments either measure the two non-zero components of the polarisation

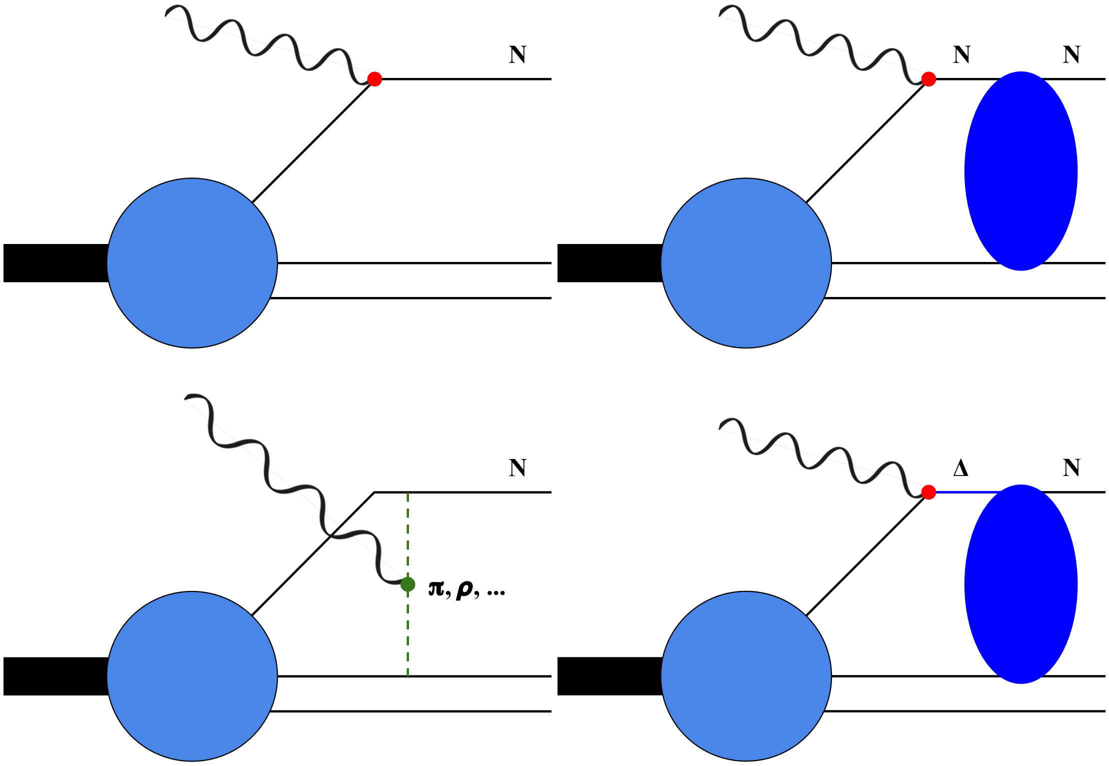

Figure 2.7: Pictorial diagrams of the leading-order effects for each electro-disintegration process. (Top Left) PWIA, (Top Right) FSI, (Bottom Left) MEC, (Bottom Right) IC.

of the recoiling nucleon for longitudinally polarised electrons incident on an unpolarised nucleon target, or the asymmetry in the scattering of longitudinally polarised electrons by polarised protons or neutrons.

In the former, the recoil polarisation method, the polarisation of the recoiling nucleon has two polarisation components, transverse, P_t, and parallel, P_l , to the momentum transfer q. It was demonstrated by Akhiezer that these could be described by

$$\begin{aligned} I_0 P_t &= -2\sqrt{\tau(1+\tau)} G_E G_M \tan\frac{\theta}{2} \\ I_0 P_l &= \frac{1}{M}(E+E')\sqrt{\tau(1+\tau)} G_M^2 \tan^2\frac{\theta}{2} \end{aligned} \tag{2.70}$$

where θ, τ, E, E' retain their meaning from before and $I_0 \propto G_M^2 + \frac{\tau}{\epsilon} G_E^2$ [46]. The form factor ratio can then be extracted by directly measuring both polarisation components in a polarimeter. The associated systematic uncertainties are much smaller than in techniques involving cross section measurements.

E12-09-16 utilises the latter technique, scattering a longitudinally polarised electron off a transversely polarised ^{3}He target, which can be treated as an effective polarised neutron target. In beam-target asymmetry measurements, the form factors can be obtained from the beam helicity asymmetry, keeping the electron and nucleon detection angles constant, but alternating the helicity of the electron beam. In the Born approximation, the elastic e-N scattering cross section can be expressed as

$$\sigma_h = \Sigma + h\Delta \tag{2.71}$$

where Σ represents the unpolarised elastic differential cross section and Δ represents the polarised contribution which is non-zero when the electron is longitudinally polarised with helicity $h = \pm 1$. The asymmetry in elastic e-N scattering is then defined as

$$A_N = \frac{\sigma_+ - \sigma_-}{\sigma_+ + \sigma_-} = \frac{\Delta}{\Sigma}. \tag{2.72}$$

The unpolarised cross section Σ for elastic scattering off a free nucleon at rest is given by Eqn. 2.62. The polarised part of the cross section is described by [47]

$$\begin{aligned} \Delta = -2\left(\frac{d\sigma}{d\Omega}\right)_{\text{Mott}} \frac{E'}{E}\sqrt{\frac{\tau}{1+\tau}}\tan\frac{\theta}{2}\Big[\sin\theta^*\cos\phi^* G_E G_M + \\ \sqrt{\tau[1+(1+\tau)\tan^2\frac{\theta}{2}]}\cos\theta^* G_M^2\Big], \end{aligned} \tag{2.73}$$

where θ^* and ϕ^* are the polar and azimuthal angles respectively of the target polarisation in the lab frame with respect to the momentum transfer as shown in Fig. 2.8. This quantity

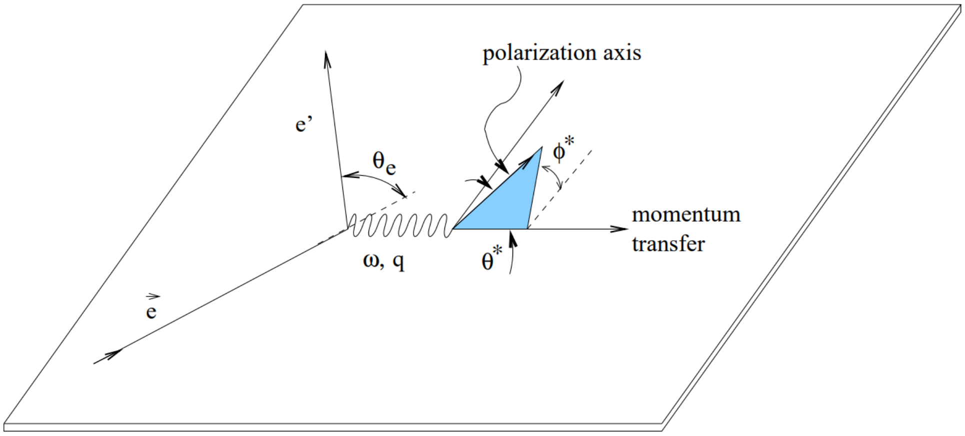

Figure 2.8: Kinematics of double polarised electron scattering. Figure amended from experimental proposal PR12-09-016 [48].

is what is measured in order to extract the form factor ratio in the final analysis.

The measured asymmetry will be reduced in reality due to a number of factors. Polarisation of the electron beam will be less than 1, typically around $P_{\text{beam}} = 0.85$ for JLab. Similarly the ^{3}He target is not 100% polarised and will likely be around $P_{^3\text{He}} = 0.50$. There are also effects which enter due to the effective polarisation of the neutrons in the target, P_n which must be assumed from theory and empirical evidence. Furthermore, numerous scattering backgrounds will complicate the analysis, which will be discussed fully in chapter 5. To name the considered backgrounds briefly; scattering due to the addition of nitrogen in the target, f_{N2}; the dilution from timing accidentals f_{acci}; contributions from pion background in the electron arm, f_π; contamination of the signal from inelastic scattering events, f_{inelas}; and nuclear effects, f_{FSI}.

The experimental asymmetry is then expressed as the product of these reductive contributions. A notation used in recent nucleon form factor literature takes the following form

$$A_{\text{exp}} = P_{\text{beam}} P_{^3\text{He}} P_n D_{\text{N}_2} D_\pi D_{\text{acci}} D_{\text{inelas}} D_{\text{FSI}} A_{\text{phys}} \tag{2.74}$$

where each D term is a direct "dilution factor" resulting from the fractional f contributions, to the final physics asymmetry. However for this thesis and analysis, and to be consistent with ongoing notation in the experimental collaboration we will follow a new notation using explicitly each f and its associated asymmetry

$$A_{\text{phys}} = \frac{A_{\text{raw}} - \Sigma_\chi f_\chi A_\chi}{P_{^3\text{He}} P_n P_{\text{beam}} (1 - \Sigma_\chi f_\chi)} \tag{2.75}$$

where χ sums over scattering from nitrogen, inelastic scattering events, timing accidentals, pion background and nuclear effects, as previously stated. The physics asymmetry can be expressed in terms of the form factors by substituting Eqns. 2.62 and 2.73 into Eqn. 2.72

$$\begin{aligned} A_{\text{phys}} = -\frac{2\sqrt{\tau(1+\tau)}\tan(\theta/2)}{G_E^2 + \frac{\tau}{\epsilon}G_M^2}[&\sin\theta^*\cos\phi^* G_E G_M \\ &+ \sqrt{\tau[1+(1+\tau)\tan^2(\theta/2)]}\cos\theta^* G_M^2] \end{aligned} \tag{2.76}$$

from which the form factor ratio can be extracted when the target polarisation is perpendicular to the momentum transfer within the reaction plane and $\theta^* = \pi/2$, $\phi^* = 0$ or π. Experimentally this is not really the case due to the varying of the momentum transfer direction in each event, non-uniformity of the field along the target and the fact that the central field direction may not be exactly the required value due to fringe effects. In reality, this technique aims to maximise the contribution to the asymmetry from the perpendicular component by keeping θ^* as close to π as possible, typically $\pm$ 10°, and ϕ^* as close to zero as possible, typically $\pm$ 20°. This results in a small reduction to the perpendicular component, and a small contribution from the parallel component, which are directly measurable in the final analysis.

2.7 Existing Data: Form Factors

Tremendous efforts have been made to continue measuring each of the form factors over the last 70 years. A thorough and recent review of the experimental history and pedagogy of each of the form factors is available in [42]. This section will attempt to provide a shortened history of measurement techniques and results. The original cross section measurements by Hoftstadter et al. in the 1950s demonstrated the elegance of eN scattering, tested the validity of the equations derived earlier in this chapter and confirmed the idea of complex nucleon structure. These early measurements of a single proton form factor were able to also be used to estimate the proton radius, which at the time was measured to be 0.77 ± 0.10 fm [12]. The magnetic form factor of the neutron was measured next in 1958 using a liquid deuterium target [49]. Through the second half of the 20th century, nucleon form factors were primarily measured at low Q^2 via the Rosenbluth separation technique. Unpolarised proton form factor measurements from cross section techniques implied a scaling law at low Q^2, $G_E^p/G_M^p \approx 1$. For the neutron it was more complicated due to the lack of a free neutron target, however G_E^n and G_M^n were still measured from quasielastic electron-deuteron scattering cross sections, up to around 0.75 and 5 GeV² respectively.

By the 1990's technology began to allow for exploitation of polarisation degrees of freedom, using polarised electron beams and either unpolarised or polarised targets. Double polarisation measurements of the proton in 2000 from Hall A (GEP-I), suggested a discrepancy in the ratio G_E^p/G_M^p from the Rosenbluth data [50]. By the GEP-II experiment this was all but confirmed [51]. Double polarisation techniques have enabled measurements of G_E^n

in particular that may not have been feasible with cross section methods, owing to the relatively small magnitude of tiny contribution from the electric form factor in the cross section at high Q^2.

Unpolarised Proton Form Factor Measurements

Measurements of G_E^p and G_M^p via cross section methods up to the turn of the century [39, 52–63] produced a data set which spanned over three orders of magnitude from $Q^2 \approx 10^{-2}$ GeV^2 up to beyond 10 GeV^2. The results for the individual form factors G_E^p and G_M^p are shown in Figs. 2.9 and 2.10 respectively. These results showed roughly constant behaviours at low Q^2 for the ratio of form factors with the dipole form factor, leading to the realisation of an apparent scaling law

$$\mu_p \frac{G_E^p}{G_M^p} \approx 1. \tag{2.77}$$

This scaling is demonstrated in Fig. 2.11 which shows the extracted ratios where applicable, for data limited in Q^2 by G_E^p. This was consistent with the QCD prediction that F_{2p}/F_{1p} should behave as $1/Q^2$ asymptotically.

However, at larger Q^2, on the order of 5 GeV^2, G_M^p is observed to begin decreasing, with fairly good consistency within errors. The picture of the electric form factor G_E^p was less clear in this high Q^2 domain, with cross section measurements losing consistency above $Q^2 \approx 1$ GeV^2. This is due to the difficulty in extracting G_E^2 (for either the proton or neutron) at large Q^2 via Rosenbluth separation, for primarily two reasons. Firstly, the $1/\tau$ term which multiplies G_E^2 in Eqn. 2.69 suppresses this term in the cross section as Q^2 increases. Secondly even at relatively small Q^2, following from the scaling relation of Eqn. 2.77 the G_E^2 contribution to the cross section will always be reduced by a factor of $1/\mu_p^2 = 1/7.78 = 0.13$.

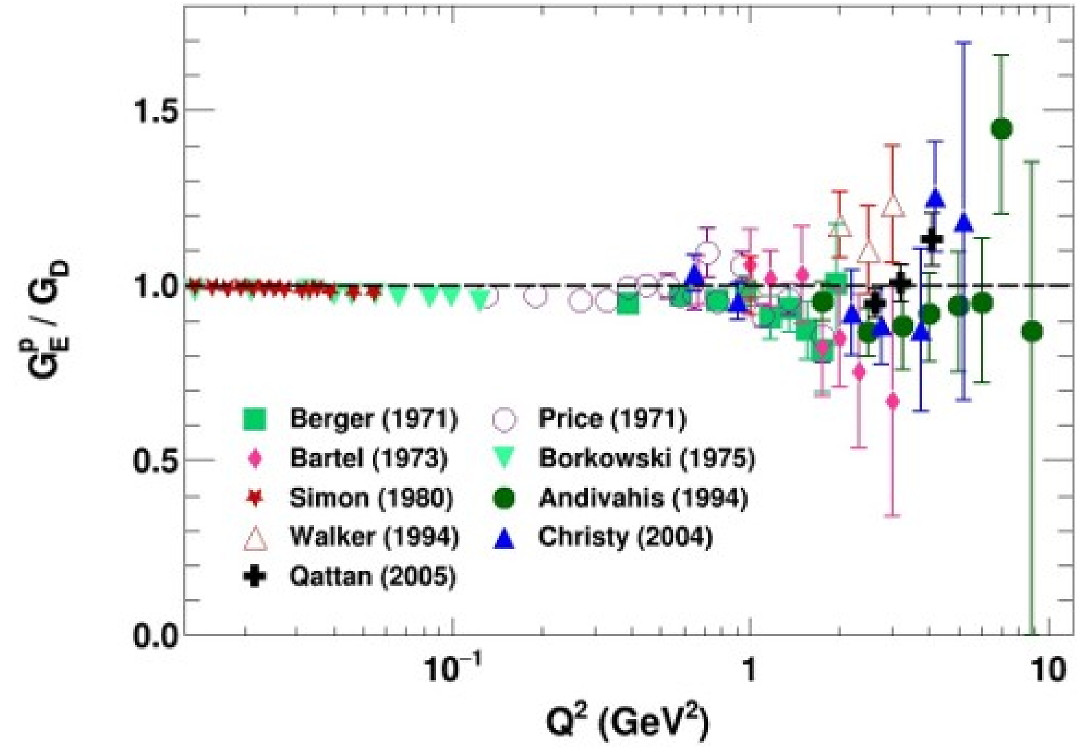

Figure 2.9: World data of measurements for G_E^p obtained via the Rosenbluth separation method. Figure from [64].

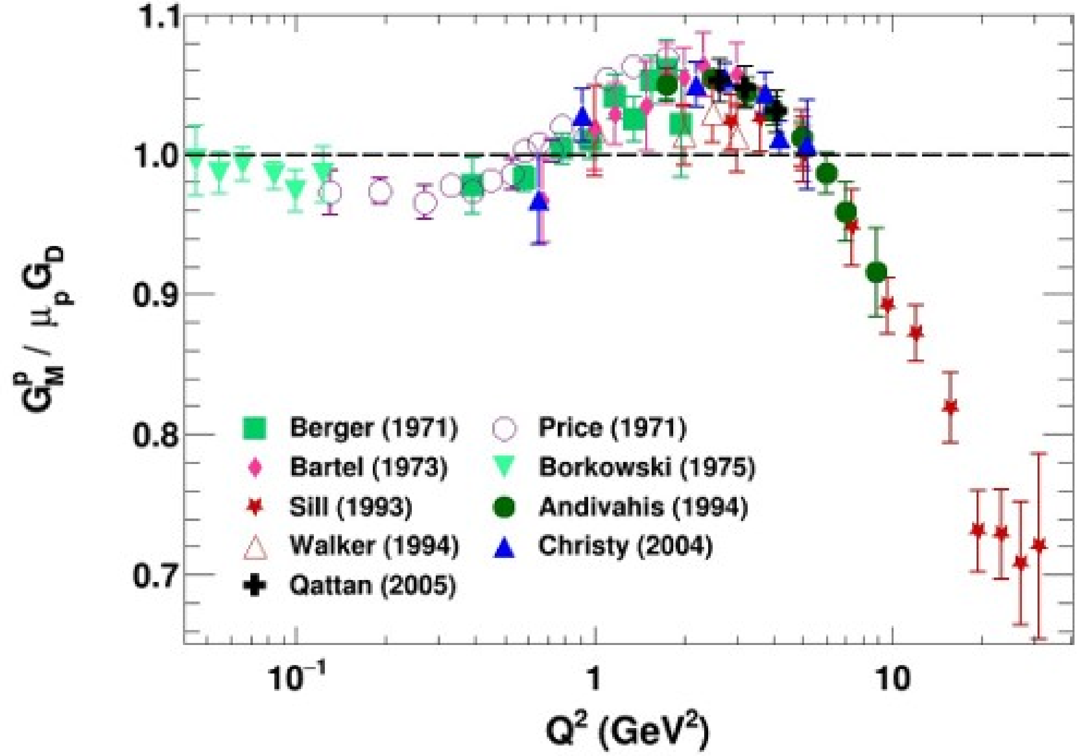

Figure 2.10: World data of measurements for G_M^p obtained via the Rosenbluth separation method. Figure from [64].

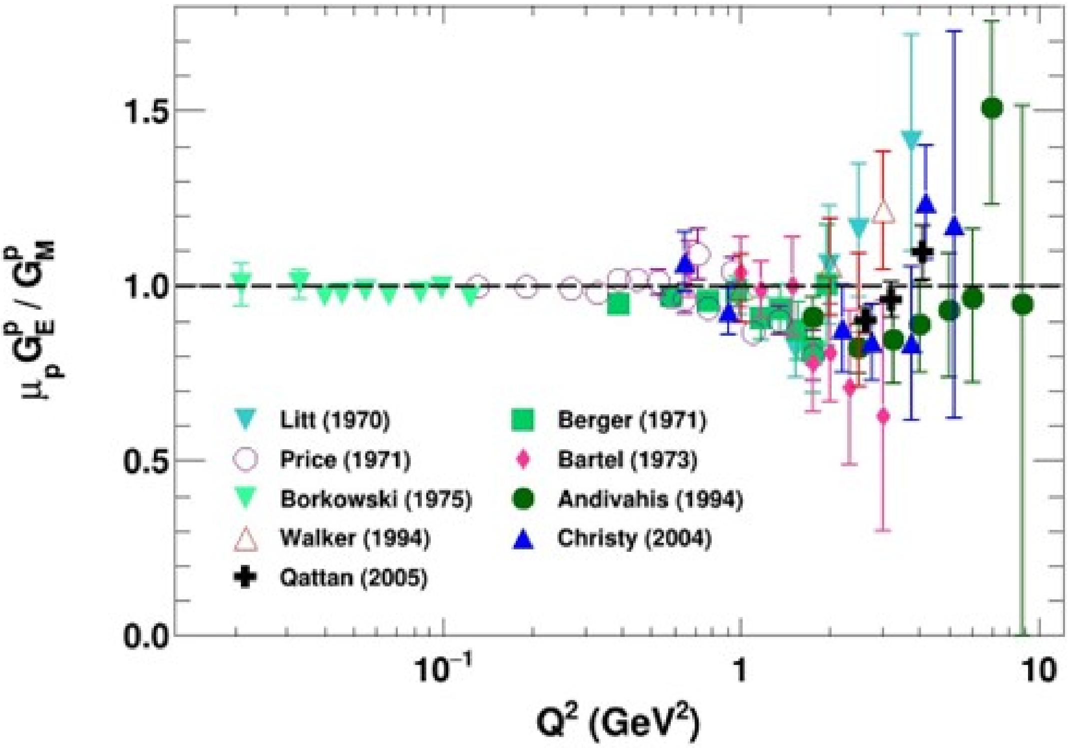

Figure 2.11: Selected proton form factor ratio data from the Rosenbluth extractions presented in Figs. 2.9 and 2.10, limited in Q^2 range due to the electric form factor. Figure from [64].

Unpolarised Neutron Form Factor Measurements

Unpolarised measurements of the neutron form factors via Rosenbluth separation had additional complications to the proton case, and as such the behaviour of the form factors was less well understood. As there is no free neutron target, experiments must resort to nuclear targets, usually light nuclei like deuterium, helium-3, helium-4 and so on. Early (1960s - 1990s) unpolarised experiments using deuterium to extract the electric form factor G_E^n typically utilised either elastic ed scattering or quasielastic ed scattering. Elastic scattering is the process in which no energy is lost in the coherent scattering of two free particles. In this case coherent elastic scattering on deuterium means the recoiling deuteron does not break up. On the other hand, quasielastic scattering deals with a small amount of energy loss owing to the fact that the quasi-free scattering of a bound particle from a nucleus is incoherent.

In the latter case, the reaction can be inclusive (only 1 particle, usually the electron is detected), semi-inclusive (electron+proton detected) or semi-exclusive (electron+neutron detected). Inclusive measurements of this nature have been performed [65–69], but there are a plethora of issues relating to corrections which result in large systematic and theoretical uncertainties on the neutron cross section. Semi-exclusive quasielastic scattering from light nuclear targets introduces further complications in the form of large proton backgrounds owing to the proton having a larger cross section as a result of a larger FF ratio; kinematic smearing of measurable quantities as a result of Fermi motion within the nucleus, and extra nuclear effects in the final state. Additionally, given the neutron is neutrally charged, it is notoriously difficult to accurately detect exclusively, and precise knowledge of the detection efficiency in a cross section measurement is critical. As such, one technique employed was the "anti-coincidence" method, in which the electron-proton cross section was measured, and electrons detected without a recoiling proton were attributed to neutrons [70].

In this vain, early cross section extractions utilised the former case of elastic $d(e'd)$ scattering [44, 71–74]. Here, the reaction is either inclusive or totally exclusive (the electron and recoiling deuteron are detected). Elastic ed scattering on the spin-1 deuteron requires a modification to the hadronic current operator for three form factors for the charge, quadrupole moment and magnetic distributions, G_C, G_Q, G_M respectively. Gourdin showed that in the impulse approximation these could be written as linear combinations to produce isoscaler electric and magnetic form factors, and derived the associated cross section. The details are outside the scope of this short review of the world data, but can be found within Ref. [75]. These results for G_E^n are shown in Fig. 2.12.

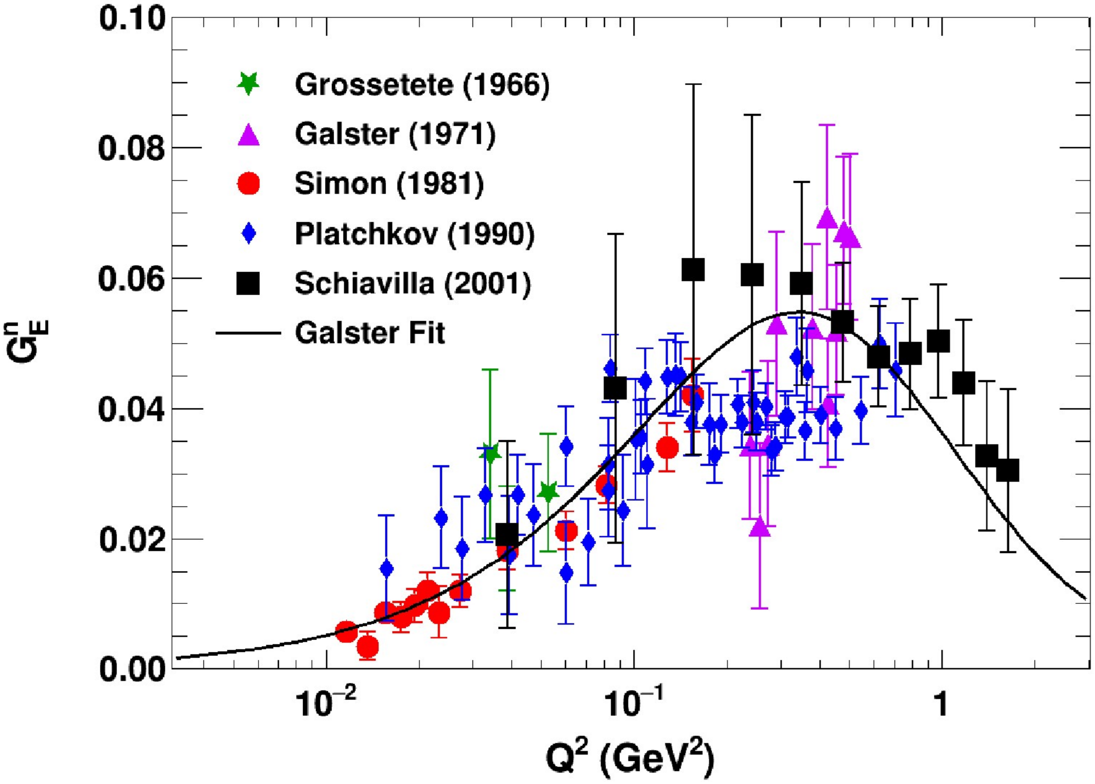

Figure 2.12: Selected data [44, 71–74] of measurements for G_E^n obtained via unpolarised elastic ed cross section methods. Figure from [64].

Unpolarised extractions of G_E^n did not exhibit the same scaling as the proton, but above 100 MeV^2 it was difficult to say anything with much certainty. The Grossetete data from Or-say [71] and the Galster data [72] were interpreted using Hamada-Johnston [76] and Feshback-Lomon [77] deuteron wavefunction models, and a fitting function was proposed by Galster, which can be seen alongside world data in Fig. 2.12, and is discussed more in Sec. 2.8.2.

Rosenbluth separation continued to be a valid method for extractions of G_M^n owing to its much larger contribution to the cross section, which reduced the systematic uncertainties involved. Again, early measurements up to 1973 employed inclusive [57, 69, 71, 78], elastic ed cross section [79, 80] and semi-exclusive $d(e,e')n$ [70, 81] techniques to extract the magnetic form factor. Single arm methods suffer as previously described from model dependent FSI corrections although not as extremely as the case for the electric form factor at higher Q^2. There are also systematic effects coming from the final meson exchange currents and deuteron wavefunction treatments in low Q^2 measurements. However, a method of great interest is the “ratio” or Durand method [82] which is less sensitive to each of these effects. In this method measurements of both neutron tagged $d(e,e'n)$ and proton tagged $d(e,e'p)$ quasielastic scattering from deuteron are made. The simultaneous measurement of both reactions allows one to form the ratio

$$R'' = \frac{\frac{d\sigma}{d\Omega}\big|\, d(e,e'n)}{\frac{d\sigma}{d\Omega}\big|\, d(e,e'p)} \tag{2.78}$$

which is insensitive to target thickness, beam intensity, electronic dead time, electron trigger efficiency, electron acceptance and electron detection and reconstruction efficiency, as these cancel in the ratio. A small nuclear correction ϵ_{nuc} is required to extract the ratio of the elastic cross sections from R'', to account for the differences in bound and free cross sections for the neutron and proton. With this correction from a suitably chosen deuteron wavefunction model the desired ratio can be extracted,

$$R' = \frac{\frac{d\sigma}{d\Omega}\big|\, n(e,e')}{\frac{d\sigma}{d\Omega}\big|\, p(e,e')} = \frac{R''}{1+\epsilon_{\text{nuc}}}. \tag{2.79}$$

Measurements of G_M^n from the ratio method and Rosenbluth cross section methods have been made with high precision up to larger momentum transfer than G_E^n to date, with the most recent publication by Lachniet et al. in 2009 [83] with a measurement at $Q^2 = 4.8$ GeV². Modern G_M^n measurements are shown in Fig. 2.13. Analysis of the datasets for experiment E12-09-019 [84] in Hall A at Jefferson Lab is currently ongoing, which seeks to extend the measurements of G_M^n to 13.5 GeV². The projected kinematic points are shown in Fig. 2.14.

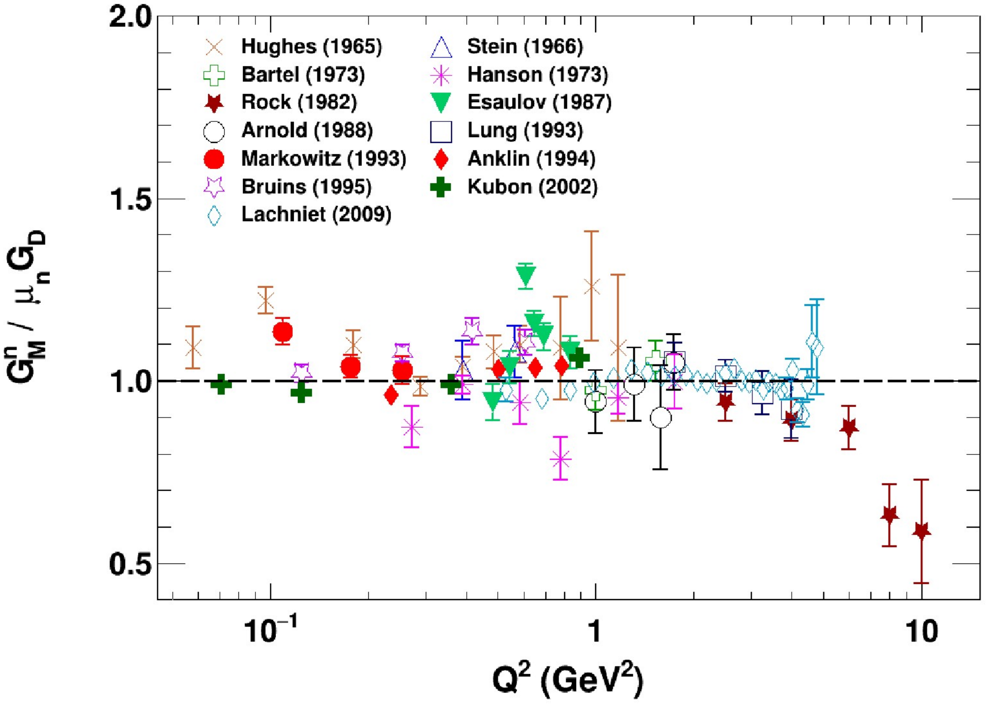

Figure 2.13: Selected data of measurements [57, 67, 78, 83, 85–93] for G_M^n obtained via the Rosenbluth separation method. Figure from [64].

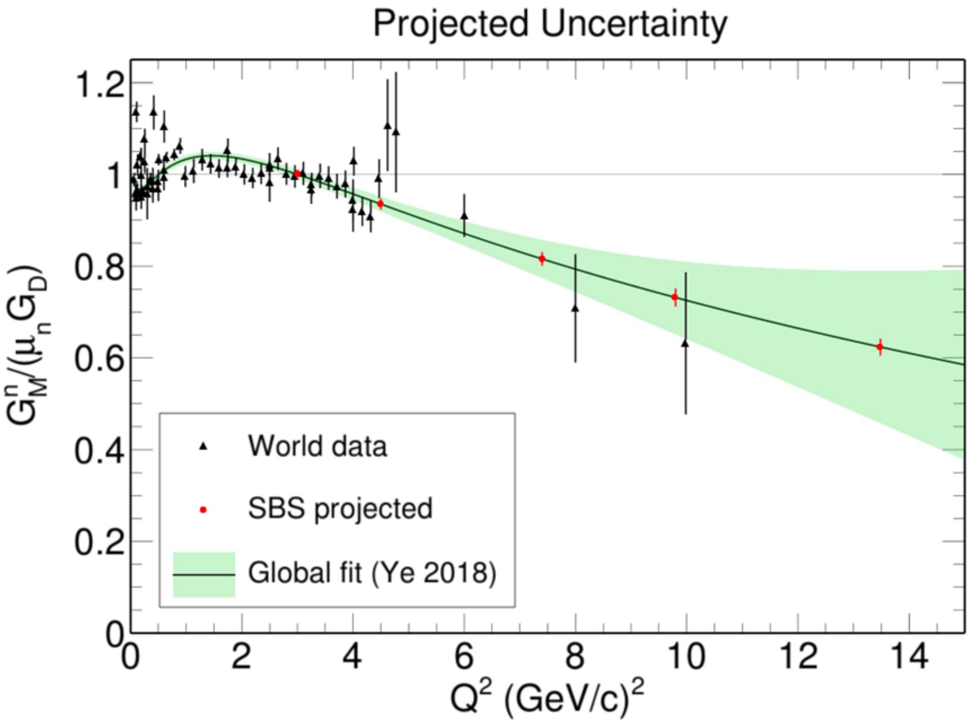

Figure 2.14: Preliminary projected data points for the E12-09-019 (GMN) experiment in Hall A at Jefferson Lab. Figure from [94].

2.7.1 Polarisation Degrees of Freedom at Jefferson Lab

Proton Form Factors G_E^p, G_M^p

Akhiezer and Rekalo demonstrated that recoil polarisation measurements would be much more sensitive to G_E than cross section measurements in which G_M dominates more and more at larger Q^2 [46]. Instead in polarisation measurements, as shown in Eqn. 2.70, G_E multiplies G_M in the transverse component of the polarisation.

Indeed this appeared to be the case when double polarisation experiments at JLab in 1998-2010; GEp(I) [50], GEp(II)[51, 95] and GEp(III) [96, 97], demonstrated a significant deviation from this previously observed constant ratio of G_E^p/G_M^p. This recoil polarisation method of extracting the ratio of G_E^p/G_M^p from measuring the polarisation of the recoil proton was made possible in part by the technological advances of CEBAF at Jefferson Lab.

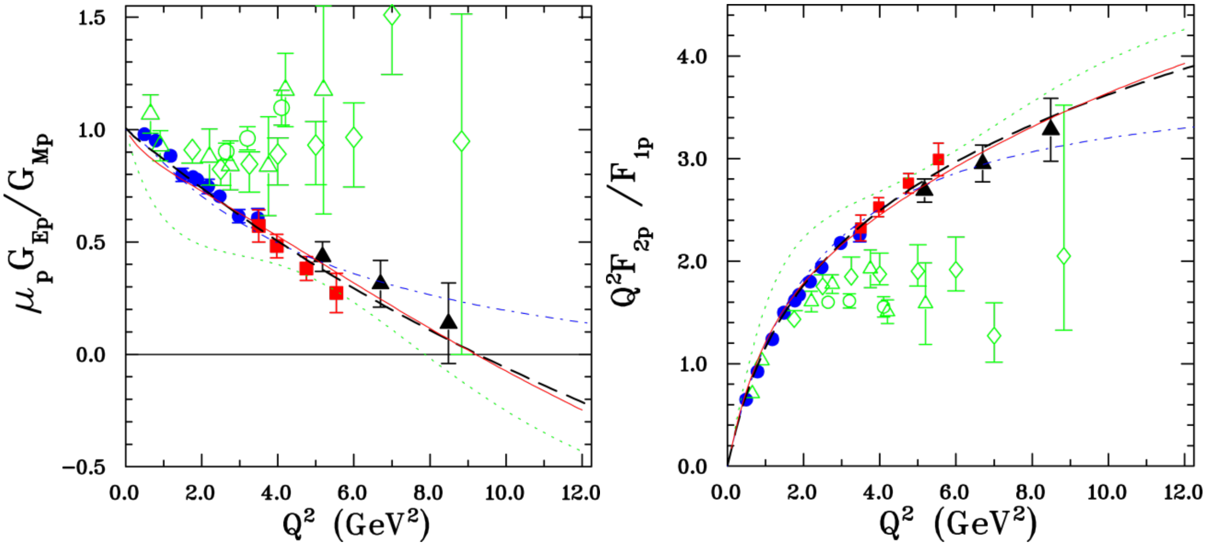

Figure 2.15: G_E^p/G_M^p and corresponding Q^2F_{2p}/F_{1p} data obtained via recoil polarisation technique at JLab [43]. Symbols: [50, 51] are circles, [95, 96] are squares, and [97] are triangles, respectively. Theoretical curves from various sources are given in [43].

The results shown in Fig. 2.15 are drastically different from that of the earlier work using the Rosenbluth method shown in Fig. 2.11 and do not support the long standing prediction of QCD that the proton form factor ratio should scale asymptotically as $1/Q^2$. The data out of polarised measurements, shown in the left of Fig. 2.15 in filled symbols, demonstrates an almost linear decrease in the form factor ratio above $Q^2 = 1$ GeV^2. The Andivihas [39] cross section data is shown in the same plot in unfilled symbols for comparison, and is better described by the scaling relation of Eqn. 2.77. As discussed in Sec. 2.5.1 this discrepancy is thought to be due to non-negligible hard two-photon contributions which are not considered in typical radiative corrections for cross section measurements. Currently the Hall A collaboration at JLab are in the process of constructing new experimental setups [98], to extend these measurements up to $Q^2 = 15$ GeV^2.

Polarised G_E^n Data

Many experiments utilising double polarisation techniques have attempted to measure the electric form factor of the neutron at small and large Q^2. A table of data published since the late 1990s is presented in Tab. 2.1

Table 2.1: Published data on G_E^n or the ratio $\mu_n G_E^n / G_M^n$ via double polarisation, preceding E12-09-016.

Publication	Facility	Year	Q^2 [GeV^2]	Reaction	Extraction
[99]	MIT-Bates	1991	0.16	^{3}He(e,e’)	$A_\perp$
[100]	MIT-Bates	1992	0.2	^{3}He(e,e’)	$A_\perp, A_\parallel$
[101]	MAMI	1994	0.31	^{3}He(e,e’n)	$A_\perp, A_\parallel$
[102]	MIT-Bates	1994	0.255	^{2}H(e,e’n)	$P_t^{(h)}, P_l^{(h)}$
[103]	MAMI	1999	0.27-0.5	^{3}He(e,e’n)	$A_\perp, A_\parallel$
[104]	MAMI	1999	0.15	^{2}H(e,e’n)	$P_t^{(h)}, P_l^{(h)}$
[105]	Nikhef	1999	0.21	^{2}H(e,e’n)	A_{ed}^V
[106]	JLab	2001	0.5	^{2}H(e,e’n)	A_{ed}^V
[107]	MAMI	2003	0.67	^{3}He(e,e’n)	$A_\perp, A_\parallel$
[108]	JLab	2004	0.5, 1	^{2}H(e,e’n)	A_{ed}^V
[109]	MAMI	2005	0.3, 0.59, 0.79	^{3}He(e,e’n)	$P_t^{(h)}, P_l^{(h)}$
[110]	JLab	2006	0.45, 1.13, 1.45	^{2}H(e,e’n)	$P_t^{(h)}, P_l^{(h)}$
[111]	MIT-Bates	2008	0.14, 0.3, 0.39, 0.42	^{2}H(e,e’n)	A_{ed}^V
[112]	JLab	2010	1.72, 2.48, 3.41	^{3}He(e,e’n)	$A_\perp, A_\parallel$
[113]	MAMI	2013	1.58	^{3}He(e,e’n)	$A_\perp, A_\parallel$
[114]	JLab	2017	0.98	^{3}He(e,e’)	$A_\perp, A_\parallel$

Measurements of particular interest are those of Riordan et al. 2010 [112] which were also performed in Hall A at Jefferson Lab as part of experiment E02-013 or more simply, GEN-I. G_E^n was measured up to 3.5 GeV² which remains the highest momentum transfer measurement to date, in an experiment with various similarities and overlaps with the topic of this work, GEN-II. As such, GEN-I (or E02-013) will be referenced in places throughout this work. The results and those of previous polarised neutron experiments from Tab. 2.1 are shown in Fig. 2.16. The method of extraction for each is dependent on the observable. A_T and $A_\parallel$ are reactions in which the transverse or parallel (or both in some cases) component of the beam-target asymmetry was measured. P_l and P_t correspond to recoil-polarisation measurements where the observable was the longitudinal and transverse component of the polarisation transferred to the struck neutron. The observable A_V^{ed} is the beam-target vector asymmetry where a polarised deuterium target has been used.

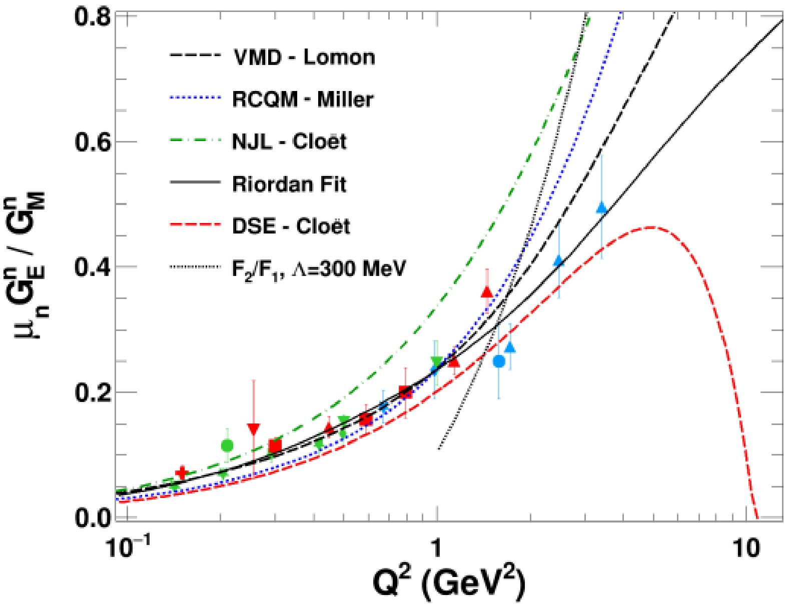

Figure 2.16: World data of measurements of the ratio of G_E^n/G_M^n obtained by double polarisation experiments preceding E12-09-016. Figure from [64].

2.8 Nucleon Form Factor parameterisations

A number of models and parameterisations have been developed in order to fit existing world data, and predict behaviour in unexplored regions of momentum transfer. Given the lack of G_E^n data in the region $3.5 < Q^2 < 10.0$ GeV² to date, models have no direct influence from G_E^n at high Q^2. An interesting aspect of this analysis will be the comparison of these predictions with the new measurements.

2.8.1 Dipole

As introduced in Sec. 2.4 the Sachs form factors can be considered as the Fourier transforms of the electric and magnetic moment distributions in the Breit frame. Assuming a spherically symmetrical charge distribution, the magnetic form factors for the proton and neutron, G_M^p and G_M^n continue to be well modelled by the scaled dipole parameterisation,

$$\frac{G_M^p(Q^2)}{\mu_p} = \frac{G_M^n(Q^2)}{\mu_n} = G_D(Q^2) = \left(1 + \frac{Q^2}{0.71\text{GeV}^2}\right)^{-2}, \tag{2.80}$$

up to around $Q^2 = 5$ GeV². This parameterisation has appropriate behaviour as $Q^2 \to 0$ since $G_D(0) = 1$ and $G_M(0) = \mu$ for both particles by definition. The low Q^2 Rosenbluth separation data for G_E^p is also described fairly well by the dipole form factor as shown in Fig. 2.11 where the ratio $\mu_p G_p^E/G_p^M \approx 1$ up to around 1 GeV². However, G_E^n does not fit this parameterisation at all since $G_E^n(0) = 0$.

2.8.2 Galster

As previously discussed, an alternative to the dipole parameterisation was developed by Galster in 1971 [72]. It has no new physics as such, merely an empirical change to better fit the data and has the form

$$G_E^n \sim \frac{-\mu_N \tau}{1+5.6\tau} G_D \tag{2.81}$$

which now matches the necessary low limit $G_E^n(0) = 0$. The unpolarised extractions of G_E^n in Fig. 2.12 is roughly matched by the fit despite relatively large errors, and low Q^2 polarised extractions are matched fairly well.

2.8.3 Kelly

A new parameterisation motivated by pQCD scaling rules was developed by Kelly in 2004 [115], to parameterise G_E^p, G_M^p and G_M^n more accurately than the dipole fit at higher Q^2. The Kelly parameterisation has the form

$$G(Q^2) \propto \frac{\sum_{k=0}^{n} a_k \tau^k}{1+\sum_{k=1}^{n+2} b_k \tau^k} \tag{2.82}$$

where a_i and b_i are parameters of the fit, given in Tab. 2.2, with $a_0 = 1$ a constant.

Table 2.2: Parameters of Kelly fit [115].

Form Factor	a_1	b_1	b_2	b_3	A	B
G_E^p	-0.24±0.12	10.98±0.19	12.82±1.1	21.97±6.8		
G_M^p/μ_p	0.12±0.04	10.97±0.11	18.86±0.28	6.55±1.2		
G_M^n/μ_n	2.33±1.4	14.72±1.7	24.20±9.8	84.1±41		
G_E^n					1.70±0.04	3.30±0.32

This fit has the appropriate limits as $Q^2 \to 0$ that $G_E^p \to 1$, $G_M^n \to \mu_n$, $G_M^p \to \mu_p$. Additionally, Kelly used a Galster-like parameterisation of G_E^n to complete the set. In 2010, Riordan et al. [112] refined the Galster fit to new world data as

$$G_E^n(Q^2) = \frac{A\tau}{1+B\tau} G_D(Q^2) \tag{2.83}$$

with the values $A = 1.70$ and $B = 2.00$.

2.8.4 Ye

Ye et al. produced a global fit to world data in 2018 for all four Sachs form factors [116]. This has the form of a polynomial expansion as follows

$$G(Q^2) = \sum_{k=0}^{\max} z = \frac{\sqrt{t_{\text{cut}} + Q^2} - \sqrt{t_{\text{tcut}} + t_0}}{\sqrt{t_{\text{cut}} + Q^2} + \sqrt{t_{\text{tcut}} + t_0}} \tag{2.84}$$

where $t_{\text{cut}} = 4m_\pi^2$ and $t_0 = -0.7$. The world data used in the fitting procedure is shown against the results of the fit in Fig. 2.17.

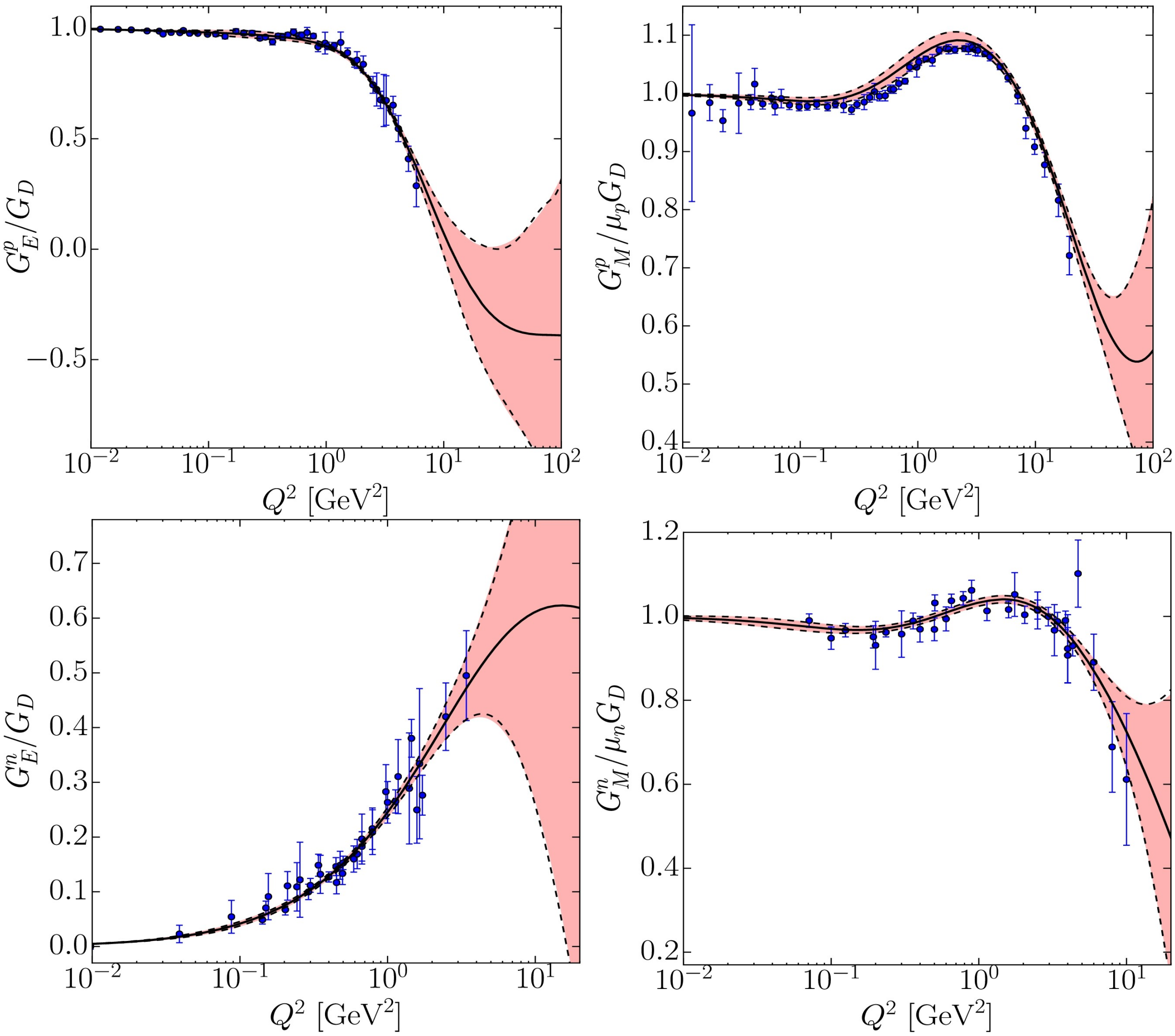

Figure 2.17: World data plotted alongside Ye parameterisation fits (solid curves) and associated error bands (red filled curves) for the proton (top) and neutron (bottom) [116].

2.9 Nucleon Models

A number of recent models have been made to explain and predict the structure of the nucleon in terms of the Sachs electromagnetic form factors. While they will not be explored in rigorous detail, a select few will be discussed for the purposes of comparison to the data under analysis. The projected data points for this work are shown against the explored models in Fig. 2.18.

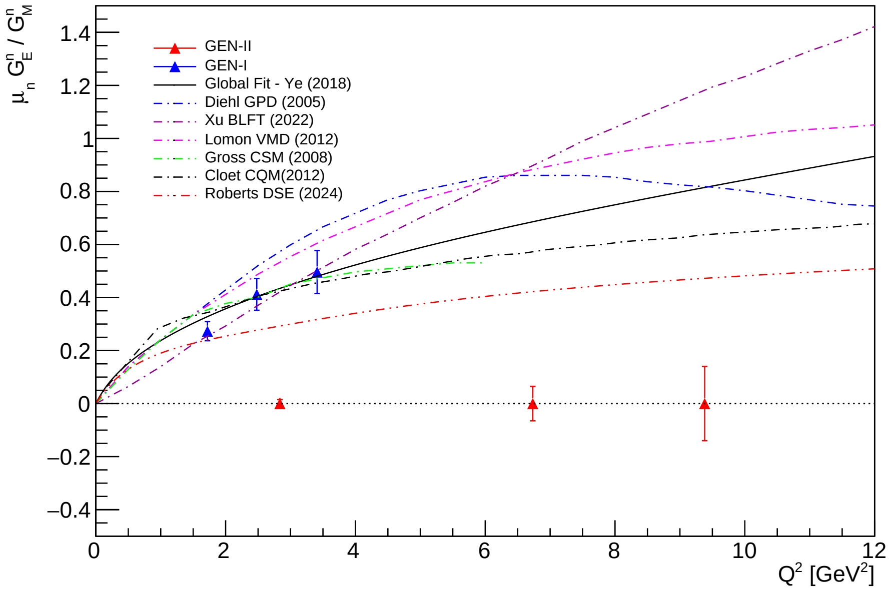

Figure 2.18: Preliminary projected data points for the E12-09-016 (GEN-II) experiment. Projected errors are statistical only, calculated based on expected beam time and model dilution factors [94].

2.9.1 pQCD

A long held tenet of pQCD is that the Pauli and Dirac form factors for a nucleon comprised of three valence quarks should scale as $F_1 \propto 1/Q^{-4}$ and $F_2 \propto 1/Q^{-6}$ in the asymptotic region. A relatively recent modification [117] is a logarithmic scaling expression which manifests as

$$\frac{F_2(Q^2)}{F_1(Q^2)} \propto \frac{\log^2\left(\frac{Q^2}{\Lambda^2}\right)}{Q^2} \implies \frac{G_E(Q^2)}{G_M(Q^2)} \propto \frac{Q^2 - \kappa\alpha\log^2\left(\frac{Q^2}{\Lambda^2}\right)}{Q^2 + \kappa\tau\alpha\log^2\left(\frac{Q^2}{\Lambda^2}\right)} \tag{2.85}$$

where $\Lambda \approx 200$ - 300 MeV, and other variables retain their usual meaning. This has described the proton data fairly well, however recent flavour separation of the neutron form factors [118] up to 4.8 GeV^2 indicated that the neutron ratio F_2^n/F_1^n does not in fact obey this scaling behaviour, for the same values of Λ.

2.9.2 Generalised Parton Distribution Based Models

Nucleon form factors are closely related to Generalised Parton Distributions (GPDs) which are accessible via measurements such as Deeply Virtual Compton Scattering (DVCS, the electro-production of a real photon), and other hard exclusive processes. Ji demonstrated in a model-independent way that the density interpretation of the form factors in the Breit frame relates to the moments of the GPDs through sum rules [119],

$$\begin{aligned} F_1^q(Q^2) &= \int_{-1}^{1} dx H^q(x,\xi=0,Q^2) \\ F_2^q(Q^2) &= \int_{-1}^{1} dx E^q(x,\xi=0,Q^2) \end{aligned} \tag{2.86}$$

where q is the quark flavour and ξ is a Bjorken-like scaling variable which is related to the momentum fraction of the initial and final state of the struck quark. As a result, the form factors $F_1(Q^2), F_2(Q^2)$ impose strict constraints on the vector $H(x,\xi,Q^2)$ and tensor $E(x,\xi,Q^2)$ GPDs. Linear combinations of the quark flavour form factors can be constructed to form the nucleon form factors [118]

$$\begin{aligned} F^p_{1(2)}(Q^2) &= \frac{2}{3}F^u_{1(2)} - \frac{1}{3}F^d_{1(2)} - \frac{1}{3}F^s_{1(2)} \\ F^n_{1(2)}(Q^2) &= -\frac{1}{3}F^u_{1(2)} + \frac{2}{3}F^d_{1(2)} - \frac{1}{3}F^s_{1(2)}. \end{aligned} \tag{2.87}$$

Diehl et al. presented a simple GPD based parameterisation of the form factors using constraints from forward parton distributions out of DIS measurements [120].

2.9.3 Dyson Schwinger Equations

The Dyson-Schwinger Equations (DSEs) are a powerful set of integral equations that can be used to study the non-perturbative aspects of bound nucleon states. They provide a framework for understanding the properties of hadrons directly from the underlying quark and gluon degrees of freedom, which are particularly sensitive to the momentum dependence in the mass dressing, which governs the transition between constituent and parton-like behaviours. Effective models or truncation schemes are required to solve the infinite tower of coupled equations for the Green's functions for a theory.

Segovia, Clöet et al. proposed a DSE model of the form factors in 2014 which predicted a zero crossing in the proton form factor ratio around $Q^2 = 9.5$ GeV² and slightly lower for the neutron [121]. This is indicated by the dashed red line in Fig. 2.16. Subsequent work then predicted this zero crossing to be more likely after 20 GeV². However more recently, Yao, Roberts et al. proposed a DSE based model using the Rainbow Ladder truncation scheme which simplifies the quark-gluon vertex and the gluon propagator, and appears to have eliminated the zero crossing for the neutron [122]. The predictions of the new scheme are shown as the red dashed line in Fig. 2.18. This highlights the importance of exploring ultra-high Q^2 regimes of elastic scattering, in order to discern these predictions.

2.9.4 Vector Meson Dominance

Models based on the assumption of Vector Meson Dominance (VMD) [123] are a subset of a method of nucleon form factor study called dispersion theoretical analysis which are reviewed in Ref. [124]. These models attempt to describe the form factors in terms of superpositions of spectral functions of meson poles. An early model which attempted to described the photohadronic interaction within the framework of VMD is that of Sakurai [125]. In this model the virtual photon transferred between the lepton and hadron which are undergoing scattering will couple to the hadron via a lower-lying vector meson such as the $\rho(700)$, $\omega(782)$ and $\phi(1020)$ which have the same J^{PC} quantum numbers as the photon.

The strength of the couplings are left as free parameters are fitted to the form factor data. VMD-based models were some of the earliest to describe well the features of the form factors, and in particular predicted the fall off of G_E^p/G_M^p observed in polarisation experiments, decades before they were performed. Early VMD fits have been extended to include more poles by Lomon [126].

2.9.5 Constituent Quark Models

Constituent quark models (CQM) are some of the earliest precursors of modern QCD and theory of strong interactions. Early non-relativistic CQM were successful in explaining the observed baryon and meson spectra as quark triplet and doublet (qqq, $q\bar{q}$) states as briefly noted in chapter 1. Gross et al. produced a Covariant Spectator Model (CSM) [127] based on the notion of three constituent quarks in which the form factors are described by a covariant nucleon wavefunction with zero angular momentum (S-wave). Clöet and Miller proposed an updated relativistic CQM (RQCM) which includes quark-diquark degrees of freedom [128].

2.9.6 Light Front Models

Hamiltonian light-front field theory is a framework for solving non-perturbative QFT problems within a light-front gauge and quantisation; and Hamiltonian matrix which is suitable for many body applications [129]. Xu et al recently proposed a method of calculating the nucleon structure with this method via Basis Light Front Quantisation [130]. Their calculation employs an effective light-front Hamiltonian with quarks as the only effective degrees of freedom, a transverse confining potential from light-front holography supplemented by a longitudinal confinement, and a one-gluon-exchange interaction with a fixed coupling. The resultant light-front wavefunctions are used to calculate the form factors for the nucleon.

Chapter 3

Experimental Set-up

In this chapter the experimental programme and set-up for E12-09-016 (GEN-II) will be discussed. GEN-II was carried out in experimental Hall A of Jefferson Lab (JLab) between October 2022 and November 2023. Founded in 1984, Jefferson Lab was initially named the Continuous Electron Beam Accelerator Facility (CEBAF), which continues to be the name of the accelerator. The first 4 GeV physics beam was taken in Hall C in 1995, and the facility was shortly renamed to the Thomas Jefferson National Accelerator Facility a year later. From 1997 experimental Halls A, B and C performed experiments up to 4 GeV beam energy, and the design energy of 6.07 GeV was reached in the year 2000. Now known as the 6 GeV era, CEBAF operated at this energy until 2012 when it was powered down in preparation of a 12 GeV upgrade. 178 experiments were completed with the original machine. JLab experiments follow an E(12)-YY-XXX naming convention, wherein YY indicates the year of initial proposal, and XXX is a number from 001 - 999 assigned to experiments in order to distinguish them. After completion of the upgrade in 2017 which included the construction of a new experimental Hall, CEBAF now provides polarised electron beams with energies up to 12 GeV and 100% duty cycle to four Halls (A, B, C and D) simultaneously.

Hall A which was originally designed to achieve a luminosity of several 10^{38} cm^{-2}s^{-1} using two identical High-Resolution Spectrometers (HRS), now houses the Super-Bigbite Spectrometer (SBS) experimental setup. SBS can achieve similar luminosities with the addition of having over an order of magnitude larger momentum and angular acceptance. This is made possible largely by novel tracking technology, discussed in Sec. 3.6.2. The SBS apparatus will host a full suite of experiments across its lifetime. Namely to date, the E12-09-019 (GMN) experimental run which was taken from Fall 2021 to Spring 2022, and the concern of this work, E12-09-016 (GEN-II).

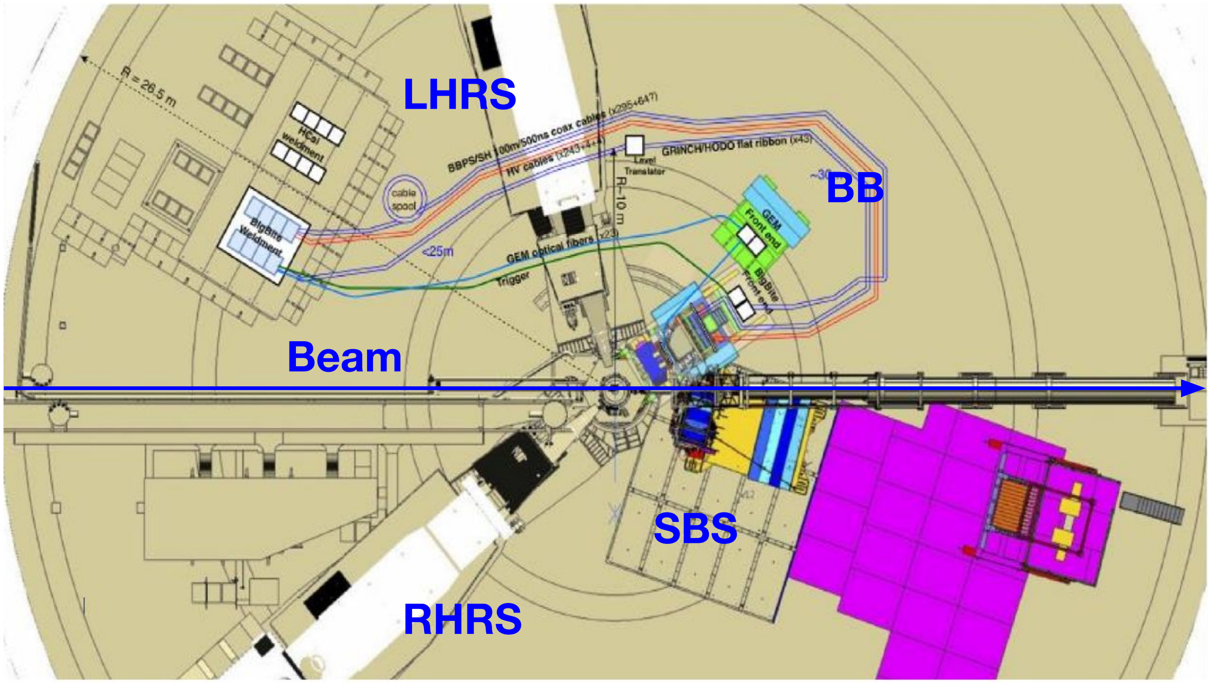

Figure 3.1: Floor plan of Hall A in 2019 during SBS experimental setup installation.

3.1 Introduction to E12-09-016

E12-09-016 was a two-arm electron-nucleon scattering coincidence experiment located in JLab's Hall A and utilised the 12 GeV CEBAF for its longitudinally polarised electrons. GEN-II began on October 10th 2022 with 2 days of commissioning runs at the lowest electron beam energy of 2.138 GeV on carbon foil targets and a glass reference cell filled with hydrogen (H_2) gas at approximately 10 bar. The target and spectrometers were orientated at the GEN2 kinematic position. GEN-II took production data on the 10 bar polarised helium-3 (^{3}He) target at three kinematic points, GEN2, GEN3, GEN4 (and a time delayed run extension named GEN4b) which are detailed in Tab. 3.1. The scope of this work concerns only kinematic 2, however outside of analysis and the differences in Tab. 3.1, the experimental set-up is consistent throughout each. A floor plan of the hall from above is shown in Fig. 3.1.

Table 3.1: Production kinematics for G_E^n-II run period.

	Q^2 [GeV^2]	E_i [GeV]	θ_e [deg]	p_e [GeV/c]	θ_n [deg]	p_n [GeV/c]
GEN2	2.92	4.291	29.5	2.69	34.7	2.37
GEN3	6.74	6.373	36.5	2.73	22.1	4.51
GEN4	9.82	8.448	35.0	3.21	18.0	6.11

The beam was rastered upstream of the target and its charge and position monitored with beam charge monitors (BCM) and beam position monitors (BPM). The charge, position and energy of electrons could be measured to a resolution appropriate for the asymmetry measurement required to extract G_E^n. The electron beam exited the beampipe through a beryllium window, and then entered the target enclosure through an opaque 3/8” lexan polycarbonate window, fixed in place by a square steel frame. The beam collided with the fixed ^{3}He target and some electrons in the beam underwent interactions within the target, producing $(e, e'N)$ reactions (among other backgrounds). Then the beam exited the enclosure through a similar lexan window downstream. The beamline continued to the beam dump at the far downstream region of the Hall.

Facing downstream, on the left hand side was positioned the large angular acceptance spectrometer known as Bigbite (BB), and on the right hand side was positioned SBS. Both spectrometers are based on large acceptance room temperature dipole electromagnets. The BB excitation coil current was set to 750 A with negative polarity, and the SBS excitation coil current was set to 2100 A with positive polarity. The former ensures up-bending electrons into the Bigbite acceptance, and the latter ensures maximal separation of protons and neutrons across the distance to the detectors as well as up-bending protons out of the SBS acceptance. A Hadron Calorimeter (HCal) was positioned 17 m (the maximum distance possible in the Hall) away from the target on the SBS arm. A coincidence trigger was used between the Bigbite and HCal calorimeters. The Hall A data-acquisition system was used to process triggers and store detector, beamline and helicity information.

Quasielastically scattered electrons were detected by BigBite. The first purpose of BigBite was to measure the momentum and angle of the electron by tracking the trajectory using Gas Electron Multiplier (GEM) chambers, and reconstructing the momentum from the angle of the track in the dispersive plane and the optics of the BigBite magnet. The second purpose of Bigbite was to provide a timing reference for events via a timing hodoscope. Recoiling nucleons were detected in coincidence using the hadron arm, which consisted of HCal and the SBS dipole magnet. The hadron arm also comprised of 6 GEM tracker layers, however these were not fully utilised for GEN-II, but will be for future experiments. The SBS magnet provided nucleon separation, and reconstructed tracks in BigBite could be projected during analysis towards the hadron calorimeter, and then compared to hit positions on the face of the calorimeter. This is the basic mechanism for event selection before kinematic cuts, which will be discussed in detail in chapter 5.

3.2 GEN-II Experimental Programme

The GEN-II proposal planned to make three measurements of G_E^n/G_M^n at four-momentum transfer values of Q^2 = 3.0, 6.83 and 9.82 GeV^2. These correspond to kinematic settings GEN2, GEN3 and GEN4 respectively. The completed final kinematic settings are detailed in Tab. 3.1. E_i is the beam energy, θ_e is the central elastic electron scattering angle, which

Bigbite was positioned at, p_e is the momentum of the scattered electron, θ_n is the angle of the scattered nucleon, which SBS was positioned at, and p_n is the momentum of the scattered nucleon.

3.2.1 E12-09-016 Data

Data for the kinematic point of interest, GEN2, was acquired between October 10th 2022 and October 30th. The data is sorted by the type of target used: multi-foil carbon target, carbon hole, single-foil carbon optics, reference cell and ^{3}He production cell. Tab. 3.2 details the amount of data acquired at each physics (H_2 or ^{3}He) target, which was deemed "good" upon first round of data quality inspection (steady beam, no excessive detector trips and uncorrupted data files). The H_2 data denoted "SBS 30%" corresponds to runs where the SBS dipole magnet was set to 30% of its maximum field strength, and similarly "SBS 100%" denotes when this field was maximal.

Table 3.2: Statistics collected for each physics target during GEN2 kinematic.

Cell Type	Run Dates	Events Recorded
H_2 Reference Cell (SBS 30%)	17th Oct	3.3 M
H_2 Reference Cell (SBS 100%)	17th Oct	2.4 M
H_2 Reference Cell (SBS 100%)	20th Oct	9.6 M
^{3}He Production Cell	17-30 Oct	182.8 M

Runs were also taken on each of the carbon targets for each kinematic point. These carbon targets are discussed in Sec. 3.4.3. Briefly, carbon hole targets are used for beam quality, stability, size and raster monitoring prior to taking production data on a fragile glass or cryogenic cell. Data was taken here at all kinematic settings during beam checkout procedures. The multi-foil carbon optics target consisted of eight foils that allow precise calibration of the Bigbite optics for a kinematic setting via use of an insertable sieve plate. The single-foil carbon optics target consisted of a single foil which can be used to calibrate optics runs by aligning to a unique known position at the target. GEN2 was the only kinematic point at which carbon optics or foil data was not taken. However since the commissioning kinematic GEN1 had the same spectrometer angles as GEN2, the optics and foil data could be used to calibrate the magnetic optics.

3.3 CEBAF

CEBAF is a 5-pass continuous wave (CW) electron accelerator, which consists of a CW polarised electron photo-injector and two 1497 MHz linear accelerators (linacs), connected by recirculating arcs. The injector produces 67 MeV polarised electrons using a polarised photocathode gun. Then, these electrons are injected into the north linac and accelerated.

The linacs are connected at the north and south side by five recirculating arcs. The "racetrack" design which is shown in Fig. 3.2 allows the electron beam to be accelerated up to five passes through both linacs. After five successive full passes, the electrons reach energies up to 11 GeV (1.1 GeV per linac) and polarisations up to 85% before delivery to Halls A, B and C. Hall D, being a further half pass around the accelerator ring, is in fact the only Hall which ever receives the full 12 GeV. The linacs' radio-frequency system splits up the 1497 MHz beam into 4.008 ns intervals during 4-Hall running, or 2.004 ns intervals during 3 Hall running using three de-phased 499 MHz lasers in the injector.

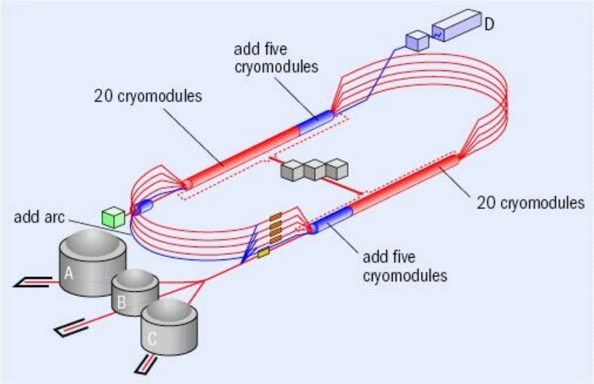

Figure 3.2: Diagram of CEBAF from 12 GeV upgrade. Experimental Halls labelled.

3.3.1 Polarised Electron Production

Circularly polarised laser light is used to excite electrons via the photo-electric effect [131] from a Gallium-Arsenide (GaAs) photocathode. GaAs is a direct band gap semiconductor, which means that photons with sufficient energy are capable of exciting electrons from the valence band directly to the conduction band. The GaAs is doped on the surface with monolayer of Caesium Dioxide (Cs_2O), which lowers the surface potential barrier. This creates a negative-electron-affinity state allowing emission from the conduction band.

Polarisation of the electrons then occurs through optical pumping between valence and conduction band states in the GaAs. Normally all four spin sub states of the $P_{3/2}$ level are degenerate. This is shown in the top of Fig. 3.3. The resultant transition into the conduction band is three times more likely to occur from the degenerate +(-)$P_{3/2}$ to the -(+)$S_{1/2}$ conduction level, than from the +(-)$P_{1/2}$ valence level to the +(-)$S_{1/2}$ conduction level. This limits the theoretical polarisation to around 50%, however this limit can be increased to almost 100% by lifting the degeneracy of the $P_{3/2}$ states, as shown in the bottom of Fig. 3.3. This is done by applying a mechanical strain to the photocathode. Jefferson Lab operates a strained super lattice GaAs photocathode, which consists of alternating layers of GaAs and GaAsP, and is able to achieve typical polarisations of 85% with quantum efficiency (QE) close to 1% [132].

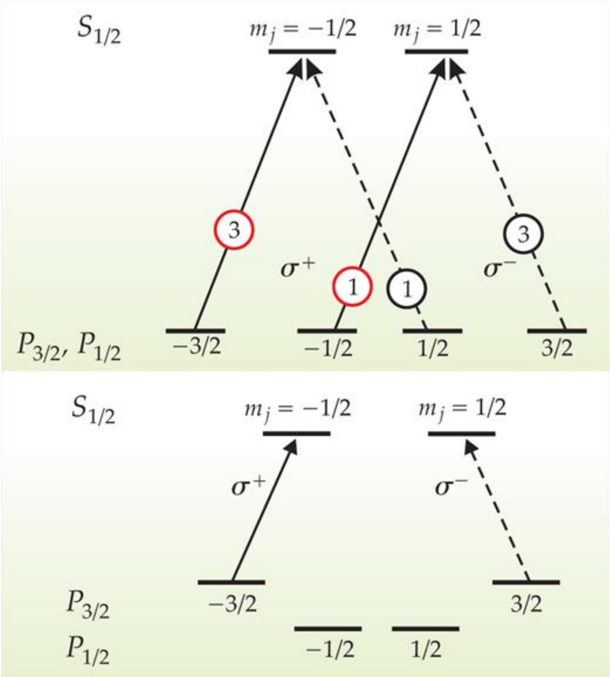

Figure 3.3: Diagram of the excitation modes for (top) unstrained GaAs verses (bottom) strained. By raising the degeneracy of the energy levels by straining the GaAs, the theoretical polarisation limit is increased from 50% to ∼100%. Image from [132].

A complete diagram of the electron source is shown in Fig. 3.4. The electron source produces electrons in one of two helicity states (+ or -). The helicity is flipped with a frequency of 30 Hz, by flipping the polarisation of the laser. This is done by “Pockels cells”, optical devices that control the polarisation of light using electric fields, which are powered by a high voltage supply. An electronic helicity board randomly generates one of two quartet sequences (+ - - + or - + + -). This signal is propagated from the helicity generator to the data acquisition systems (DAQs) in all of the Halls and to the Pockels cell HV supply, which in turn flips the field of the Pockels cell, and the resultant polarisation of the laser. An insertable half-wave plate (IHWP) can be placed in the path of the laser before it is incident on the photocathode. This has the effect of flipping the helicity if it is in place. To know which HV setting produces +(-) helicity states several factors need to be known. The angle of the Pockels cell fast axis with respect to the laser linear polarisation, polarity of the Pockels cell and position of the IHWP (in or out), the parity conservation of the photocathode (whether it preserves the photon helicity). The spin must then be propagated through a Wien filter and then the precession of the spin must be accounted for as the electron travels through magnetic fields around the accelerator. Finally the helicity signal in the DAQ must be verified against the correct initial circular polarisation state of the laser.

The helicity of the beam was measured in a dedicated parity DAQ, which keeps track of the many factors mentioned which influence the final helicity. No direct calibrations are applied to the helicity information, however the final helicity taken for a given event is correct up to a potential sign flip as a result of the half wave plate. The half wave plate status is tracked in the data stream. A value of -1 corresponds to the HWP being out, and a value of 1 corresponds to it being in place. Since the helicity is also ± 1 then the true value is simply a product $h_{\mathrm{IWHP}} \cdot h_{\mathrm{DAQ}}$. However importantly this must be calibrated against the absolute sign of the Möller asymmetry, since this is a known physics asymmetry. This amounts to a final factor of ± 1. The HWP state for a given kinematic setting which produces a positive Möller asymmetry sign, is the state which should have no further flip. i.e. a factor of 1. Then the opposite HWP state acquires a factor -1. Determination of the Möller asymmetry and beam polarisation are discussed in Sec. 3.3.3.

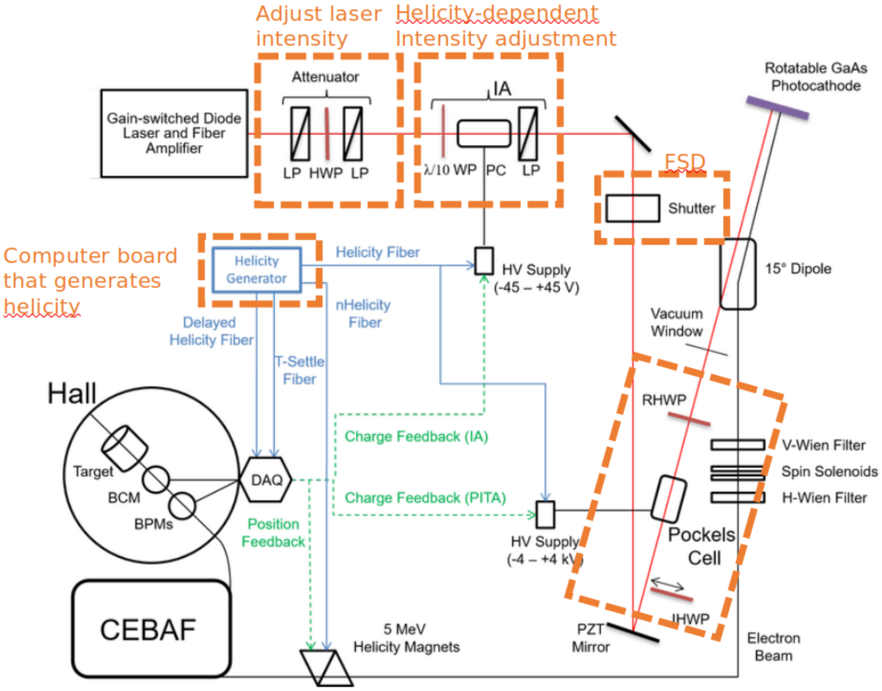

Figure 3.4: Diagram of the electron source. Laser light is propagated through a system of filters and mirrors to the photocathode. Electrons are then extracted to CEBAF. Image from [133].

3.3.2 Acceleration and Delivery to Hall A

Electrons emitted from the photocathode are fired into the injector by a 100 kV DC electron gun [134], and the injector accelerates them up to 67 MeV before entry into the north linac. The linacs operate using Superconducting Radio-Frequency (SRF) cavities constructed from Niobium cells, which are held at 4.2 K by cryogenic liquid helium. Prior to the CEBAF 12 GeV upgrade, each linac consisted of 20 C20 cryomodules, which each housed five Niobium cells. The C20 is capable of up to 20 MeV acceleration per module, which resulted in a maximum beam energy of 4 GeV after five passes around each linac. Over time, cryomodules have been replaced, refurbished and upgraded with C50 and C75 modules leading to increased beam energy and performance. The 12 GeV upgrade included the addition of five new C100 cryomodules to each linac, which house eight Niobium cells. These C100 modules have an average cavity gradient of 12.5 MV/m and are capable of 100 MeV total acceleration. As of the time of E12-09-016, each linac contains 25 cryomodules which are a combination of the 4 types due to continuous refurbishment efforts. Each linac then is capable of producing 1.1 GeV, and therefore each recirculated beam reaches 2.2 GeV [135]. Halls A, B and C can receive beam energies in $\frac{1}{5}$ multiples of the maximum 5 pass energy of 11 GeV (2.2, 4.4, 6.6 8.8, 11 GeV), while the beam can be recirculated at the north arc a further time to provide one extra half pass of energy, resulting in a maximum 12 GeV beam for Hall D. An extraction system at the south linac uses a series of RF separators, gates and magnets to extract the beam for each Hall at the correct pass. A diagram of this system is shown in Fig. 3.5.

During three Hall operations, three interleaved 499 MHz bunch trains are injected into the 1497 MHz linacs, and extracted using an RF separator frequency at 1/3 of the fundamental accelerator frequency. From 1 pass up to 4 pass, horizontal extraction at 500 MHz is used whereby the beam may be deflected to one of Halls A, B or C per bunch. At 5th pass, 500 MHz vertical extraction is used, wherein all three Halls can have the maximum energy at the same time. At 5th pass with four Halls running, a new 750 MHz vertical extraction is used wherein all four Hall lasers run at 250 MHz, and Hall D fills the “empty” buckets [136]. After extraction at the RF separator, the beam travels to the beam switchyard (BSY), where it is diverted by a series of magnets and sent along the Hall A beamline.

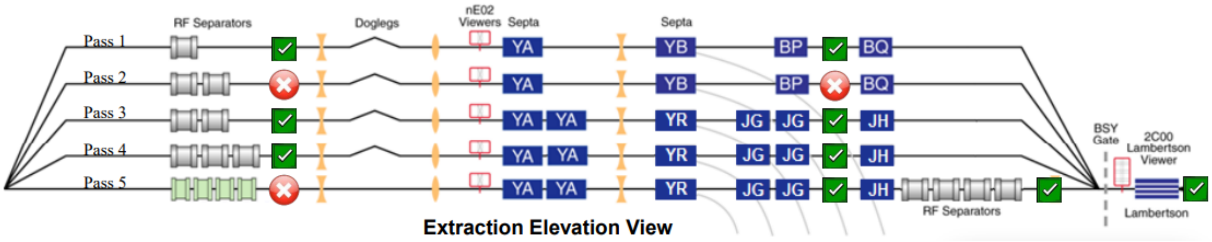

Figure 3.5: Diagram of the Extraction system at the south linac towards Halls A, B and C. The combination of separators and gates changes based on the pass of the extraction. Image from [136].

3.3.3 Hall A Beamline

The Hall A beamline transports the beam from the BSY to the target. A complex system of dipole and quadrupole electromagnets are used to steer and focus the beam from the entrance shield wall to the target, after which the beam travels further downstream eventually reaching the beam dump. The beamline also contains various energy and position monitoring equipment, ion chambers and vacuum pumps, as well as both a Möller polarimeter and

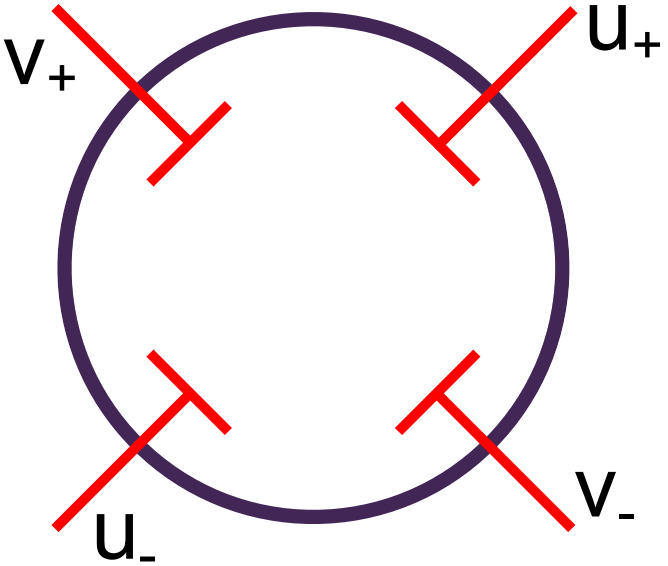

Figure 3.6: Beam Position Monitor (BPM) cavity showing the orientation and labels of the four antennae. BPMA and BPMB are identical in this regard. Image from [138].

a Compton polarimeter. The beam position, charge, energy and polarisation are monitored via different methods described in the following sections.

Beam Position Measurement

The beam position is monitored continuously by two sets of Beam Position Monitors (BPM) located 7.524 m (BPMA) and 1.286 m (BPMB) upstream of the target centre position [137]. BPMs consist of a resonant cavity with a fundamental frequency which is equal to the frequency of the beam. The cavity contains four antennae positioned coaxially around the beamline, rotated 45° relative to the vertical and horizontal axis of the beamline, 90° relative to each other and labelled $u(v)_\pm$ as shown in Fig. 3.6. As the beam traverses the cavity a signal is induced in each antennae which is inversely proportional to the beam's position. Due to this, the difference-sum ratio of the amplitudes of the signal in antennae opposite each other is directly proportional to the distance between the beam and the midpoint between the two antennae [138],

$$\begin{aligned} u &= \frac{u_+ - u_-}{u_+ + u_-}, \\ v &= \frac{v_+ - v_-}{v_+ + v_-}. \end{aligned} \tag{3.1}$$

This technique provides a precision of 100μm for beam currents above 1μA [139].

The BPMs are calibrated from more precise absolute measurements using the Hall A harp wire scanners. These consist of two vertical wires and a horizontal wire which are strung across a movable frame. The wires also have a signal induced proportional to the distance to the beam, and as the frame is moved through a low current beam, the profile and position can be measured. [140]. Harp scans interfere destructively with the beam which means data taking must be stopped to perform these measurements. It is very typical after a long period of no data taking to perform harp scans during “beam checkout” in order to safely restore the beam to the Hall and avoid damaging sensitive electrical equipment, detectors and targets. The position accuracy of the wire harp beam profile is on the order of 20 μm. Making this measurement with the known angles and positions of the harps provides a highly accurate reference coordinate which the BPM can then be calibrated against.

Beam Raster

An electron beam with a spot size on the order of several hundred μm and operated at the currents and intensities typical of Hall A, is capable of destroying a target. To avoid this, the beam is moved across the face of the target in a process called rastering. The Hall A fast raster uses two perpendicular coils located 17 m upstream of the target. When a current is applied to the coils they produce dipole magnetic fields which can steer the beam horizontally and vertically. A 5 x 5 mm^2 circular raster was employed for most of GEN-II. The absolute beam position must be calculated from raster and BPM information. The position offsets introduced by the raster are described by

$$\begin{aligned} x^{\text{rast}} &= O_x + A_x I_x^{\text{rast}}, \\ y^{\text{rast}} &= O_y + A_y I_y^{\text{rast}}, \end{aligned} \tag{3.2}$$

where I_x, I_y are the average currents in each dipole and O_x, O_y, A_x, A_y are coefficients which are calibrated from harp scans and the pedestal-subtracted BPM information.

Beam Charge Measurement

Beam charge is measured by the Hall A Beam-Current Monitor (BCMs) system which consist of a Parametric Current Transformer (PCT) called the Unser monitor after its pioneer [141], and two RF cavities on each side of the Unser [142]. The Unser is an absolute measurement device with a very stable gain, and the BCM RF cavities are able to be calibrated against it. The cavities are cylindrical waveguides tuned to the beam frequency which produce a voltage proportional to the beam current [137].

In a beam-spin asymmetry measurement like E12-09-016 false asymmetries can arise from the beam charge. The BCM data can be used to extract the beam charge asymmetry ($A_{\text{Beam Charge}}$) which is defined as

$$A_{\text{Beam Charge}} \equiv \frac{h_+(I) - h_-(I)}{h_+(I) + h_-(I)}$$

for positive (h_+) and negative (h_-) helicity states respectively. This is also true to a lesser extent for changes in the beam position. It is therefore important to measure any beam charge asymmetry (as well as beam position asymmetry) that arise when the helicity of the beam is flipped. These effects are a measure of the "parity quality" [143] of the beam and parity violating experiments which require quality on the order of parts per million (ppm) are typically much more sensitive [144]. Nevertheless it is crucial to measure these effects even in E12-09-016. The beam charge asymmetry was checked periodically through kinematics by Paul King (Ohio University) and Don Jones (Jefferson Lab), and if it began to become too large (on the order of 1000 ppm) the half wave plate state was reversed in order to constrain the systematic errors introduced by a large beam charge asymmetry.

Beam Energy Measurement

Experiments in Hall A typically require a knowledge of the absolute beam energy of $dE/E = 10^{-4}$. The energy of the beam is monitored via the "Arc" method which uses a portion of the beam transport line as a magnetic spectrometer [145]. The arc is comprised of 8 dipole magnets and 9 quadrupole magnets which bend the beam 34.3° achromatically. However, by turning off the quadrupoles the arc can be operated in dispersive mode in which the bend angle is now energy dependent (no longer achromatic). The field integral of the dipoles $\int B \cdot dl$, energy of the beam E, and bend angle θ are related by

$$E = c\frac{\int B \cdot dl}{\theta} \tag{3.3}$$

for c the speed of light in units of [GeV rad/Tm]. The field is measured in a discrete ninth dipole. By measuring the beam position with BPMs before and after the dipole, the bend angle can be determined up to a resolution of 0.001°. The absolute energy and spread can then be calculated to within the required accuracy [146].

Beam polarisation Measurement

The polarisation of the beam is not measured in real time during running. Instead, separate invasive Möller measurements are taken opportunistically throughout kinematic periods. Möller measurements use the Hall A Möller Polarimeter to utilise the pure QED process of double polarised Möller scattering. The $e+e \rightarrow e+e$ differential cross section is calculable in QED and in the centre-of-mass (CM) frame is given by

$$\frac{d\sigma}{d\Omega} = \frac{d\sigma_0}{d\Omega}\left[1 + P_t^{\parallel} P_b^{\parallel} A_{zz}(\theta)\right] \tag{3.4}$$

where $\frac{d\sigma_0}{d\Omega}$ is the unpolarised cross section contribution, $P_b^{\parallel}$ and $P_t^{\parallel}$ are the polarisations of the beam and target electrons respectively, and $A_{zz}(\theta)$ is the analysing power of the reaction

[147]. The analysing power depends on the CM scattering angle θ,

$$A_{zz}(\theta) = -\sin\theta^2 \frac{8-\sin\theta^2}{(4-\sin\theta^2)^2}. \tag{3.5}$$

The electron beam is incident on an iron foil magnetised to saturation in a 4 T holding field. Pairs of recoil electrons are detected at or near 90° in order to avoid backgrounds and maximise the analysing power. The scattered electrons are diverted 2 m upstream through a system of quadrupole magnets to an adjustable collimator, and then deflected through a dipole magnet towards an exit collimator and finally absorbed by calorimeters within a shielding hut. A side view of this configuration is shown in Fig. 3.7. The asymmetry in counting rate for the two helicity states is measured and the scattering angle can be reconstructed from the hit positions and polarimeter optics, from which the beam polarisation can be extracted from Eqn. 3.4 with <1% statistical and ≈ 0.5% systematic uncertainty.

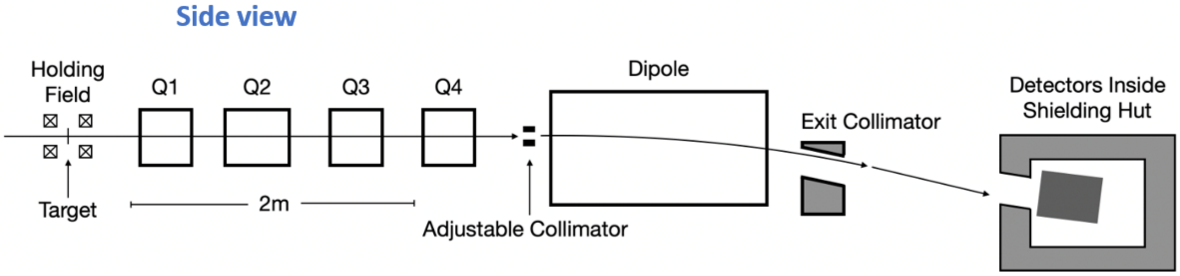

Figure 3.7: Side view of the Hall A Möller polarimeter. Image from [148].

3.4 Targets

Several targets were used throughout the experiment. Polarised ^{3}He cells were used for production runs and were swapped out after reaching an accumulated charge threshold (or after a rupture event). An empty target setting existed primarily for initial monitoring of the beam position and raster during beam-tuning and checkout. Three carbon targets were used: carbon hole for beam position and size tuning; and multi-foil and single-foil for calibrations of the Bigbite spectrometer optics. A reference cell was also used, which could be left empty and used for calibrations and background studies, or filled with H_2 and used to measure elastic electron-proton events at each kinematic setting for detector calibrations and asymmetry corrections.

A target ladder was custom manufactured for the experiment and housed all of the above targets. The ladder was able to be remotely moved vertically up and down in order to select between the target in use at any given time. Each target then corresponded to a specific vertical position. The head of the ladder was fixed to a ceramic base plate, which itself formed part of the ^{3}He target structure, and was fixed in place at the bottom of a ceramic oven. This was in turn connected to the oven heater column which extended upwards towards the vertical controlling unit. The whole system rested inside a set of Helmholtz coils, which in turn were positioned inside a 0.25" thick iron box called the target enclosure. The complete structure is shown in Fig. 3.8. The orange polycarbonate frame which can be seen is the ladder.

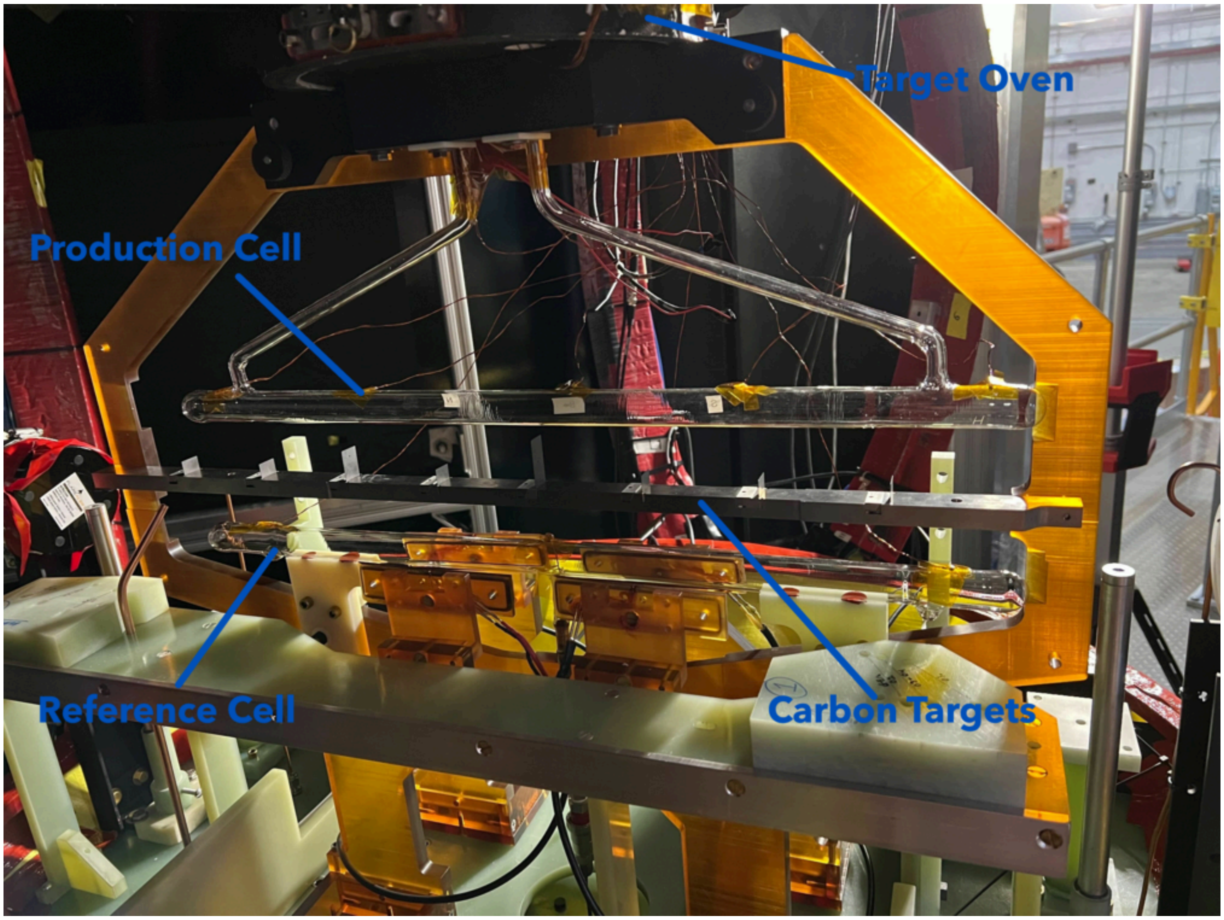

Figure 3.8: A photograph of the full target ladder showing the production cell, reference cell, and titanium beam holding carbon foils.

3.4.1 Polarised ^{3}He Target

This experiment utilised a polarised ^{3}He target first constructed for JLab experiment E94-010 in Hall A, and used in several others including E02-013 (GEN-I). The target design is based on the spin-exchange optical pumping (SEOP) technique. This is a two step process in which an alkali-metal is polarised through optical pumping and subsequently the ^{3}He nuclei are polarised through hyperfine interactions in collisions with the alkali-metal. The general design of the glass cells which contain the ^{3}He gas consists of a spherical pumping chamber (PC) at the top, two long transfer tubes extending downwards, and a 60 cm long narrow target chamber (TC) which the beam interacts within. In previous iterations, diffusion between the pumping chamber and the target chamber was fairly slow, which limited the target's current-handling capability. Dubbed the "Stage II" polarised ^{3}He target, the new glass cells were designed and manufactured at the University of Virginia in collaboration with Michael J. Souza (Princeton University). This new upgraded design for GEN-II had two transfer tubes instead of one, resulting in convection-based circulation of the gas. This allows running at up to 8 times higher luminosities than GEN-I.

The pumping chamber contained ^{3}He gas, a mixture of rubidium and potassium (Rb/K) alkali-hybrid metal and a small fraction of nitrogen (N_2) gas. The pumping chamber rested within a ceramic oven, which would be heated to varying temperatures over 200 degrees Celsius in order to vaporise the alkali mixture. The oven was attached to a heater column which was installed above the target enclosure. A 794.7 nm red laser was incident upon mirrors which were attached on opposite ends of the oven. One of these mirrors is shown on the left of Fig. 3.9, in the process of mounting to a base plate. This base plate was then attached to the wing of the oven, shown on the right of Fig. 3.9, through the three visible bolt holes. The mirrors were coated in 794.7 nm reflective quarter-wave microfilm, and reflected the laser light into the oven through a glass window which was also coated in microfilm. The oven was sealed at the bottom by an insertable ceramic base plate. The target cell was attached to this base plate at two holes which the transfer tubes passed through. The transfer tubes were sealed in place at these holes via room temperature vulcanising (RTV). The base plate in turn was secured to the target ladder via a ceramic bracket, to ensure structural integrity of the whole system. A small heater strip was placed on one of the transfer tubes to provide localised heating, which would in turn drive convection.

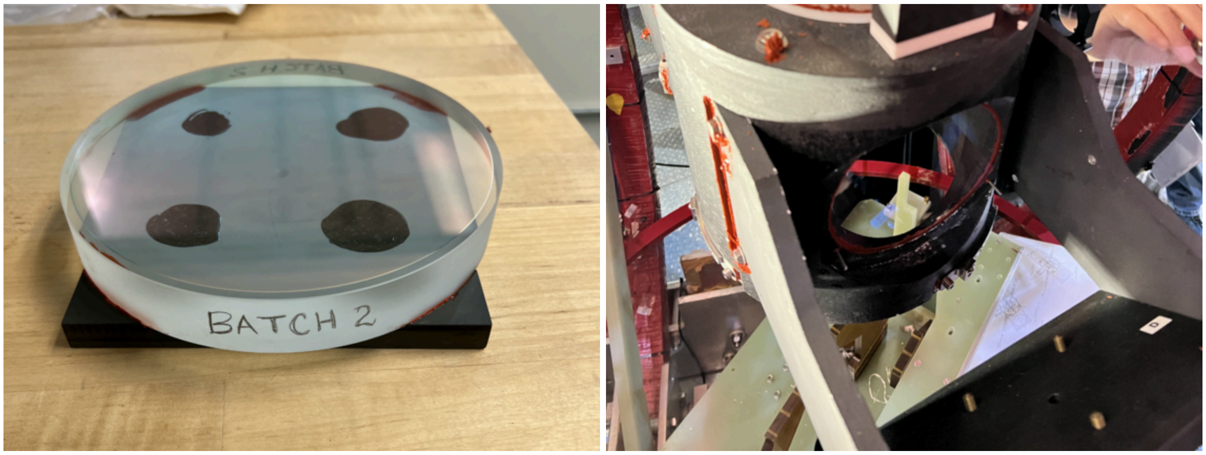

Figure 3.9: (Left) mirror mounted with RTV and glue to ceramic mounting plate, which has holes on the bottom to accommodate the oven wing bolts. (Right) Top view of the target oven during installation work. The arm structure has a 45 degree tilt which will house the mirror. An identical second arm and mirror sits 180 degrees opposite.

^{3}He As an Effective Neutron Target

Neutrons decay with a mean lifetime of approximately 880 seconds [149] which presents the experimental challenge that no free neutron targets exist. As such light ion species such as deuterium (^{2}H) or in the case of this experiment ^{3}He can be chosen as suitable effective neutron targets. The approach of using ^{3}He to study elastic form factors of the neutron has been theoretically studied [150–152] and calculations for inclusive and exclusive electron-^{3}He scattering have been performed [152–155]. The neutron polarisation in ^{3}He as well as the general three-nucleon wavefunction have been computed in many works via the Faddeev equations [156] and variational approaches [157–161]. In its ground state, the ^{3}He wavefunction spin component is dominated by a configuration in which the two proton spins anti-align. The contributions to the spin wavefunction are illustrated in Fig. 3.10, which shows the relative contributions of the S, D and S' states. The result is a nucleus where the neutron carries $\sim$86% of the total spin [162].

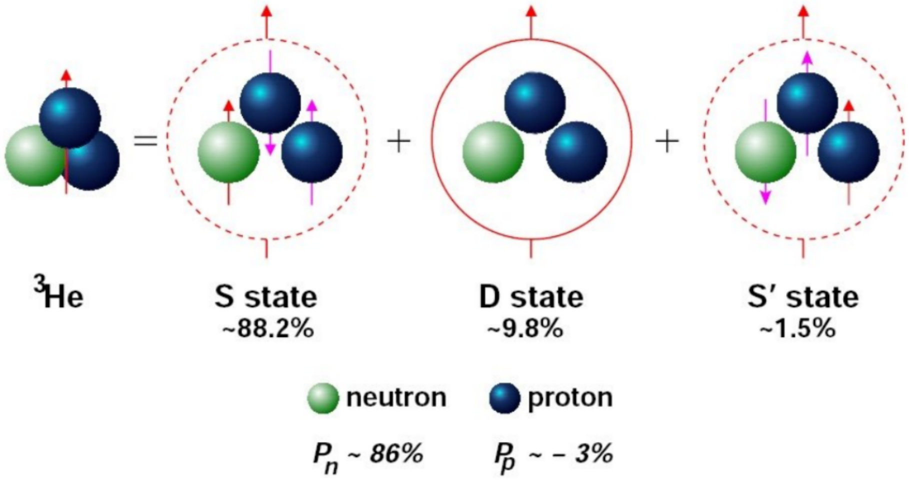

Figure 3.10: Dominant partial-wave spin contributions to the ^{3}He nucleus.

The effective neutron polarisation in experiments involving DIS scattering has been shown by several calculations to agree with this value [158, 159]. However in the quasielastic analysis presented in this work, inelastic events in our final data sample are suppressed by the choice of cuts, particularly on the missing transverse momentum of the nucleon. This has the effect of selecting out portions of the ^{3}He wavefunction with lower momentum. In particular, it suppresses the degree to which the D state contributes, in which the three nucleons have their spins aligned opposite to the nuclear polarisation. This has been shown in GEN-I to increase the effective neutron polarisation to $> 95\%$ for all of the values of momentum transfer measured [112]. The neutron polarisation and nuclear corrections to the final physics asymmetry are discussed more fully in Sec. 5.10.

Spin Exchange Optical Pumping

Spin exchange optical pumping is a powerful technique to polarise ^{3}He. The process involves two main steps: optical pumping of the alkali metal vapour and subsequent spin exchange between the polarised alkali metal atoms and the ^{3}He gas atoms. The alkali vapour and ^{3}He gas are both present in the pumping chamber, and the entire system is placed in a magnetic holding field via the Helmholtz coils. This induces Zeeman splitting of the energy levels in the ground state ($^4S_{1/2}$ for potassium, $^5S_{1/2}$ for rubidium, corresponding to principal quantum number $n = 4, 5$ respectively) of the valence electrons of the alkali vapour, which separates the $m_s = -1/2$ and $m_s = 1/2$ levels.

In the first stage of traditional SEOP, a circularly polarised laser tuned to the D1 transition of the alkali metal (in this case 794.7 nm for Rb) excites the electrons from the spin down S ($m_s = m_j = -1/2$) level to a spin up sub level in the P state ($m_s = 1/2$). The excited electrons spontaneously decay back to the ground state, either via direct decay to the $S_{+1/2}$ state, or through collisional mixing into the $P_{-1/2}$ state and further decay into $S_{-1/2}$ level as depicted in Fig. 3.11. The presence of nitrogen suppresses re-radiation via nonradiative quenching of excited atoms [163] to the $S_{1/2}$ level. In addition to quenching the nitrogen can also undergo fine structure collisional mixing and contribute to excited-state spin relaxation [164] and broadening of the absorption lines of alkali metals [165]. The latter in some scenarios would enhance the efficiency of optical pumping, however narrowband lasers are used in this experiment which are even more efficient at optical pumping [166]. Fortunately the former, nitrogen induced spin relaxation, is a minor effect particularly at larger pressures (> 1bar) [167].

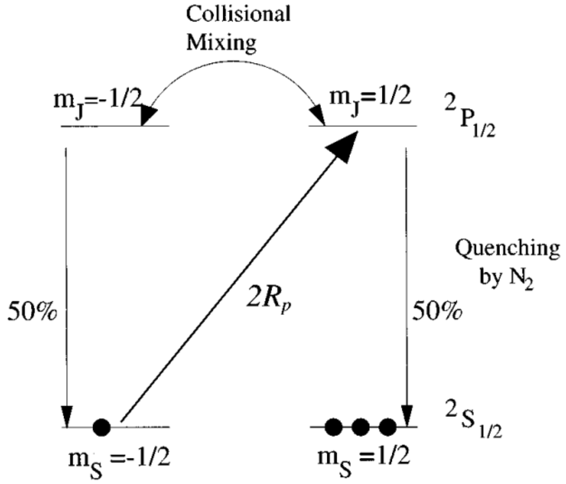

Figure 3.11: Example of the process of optically pumping an alkali gas. In this example the ground state is $^2S_{1/2}$ corresponding to Lithium, however the process is analogous across the increasing principal quantum number n of the alkali metals. Image from [163].

The polarisation of the rubidium can be described by the optical pumping rate R and the relaxation rate of the metal Γ_{Rb}:

$$P_{\text{Rb}}(t) = \frac{R}{R + \Gamma_{\text{Rb}}}(1 - e^{-\frac{t}{\tau}}) \tag{3.6}$$

where the factor $\tau = \frac{1}{R+\Gamma}$ is the characteristic time constant for optical pumping [168] which determines the time taken to reach equilibrium ($P = \frac{R}{R+\Gamma}$). This is expected to be on the order of milliseconds. The optical pumping rate is given by the integral over laser frequency v,

$$R = \int_0^{\infty} \Phi(v)\sigma_1^{\text{Rb}}(v)dv, \tag{3.7}$$

where $\Phi(v)$ is the laser flux and σ_1^{Rb} is the unpolarised rubidium photon absorption cross section for the D1 transition [169]. For a narrowband 794.7 nm laser with ~ 0.2 nm linewidth, v is approximately a delta function, and the rate is effectively equal to the product of the single wavelength flux and cross section. The absorption cross section typically peaks around the excitation frequency, therefore the rate is maximised with narrowband lasers.

In the second stage of SEOP, the polarised Rb atoms collide with ^{3}He atoms. During these collisions, the polarised spin of the Rb electron is transferred to the nucleus of the noble gas atom via hyperfine interactions. The spin-exchange rate in the fast diffusion limit (in which transfer rates approach infinity) is given by

$$\langle \gamma_{\text{se}} \rangle = f_{\text{PC}} k_{\text{se}}[\text{Rb}], \tag{3.8}$$

where f_{pc} is the fraction of the ^{3}He in the pumping chamber, and k_{se} is the spin exchange constant for rubidium. The time-dependent polarisation of the ^{3}He can then be described by

$$P_{\text{He}}(t) = P_{\text{Rb}} \frac{\gamma_{\text{se}}}{\gamma_{\text{se}} + \Gamma_{\text{He}}} \left(1 - e^{-t(\gamma_{\text{se}} + \Gamma_{\text{He}})}\right) \tag{3.9}$$

where P_{He} is the nuclear polarisation of the ^{3}He, P_{Rb} is the polarisation of the Rb vapour, γ_{se} is the cell averaged spin-exchange rate between the ^{3}He and the alkali-metal and Γ_{He} is the spin relaxation rate of ^{3}He nuclei due to any other processes. From this equation we can see that with sufficient laser power such that $R >> \gamma_{\text{Rb}}$ and density of rubidium such that $\gamma_{\text{se}} >> \Gamma_{\text{He}}$, then the polarisation would approach 100%. In reality this has never been achieved, primarily due to what is now a well documented and empirically established but otherwise unexplained relaxation mechanism [170]. Eqn. 3.9 can be modified accordingly for the state of equilibrium,

$$P_{\text{He}} = \langle P_{\text{Rb}} \rangle \frac{\langle \gamma_{\text{se}} \rangle}{\langle \gamma_{\text{se}} \rangle (1 + X) + \langle \Gamma_{\text{He}} \rangle} \tag{3.10}$$

where each term is now time averaged, (denoted by $\langle x \rangle$) and the factor $(1 + X)$ accounts for this relaxation mechanism. This provides an upper constraint of $\frac{1}{1+X}$ on the polarisation of the ^{3}He. The overall efficiency of this spin transfer towards this limit depends on the density of the alkali metal vapour, the temperature, the pressure of the noble gas, and the presence of quenching gas.

Alkali-Hybrid SEOP

The addition of Rb/K alkali hybrid in place of solely Rb was first performed for GEN-I and allows more efficient transferring of the polarisation to the ^{3}He due to their optimally paired spin exchange rates, improved collisional dynamics, and balanced relaxation properties. When the ratio of the vapour density of the two metals $D \equiv \frac{\rho_{\mathrm{K}}}{\rho_{\mathrm{Rb}}}$ is very small ($D << 1000$), collisions between the two occur maximally which results in $P_{\mathrm{K}} = P_{\mathrm{Rb}} = P_{\mathrm{Alk}}$. Potassium vapour pressure is higher than rubidium at a given temperature. So at certain optimal temperatures for SEOP (200-250 °C), the vapour pressures of Rb and K together can be tuned to maximise the density of alkali metal atoms available for spin exchange without requiring excessively high temperatures.

Now the ^{3}He is polarised by hyperfine interactions from both metals. However, the spin exchange rates between alkali metals and noble gases vary. Potassium has a 15 times higher spin exchange rate with ^{3}He compared to rubidium. The equilibrium equations for the polarisation have the same form, but the components are modified to account for spin exchange and relaxation components of the K:

$$\begin{aligned} \Gamma_{\mathrm{Alk}} &= \Gamma_{\mathrm{Rb}} + D(\Gamma_{\mathrm{K}} + 2k_A) \\ \langle \gamma_{\mathrm{se}} \rangle &= f_{\mathrm{pc}} k_{\mathrm{se}} \left[1 + D\left(\frac{k'_{\mathrm{se}}}{k_{\mathrm{se}}} \right) \right] \end{aligned} \tag{3.11}$$

where Γ_{K} is the spin-relaxation rate of potassium, k_A is the average Rb-K spin relaxation rate and k'_{se} is the K-^{3}He spin-exchange rate constant. Potassium typically has a longer spin relaxation time compared to rubidium. By using a hybrid mixture, the overall relaxation rates can be balanced for an optimal ratio D to sustain higher polarisation levels for longer periods, improving the efficiency of polarisation transfer to the ^{3}He [169].

Additionally a single alkali metal vapour can become optically thick at high densities, meaning that the laser light is heavily absorbed near the entry point and does not penetrate deeply enough to polarise atoms throughout the cell uniformly. By using a mixture of Rb and K, the total optical depth is effectively distributed between the two species, allowing more uniform and efficient pumping. Ultimately, the convection voltage/current settings, oven temperature and laser power were tweaked through the experiment in efforts to maximise the polarisation of each cell, in line with the above ideas.

3.4.2 Reference Cell

A 60 cm long glass cell was attached to the bottom of the target ladder. This reference cell, depicted in Fig. 3.12, was developed at The College of William and Mary. It consisted of the target chamber and a single transfer tube that was connected to a nozzle and hose, which were subsequently fed from a pumping system below the target enclosure. This cell could be remotely vented and filled. For this experiment it was primarily used to take data on H_2 gas at a similar pressure to the production cell to use for detector calibrations.

Figure 3.12: Reference cell prior to installation.

3.4.3 Carbon Targets

Eight carbon foils were fixed on a titanium support rod which was in turn fixed to the target ladder. The ladder vertical control settings had three separate positions on the carbon foils, which would allow the beam to hit one of the three settings; “hole”, “optics” or “foil”. An illustration of the carbon target is presented in Fig. 3.13, which shows the z coordinate of each foil, and the path of the beam towards the downstream direction passing through the foils at each setting.

As shown in Fig. 3.13, on the single-foil carbon optics target, the beam would be centred on one carbon foil. This target was used to calibrate the carbon optics data. Reconstructed tracks on the foil necessarily have a known single z-axis position along the target. By align-

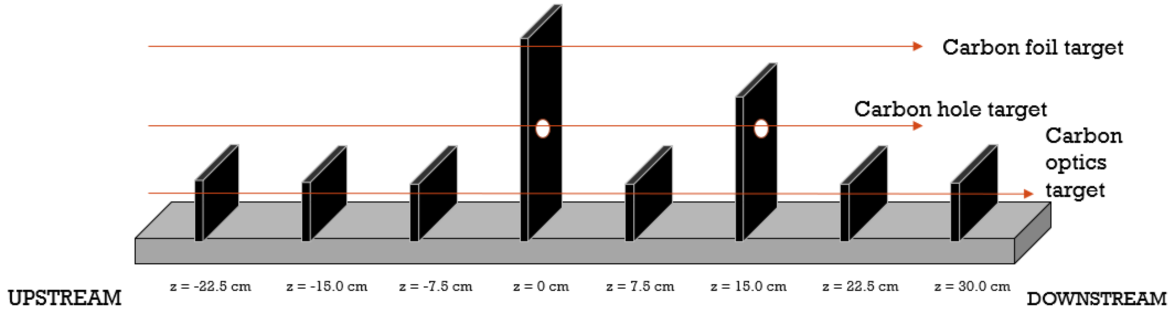

Figure 3.13: Depiction of carbon target z positions along the beamline, and beam positions of the three target settings. Image from [171].

ing the optics data with the magnets on and sieve plate in, to the foil data with the magnets off, the carbon optics were properly calibrated. The carbon hole target had the beam striking two foils with holes at the centres. This was used during beam restoration procedures to check that the beam spot, rastering and position were working. The size and shape of the hole could be reconstructed at the target via the optics which is shown in Fig. 3.14. The current of the vertical and horizontal rasters for reconstructed tracks are plotted in 2D. The small hole at the centre of the coloured distribution indicates the hole on the target. The multi-foil carbon optics target had the beam striking all eight foils directly with no holes. This was used for optics calibration with an insertable sieve plate attached to the Bigbite magnet. The optics calibration is discussed in Sec. 4.6.

3.5 Coordinate Systems

There are three coordinate systems used in Hall A: the standard lab (or Hall) coordinate system and the transport coordinate system which is different for both spectrometers. The Hall coordinate system (HCS) has an origin at the centre of the target. $\hat{z}$ is in the nominal downstream direction of the beam, towards the beam dump. $\hat{y}$ points up towards the ceiling, and $\hat{x}$ forms a right handed system $\hat{x} = \hat{y} \times \hat{z}$ pointing left of the beamline as viewed looking in the downstream direction. The transport coordinate system (TCS) also has the origin at the centre of the target. $\hat{z}$ faces the central axis of the spectrometer in question. $\hat{x}$ points downwards and $\hat{y}$ forms a right handed system $\hat{y} = \hat{z} \times \hat{x}$. Since the momentum of the beam $\vec{k}_i$ is along the $\hat{z}$ axis of the lab frame, then in the transport frame this is

$$\vec{k}_i = \begin{pmatrix} 0 \\ -\sin\theta_{\text{spec}} \\ \cos\theta_{\text{spec}} \end{pmatrix} \tag{3.12}$$

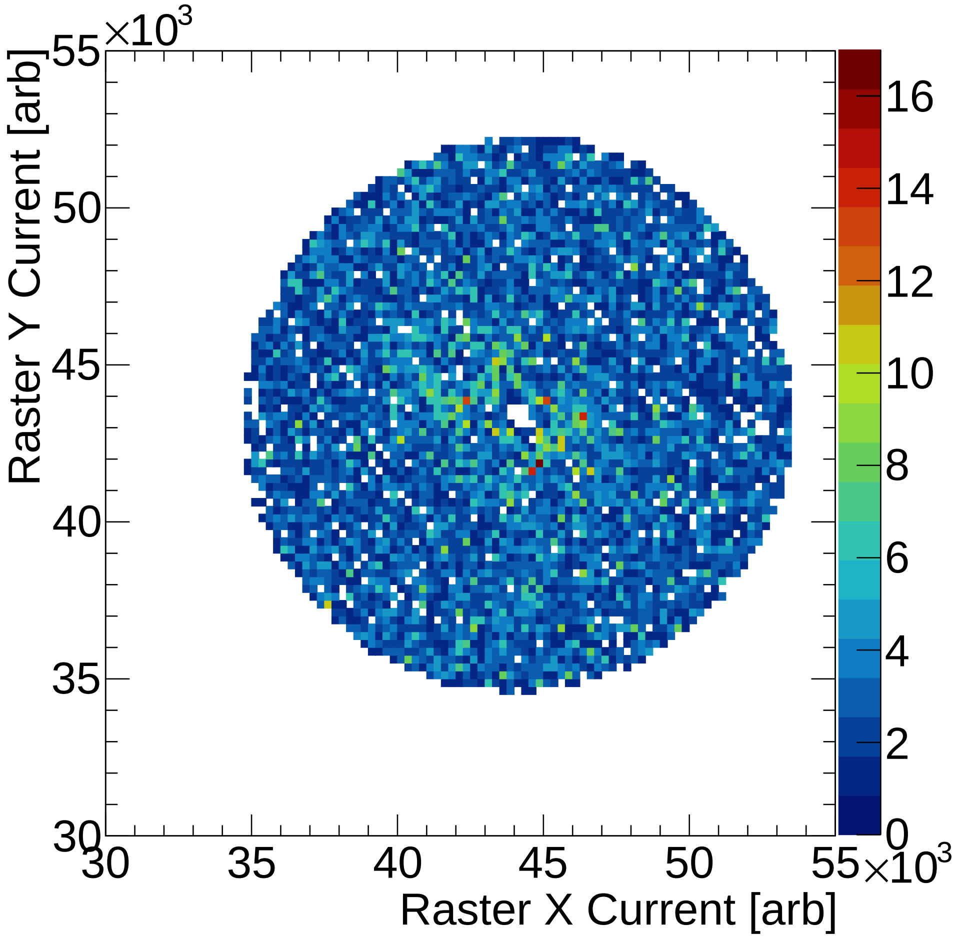

Figure 3.14: An online monitoring plot from a carbon hole run during GEN2. The coloured bins indicate the x-y currents of the raster for reconstructed tracks. The shape of the distribution indicates the raster shape, and the carbon target hole is visible in the centre, where no tracks will have been reconstructed.

where θ_{spec} is the in plane horizontal angle of the spectrometer in the lab frame. Then defining ψ to be the angle between the momentum and projection onto the $y-z$ plane and ϕ to be the angle between the projection onto the $y-z$ plane and the z axis,

$$\tan\psi = \tan\theta\cos\phi \tag{3.13}$$

and the momentum transfer vector is

$$\hat{q} = \begin{pmatrix} \sin\psi \\ \cos\psi\sin\phi \\ \cos\psi\cos\phi \end{pmatrix}. \tag{3.14}$$

3.6 Electron Arm: Bigbite

The Bigbite spectrometer was initially constructed for use in electron scattering experiments at the Internal Target Facility of the Amsterdam Pulse Stretcher (AmPS) ring at the National Institute for Subatomic Physics (NIKHEF) [172]. Bigbite is a magnetic spectrometer comprised of a single dipole magnet which earns its name by virtue of a combined large solid angle and momentum acceptance for a spectrometer. The full electron arm of the experiment comprises the Bigbite magnet and a new complementary detector stack which can be seen fully in Fig 3.15. Bigbite is located on the left hand side of the downstream beam, at a central angle as close to the elastic electron scattering angle as possible, for a given kinematic setting. The detector stack is situated on a platform, which is fixed at a radial distance from the target enclosure by a steel beam, and the platform can rotate out from the beamline at a polar angle range of $0 < \theta_{\mathrm{BB}} < 90^{\circ}$, however physical limitations apply due to the existence of the beamline at $\theta = 0$, and the decommissioned Left High Resolution Spectrometer (LHRS) which still exists in the Hall. The detector stack consists of a variety of subsystems which are detailed in the following subsections.

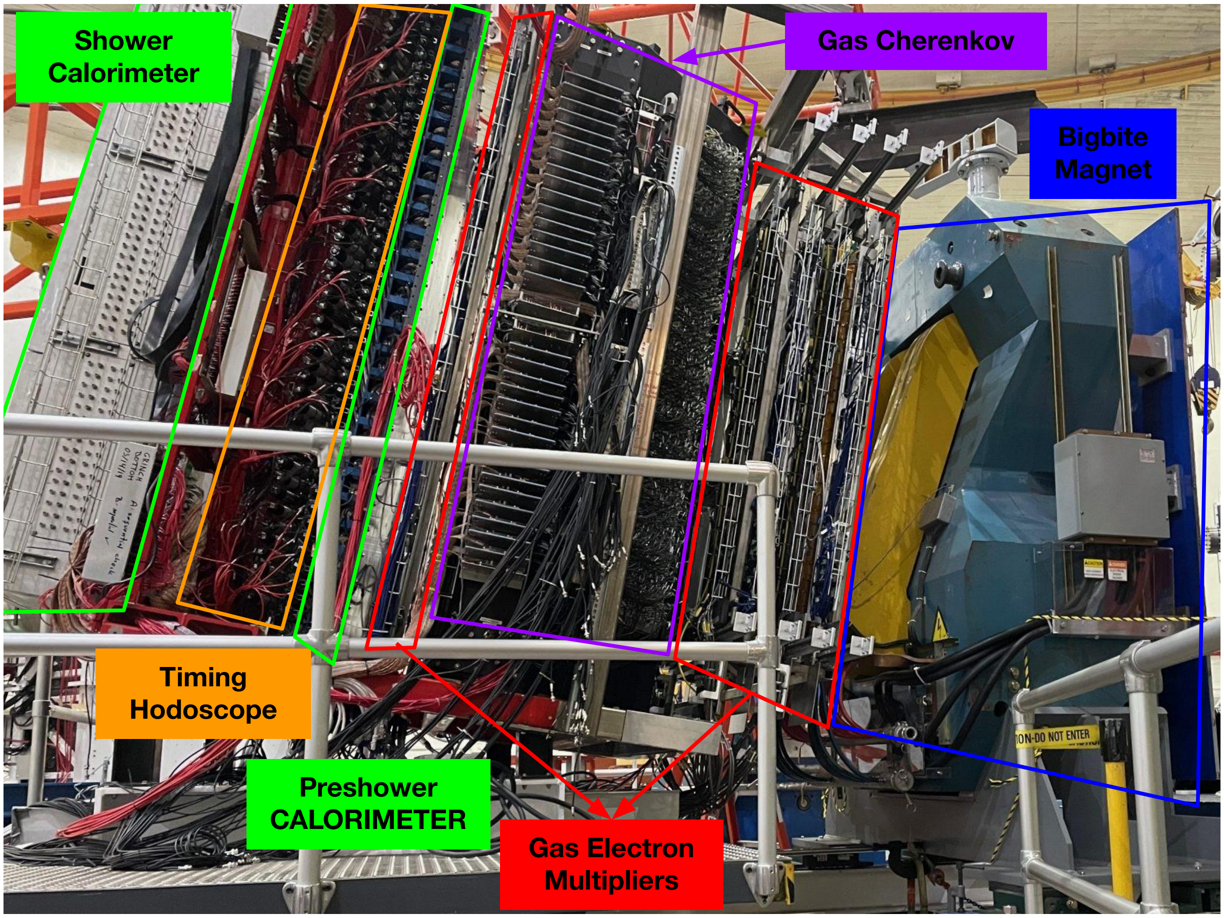

Figure 3.15: Bigbite as seen from left of spectrometer centre (upstream direction towards right of image, downstream direction towards left of image) annotated with subsystem names.

3.6.1 Bigbite Dipole Magnet

The Bigbite magnet is an H-shaped dipole with a 25cm gap. The opening on the front face is perpendicular to the central trajectory and axis of the spectrometer, and the exit has a pole face rotation of 10°. This enhances the field integral for particles which enter at the top region of the magnet, whilst reducing the field integral for particles which enter at the bottom region. This makes the dispersion more uniform across the acceptance of the spectrometer [173]. Bigbite acquires its name from its large angular and momentum acceptance. For example at kinematic setting 2, Bigbite has a solid angle acceptance of approximately 30 msr, and a momentum bite of approximately $0.4 \leq p \leq 3.5$ GeV. The magnet consists of a low-carbon steel yoke and polar components, copper pipe water-cooled coils, and support clamps which accommodate an insertable sieve slit plate. The total mass of the spectrometer is over 20 tonnes. The magnet is positioned 1.63 m away from the centre of the target for all kinematic settings. The distance from the front face to the centre of the dipole is 31.0 cm, and the distance along the central trajectory from the centre of the magnet to the back face is 68.5 cm. A full technical drawing is shown in Fig. 3.16 from experiments E-06-010/E-06-011 (Transversity) for scale.

3.6.2 Bigbite Gas Electron Multiplier Trackers

Gas Electron Multipliers (GEMs) are used in this experiment for tracking the electron position and trajectory, and reconstructing its momentum. Bigbite has five GEM trackers, or “layers”. There are four GEM layers on the front of the spectrometer, located between the BigBite magnet and the rest of the detector stack. The fifth rear GEM layer is located further downstream, in the middle of the detector, between the “GRINCH” Cherenkov and the preshower calorimeter. As a particle traverses the GEMS, each layer measures a 2D position in x-y space. The positions on each layer can then be combined along the z direction to form a track. This track can be projected backwards towards the magnet, and with an optics model, the initial trajectory and momenta at the target can be reconstructed.

Traditional tracking methods such as wire chambers while having excellent spatial resolution, are typically limited in their rate handling capabilities on the order of 10 kHz/cm^2, as a result of space charge and occupancy issues. An advantage of running with GEM trackers is their ability to handle much higher rates, on the order of 500 kHz/cm^2, while maintaining a spatial resolution of around 70 μm. This is made possible because the small hole sizes in the GEM foils screen the movement of ions towards the readout electrode, and due to the very short drift distances of the charge. This reduces the build up of space charge which is typical in wire chamber designs and often results in large ion tails in the signal. By removing this occupancy bottle-neck the avalanche can reach the readout in around 100 ns, which is orders of magnitude faster than traditional wire chambers. Ultimately this makes

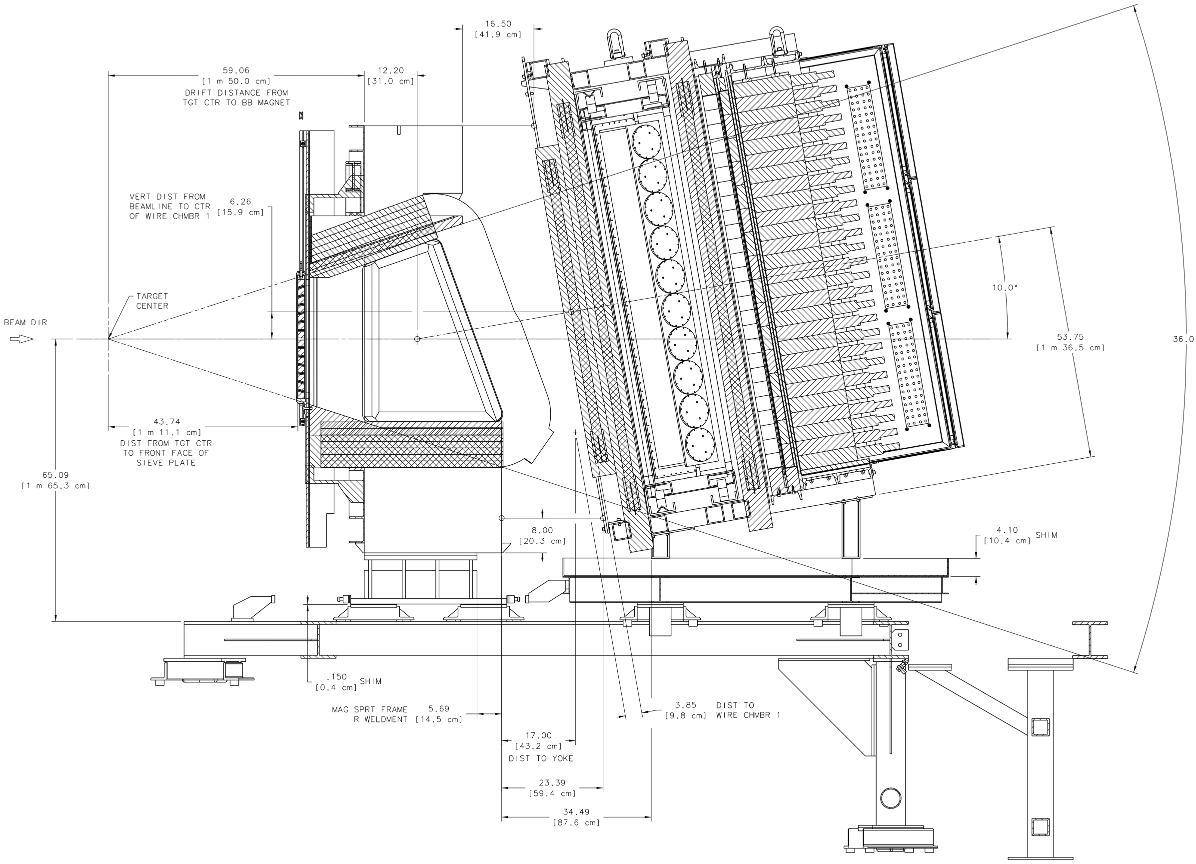

Figure 3.16: CAD Drawing of the Bigbite spectrometer during Transversity experiment E06-010. Detector stack subsystems have changed, but the magnet dimensions remain the same in E12-09-016.

the GEMs much faster tracking detectors and therefore able to handle much higher rates [174]. This technology enables the SBS program to run at high luminosity and acceptance simultaneously.

In experiment E12-09-016 all of the GEMs used were manufactured and produced by the University of Virginia (UVa). GEMs are gaseous ionisation detectors for charged particles originally introduced in 1997 [175]. They consist of a drift cathode foil at the front of the detector on the particle entrance plane, one or more GEM foil layers and a readout board on the exiting plane. Relatively large voltages are applied across the GEM foils, producing a gain of around 20 per foil layer. In this case of triple-gems the resultant gain is 8000 on average. A GEM foil is typically a 50 μm thick polyimide foil coated with ~5 μm of copper. The readout plane consists of two sets of thin copper strips separated by an insulating layer of polyimide [176].

In production conditions, all GEMs ran an Ar/C0$_2$ (75/25) gas mixture. This could be switched to N$_2$ gas during standby or testing periods. When a charged particle traverses the GEM, the gas mixture is ionised which produces further charged particles. These continue to propagate and accelerate through the electric fields within the drift and hole regions of the GEM until eventually the amplified signals from the avalanche are detected on the electronic readout board. Fig. 3.17 shows an illustration of the avalanche caused by an ionising particle traversing a single GEM layer.

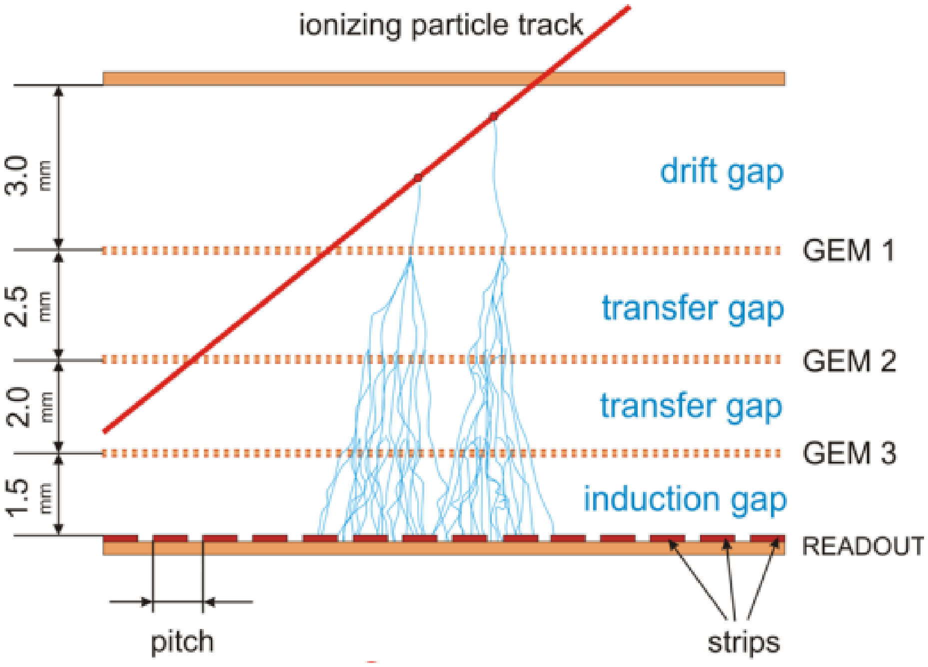

Figure 3.17: An example of the avalanche produced by a single ionising particle travelling through the layers of a Triple-GEM. The number corresponds to foil layers in a single GEM detector. The signal is amplified through each foil and eventually reaches the readout plane. Image from [177].

Layers 1-4 were all “UV” layers. UV corresponds to trackers with the internal copper strips orientated at 30(U) and 150(V) degrees to the x-axis, with a stereo angle of 60 degrees between them, within the local xy plane of the layer. The UV layers consist of a single large module (active area of 40 x 150 cm^2). The fifth GEM tracker at the rear is an “XY” layer, which has the copper strips at a simpler Cartesian style orientation where the X and Y axes are orthogonal to each other. The copper wires cannot be constructed vertically along the entire 2 m length, so the XY layer consists of four modules stacked vertically (each with an active area of 60 x 50 cm^2). Both types of layer are shown in full with dimensions annotated in Fig. 3.18 before installation. The UV GEM foils have a total 3840 readout channels in both the U and V directions for a total of 7680 per layer, and are divided into 20 rectangular sectors for readout. The XY GEMS have 1280 X strips and 1536 Y strips per module, for a total of 11264 in the layer. As a result there are 41984 GEM channels potentially firing within any given event. When running at the high luminosities typical of Hall A, this results in a relatively enormous amount of data per second.

The GEM modules are read out by APV25 readout cards (APVs) which are analogue readout cards originally designed as pipeline ASICs for the CMS tracker read-out system at CERN

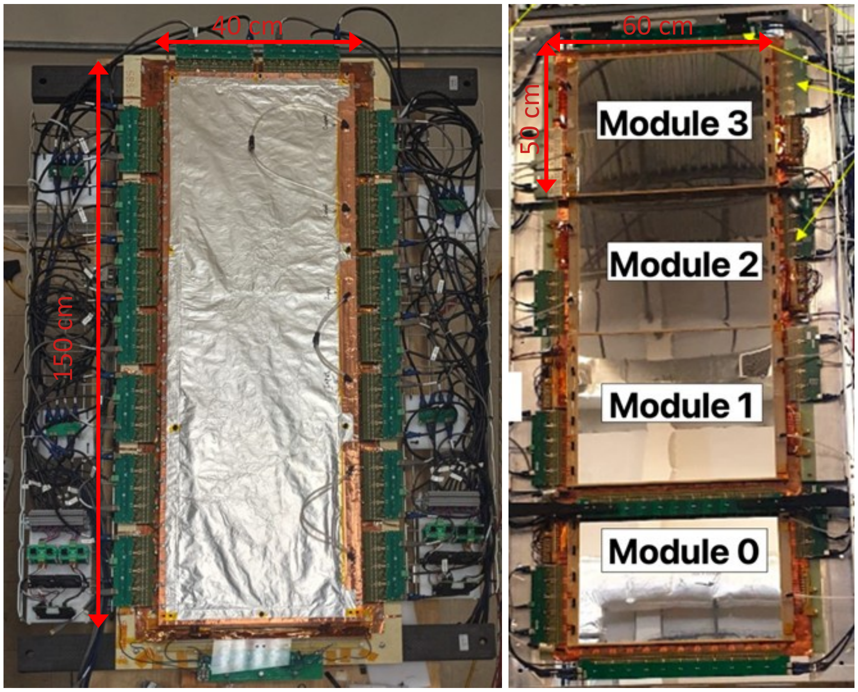

Figure 3.18: (Left) Single UV GEM layer. (Right) An XY GEM Layer comprised of 4 modules labelled 0 through 3. Image from [176].

[178]. The cards have 128-pin connectors and are grounded directly into the GEM readout boards to interface with 128 strips each. As a result, 60 APV25 cards are required to read out a UV layer, for a UV total of 240, and 188 for the XY giving a final total of 300 cards. The APVs are triggered to collect raw signals via a parallel trigger logic, which are processed through Multi-Purpose Digitiser (MPDs) [179]. These are in house JLab boards with Versa Module Eurocard Bus (VME) interface, which receive analogue data streams and digitise them, and then feed them further through the DAQ pipeline. The signals are sent to VXS Trigger Processors (VTPs) [180], which are the central trigger processor in the GEM DAQ system. Finally the signals are sent through a network interface to the CODA data acquisition software hosted on a local machine in the counting house [176].

3.6.3 GRINCH Cherenkov Detector

The **G**as **RIN**g **CH**erenkov (GRINCH) detector is a heavy-gas Cherenkov threshold detector, designed to provide particle identification between electrons and pions up to a threshold momentum. The GRINCH consists of 510 1-inch photo-multiplier tubes (PMTs) in a honeycomb array, and four highly reflective cylindrical mirrors within the body of the detector. The total volume of the detector is filled with heavy Octafluorocyclobutane (C_4F_8) gas.

The GRINCH is situated in the BB detector stack between the front GEM trackers and the fifth rear GEM tracker. In Fig. 3.19 this is shown as an illustration and with a photograph from the Hall, with the GRINCH labelled.

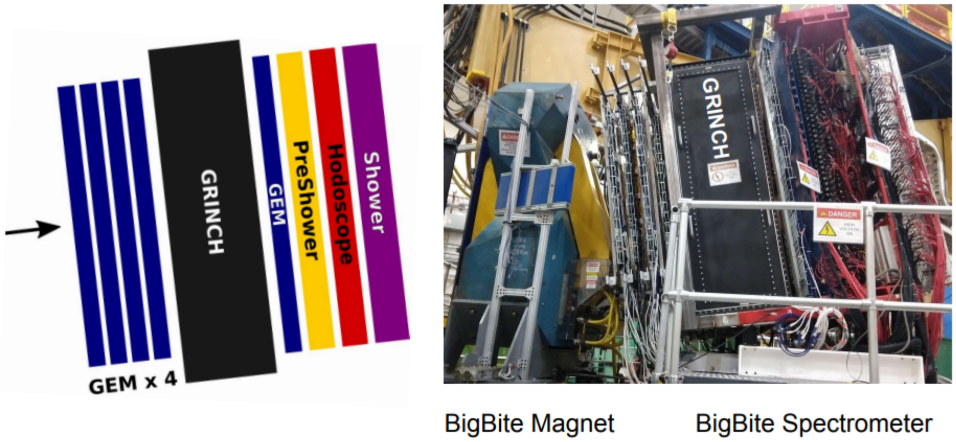

Figure 3.19: The GRINCH detector installed in the BigBite stack. Highlighted in black in the illustration on the left, its position between the rear and front GEM layers is more clearly demonstrated. On the right viewed from right of spectrometer centre (downstream beam to towards left of image). Image from [181].

The particle identification between electrons and pions is achieved via the different signals they produce by Cherenkov radiation, below the threshold momentum. Cherenkov radiation is a phenomenon in which a charged particle travelling faster than the phase velocity of light in a dielectric medium produces photons. The geometry of the inside of the detector is shown in Fig. 3.20. The incoming particles produce electromagnetic shockwaves which propagate towards the reflective mirrors. These are set at an angle such that the photons are reflected back towards the PMTs, while the electrons of interest propagate cleanly through the rest of the detector stack.

Recall that the index of refraction n_i and phase velocity v_i of two mediums are directly related by Snell's Law

$$\frac{v_1}{v_2} = \frac{n_2}{n_1} = n_{12}. \tag{3.15}$$

A perfect vacuum has a refractive index of 1, and the speed of light c. With the knowledge of the rough expected momenta and mass of the particles, the speed can be calculated from the beta factor $\beta = \frac{p}{\sqrt{m^2+p^2}}$ and a medium can be chosen such that the resultant phase velocity v_2 is lower than the particle velocity. In this way the index of refraction of the gas can then be used to discriminate between velocities. C_4F_8 has a refractive index of 1.00132 at 405 nm laser light, 1 atmosphere pressure (n = 1.00129 at 632.8 nm, 1 atm) [182]. The resultant phase velocity at n_2 = 1.00132 is 0.9968c. Electrons above 1 GeV have a beta factor of at least 0.999(6) owing to their small mass. However, pions with a mass of 140 MeV do not exceed the phase velocity of the gas until about 2.7 GeV. This is the resultant GRINCH "threshold".

The Cherenkov light cones from electrons appear as clusters on the PMT array due to the path length of the light cone in the GRINCH. A light cone can then be detected as a

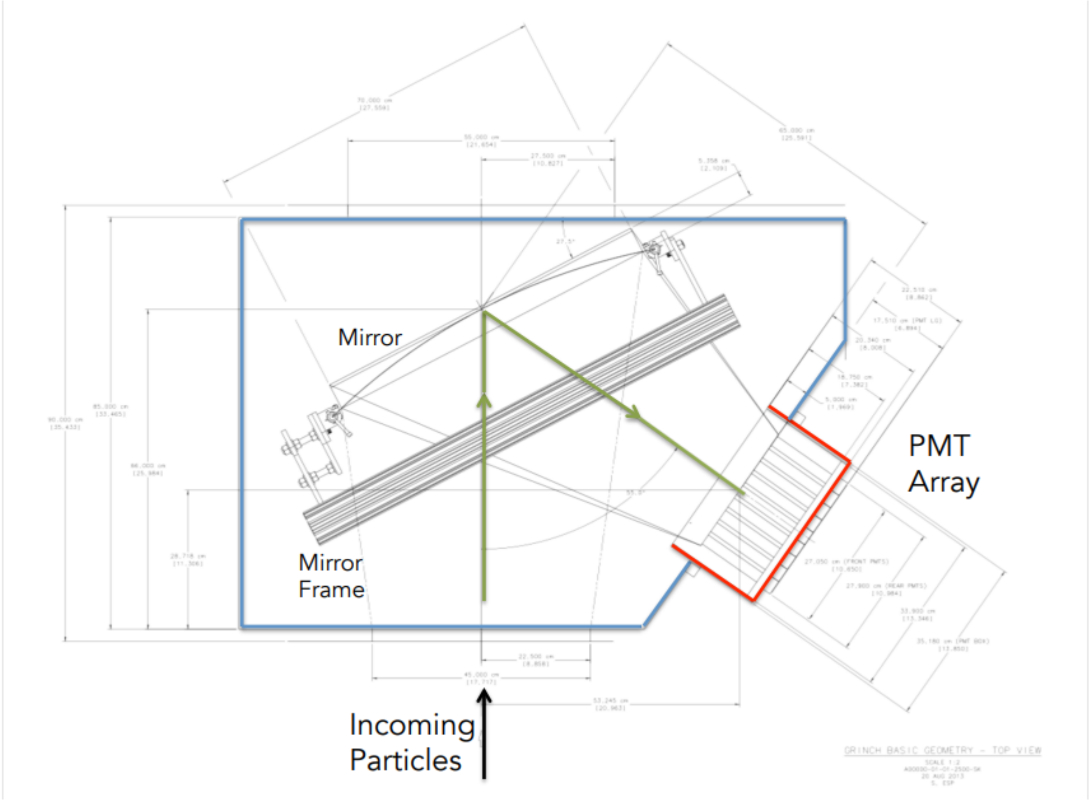

Figure 3.20: Top down view of the inside of the GRINCH detector. The incoming charged electrons produce a Cherenkov boom up to the threshold of 2.7 GeV. Above this both pions and electrons can produce signals. The photons are reflected backwards by the mirrors into the PMT array. Image from [182].

"ring" using signals from the PMTs via a clustering algorithm, which requires at least three or more neighbouring PMTs to form a cluster. By matching the position of the cluster to the best track and looking at the difference in cluster sizes associated with electron's and pion's light cones, this allows for discrimination between pions and electrons at the same momentum or energy, up to the GRINCH pion threshold of 2.7 GeV [181].

The PMTs convert the incident light to photoelectrons in the photocathode. The photoelectrons then are guided through the various dynodes in the PMT, ultimately creating an avalanche of electrons. The electron avalanche then reaches the anode, producing a measurable current signal. All detectors in the SBS experimental setup, with the exception of the GEMs, are read out by PMTs in this way.

Signals from each PMT in the GRINCH (and Timing Hodoscope) are extracted to custom made amplifier/ discriminator front-end cards designed by University of Glasgow and manufactured by Zott, which are based on the NINO ASIC [183]. The NINO card is a high speed discriminator which has a low voltage power input as well as a threshold voltage. The cards have 16 channel input and separate 16-channel digital (LVDS) and analogue outputs. The signals from the NINO cards are then then read out to VME-based CAEN v1190 Time-to-Digital Converters (TDCs) [184]. These are multihit TDCs with a 40 MHz clock input and

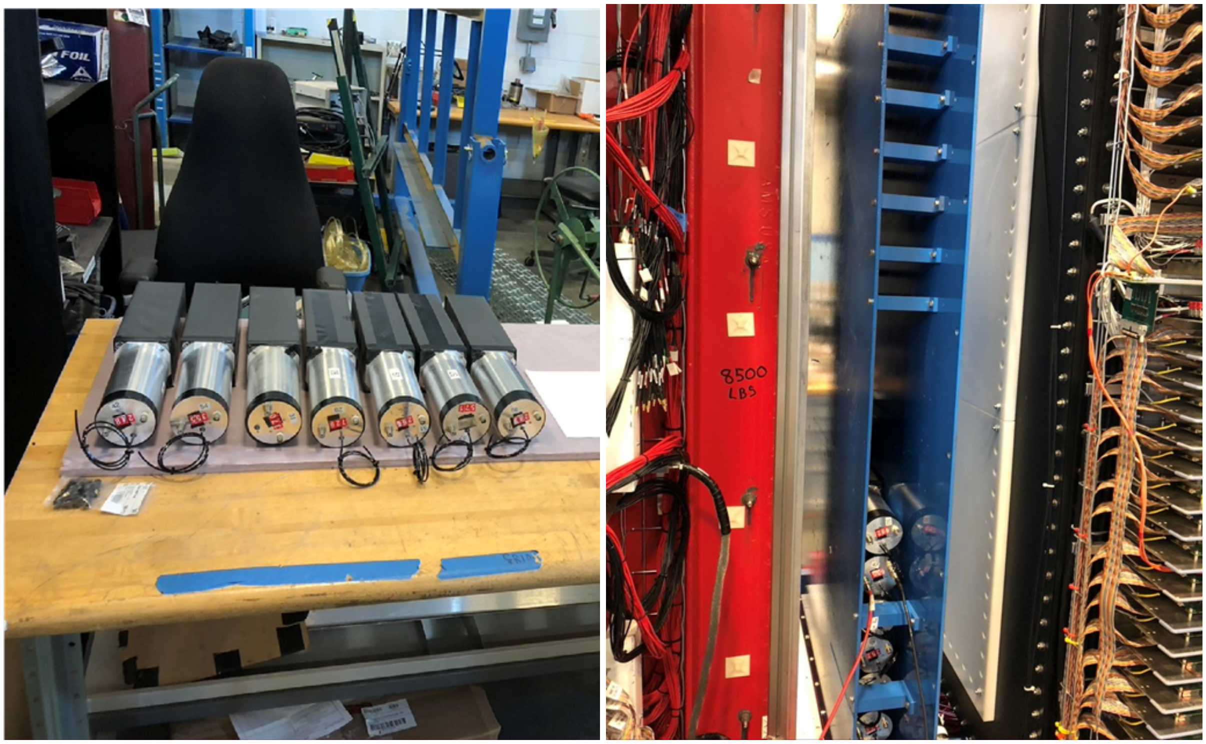

Figure 3.21: (Left) Preshower blocks being constructed, shielded in MuMetal and light tight black tape, and attached to PMTs. (Right) Side view of the Preshower during installation with blocks being slid into the iron housing structure shown in blue. Image from [186].

100 ps resolution per channel.

3.6.4 Bigbite Calorimeters

The Bigbite calorimeter system comprises a pair of lead-glass electromagnetic calorimeters (EMCals). The first EMCal named the Preshower (PS), sits downstream of the GRINCH detector. It is comprised of 52 radiation hardened (9 x 9 x 29.5) cm^3 blocks of TF1 lead glass, which are shown in Fig. 3.21 during construction, attached to PMTs. TF1 is a Cherenkov material consisting of PbO (52.2%), SiO_2 (41.3%), K_2O (7.0%) and As_2O_3 (0.5%) [185]. Electromagnetic cascades in the lead glass produce Cherenkov radiation (light), which is detected by the PMTs. The right hand side of Fig. 3.21 shows the PMTs pointing out the side of the detector stack, as the blocks are installed. The preshower blocks are stacked in a configuration of 26 rows of 2 columns facing each other as shown in Fig. 3.23. This particular orientation, with the long side perpendicular to the particle trajectory, causes particles to pass through the detector partially absorbed due to the relatively small thickness, and results in an electromagnetic shower which hits subsequent detectors. Each block is covered in MuMetal shielding and the signals from a block are read out by a PMT.

The second detector named the Shower (SH), is positioned downstream of the Timing Hodoscope which in turn is downstream of the Preshower. The Shower is comprised of 189

(8.5 x 8.5 x 34) cm^3 TF1 blocks which are shown during installation in Fig. 3.22. These are stacked in a configuration of 27 rows of 7 columns facing the spectrometer central axis as shown in Fig. 3.23. This orientation with the longest dimension of the blocks parallel to the central axis of Bigbite allows all of the remaining energy from the original particle to be absorbed by the much larger thickness of material. The shower has a layer of MuMetal shielding on the exterior of the system as well as between each row. Signals from each of the BBCal module PMTs are read out to FADC250 Flash Analogue-to-Digital Converters (FADCs) [187] through custom-made front end summer/amplifiers [188]. The FADC250 is a custom manufactured 250 MHz pipelined ADC module designed by JLab. This provides timing and energy deposition information.

Electrons and photons interact with matter through fairly well understood QED processes. Electromagnetic interaction with the absorber material produces a cascade of secondary particles through pair production, Compton scattering and bremsstrahlung. The secondary particles go on to produce more particles through subsequent interactions, ultimately creating an electromagnetic shower. As the cascade develops, the secondary particles lose energy through ionisation, excitation of atoms, and radiation. These energy loss mechanisms lead to the creation of more particles and photons, resulting in an exponential increase in the number of particles within the cascade. The cascade grows in size and density as more particles are produced, with the energy being redistributed among the particles through successive interactions. The electromagnetic shower reaches its maximum development when the energy of the particles becomes comparable to the energy required to produce new particles. Eventually if there is sufficient thickness and density of absorber material, the energy of the particles within the cascade decreases to the point where their interactions with the material are no longer significant, and the cascade comes to an end. The remaining particles continue to lose energy through ionisation and radiation until they come to rest [190].

For electrons the total energy in BBCal ($= E_{\text{PS}} + E_{\text{SH}}$) should be almost exactly the same as the momentum reconstructed from tracks in GEMs using the BB optics. The ratio of energy to momentum (E/P) can be used in analysis as a particle selection cut. Additionally the reconstructed Preshower energy deposition can provide a handle on pion background rejection. These ideas will be explored in Sec. 5.1.1. In addition to measuring the scattered electron energy, BBCal is used as the primary trigger for Bigbite and provides a trajectory constraint on the track search region for the GEMs.

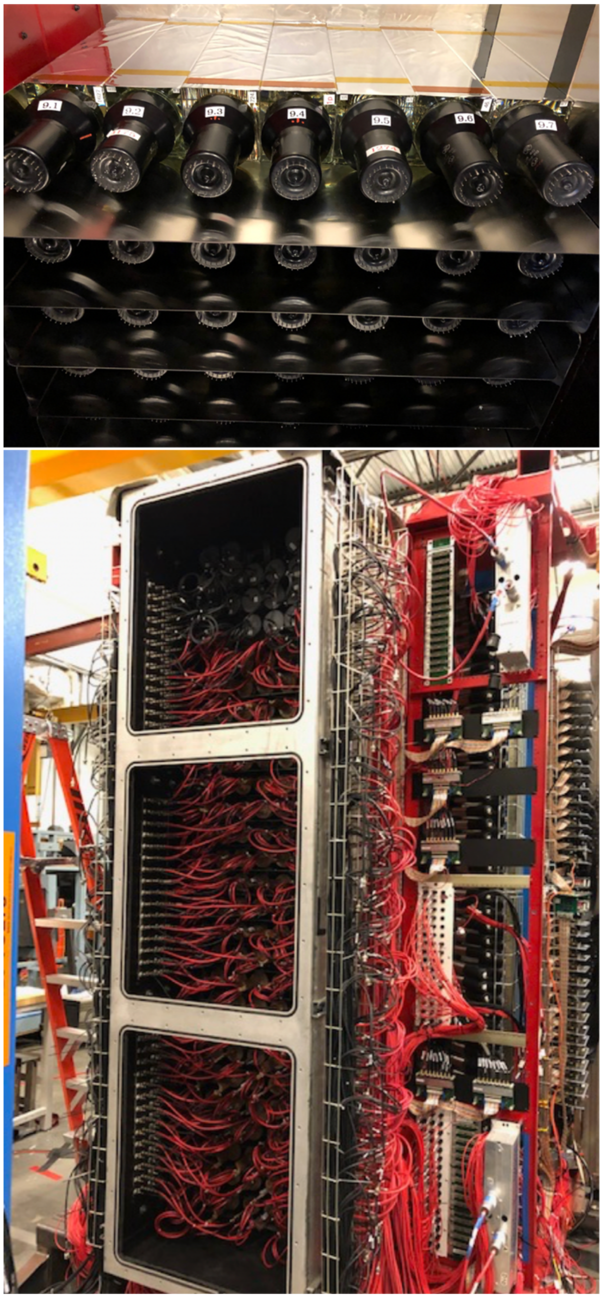

Figure 3.22: Top: Shower blocks during construction, begin shielded in MuMetal, and layers of MuMetal between rows. Bottom: Back view of the Shower during initial installation and cabling in a test lab, showing the scale and arrangement of the detector. Images from [186].

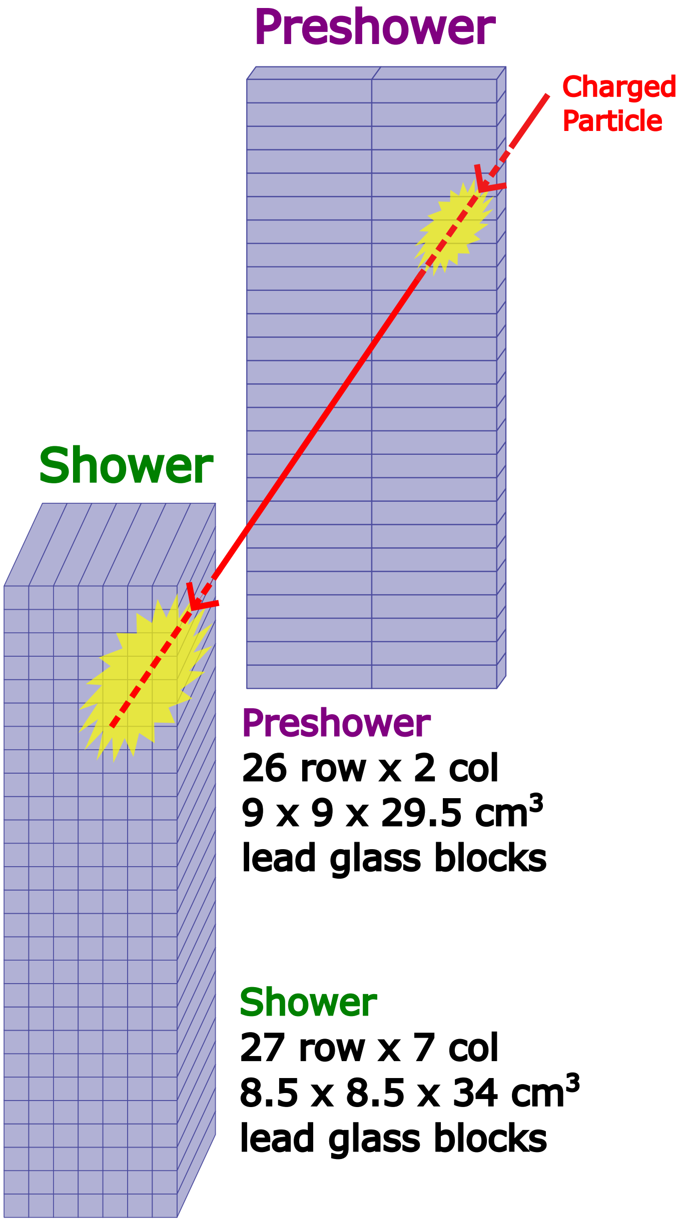

Figure 3.23: Drawings of BBCal Shower and Preshower calorimeters, with lead glass block size and geometry specified. The scattered electron interacts with the preshower, and the subsequent EM shower interacts with the shower detector. Image from [189].

3.6.5 Timing Hodoscope

The Bigbite timing hodoscope (TH) is a scintillator array positioned between the preshower and shower calorimeters. The hodoscope's function is to provide a high precision timing reference, with high efficiency over the range of momenta that Bigbite is intended to analyse.

The timing hodoscope consists of 89 EJ200 plastic scintillating bars of dimensions 600 x 25 x 25 mm^3, stacked vertically. The ends of each bar are glued with light-curable plastic bonding adhesive (Dymax 2094) to Eljen Technologies UVT acrylic rod light guides, which have a diameter of 24 mm. These light guides alternate between curved and straight geometries to allow for the closest packing of the detector within a constrained space, and to minimise gaps between scintillator bars. Each light guide is coupled to an Electron Tubes ET9124SB single channel PMT, for a total of 178 readout channels. The PMTs are housed within in-house assemblies which incorporate MuMETAL shielding, and coupled to custom voltage divider bases. The high voltage for each channel can be adjusted individually.

Figure 3.24: Diagram of the Bigbite Hodoscope which is a vertical stack of scintillating bars positioned between the shower and preshower calorimeters. Image from [191].

When a particle traverses a bar it scintillates light, which propagates along the light guides to the PMTs on each end. The signals from each PMT are read out by the same type of NINO ASIC front end card as the GRINCH. The first hit in the multi-hit TDC within the DAQ acquisition window is taken as the time for the channel and read out to the data files. In some cosmic-ray studies, a separate trigger paddle is used, which sits centrally above the hodoscope x-y plane. The signals from the NINO cards are then read out to CAEN v1190 TDCs. This allows the hit times to be extracted, as well as providing some raw pulse height information which can be reconstructed via the time-over-threshold capability offered by the NINO ASIC. A subset of 64 channels (32 bars) also have signals read out to FADCs, however these are not fully utilised in the final analysis due to the limited acceptance provided, but are used in some calibration procedures.

3.7 Hadron Arm: SuperBigBite

The SuperBigbite spectrometer acts as the hadron arm for the experiment, positioned to the right hand side of the beam as viewed in the downstream direction. SBS consists of a hadronic calorimeter, a dipole magnet and a stack of GEM layers which will be utilised in future experiments, however were not employed for this experiment and as such are not discussed. The HCal and SBS magnet can both be seen in full in Fig. 3.25.

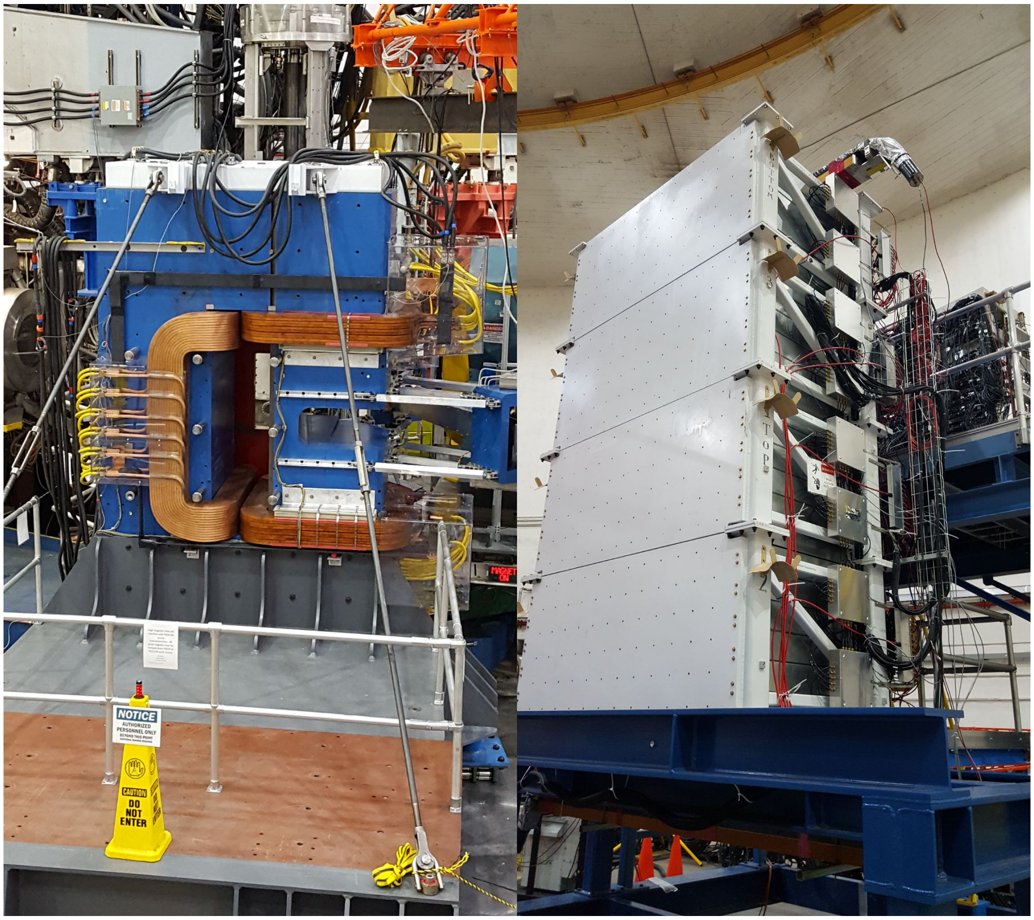

Figure 3.25: (Left) Hadron Calorimeter (HCAL) shown from the front, which sits on a steel platform 75 cm vertical from the Hall floor. (Right) SBS Dipole Magnet photographed from behind (downstream looking upstream).

3.7.1 SBS Magnet

The main component of SBS is the 48D48 dipole magnet, previously used at the Alternating Gradient Synchrotron accelerator in Brookhaven National Laboratory. 48D48 is a 100 ton iron dipole magnet with a 45.72 x 121.92 x 121.92 cm^3 field volume, maximum field of 1.3 T and field integral of $\approx$ 1.6 Tm at 2.1 kA coil excitation current. The SBS name arises from its large intermediate solid angle, which is approximately 70 msr. Previous high resolution spectrometers of JLab such as LHRS and RHRS of Hall A, and HMS and SHMS of Hall C, had solid angles on the order of 4-6 msr. The magnet sits on a support platform, which allows rotation of $10 \leq \theta_{\text{SBS}} \leq 40^{\circ}$, and a distance to the target of $1.6 \leq D_{\text{SBS}} \leq 3.5$ m.

Each pole has a single water-cooled coil with 120 turns of copper conductor, and the magnet is positioned such that the field direction is horizontal in the lab frame. The coil on the beamline side of the magnet was altered to account for the presence of the beamline at extreme forward angles. A cut-out in the iron core was machined to allow the beamline to actually pass through the magnet at these very small forward angles. This is visible in Fig. 3.25, where it can be seen that the beamline side coils have a different geometry than the other side, and there is a cut-out in the core.

3.7.2 Hadron Calorimeter

The Super Bigbite calorimeter (HCal) is a hadronic sampling calorimeter, consisting of 12 columns x 24 rows (288 total) matrix of modules or blocks. Each block is 15 cm x 15 cm x 1 m and consists of 40 interleaved layers of iron and scintillator plates. The thickness of the scintillator and iron plates is 5 mm and 20 mm, respectively. Both the scintillator and iron plates as well as a PMT are enclosed in a rectangular container with a cover. Both are made of 1.4 mm thick steel sheets. A wavelength-shifting bar made of Saint-Gobain BC-484 bisects the module in the long direction. A custom light guide directs scintillated light from the bar to the PMT. A complete schematic of this setup is shown in Fig. 3.26.

The purpose of HCal is to detect recoiling protons and neutrons, measuring their position and energy deposition and providing a high resolution time for the hit. In addition to electromagnetic interactions which occur in electromagnetic calorimeters, hadrons interact with the nuclei of the absorber material in a hadronic calorimeter primarily through the strong nuclear force. These interactions are more complex than the electromagnetic interactions occurring in electromagnetic calorimeters. Inelastic collisions lead to the production of secondary hadrons, such as pions, kaons and nucleons. These secondary particles then further interact with the absorber material, generating more secondary particles and forming a hadronic shower. As the hadronic shower develops, secondary particles deposit their energy in the active material layers. In scintillator-based systems, charged particles excite the scintillator material, causing it to emit photons. The emitted photons are collected

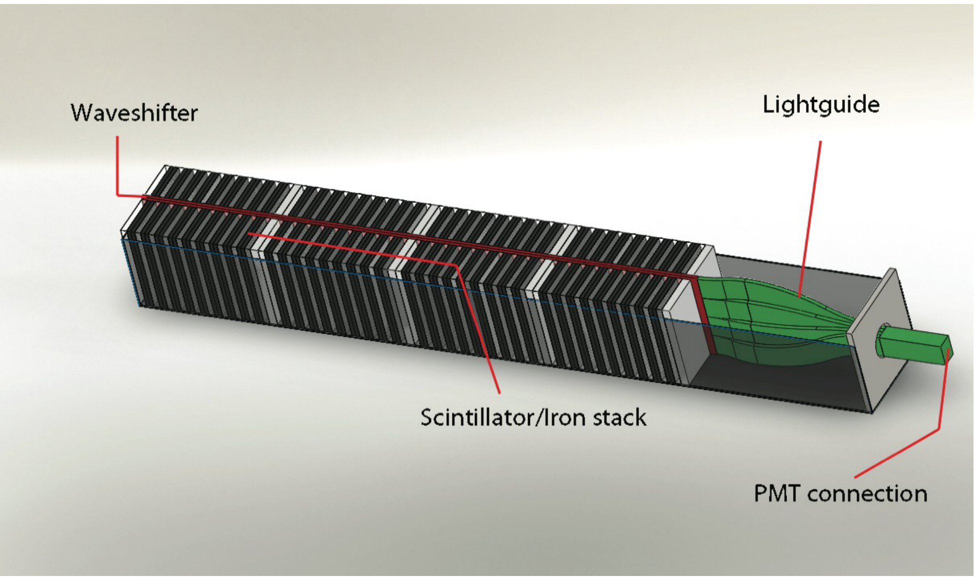

Figure 3.26: Picture of HCAL module design. Image from [192].

by PMTs. The signals from the PMTs are amplified and digitised by the detector's electronics. The amplitude of these signals is proportional to the energy deposited by the hadronic shower in the calorimeter.

Signals from each of the 288 module PMTs are read out to FADC250s and F1TDCs [193], all of which are located in a VXS crate in the DAQ bunker. The fADCs provide information on the energy deposition in a block. Both the FADCs and F1TDCs provide timing relative to the BigBite trigger. The position for a hit is taken as the centre of the block that fires. The block with the highest energy is designated a local maxima and local blocks are clustered around it. Multiple clusters can be reconstructed around local maxima per event. The position resolution of a cluster can be improved below simply the size of a block by an energy weighted mean of blocks in a cluster.

The detector has been measured to have an internal timing resolution of 1.3 ns, position resolution of approximately 6 cm, and energy resolution of 30-50%, varying at different kinematic settings [194]. HCal is a sampling calorimeter, where only a fraction of the total energy is directly measured by the active material. The rest of the energy is deposited in the absorber material. The overall energy resolution depends on the fraction of energy sampled and the statistical fluctuations in the shower development. The energy resolution of a hadron calorimeter is typically worse than that of an electromagnetic calorimeter due to the more complex nature of hadronic interactions and the larger fluctuations in the shower process. The resolution generally improves with increasing energy [190]. HCal has an expected sampling fraction of $\approx 5\%$ from simulated geometry, however as show in Sec. 4.4.3 the data suggests this is closer to 11%. This means for example, that nucleons which enter the face of HCal with 2.37 GeV momentum corresponding to a kinetic energy of about 1.6 GeV, on average an energy of around 170 MeV will be measured. HCal forms part of the coincidence trigger for the experiment which will be discussed in Sec. 3.9.1.

3.8 Magnetic Optics and Momentum

Charged particles which traverse the BB and SBS spectrometers are deflected by the dipole magnets in each arm respectively. Therefore the position and trajectory of particles measured in the spectrometers must be reconstructed backwards through the magnetic field to original positions and trajectories at the interaction vertex inside the target. The method of performing this reconstruction is called "magnetic optics" or simply "optics". In Bigbite this is done by inserting a "sieve" plate in front of the magnet and taking data on the carbon optics target. Both the sieve and carbon foils are surveyed prior to running, such that the position of the holes on the sieve and the $\hat{z}$ position of the eight foils are well known. These known factors can then be used to project tracks formed in the GEMs back towards the target. This method is not employed on the SBS side due to the fact that the SBS magnet had no sieve plate at the time, and the SBS GEMs were not fully in use. The BB sieve plate is pictured in the left of Fig. 3.27 and the hole pattern can be clearly seen. The reconstructed particle position in x and y at the sieve's location is shown in the right hand side for a sample of optics calibration data. The hole pattern can also be clearly seen in the reconstruction, indicating good optics reconstruction of the track trajectory in events.

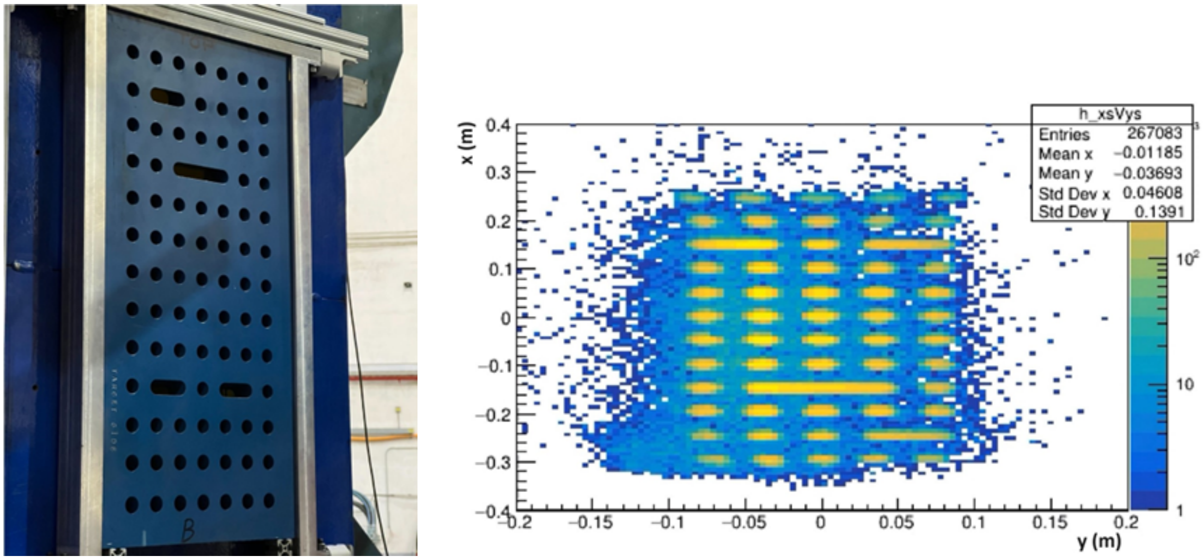

Figure 3.27: (Left) The sieve plate. (Right) Reconstructed events for kinematic setting 3 with the sieve plate in place in front of Bigbite. The sieve hole pattern can be clearly seen. Figure from [195].

The particle momentum for tracks recorded in Bigbite is not measured directly but inferred from the reconstructed bend angle. The momentum relative to the central momentum δ_p is the variable directly extracted by the optics, which is detailed in Sec. 4.6. δ_p, the

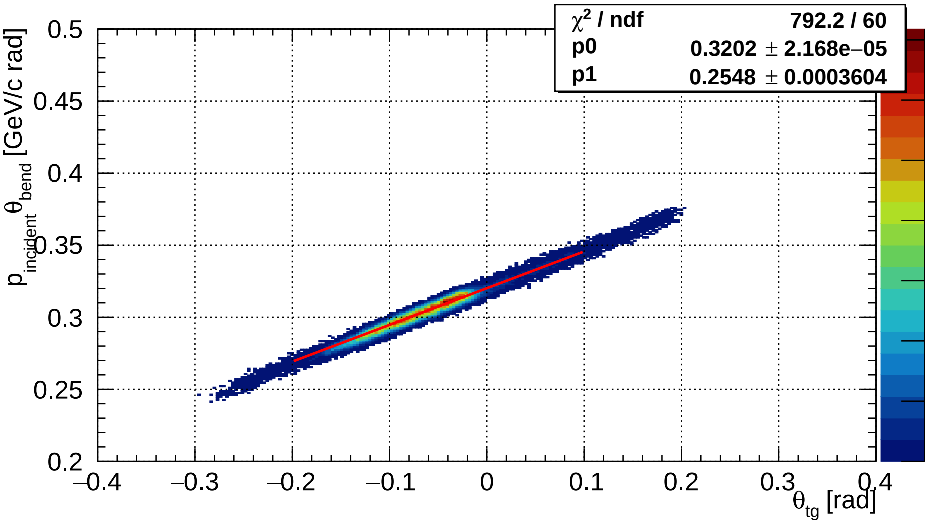

Figure 3.28: Elastic scattering from H_2 in Bigbite, showing that the relationship between $p_{\text{incident}}\theta_{\text{bend}}$ and θ_{tg} is linear.

momentum and the bend angle are related to the field integral by

$$\delta_p = p\theta_{\text{bend}} \propto \int B \cdot dl \tag{3.16}$$

where p is the particle's momentum, θ_{bend} is the angle of deflection through the magnet, B is the field strength and dl is the particle's path length. The left hand side of Eqn. 3.16 should be correlated with the original angle of the particle in the dispersive plane, θ_{tg}. The correlation is plotted from elastic scattering off hydrogen in Fig. 3.28 which has a clear linear relationship. The momentum is fitted as

$$p = A\frac{1 + B\theta_{\text{tg}}}{\theta_{\text{bend}}} \tag{3.17}$$

for coefficients A and B. The final reconstructed momentum is then extracted from δ_p, A and B. Further calibration of the momentum against beam position is explored in Sec. 4.6.3

3.9 Electronics and Data Acquisition

JLab experiments use the CEBAF Online Data Acquisition (CODA) [196] system for data taking. CODA was developed by the JLab DAQ group and is based on a main server interacting with a database in which all the DAQ components update their status. Typically the readout crates host a single board computer which runs a Read Out Controller (ROC) program that controls the outflow of data from the electronics. The ROCs send the data through a high-speed network link, usually Ethernet, to a computer running the Event Builder program, which uses the data from the ROC to check synchronisation and build the event. Finally the

Event Recorder writes out the data into binary event IO (EVIO) files on the local file storage system, which can later be decoded for physics use. These files are eventually moved to a tape based mass storage system for long term storage. Slow controls are provided by The Experimental Physics and Industrial Control System (EPICS) [197]. EPICS is a set of open source software tools, libraries and applications used commonly in experimental physics. EPICS is used to record information on the status of the accelerator and Hall, and as a means of remotely controlling hardware.

3.9.1 Triggers

Given the large luminosities typical of Hall A, and the large acceptance of the spectrometers, there is a huge rate of low energy particles striking detectors. The DAQ system can only handle a rate of around 5 kHz, at which it begins to saturate. Given these facts, recording every particle event in the detectors is completely impractical. CODA is therefore prompted to record an event upon certain criteria referred to as a trigger. A trigger relies on the amplitude of signals from a detector system to quickly determine whether to record an event. Triggers typically have two main aspects, the threshold and prescale. As the name suggests the threshold determines the minimum amplitude of the signal in the detector system which forms the trigger, for an event to be recorded. The threshold for a given trigger is adjustable on the DAQ software. Users set a value in mV, which corresponds to a physical energy value in GeV. Only events in which the detector system measures a signal with a corresponding amplitude above this will trigger the DAQ. The prescale tells the DAQ how often to trigger an event. A prescale of *N* results in accepting 1 in every *N* triggers.

Table 3.3: Triggers used in E12-09-016.

Trigger	Description
1	BBCal Trigger
2	HCal Trigger
3	Coincidence
4	GRINCH LED Pulser

Multiple triggers were utilised in E12-09-016, shown in Tab. 3.3. At the heart of the experiment is the Bigbite calorimeter trigger, which defines the start of an event. The HCal trigger is independent of the BBCal trigger, and typically experiences large rates meaning it is never used in isolation. The coincidence trigger is a logical AND of these two. Comprehensive logic diagrams for each of the three physics triggers are available in Appendix A. The functionality of each will be summarised in this section. An LED pulser trigger was present for the GRINCH which was always running at a low rate and will also be discussed.

The BBCAL trigger modules are composed of overlapping sums of shower and preshower blocks as shown in Fig. 3.29. All of the 25 BBCAL trigger modules are continuously combined in an OR analogue sum and sent to a system of discriminators which check the analogue sum against the threshold. When this analogue sum is over the threshold this produces the BBCAL logical trigger signal which is then sent to the trigger interface (TI) in the DAQ bunker. An integrated trigger supervisor (TS) then sends the signal to each of the subsystem crates, which begins reading data from a configurable lookback window and writing it to the output file. During experimental running, at the beginning of each new kinematic setting the BBCal trigger threshold is set to a rough value in mV corresponding to the desired low GeV value, and then exact calibration can be done. The running value is chosen to be safely lower than the quasielastic electron energy to avoid losing good events. For kinematic setting 2 for example, with a central QE electron energy of 2.69 GeV, this threshold corresponded to ≈ 1 GeV.

The HCAL trigger is an independent trigger which is similarly formed by an OR analogue sum of overlapping regions. Blocks are grouped into 24 modules of 4x4, and 10 overlapping regions of these modules are summed. The construction of this is illustrated in Fig. 3.30, where the black lines indicate individual HCal blocks, the red lines show the grouping of blocks in their respective modules, and the blue circles indicate the regions of overlap between the corners of four modules which are considered as sums. The HCal trigger threshold is set fairly low due to the poor energy resolution of the detector which results in large rates on the order of MHz for HCal. However, this trigger is never used on its own as these rates would overload the DAQ limit of ≈ 5 kHz.

The coincidence trigger is a logical AND of the BBCal and HCal trigger signals. This is used as the primary physics trigger for E12-09-016 since the exclusivity of the measurement means that non coincident events are not useful. However, the BBCal single arm trigger is prescaled in to varying extents on a run by run basis (typically during Hydrogen runs) as high momentum electron events can be useful for diagnostics and calibrating detector response. The final trigger is an LED which pulses light to the GRINCH at a very low rate in order to trigger events. This is used primarily for testing, however was useful during production running as it functioned as a low rate life support for the DAQ that could and would otherwise crash or corrupt data in the event of an interrupted beam.

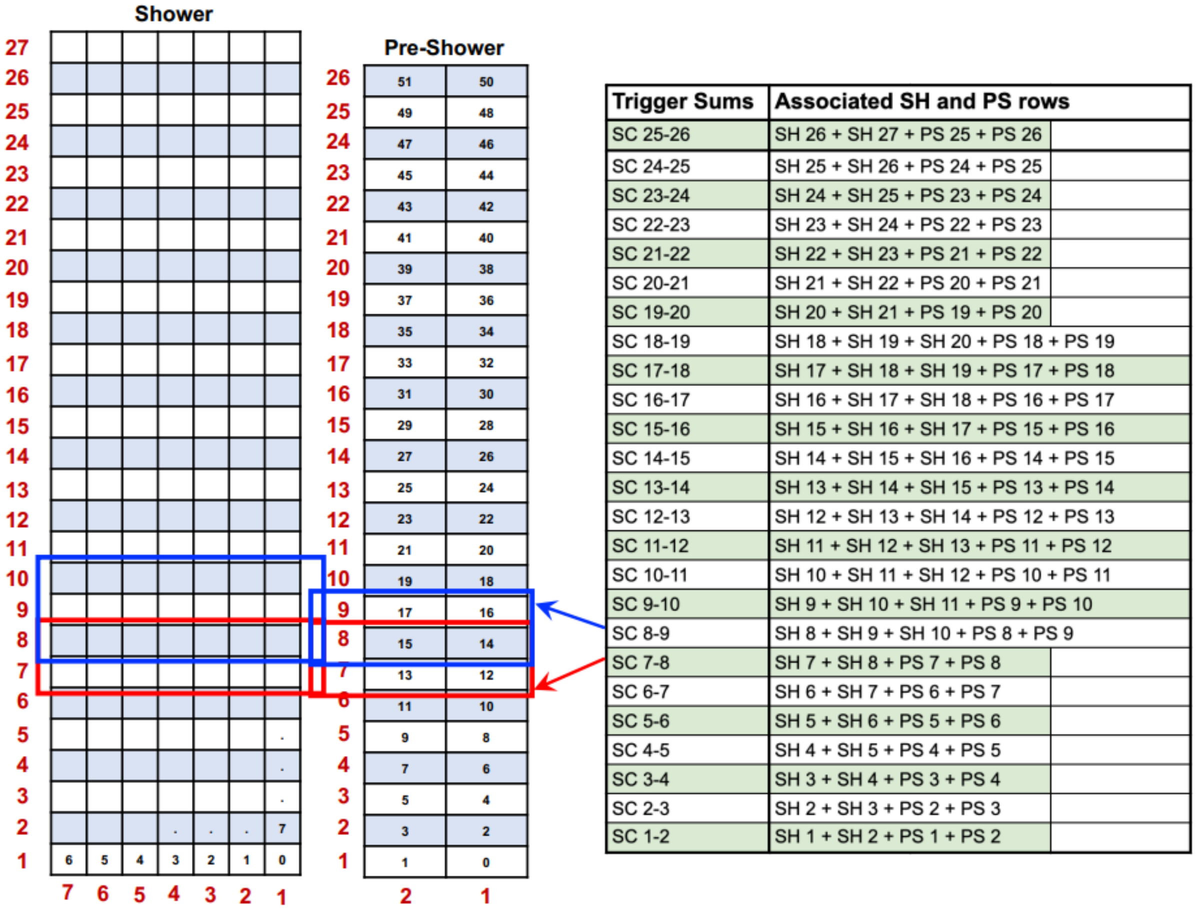

Trigger Sums	Associated SH and PS rows
SC 25-26	SH 26 + SH 27 + PS 25 + PS 26
SC 24-25	SH 25 + SH 26 + PS 24 + PS 25
SC 23-24	SH 24 + SH 25 + PS 23 + PS 24
SC 22-23	SH 23 + SH 24 + PS 22 + PS 23
SC 21-22	SH 22 + SH 23 + PS 21 + PS 22
SC 20-21	SH 21 + SH 22 + PS 20 + PS 21
SC 19-20	SH 20 + SH 21 + PS 19 + PS 20
SC 18-19	SH 18 + SH 19 + SH 20 + PS 18 + PS 19
SC 17-18	SH 17 + SH 18 + SH 19 + PS 17 + PS 18
SC 16-17	SH 16 + SH 17 + SH 18 + PS 16 + PS 17
SC 15-16	SH 15 + SH 16 + SH 17 + PS 15 + PS 16
SC 14-15	SH 14 + SH 15 + SH 16 + PS 14 + PS 15
SC 13-14	SH 13 + SH 14 + SH 15 + PS 13 + PS 14
SC 12-13	SH 12 + SH 13 + SH 14 + PS 12 + PS 13
SC 11-12	SH 11 + SH 12 + SH 13 + PS 11 + PS 12
SC 10-11	SH 10 + SH 11 + SH 12 + PS 10 + PS 11
SC 9-10	SH 9 + SH 10 + SH 11 + PS 9 + PS 10
SC 8-9	SH 8 + SH 9 + SH 10 + PS 8 + PS 9
SC 7-8	SH 7 + SH 8 + PS 7 + PS 8
SC 6-7	SH 6 + SH 7 + PS 6 + PS 7
SC 5-6	SH 5 + SH 6 + PS 5 + PS 6
SC 4-5	SH 4 + SH 5 + PS 4 + PS 5
SC 3-4	SH 3 + SH 4 + PS 3 + PS 4
SC 2-3	SH 2 + SH 3 + PS 2 + PS 3
SC 1-2	SH 1 + SH 2 + PS 1 + PS 2

Figure 3.29: BBCAL trigger system blocks composed of overlapping combinations of shower and preshower blocks. Image from [198].

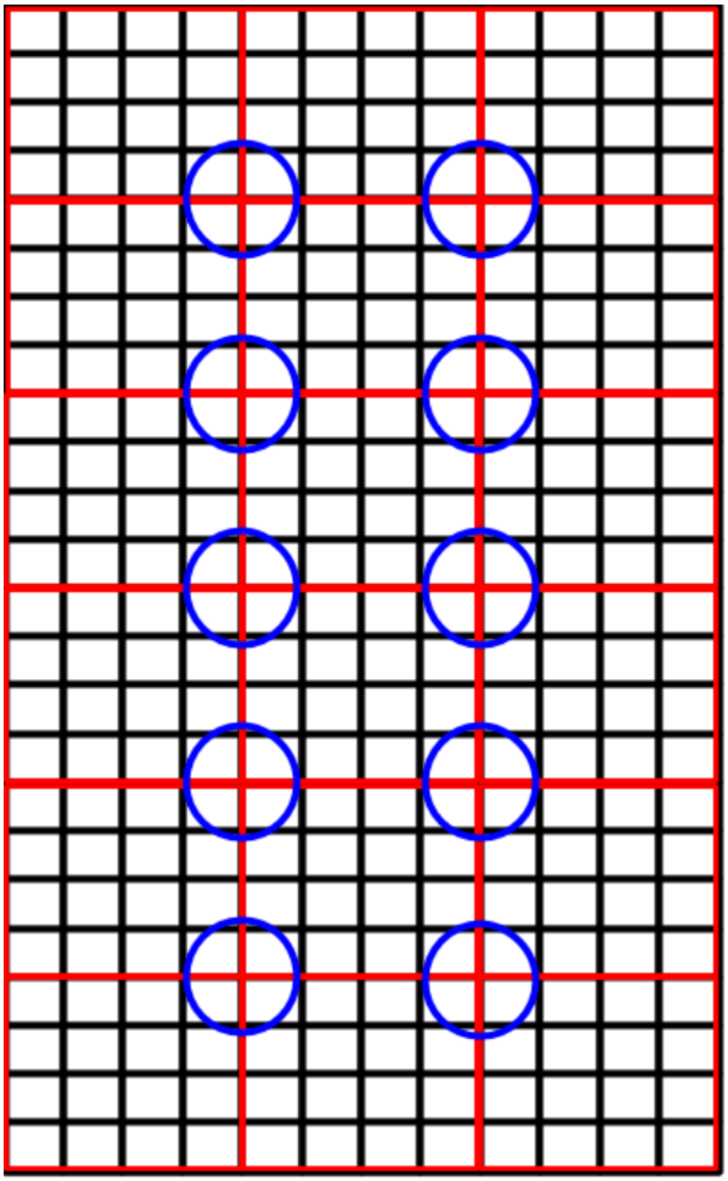

Figure 3.30: HCal trigger system blocks composed of overlapping 8 x 8 regions of the detector. Image from [199].

3.10 Analysis Software

Hall A utilises a standard object-orientated analysis framework called the Hall A analyzer or Podd [200], which is built upon CERN's ROOT library [201]. The analyzer is made up of classes which handle common analysis tasks involving standard Hall A experimental equipment. Specific to Hall A SBS experiments is the SBS-offline suite of C++ classes which directly integrate into analyzer to provide specialised data processing and reconstruction algorithms for the SBS detectors [202]. SBS-offline is utilised through a suite of scripts and databases known as SBS-Replay [203]. This contains calibration parameters for all systems and detector mapping, with information in the databases timestamped to match different experimental kinematic settings.

SBS-offline decodes the raw EVIO files produced by CODA and analyses individual detector channels and writes the desired output information to human readable histogram(s) and ROOT tree(s) within a ROOT file. The output can contain all detector outputs from raw detector hit information to higher level constructed quantities like track and cluster information, and has necessary EPICs slow control information such as beam energy, position and helicity. However there is limited physics reconstruction here, namely single arm electron kinematic quantities like quasi-invariant mass squared W^2 and momentum transfer Q^2. Throughout the analysis contained in this work, an analysis library has been constructed to analyse the rootfiles produced by SBS-Offline and perform the necessary steps in extracting G_E^n [204].

3.11 Monte Carlo Simulation: G4SBS

A fully realistic simulation for the SBS experimental suite called G4SBS [205] was built on the Geant4 framework [206]. The simulation contains physically accurate representations of the detectors and materials used in the experiment. Fig. 3.31 shows the full experimental setup rendered visually in Geant4. G4SBS contains built in physics event generation for a number of processes. An elastic generator uses the known Rosenbluth scattering cross sections of protons and neutrons to produce scattering angles for the recoil electron and nucleon. Parameterisations for Fermi motion of ^{2}H and ^{3}He are available in the form of momentum distributions. Final state particles are propagated through the detector materials for realistic energy deposition and time of flight simulation.

Additional generators exist for the purpose of modelling backgrounds. A single arm pion generator [207] based on the WISER model [208] and a pion photoproduction generator (WAPP) are used to estimate the residual pion contamination in Bigbite after cuts. An inelastic event generator based on the Bosted-Christy [209, 210] parameterisation of inclusive resonance scattering is used to model the background shape of the distribution of kinematic

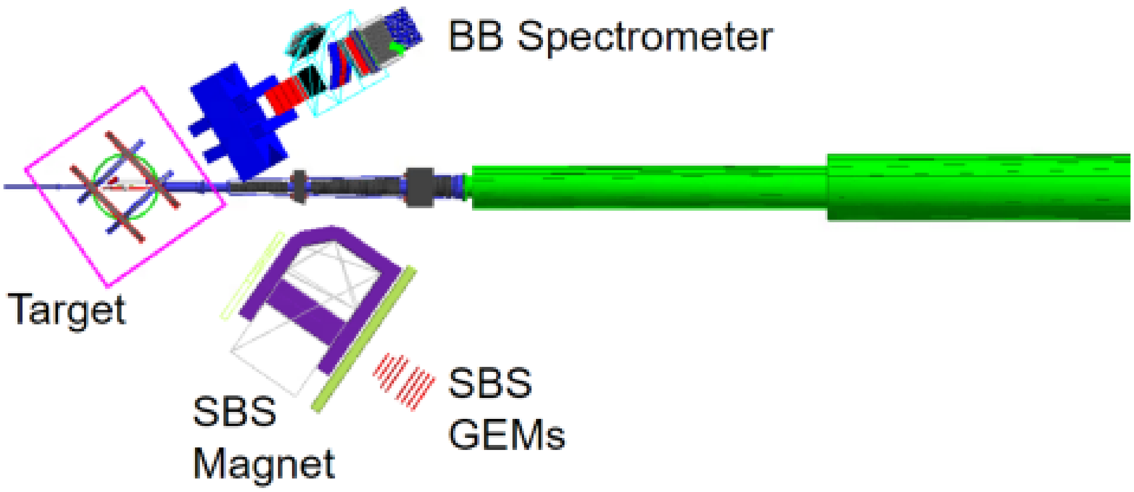

Figure 3.31: Picture of experimental setup in G4SBS.

variables in the final analysis. Each of these generators is necessary to determine the signal and background yields in the final quasielastic event sample are used to form the physics asymmetry of interest.

A parallel software library, libsbsdig [211], was developed in order to digitise the raw output of G4SBS to a form readable by the decoder in the analyzer, such that simulated data could be fully propagated through the analysis machinery to study reconstruction and detector effects. The libsbsdig software converts raw hits on Geant4 detector volumes into pseudo detector data by reading in channel maps from a Monte Carlo database within SBS-Replay. A simulation decoder class in SBS-offline can then be used to create output rootfiles of G4SBS data with the same structure as real production data replays. This conveniently allows direct comparison of simulation and data within the same analysis framework.

Chapter 4

Detector and Target Calibrations

This chapter will detail the calibration procedures performed on the detector systems, target data and beamline monitoring systems. While the beamline remains unchanged from previous Hall A experiments, the target and all of the SBS detector systems are fairly novel. Given this, the detector calibrations in particular were developed from scratch prior to experiment E12-09-019 (GMN) production running and fine tuned throughout. In light of this great thanks are owed to the GMN students for developing these procedures. The calibration for each subsystem has since been refined and repeated for the GEN-II kinematic settings by students to whom reference will be given in the relevant subsections.

4.1 Kinematic Setting Notes

Kinematic setting 2 (GEN2) was the first setting which took data on a production ^{3}He target. During this period of time the collaboration were still trying to completely understand the performance of a completely new target cell. In particular the polarisation was not well understood early in the kinematic setting. As will be discussed in Sec. 4.2.1, the target polarisation is measured and calibrated through the polarimetry methods of NMR and EPR. At this time a signal was missing from an NMR lock-in channel, which degraded the measurements. The resultant calibrations for this subset of the polarimetry data are still being understood as a consequence. Furthermore, the technique of measuring and calibrating the polarisation was still being iteratively tuned. As a result parameters of the method such as the field sweep speed were being changed, which affected the uncertainties on the polarisation data. Finally, the performance of the target cell itself was still being understood. The target oven temperature, field strength, laser power and convection voltage were all being tuned in an ad-hoc fashion in order to study the response of the polarisation spin-up and ultimately maximise the potential polarisation of the target.

This kinematic setting saw no data taking on carbon targets, since the GEM alignment could be performed at the commissioning setting (kinematic setting 1) because Bigbite didn't move between these settings. As a result both the optics calibration and calculation of nitrogen dilution in the final asymmetry must be performed through alternative methods than the standard methods which are applied in kinematic settings 3, 4a and 4b. The optics calibration must rely on a starting optics model from Monte Carlo simulation as discussed in Sec. 4.6. The nitrogen dilution must use extrapolated estimates from kinematic settings 3 and 4 for, until such time as a nitrogen target is implemented into the simulation. This is discussed in Sec. 5.9.

4.2 Target Calibrations

The target polarisation was measured roughly every three hours during production running by the nuclear magnetic resonance (NMR) procedure as detailed in Sec. 4.2.1. The target expert on shift would run the NMR software which was largely automated, and this would produce an analogue electrical signal in an NMR coil. The induced voltage due to this current was read out in the NMR software in mV and could then be later calibrated via electron paramagnetic resonance (EPR) polarimetry, as discussed in Sec 4.2.2, to produce a polarisation value as a percentage. EPR calibrations were performed for sets of NMR data through the experimental running by various members of the target group. Minute by minute polarisations were acquired by a linear interpolation between each three hour data corrected data point. The polarisation for an event was matched via time stamp and each event was weighted by the polarisation. Offline density corrections and the event by event extrapolation of the data was performed by graduate student Hunter Presley (University of Virginia).

4.2.1 NMR Polarimetry and Adiabatic Fast Passage

NMR measurements are performed by taking the nuclei in the holding field, and applying a perpendicular rotating radio frequency (RF) field. The resultant precession around the effective field causes a resonance which produces a signal in nearby pickup coils that is proportional to the polarisation of the target. The proper resonance conditions can be found through adiabatic fast passage (AFP). AFP is the method of reversing the spins of the nuclei by changing the holding field in the presence of an RF field in such a way that the spins of the nuclei can flip, but do not have time to relax. The reversal will sweep through a resonance that produces the desired electromagnetic field (EMF) signal in the coils.

The ^{3}He nuclei have a magnetic moment $\vec{M} = \gamma\vec{S}$ where $\vec{S}$ is the spin of the atom, and γ is the gyromagnetic ratio of ^{3}He. The Helmholtz coils produce a holding field, $\vec{H}_0$. When a rotating RF field $\vec{H}_R$ with a frequency ω_R is applied perpendicular to $\vec{H}_0$, the magnetic moment will precess around the effective field H_e [212]

$$\frac{d\vec{M}}{dt} = \gamma\vec{M} \times (\vec{H}_0 + \vec{H}_R) = \gamma\vec{M} \times \vec{H}_e. \tag{4.1}$$

Defining $\vec{H}_0$ to be in the $\hat{z}$ direction, then in the frame of a rotating field with frequency $-\omega_0$ the effective field can be rewritten as

$$\vec{H}_e = \left(H_0 - \frac{\omega}{\gamma}\right)\hat{z} + \vec{H}_R. \tag{4.2}$$

The precession of the spins follows this effective field under AFP conditions. When AFP is applied, the angle between $\vec{H}_e$ and $\vec{H}_0$ in the rotating frame, θ is given by

$$\tan\theta = \frac{H_R}{H_0 - (\omega/\gamma)} = \frac{\omega_R}{\omega_0 - \omega}, \tag{4.3}$$

where $\omega_0 = \gamma H_0$ is the Larmor frequency of the spin in the applied field $\vec{H}_0$ [212]. Through this method either the holding field or frequency of the RF field can be swept such that the ^{3}He nuclei start to precess, pass through resonance, and align 180 degrees from the original orientation. It is vital to ensure that the AFP (or adiabaticity) criterion is held

$$\frac{1}{T_{^3\mathrm{He}}} \ll \frac{1}{H_R}\left|\frac{dH_R}{dt}\right| \ll \omega \tag{4.4}$$

where $T_{^3\mathrm{He}}$ is the spin relaxation time of the ^{3}He atoms [212]. The adiabatic criterion ensures the equilibrium of the system. If the sweep is too slow the spins have time to relax mid transition. However if it is too fast then the field direction changes more quickly than the spins can reorient themselves, and the equilibrium breaks down.

During the experiment, the polarisation signal was measured by sweeping the holding field up, until the spins flip, and then by sweeping the field back down, until the spins are back in the original orientation. The AFP sweep was performed twice in order to preserve the polarisation of the ^{3}He as well as maintain a constant direction of polarisation. The initial parameters of the sweep were in line with the GEN-I target, sweeping the holding field from 25 to 32 G, with an RF frequency of 91 kHz and field strength 90 mG. This was fine tuned for each target cell throughout the running of the experiment.

NMR is considered to be minimally invasive as it produces polarisation losses on the order of 1%. The NMR produces an analogue signal in the coils proportional to the polarisation, given by

$$\begin{aligned}
s &\propto \frac{\omega_R}{\sqrt{(\omega_0-\omega)^2+\omega_R^2}} \\
s &\propto \frac{P_{^3\mathrm{He}}\mu_{^3\mathrm{He}}H_R}{\sqrt{(H_0-\frac{\omega}{\gamma})^2+H_R^2}} \\
s &= P_{^3\mathrm{He}}\cdot n_{^3\mathrm{He}}\cdot \Phi \cdot \mu_{^3\mathrm{He}}\cdot C_{\mathrm{electric}}
\end{aligned} \tag{4.5}$$

where $P_{^3\mathrm{He}}$ is the polarisation of the target, $n_{^3\mathrm{He}}$ is the density of the target, Φ is the magnetic flux through the coils and $\mu_{^3\mathrm{He}}$ is the magnetic moment of the nuclei. C_{electric} is a conversion constant from the signal reading in mV to polarisation that depends on the experimental setup, and must be calibrated to obtain a true polarisation value in percent. The electron paramagnetic resonance (EPR) technique was used to do this.

4.2.2 EPR Polarimetry

EPR is a technique which utilises the Zeeman effect to measure the polarisation of unpaired electrons in an atom, and extract the NMR calibration factor. In the presence of an external magnetic field, the spins of unpaired electrons in the alkali metals will align parallel or anti-parallel with the field. The total contribution to the splitting is given by

$$H_0 = H + \Delta H \tag{4.6}$$

where H is the external field and ΔH is the small contribution from the polarised ^{3}He. The spins of the nuclei can be flipped via AFP as before, which results in a net change in the resonance frequency. By flipping the spins twice and performing a measurement of this shift for opposite target polarisations, the contribution arising purely from the nuclei can be isolated. Now, instead of sweeping the holding field as in the NMR, the frequency of the field is swept in order to keep the holding field constant and isolate ΔH. The frequency of the field is swept through an EM range of around 58 kHz, and the resonance is detected at the frequency that the energy level splitting occurs. The shifts due to alignment and anti-alignment are

$$\begin{aligned}
\Delta\nu_+ &= \Delta\nu_{^3\mathrm{He}} + \Delta\nu_{H_0} + \Delta\nu_{\mathrm{other}} \\
\Delta\nu_- &= -\Delta\nu_{^3\mathrm{He}} + \Delta\nu_{H_0} + \Delta\nu_{\mathrm{other}} \\
\implies \nu_{^3\mathrm{He}} &= \frac{\Delta\nu_+ - \Delta\nu_-}{2}
\end{aligned} \tag{4.7}$$

where $\Delta\nu_{^3\mathrm{He}}$ is the contribution to the splitting from the polarisation of the ^{3}He, $\Delta\nu_{H_0}$ is the contribution from the holding field, and $\Delta\nu_{\mathrm{other}}$ is the sum of any other external contributions which may arise.

This frequency splitting can be directly related to the polarisation by

$$\Delta\nu_{^3\mathrm{He}} = \frac{d\nu_{\mathrm{EPR}}(F,M)}{dH} C n_{^3\mathrm{He}} \mu_{^3\mathrm{He}} P \tag{4.8}$$

where C is a dimensionless constant related to the cell geometry, and $\frac{d\nu_{\mathrm{EPR}}(F,M)}{dH}$ is a well known function in the literature and calculable from the Breit-Rabi equation [213]. Assuming a perfectly spherical pumping chamber, the EPR frequency is then expressed as

$$\Delta\nu_{^3\mathrm{He}} = \frac{8\pi}{3} \frac{d\nu_{\mathrm{EPR}}(F,M)}{dH} \kappa_0 \mu_{^3\mathrm{He}} P \tag{4.9}$$

where now κ_0 is a dimensionless constant with a dependence on the cell temperature, which is measured experimentally. The absolute polarisation can be directly extracted from here. EPR calibrations involved performing an NMR, following by an EPR, followed by a second NMR. From this the exact calibration constant could be determined for NMR measurements on a cell.

4.2.3 Density Corrections

The pressure in the target at time of construction and sealing was around 10 bar, meaning the density at room temperature is also around 10 times that of air. The temperature of the target oven is controlled by a feedback system which causes oscillation around a central value. However for the EPR calibrations to be consistent, the temperature of the pumping chamber and the target chamber should be steady. When this is not the case, fluctuations in temperature result in fluctuations in density and therefore the measured calibration constant.

NMR signals can be used to account for these density fluctuations, owing to the direct proportionality between the density in the chamber and the signal that a given pickup coil measures. Assuming that the pressure P stays constant throughout the cell, then by the ideal gas law

$$P = \frac{N_T f_{\mathrm{PC}} k_B T_{\mathrm{PC}}}{V_{\mathrm{PC}}} = \frac{N_T f_{\mathrm{TC}} k_B T_{\mathrm{TC}}}{V_{\mathrm{TC}}} \tag{4.10}$$

where N_T is the total number of molecules in the cell, $f_{\mathrm{PC(TC)}}$ is the fraction of molecules in the pumping (target) chamber, k_B is the Boltzmann constant, $T_{\mathrm{PC(TC)}}$ is the temperature in the pumping (target) chamber and $V_{\mathrm{PC(TC)}}$ is the volume of the pumping (target) chamber. Eqn. 4.10 can be rearranged for the ratio of the fractions of molecules in the pumping chamber to the target chamber

$$\frac{f_{\mathrm{PC}}}{f_{\mathrm{TC}}} = \frac{T_{\mathrm{TC}} V_{\mathrm{PC}}}{T_{\mathrm{PC}} V_{\mathrm{TC}}}. \tag{4.11}$$

The NMR signal from Eqn. 4.7 in the coils measuring the pumping chamber and target chamber can also be written as a ratio, R_1

$$R_1 = \frac{s_{\text{PC}}}{s_{\text{TC}}} = \frac{K_{\text{PC}} f_{\text{PC}}}{K_{\text{TC}} f_{\text{PC}}} \tag{4.12}$$

where $K_{\text{TC(PC)}}$ are the absorbed constants of Eqn. 4.7. If we consider the case of two NMR measurments at different temperatures and pressures, R_1 and R_2, then a further ratio can be formed

$$R = \frac{R_1}{R_2} = \frac{f^1_{\text{PC}} f^2_{\text{TC}}}{f^2_{\text{PC}} f^1_{\text{TC}}}. \tag{4.13}$$

The term R or Eqn. 4.13 will be referred to as the “super ratio”.

The relationship between the fractions f in either chamber, for two discrete NMR measurements must be related linearly, and so can be written

$$\begin{aligned} f^2_{\text{PC}} &= \alpha f^1_{\text{PC}} \\ f^2_{\text{TC}} &= \beta f^1_{\text{TC}} \end{aligned} \tag{4.14}$$

for arbitrary constants α, β. By keeping in mind the fact that $f^{1(2)}_{\text{PC}} + f^{1(2)}_{\text{TC}} = 1$, Eqn. 4.13 can be rewritten as

$$R = \frac{(1 - f^1_{\text{TC}}) f^2_{\text{TC}}}{f^1_{\text{TC}}(1 - f^2_{\text{TC}})} = \frac{f^1_{\text{PC}}(1 - f^2_{\text{PC}})}{(1 - f^1_{\text{PC}}) f^2_{\text{PC}}} \tag{4.15}$$

and then by substituting in Eqn. 4.14 yields

$$R = \frac{(1 - f_{\text{TC}})\beta f_{\text{TC}}}{f_{\text{TC}}(1 - \beta f_{\text{TC}})} = \frac{f_{\text{PC}}(1 - \alpha f_{\text{PC}})}{(1 - f_{\text{PC}})\alpha f_{\text{PC}}} \tag{4.16}$$

where we have dropped the now trivial 1 superscript for convenience. Finally, with the relationships in Eqn. 4.16, α and β can be explicitly written in terms of R and $f_{\text{PC(TC)}}$

$$\begin{aligned} \beta &= \frac{R}{R f_{\text{TC}} + 1 - f_{\text{TC}}} \\ \alpha &= \frac{1}{R - R f_{\text{PC}} + f_{\text{PC}}}. \end{aligned} \tag{4.17}$$

Since R can be calculated directly from the signal information out of the pumping and target chamber for two different NMR measurements, and $f_{\text{PC(TC)}}$ can be calculated from the temperature that is tracked over time, and the volume which is known from the geometry, then α and β can be calculated. Finally the change in calibration constants can be corrected for by

$$\begin{aligned} C^2_{\text{PC}} &= \frac{1}{\alpha} C^1_{\text{PC}} \\ C^2_{\text{TC}} &= \frac{1}{\beta} C^1_{\text{TC}}. \end{aligned} \tag{4.18}$$

To correct these density fluctuations across the full range of polarisation measurements for a kinematic setting, the calibration constant extracted for a reference point that is well understood through EPR measurements is chosen. This is $C^1_{\text{TC(PC)}}$. From there α^i and β^i are calculated using the first NMR measurement of the chosen EPR calibration point, for all other NMR measurements i, using Eqn. 4.17. The calibration constants for all measurements, $C^{2,i}$ are then adjusted with Eqn. 4.18 [214].

The results of the first pass of this calibration procedure by Hunter Presley are shown in Fig. 4.1. The NMR constants before calibration are shown in blue, and after calibration in red. It can be seen that for all data points the NMR constants increase in magnitude after this calibration, which means that the absolute polarisation of the target that is reconstructed also increases. This is an important calibration as it allows us to access the correct polarisation in the final physics analysis.

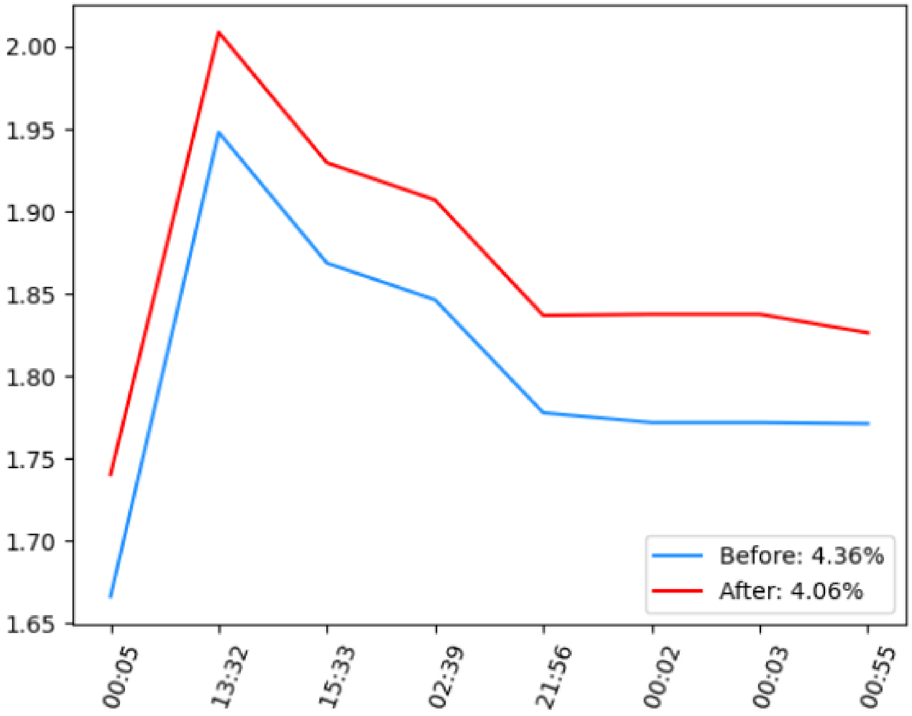

Figure 4.1: NMR constants calibrated over time [214].

The uncertainties for the procedure on all target cells are shown in Fig. 4.2. In particular target cell Hunter which was installed for all of kinematic setting 2 is shown in dark blue (for original slow sweep setting of 1.2 G/s) and light blue (for the later fast sweep setting of 5

G/s). There are two different sweep speeds as this was the first target of the experiment and the NMR procedure was still being optimised for smaller polarisation losses per sweep. The error on a given EPR calibration is taken simply as the standard deviation over the square root of the sample size [214]. The density corrected errors for both settings of target cell Hunter peak around 2.25% and are shown explicitly for each data point in Fig. 4.3.

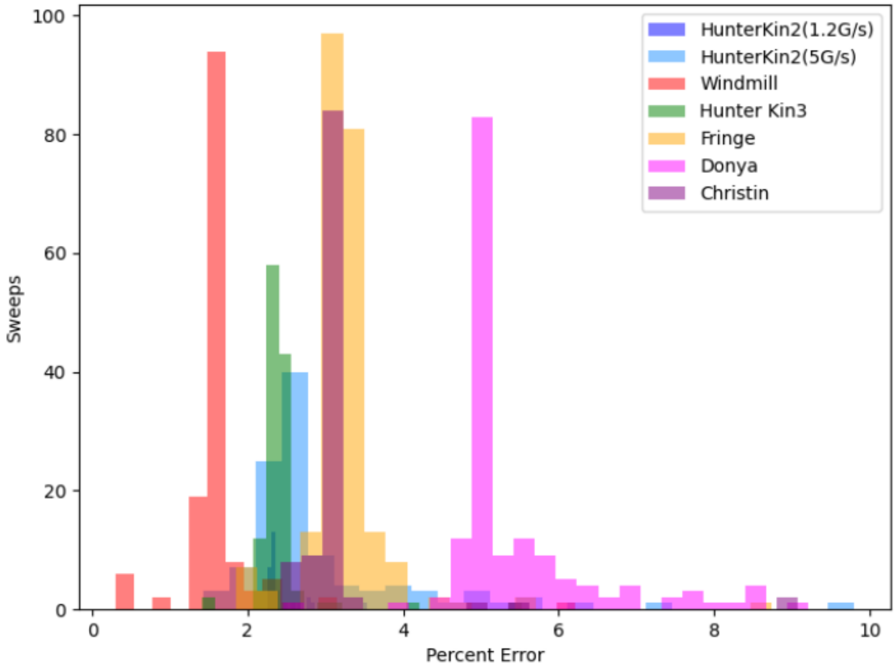

Figure 4.2: Errors for NMR constant calibration for all cells [214].

The density corrected NMR measurements for target cell Hunter during kinematic setting 2 are shown in Fig. 4.3. As stated a minute by minute interpolation of these data points was performed, and events are time-stamp matched to a polarisation value during the final analysis. The unweighted average polarisation over the final data sample of quasielastic neutron events is measured as 37.9%. The correct statistical propagation of the error on each point through the interpolation is still ongoing. For now a minute by minute interpolation of the errors on each measurement is also performed to get an error on each interpolated value. The average error on the unweighted polarisation is 1.9%. This is largely dominated by large errors on early data which was measured with a slower sweep speed, while the NMR procedure was being iteratively tuned. Additionally at this time one NMR lock in channel was missing, so only upstream information was used instead of the combined upstream and downstream information from the coils.

4.2.4 Angular Error From A|| and Compass Measurements

The exact direction of the total combined field in the Helmholtz coils at the target had to be known to 0.01 deg. The field was not perfectly uniform across the length of the target, but

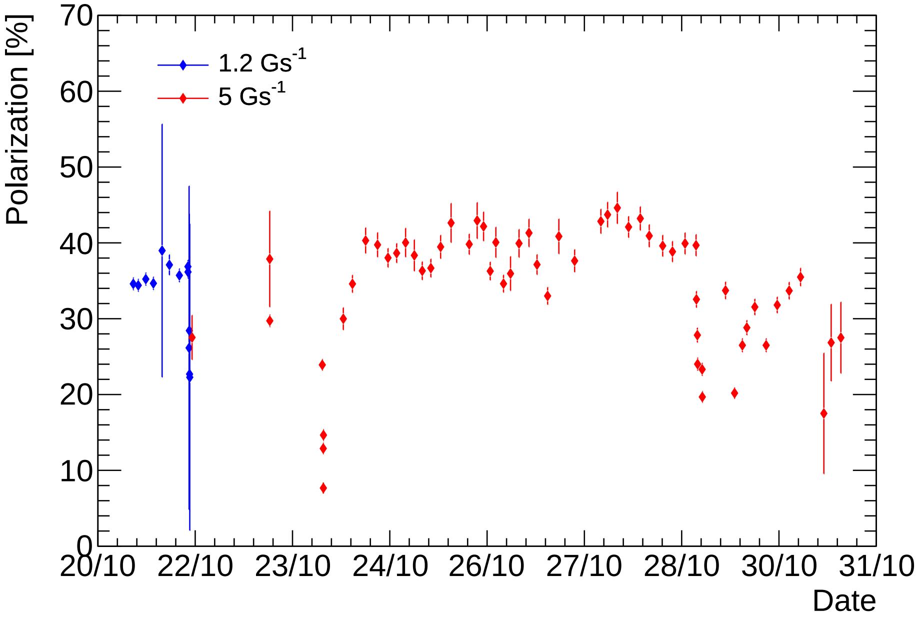

Figure 4.3: Polarisation over time, calculated from calibrated NMR data for target cell Hunter during GEN2 kinematic setting.

could be modelled and corrected for. The field directions were measured at the start of each kinematic setting by a compass device. An OPERA calculation was performed using TOSCA field maps to get the correct form of the function describing the polar and azimuthal angles of the field direction. The measured polar and azimuthal angles at the centre of the target were used as the minima/maxima for the polynomial functions and the shape was attained from the OPERA data, as a function of the target z-vertex position v_z,

$$\begin{aligned}\theta_{\mathrm{vz}} &= A v_z^2 + B v_z + C \\ \phi_{\mathrm{vz}} &= D v_z^2 + E v_z + F.\end{aligned} \tag{4.19}$$

Unfortunately, the simulation which will be used to finalise this polynomial fit is still in progress. As a result, an earlier simulation for a different kinematic point is used to estimate the parameters of Eqn. 4.19. A previous OPERA simulation of the field at kinematic setting 3 demonstrated an empirical deviation of 1.4° in θ and 1° in ϕ between the centre of the target and the edges at ± 30 cm, with a shape that is approximately a polynomial of order two. As such the function for kinematic setting 2 has been approximated combining this absolute deviation and the compass measurements at the correct setting. These measurements found that the absolute field direction at $z = 0$ was $\theta = 61.65°$ and $\phi = 1.25°$, and the deviation across the length of the target are negligible to the final systematic uncertainty.

4.3 Beamline

4.3.1 Beam Polarisation

The beam polarisation was measured at intervals throughout experimental running via Möller polarimetry as detailed in Sec. 3.3.3. These measurements were performed by the Möller polarimetry group. The data was analysed and calibrated by Faraz Chahili (Syracuse University). The results of all measurements taken at all kinematic settings are presented in Fig. 4.4.

As discussed in Sec. 3.3.1 an insertable half-wave plate (IHWP) can be positioned in the path of the laser within the electron source before it strikes the photocathode. This has the effect of flipping the helicity of the photons, and the resultant longitudinal polarisation of the electrons. As such, measurements of the beam polarisation are taken at both half-wave plate settings. These are denoted in blue (HWP in) and red (HWP out) in Fig. 4.4.

As also mentioned in Sec. 3.3.1 the electrons produced out of the GaAs photocathode pass through a Wien filter, which is physically orientated at a given azimuthal angle. The beam polarisation needs to be measured after every Wien angle change. The polarisation taken for a given set of events was the weighted average of measurements at a given Wien angle. Where necessary for kinematics settings with multiple Wien angle settings, polarisation for an event is simply time-stamp matched to the polarisation value closest in time. More discrete time interpolation of the polarisation values was deemed unnecessary due to the small number of measurements over large timescales. For kinematic setting 2 it is fairly trivial since there was only one Wien angle, and therefore one beam polarisation average.

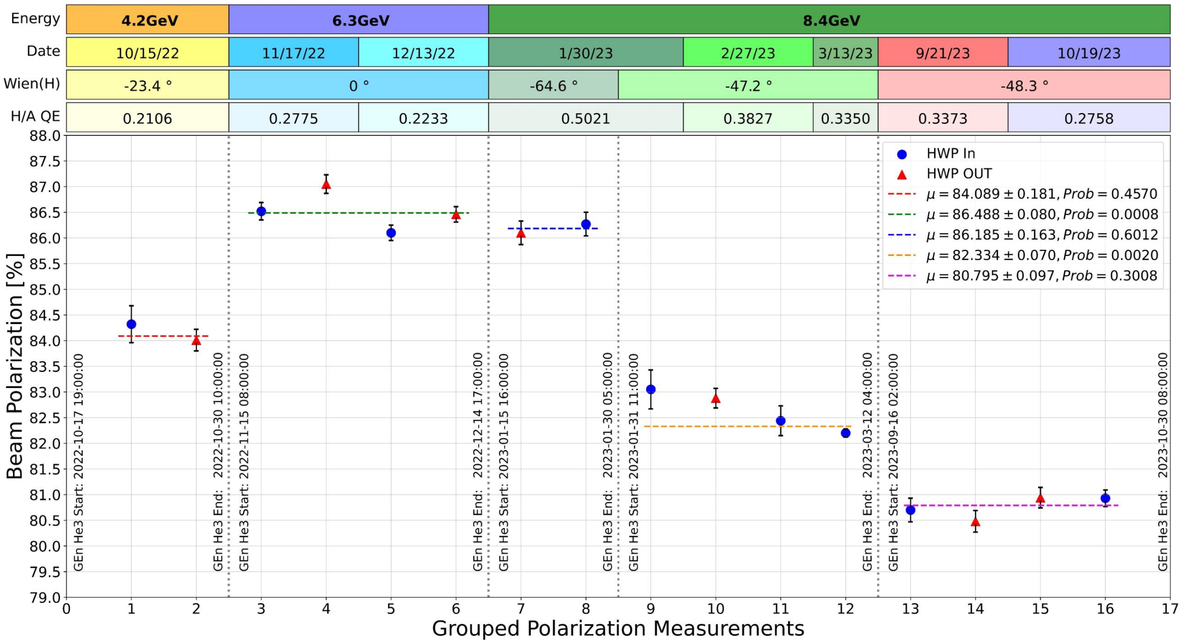

Figure 4.4: Hall A Möller results across GEN-II kinematic settings. Figure from [215].

The measurements taken in Halls A and B during the period of kinematic setting 2 are shown in Fig. 4.5. The Hall A measurements are shown in blue triangles with up orientation representing the HWP in and down orientation representing the HWP out states. The Hall B measurements are given by red triangles with left(right) orientation being HWP in(out). An average is taken for each Hall from the measurements at each half wave plate setting. The Hall B data has more measurements across a longer period of time, which is generally more favourable. However due to differences in experimental technique, the Hall B Möller measurements have much larger systematic uncertainties. Given the much more precise nature of the Hall A Möller data, we elect to use the average value of the single Hall A Möller run for all of kinematic setting 2. The final values taken in the exploratory physics analysis of kinematic setting 2 is 84.089 ± 0.181%.

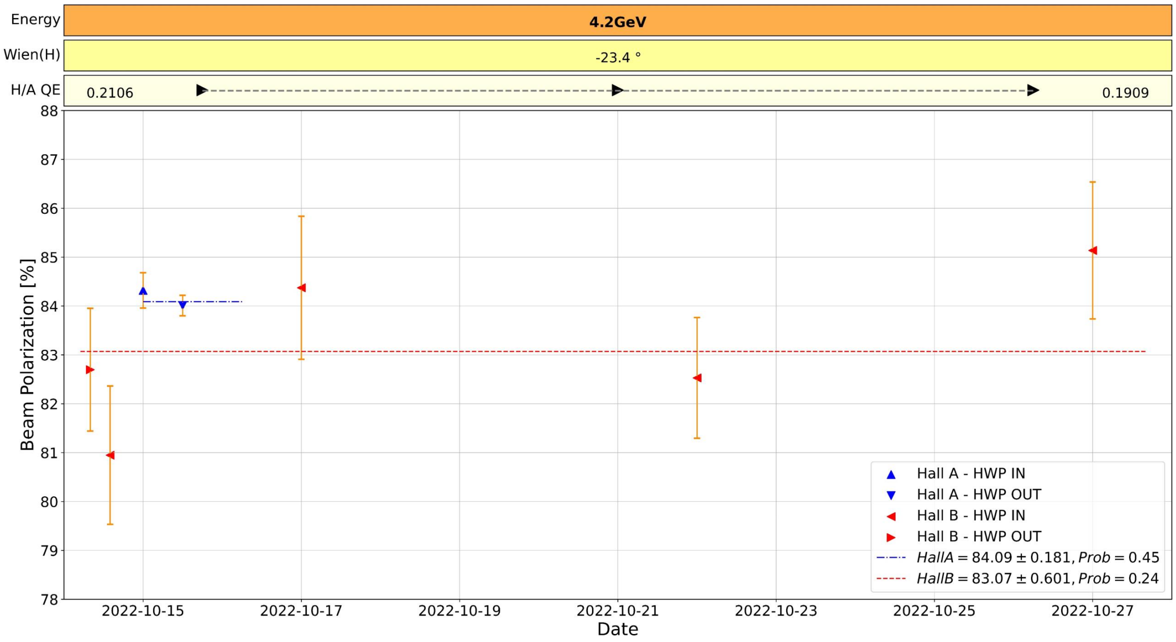

Figure 4.5: Möller Measurements from Halls A and B during GEN2 kinematic setting. Figure from [215].

Helicity

The helicity of the electron is altered by various effects between its emission from the GaAs photocathode, and its entry to the hall, as described in 3.3.1. It is known generally that the Möller asymmetry is negative when formed by subtracting the number of events with target and beam spins anti-aligned from the number which are aligned [216]

$$A = \frac{N_{\uparrow\uparrow} - N_{\downarrow\uparrow}}{N_{\uparrow\uparrow} + N_{\downarrow\uparrow}}. \tag{4.20}$$

In the Hall A Möller polarimeter the magnetic field of the target points downstream which means the spins of the target electrons point upstream along the beam [133]. Due to this the correct form of the asymmetry in Eqn. 4.20 is

$$A_{\text{Möller}} = \frac{N^+ - N^-}{N^+ + N^-} > 0, \quad A_{\text{Möller}} = \frac{N^- - N^+}{N^- + N^+} < 0. \tag{4.21}$$

As such forming the asymmetry in this way, with $h = +1$ corresponding to positive helicity and $h = -1$ corresponding to negative helicity, then the half wave plate state which gives a positive physics asymmetry is the state which is correct, i.e. requires no extra flip in the data analysis. Tab. 4.1 lists the asymmetry and beam polarisation sign for each Möller measurement shown in Fig. 4.4. It can be seen that for kinematic setting 2, the Möller asymmetry and beam polarisation are positive when the half wave plate is removed. This means that the correct asymmetry requires no further work. For all other kinematic settings the opposite is true, and an extra factor of -1 would be included in each helicity value during analysis to attain the correct asymmetry sign.

Table 4.1: Möller polarimetery results for E12-09-016. The sign of the beam polarisation can be used to determine the correct sign of the physics asymmetry for a given half wave plate state.

Date	IHWP State	$A_{\text{Möller}}$	σ_A	Beam Pol Sign
		GEN2		
15/10/22	out	0.052499	0.000330	+
15/10/22	in	-0.045866	0.001054	-
		GEN3		
16/11/22	out	-0.053610	0.000112	-
16/11/22	in	0.053281	0.000105	+
13/12/22	out	-0.053243	0.000094	-
13/12/22	in	0.053025	0.000095	+
		GEN4a		
30/01/23	out	-0.053341	0.000139	-
30/01/23	in	0.053468	0.000145	+
27/02/23	out	-0.051347	0.000116	-
27/02/23	in	0.051072	0.051072	+
13/03/23	out	N|A	N|A	N|A
13/03/23	in	0.051164	0.000047	-
		GEN4b		
21/09/23	out	-0.049856	0.000133	-
21/09/23	in	0.049995	0.000142	+
19/10/23	out	-0.050146	0.000124	-
19/10/23	in	0.050137	0.000099	+

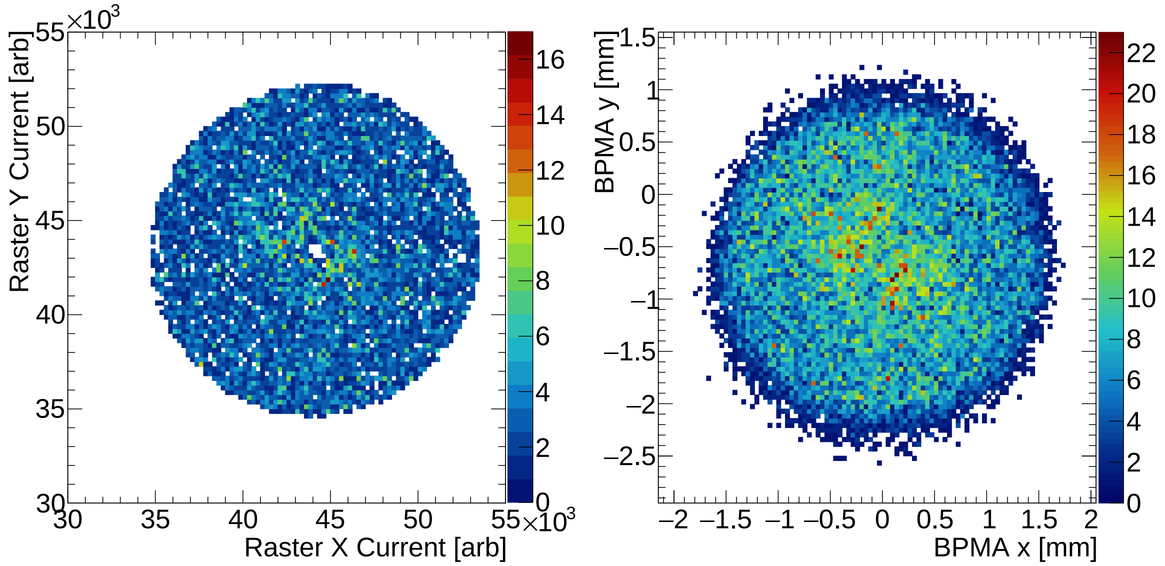

Figure 4.6: (Left) Faster raster current in arbitrary raster units. (Right) Beam position from BPMA in mm. GEN2 ^{3}He data set, Run 2200.

4.3.2 Beam Position Calibration

The beam position monitoring is described in Sec. 3.3.3, and the beam is rastered around a 5 x 5 mm^2 circle on the face of the cell as described in the same section. The absolute beam position needs to constructed from the BPM and raster information and calibrated using the carbon hole target. The beam position measured by the BPMs is given by

$$\begin{bmatrix} x \\ y \end{bmatrix}_{\text{BPMA(B)}} = \begin{bmatrix} C_{x,u} & C_{x,v} \\ C_{y,u} & C_{y,v} \end{bmatrix} \begin{bmatrix} u \\ v \end{bmatrix}_{\text{BPMA(B)}} + \begin{bmatrix} C_{x,\text{off}} \\ C_{y,\text{off}} \end{bmatrix}_{\text{BPMA(B)}} \tag{4.22}$$

where (u, v) are the initial BPM values described by Eqn. 3.1 and $C_{x/y,u/v}$ are scaling parameters and $C_{x/y,\text{off}}$ are offsets which are calibrated. The BPMs are calibrated initially using position measurements from the Hall A harp scanners introduced in Sec. 3.3.3, which provide an absolute position measurement. This known absolute position can be compared to the BPM distribution for a number of runs and a matrix inversion provides the corrected BPM scaling parameters [137].

The electronics which record the BPM information are delayed and as such are de-synced from events. However the raster information is not out of time and is accurate to the nearest event (keeping in mind that the EPICs readout is around every two seconds). Therefore the BPM information can be used to calibrate the centre position of the raster from arbitrary raster units to metres over many events. Recall from 3.2 that the beam positions obtained from the raster are given by

$$x^{\text{rast}} = O_x + A_x I_x^{\text{rast}},$$
$$y^{\text{rast}} = O_y + A_y I_y^{\text{rast}}.$$

The coefficients $O_{x(y)}, A_{x(y)}$ are calibrated by comparing the raster current to the beam position from the calibrated BPM positions. Fig. 4.6 shows the 2D distribution of the raster coil current in the x and y directions on the left, and the reconstructed BPM position in BPMA on the right. The mean and RMS position of the BMP and raster are compared and the coefficients are extracted by

$$A_{x(y)} = \frac{\Delta x(y)_{\text{BPM}}}{\Delta I^{\text{raster}}_{x(y)}} \tag{4.23}$$

$$O_{x(y)} = \mu_{x(y)_{\text{BPM}}} - \mu_{I^{\text{raster}}_{x(y)}} A_{x(y)} \tag{4.24}$$

where μ and Δ denote the mean and RMS of each position measurement respectively.

The calibrated BPM information can also be used to calculate the position of the beam at the target

$$\text{BPM}_{\text{tg}} = \left(\text{BPMB}_{x(y)} - \text{BPMA}_{x(y)}\right)\frac{\text{BPMA}_D}{\text{BPM}_D} + \text{BPMA}_{x(y)}, \tag{4.25}$$

where $\text{BPMA(B)}_{x(y)}$ is the $x(y)$ position recorded by each BPM, BPMA_D is the distance between the centre of the target and BPMA, and BPM_D is the distance between BPMA and BPMB. The process of calibrating the BPM and raster can be performed iteratively to fine tune the final beam position measurement. The final calibrated beam position at the target is then calculated as

$$x(y)_{\text{beam}} = \text{BPM}_{x(y)} + x(y)^{\text{rast}} \tag{4.26}$$

where $x(y)^{\text{rast}}$ is given in equation 3.2.

4.4 Detector Calibrations

The response of individual detectors is usually calibrated any time an experimental condition changes, such as the kinematic setting as one large extreme, or a single channel high voltage change on a smaller scale. Typically every system was calibrated before the first experimental run of E12-09-019 using cosmic muon data, and subsequently calibrated throughout the ongoing analysis efforts for that experiment. Those calibrated values feed into the initial starting conditions for E12-09-016, for which we again revisit each detector's calibration steps per kinematic setting. Beamline, optics, momentum reconstruction and GEM calibrations were performed by Sean Jeffas (University of Virginia) [217–219]. Energy calibration for BBCal and HCal was done by Kate Evans (College of William and Mary) [220] and Hunter Presley (University of Virginia) [221] respectively. The GRINCH was uncalibrated for the first pass replay of the data used in this analysis, however subsequent work on timing alignment has been performed by the author and Jack Jackson (College of William and Mary) and will be discussed [222]. The BBCal and HCal timing are aligned to the hodoscope, but have no dedicated timing calibrations in this pass of data. The hodoscope was calibrated for Pass 1 by the author [223]. Further global timing analysis of all systems has since been performed, with aspects ongoing.

Cosmic Muon Calibrations

Muons from cosmic rays typically reach earth at sea level with a flux of around 1 muon per square centimetre per second, and a mean energy of 4 GeV. This makes them excellent candidates for calibrating detectors in experiments with GeV energy electrons. Dedicated DAQ running periods known as cosmic runs are taken (typically overnight to accumulate reasonable statistics) with specific trigger setups more sensitive to cosmic muons than the single arm and coincidence triggers used in beam conditions.

Hydrogen (H_2) Data Calibration

It is also common to dedicate a portion of planned beam time to taking data on a hydrogen (H_2) target in experiments like E12-09-016. This data can be used to further calibrate detectors for electron and nucleons due to elastic scattering at the same kinematic values as the production helium-3 (^{3}He) data, but with better precision due to the absence of nuclear effects which smear out reconstructed kinematic distributions.

4.4.1 GEM Tracking

Data out of the GEMs is fairly complex and requires many steps to fully analyse. Raw data at the strip level is first processed to remove noise through a pedestal subtraction and "common mode" algorithm filtering. The BBCal trigger blocks provide a physical region that the particle which should be responsible for a track must have hit. By projecting this region backwards towards the GEM plane, a constraint region can be formed. Then inside the calorimeter constraint region 1D clusters of strips are formed, and then 2D hit combinations. From these the tracks between multiple layers are formed. A complete and detailed explanation of this entire reconstruction is available in the thesis of Sean Jeffas [195]. This section will attempt to summarise the reconstruction process and calibration procedures involved in E12-09-016.

Online Data Treatment

The signal in a GEM APV25 readout card (APV) for one event is made up of six 25 ns time samples for an event width of 150 ns. In an event each sample has a baseline with a non-zero ADC offset called the "common mode". This is calculable from a "pedestal run" where a small number of statistics are collected with no beam and an artificial trigger. This results in events with only noise remaining from which the mean μ_{ped} and standard deviation σ_{ped} are calculated for each APV and uploaded to the VXS Trigger Processor (VTP). The pedestal mean is subtracted from the signal in real time and the common mode fluctuations can be calculated.

One of three common mode algorithms is employed to align the differing baselines of each sample. This is programmed into the VTP and acts in real time. The "Sorting Method" was used before running to test the common mode but is too memory intensive for the VTP FPGA during production running. An experimental "Histogramming Method" has been developed and is under further study. An algorithm was developed by Danning Di (University of Virginia) which does not require individual strip information to be stored in real time and thus reduces the hardware bottleneck sufficiently to be used in beam conditions. This is now called the "Danning Method" and is described in the thesis of Di [224]. The Danning method was used exclusively during production data taking.

After the signal is common mode and pedestal subtracted, the signal will have the noise aligned around zero with real signals as peaks. The final step in background removal is "zero suppression". A $5\sigma_{\text{ped}}$ cut is applied to the sum of all six time samples for a channel, $ADC_i > 5\sigma_{\text{ped}}$. Strips within 5σ of the pedestal noise are discarded, which greatly reduces the occupancy, which would otherwise totally saturate the DAQ.

Offline Track Reconstruction

1D clustering is performed over strips which pass the zero suppression for a given axis of a layer. First local maxima are found from the list of all strips. Then each local maximum is compared to the next on its left and right hand side. If these are more than eight strips apart they remain separate clusters. If not the strip with smallest signal between them is found and labelled a valley. Then the difference between the signal amplitude of the peak and the valley is found, known as the prominence. A condition is checked to determine whether the local maximum should be considered its own cluster based on the prominence. Next the new list of local maxima is looped over again. This time the distance criteria is four strips. Now the timing of strips is checked relative to the maximum strip. The signal amplitudes are compared to a predetermined cut. If a strip passes each of these criteria it is added to the cluster, and the iteration moves left. Afterwards this is repeated moving right. A 1D cluster is formed using all the strips that pass the previous steps. If the cluster position is not within the calorimeter search region it is discarded. Finally, clusters that do not pass a cluster ADC sum threshold or do not have at least two strips are discarded.

All possible 2D combinations of overlapping 1D clusters between U and V, or X and Y layers are formed into "hits". Another set of criteria are applied based on the calorimeter search region, the time difference between two clusters, the ADC signal correlation and the ADC signal asymmetry. If all 2D clustering criteria are met, a list of 2D hits are formed for the module. The list of 2D hits for all modules must be iterated to construct straight line tracks. First, a minimum number of layers with hits is required to form a track. For Bigbite in GEN-II, this is three. All possible combinations of hits from the two most outer layers are formed into track candidates, and the projection is checked backwards towards the target and forwards towards the calorimeter constraint region. If these fail the candidate is discarded. Next the remaining tracks are looped over and all combinations of hits in intermediate layers are considered. For each new candidate, a straight line is fit and the χ^2 is checked within some predetermined cut. Again the straight line is projected backwards towards the target and forwards to the constraint region. If these three criteria are passed, the track is added to the final list of good tracks and recorded in the analyzer output, for use in physics analysis.

Alignment

The position of each GEM module needs to be known with enough precision for the SBS-offline software to find tracks with $\approx 10^{-4}$m resolution. Each module can be described by six variables which describe the absolute position of the centre of the module and the absolute pitch, roll and yaw of the plane of the module relative to the centre. The centre of a module is defined as

$$\vec{x}_{\mathrm{mod}} = \begin{pmatrix} x_0 \\ y_0 \\ z_0 \end{pmatrix} \tag{4.27}$$

where x_0, y_0, z_0 are x, y, z position coordinates of the centre of the module in metres. The rotations associated with the pitch, roll and yaw are defined by the matrices R_x, R_y, R_z

$$R_x = \begin{pmatrix} 1 & 0 & 0 \\ 0 & \cos(\theta_x) & -\sin(\theta_x) \\ 0 & \sin(\theta_x) & \cos(\theta_x) \end{pmatrix}$$
$$R_y = \begin{pmatrix} \cos(\theta_y) & 0 & \sin(\theta_y) \\ 0 & 1 & 0 \\ -\sin(\theta_y) & 0 & \cos(\theta_y) \end{pmatrix} \tag{4.28}$$
$$R_z = \begin{pmatrix} cos(\theta_z) & -\sin(\theta_z) & 0 \\ \sin(\theta_z) & \cos(\theta_z) & 0 \\ 0 & 0 & 1 \end{pmatrix}.$$

The absolute position for a hit is then given as

$$\vec{x}_{\text{hit}} = \vec{x}_{\text{mod}} + R\vec{x}_{\text{hit,local}} \tag{4.29}$$

where $\vec{x}_{\text{hit,local}}$ is the hit position in the local GEM geometry. If the position of a track at each module is calculated before calibration for each event then a χ^2 can be formed

$$\chi^2 = \sum_{i=0}^{N_{\text{hits}}} (x_{\text{hit}} - x_{\text{track}})^2 + (y_{\text{hit}} - y_{\text{track}})^2. \tag{4.30}$$

A minimisation is performed to extract the six parameters for each module. The results of this minimisation for each module are shown in Fig. 4.7. The residuals of each are aligned at zero with resolutions on the order 50 - 100 μm. Recall that modules 4-8 comprise layer 5, whilst modules 1-4 are the entirety of layer 1-4 respectively. As such the resolution of the individual modules on the rear tracker is improved, because much of the noise which may affect the fits is blocked by the dense material of the Cherenkov.

Gain Matching

The gain of APV cards must be calibrated to remove variations in ADC values recorded for particles of similar energy. As mentioned in Sec. 4.4.1 the 2D clustering method involves a cut on the ADC asymmetry between the two directions of the overlapping strips. As such any bias in the amplitudes recorded in the ADC as a result of mis-matched gain values directly impacts 2D clustering and therefore overall track reconstruction.

The gain coefficient for an APV j on GEM module i is

$$ADC_{ij} = G_i G_j ADC_{\text{raw}} \tag{4.31}$$

where G_i is the gain for the module, G_j is the gain for the APV and ADC_{raw} is the raw mea-

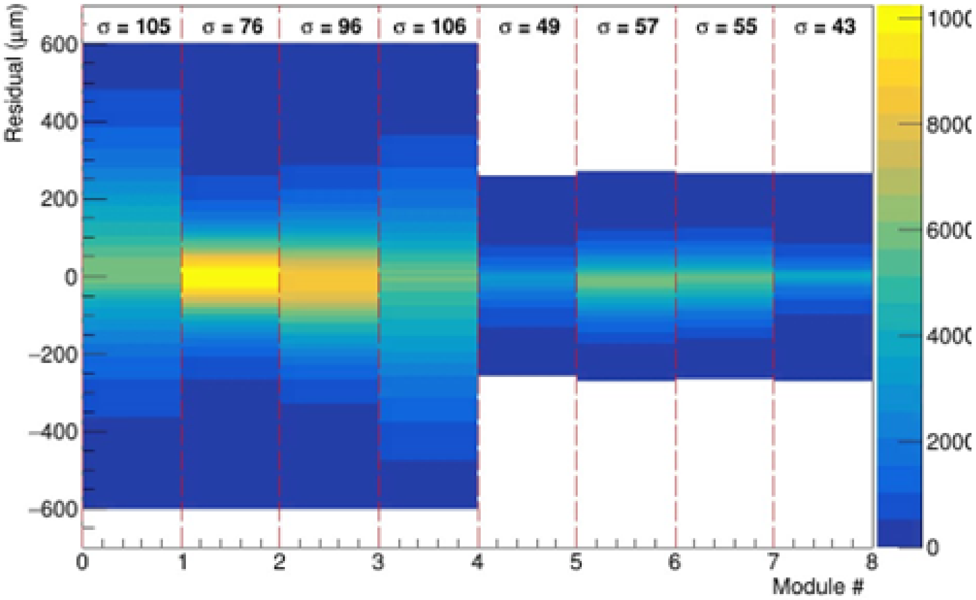

Figure 4.7: Residuals after GEM alignment calibration. Modules are aligned near zero and resolution is shown in the top of the plot. Figure from [195].

sured ADC signal. The ADC asymmetry between two clusters u, v is defined as

$$ADC_{\text{asym}} = \frac{ADC_{\text{clus},u} - ADC_{\text{clus},v}}{ADC_{\text{clus},u} + ADC_{\text{clus},v}}. \tag{4.32}$$

For APVs i along U-axis and j along V-axis the associated average asymmetry after gain matching calibration are labelled $A_{u,i}$ and $A_{v,j}$ respectively. The asymmetry combination between the two axes A_{ij}, is then defined as

$$A_{ij} = \frac{A_{u,i} - A_{v,j}}{A_{u,i} + A_{v,j}}. \tag{4.33}$$

Then the weighted average between the U and V layers for a module is calculated as

$$A_{u/v,\text{mod}} = \frac{\sum_{i=0}^{N_{u/v}} N_{u/v,i} A_{u/v,j}}{\sum_{i=0}^{N_{u/v}} N_{u/v,i}} \tag{4.34}$$

where $N_{u/v}$ is the number of U and V strips (which are equal to each other) in a given module. Two quantities can be formed for a module, $A_{iv,\text{mod}}$ and $A_{u,\text{mod},j}$ which represent the asymmetry combination between APV $i(j)$ on the U(V) axis and the weighted average axis asymmetry on the V(U) axis. These are defined as

$$\begin{aligned} A_{iv,\text{mod}} &= \frac{A_{u,i} - A_{v,\text{mod}}}{A_{u,i} + A_{v,\text{mod}}} \\ A_{u,\text{mod},j} &= \frac{A_{u,\text{mod}} - A_{v,j}}{A_{u,\text{mod}} + A_{v,j}}. \end{aligned} \tag{4.35}$$

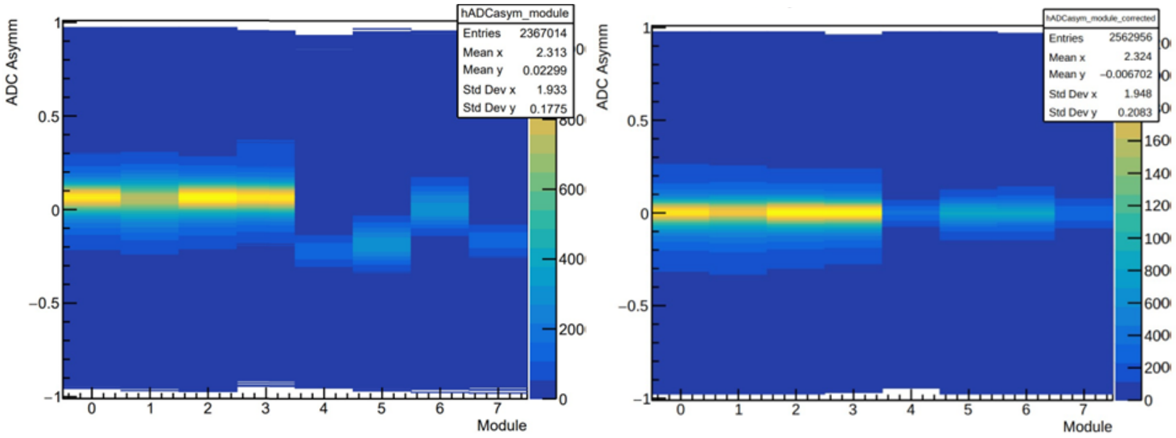

Figure 4.8: (Left) GEM ADC asymmetry vs module before gain calibrations and (right) after the calibrations. Figure from [195].

Eqns. 4.32 4.33 and 4.35 can be combined to form a χ^2 of the form

$$\chi^2 = \sum_{i=0}^{N_U}\sum_{j=0}^{N_V}\left(\frac{A_{i,j,raw} - A_{i,j}}{\sigma_{A_{i,j,raw}}}\right)^2 + \sum_{i=0}^{N_U}\left(\frac{A_{u,j,raw} - A_{iv,\text{mod}}}{\sigma_{A_{i,raw}}}\right)^2 + \sum_{j=0}^{N_V}\left(\frac{A_{v,j,raw} - A_{u,\text{mod},j}}{\sigma_{A_{j,raw}}}\right)^2. \quad (4.36)$$

The χ^2 in Eqn. 4.36 is solved to minimise both the asymmetries between U and V APVs, and the average asymmetry in a module. This minimisation produces the initial gain parameters G_i, G_j introduced in Eqn. 4.31. Fig. 4.8 shows the result of this calibration compared to the raw asymmetries for kinematic setting 2.

4.4.2 Bigbite Calorimeter

The BBCal ADC times are aligned to the hodoscope TDC times [225]. This was initially performed as part of the GMN calibrations [226], and then re-aligned for the GEN kinematic settings individually. The BBCal energy reconstruction was calibrated in pass 1 by Kate Evans [220]. A summary of the method and results for the calibration of the kinematic setting 2 data is provided in this section. BBCal measures the energy of the elastically scattered electrons in Bigbite and provides the trigger for the spectrometer arm. As such, a well calibrated energy is required. For kinematic setting 2, H_2 data can be used to achieve a clean elastic event sample and allow for a high quality calibration. A χ^2 is formed over all of the calorimeter blocks

$$\chi^2 = \sum_{i=0}^{N}\left(p_e^i - \sum_{k=0}^{M} C_k A_k^i\right)^2 \quad (4.37)$$

where p_e^i is the momentum of the track as reconstructed by the optics, i is a sum over events in the data set, k is a sum over the individual BBCAL blocks, C_k is the gain coefficient of block k and A_k^i is the BBCal ADC reading for that block in a given event. A minimisation of χ^2 is performed in order to solve for all C_k. Ideally the energy reconstruction will yield a ratio of close to unity with the momentum, $E/p \approx 1$. The better the resolution (i.e the smaller the σ of the Gaussian fit to E/p) the better the reconstruction.

A summary of the results of the calibration are shown in Fig. 4.9. The resolution of the ratio E/p is compared before and after calibration, and any correlation across momentum range are corrected for. Additionally the ratio is monitored for stability over runs. Kinematic setting 3 was calibrated in the same way. Kinematic settings 4A and 4B required use of ^{3}He data due to a lack of H_2 data as previously discussed.

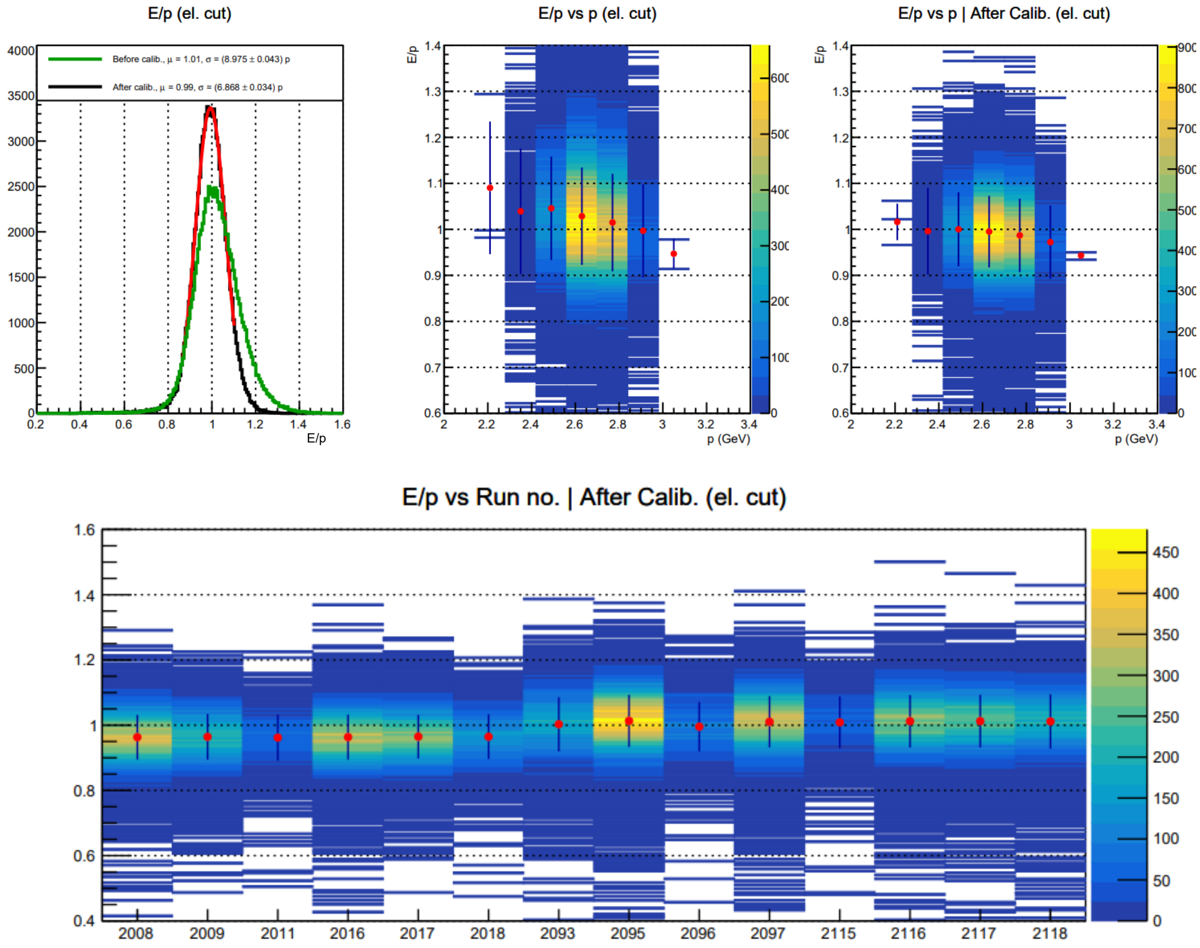

Figure 4.9: E/p resolution before and after calibration for (top) all data and (bottom) measured across runs. The top left plot shows the resolution before (green) and after (black) calibration. Figures from [220].

4.4.3 Hadron Calorimeter

HCal energy reconstruction and timing were calibrated in pass 1 by Hunter Presley [221]. The ADC and TDC timing spectra are simply aligned relative to the timing hodoscope. The ADC and TDC energy weighted times for HCal clusters in QE events are shown in black in the top of Fig. 4.10. The dashed red lines indicate 3σ timing cuts. These cuts remove low energy noise and tails in the measured energy spectrum. This is visible in the bottom left of Fig. 4.10, which shows the measured energy before the timing cut in black, and afterwards in dashed red. The sampling fraction is illustrated similarly in the bottom right, which is the focus on the energy calibration.

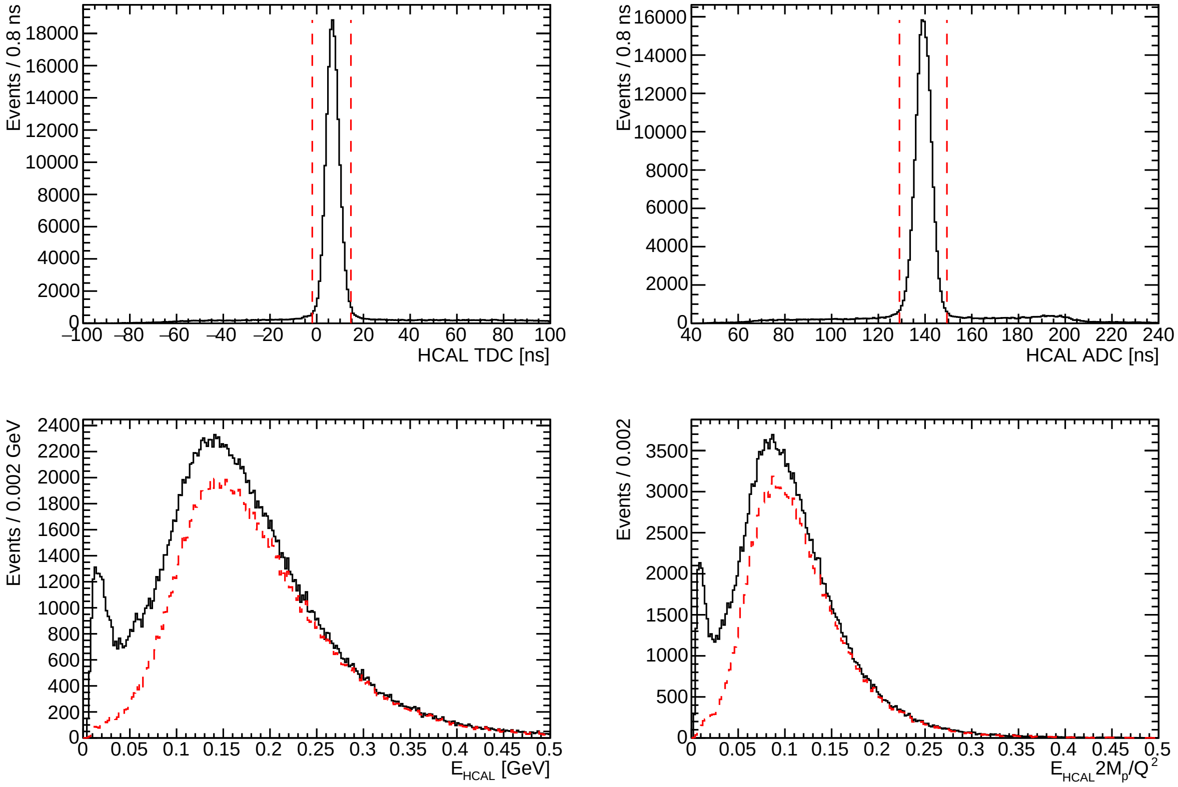

Figure 4.10: The HCal cluster TDC time (top left), ADC time (top right), measured energy (bottom left) and measured fraction of elastic nucleon energy (bottom right) in black. The dashed red lines on the top figures indicate 3σ cuts on the TDC and ADC times, and the dashed red plots in the bottom figures indicate the resulting distributions after these cuts. GEN2 H_2 dataset.

The energy reconstruction calibration is performed in a very similar manner to the aforementioned method for BBCal. A χ^2 is formed over all blocks

$$\chi^2 = \sum_{i=0}^{N} \left(E^i - \sum_{k=0}^{M} C_k A_k^i \right)^2 / \sigma_E^2 \tag{4.38}$$

where i sums over all events and k sums over all blocks which recorded a hit. E_i is the expected energy of the nucleon in that event and σ_E^2 is the energy resolution of the detector, which are related to the sampling fractions (SF). The SF of HCal are on the order of 5% - 10% and are initially determined for each kinematic setting from Monte Carlo. A factor R is defined which relates the true sampling fraction S_f^* to the ideal MC value

$$S_f^* = RS_f. \tag{4.39}$$

The kinetic energy acquired by the nucleon from rest is determined as

$$E_i = \nu_i S_{f,i}^* \tag{4.40}$$

where ν has the standard kinematic definition $\nu = E - E' = \frac{Q^2}{2M_p}$ (the energy exchanged by the incoming electron). The ratio of measured energy to elastic nucleon kinetic energy (E/ν) is shown in the bottom right of Fig. 4.10. This is calculated over all blocks and is shown in Fig 4.11 against the dispersive (left) and non dispersive (right) directions of HCal. The mean SF in each bin is indicated by the red markers. The deviation across HCal indicates the non-uniformity of energy reconstruction, demonstrating the importance of the calibration.

The energy resolution is then approximated based on an ideal calorimeter as

$$\sigma_E^2 \approx \nu_i S_{f,i}^*. \tag{4.41}$$

Eqn. 4.39, 4.40 and 4.41 into Eqn. 4.38 yields the final expression

$$\chi^2 = \sum_{i=0}^{N} \frac{\left(E^i - \sum_{k=0}^{M} C_k A_k^i\right)^2}{\nu_i S_{f,i}}. \tag{4.42}$$

Similarly to the BBCal calibration a minimisation is performed to determine each C_k and R. H_2 data taken at kinematic setting 2 was used to calibrate HCal. There were no subsequent hardware or power supply changes throughout all kinematic settings therefore only one calibration was required. As such the GEN2 calibration was applied to all datasets.

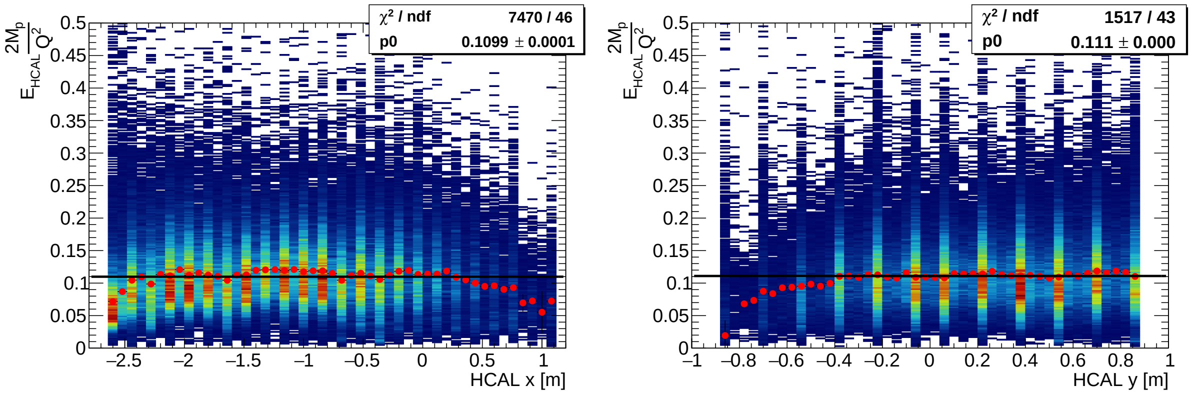

Figure 4.11: HCal measured fraction of elastic nucleon energy vs (left) the dispersive (x) direction and (right) the non-dispersive (y) direction. Red markers indicate the mean of each bin.

4.4.4 Cherenkov Calibration

The GRINCH needs to be calibrated for timing peaks in all channels to accurately separate pions and electrons based on the difference in β factor in the refractive medium. A global timing offset value was put into the offline replay database at the beginning of the experiment in order to get the signals from all channels into a common window. However, changes to the read back window cause significant shifts in the timing peaks of the channels. As a result a calibration of the offset for the peak must be performed for all channels whenever the window shifts. This happened in particular during H_2 data taking near the beginning of the kinematic setting 2 period. A consequence of this is uncalibrated GRINCH times in the "pass 1" production dataset.

A timing window cut is applied in the cluster formation stage of offline analysis. This means that even if an electron from a good GEM track forms a good cluster in the GRINCH, if the time is outside of the window then this cluster will not be track matched. This causes the common GRINCH analysis cuts for pion and electron separation to fail. An important task before a second data replay pass then has been to calibrate these timing offsets and to verify the resulting physics impact of the GRINCH cuts in the analysis.

The author worked closely with Jack Jackson in analysing the leading edge time distributions of hits in the GRINCH to generate new timing offsets, and applying various cuts on new GRINCH clusters to suppress the pion background in the final data sample. Fig. 4.12 shows the cluster mean time before (red) and after (black) alignment. Importantly, the red distribution is flatter and has an unusual periodicity. This is because the true peak is so far offset from the central window ±50ns that the only signals that fall within the window are random noise. In contrast the black distribution after all channels have been aligned has a much more expected shape around zero. This is indicated more clearly in Fig. 4.13, which shows the raw leading edge time for all PMTs. On the left of the figure all the channels are globally offset by around 125 ns, as well as misaligned. On the right hand side, they can be seen to be well aligned around zero.

The impact on physics analysis from a first pass of timing alignments for the GRINCH can be investigated. A common way to assess the capabilities of the GRINCH is by looking at the Preshower energy distribution, which typically exhibits two clear peaks - a low lying peak around 100 MeV corresponding to pions and a broader higher energy peak corresponding to electrons. These are clear in black in the left and right of Fig. 4.14. GRINCH clusters are matched to tracks by cuts on the absolute distance of the average centre of the cluster to the projected position of a track. GRINCH clusters also exhibit on average larger clusters for electrons. By choosing events where the primary GRINCH cluster was track matched, and had a fairly large cluster size (i.e. $\geq 2,3$) one can begin to examine how the calibrations improve the ability to match the pion and electron peaks. The left of Fig. 4.14 shows various cuts on the preshower energy distribution before the calibrations, and it is clear that the

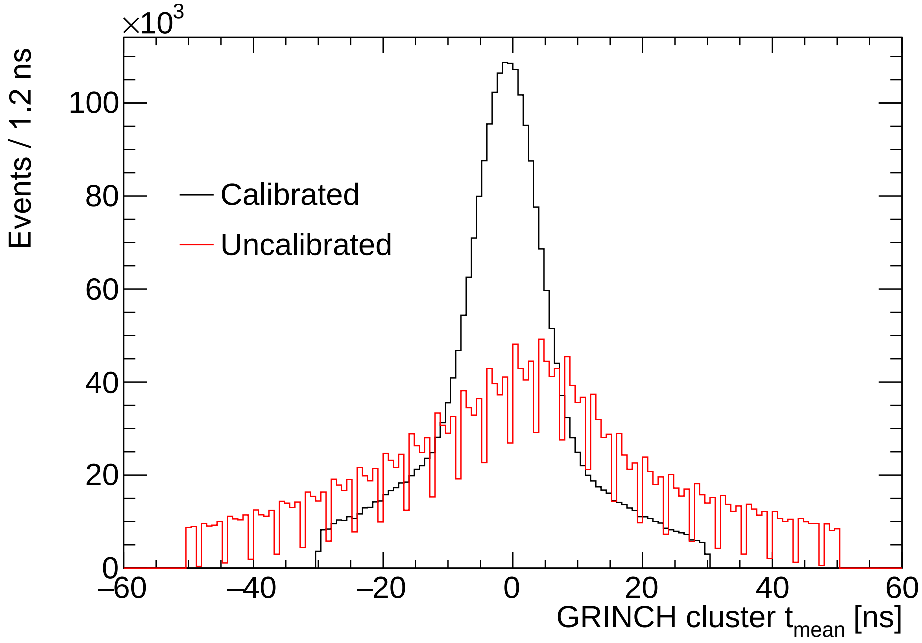

Figure 4.12: The cluster mean time of the GRINCH (red) before alignment and (black) after alignment of all channels, for GEN2 data.

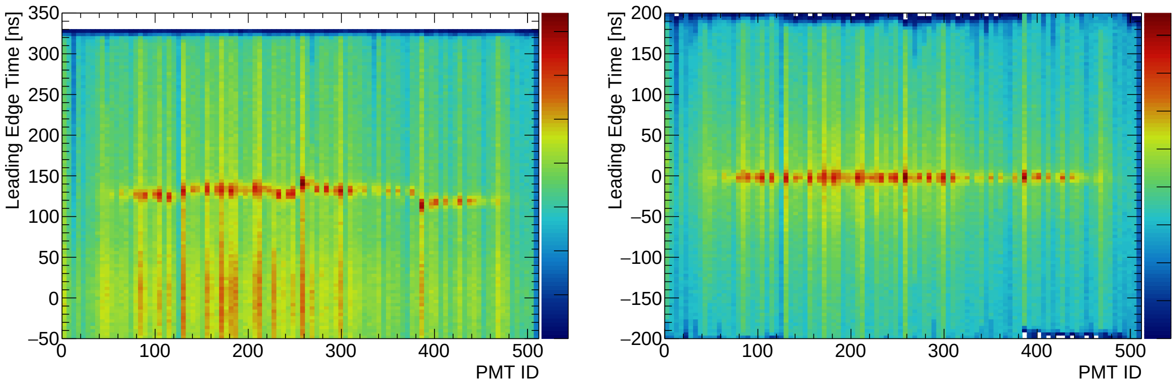

Figure 4.13: Leading edge time of raw hits in the GRINCH vs the PMT number for all channels (left) before calibration and (right) after calibration. Select run 2095 from GEN2 H_2 dataset.

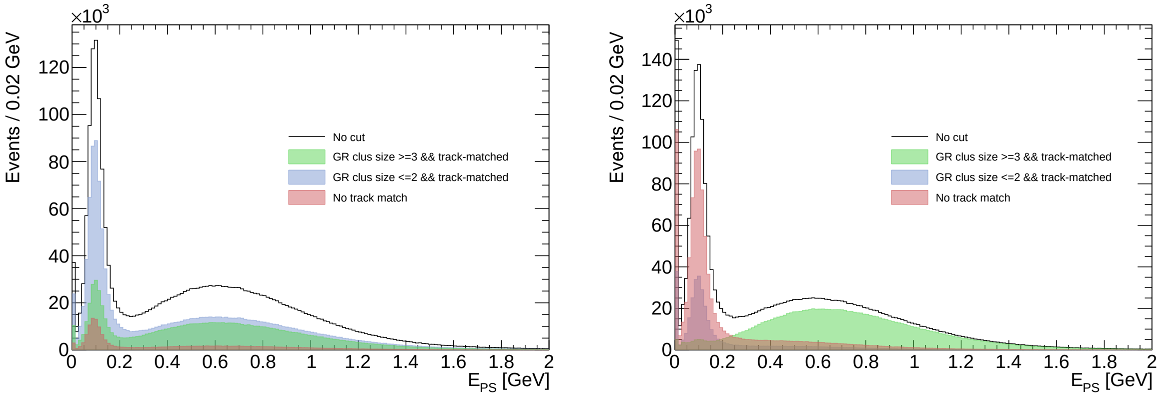

Figure 4.14: Preshower energy distribution with various cuts denoted in the legend, (left) before GRINCH timing calibration and (right) afterwards. GEN2 H_2 dataset.

efficiency of pion rejection and electron selection is poor. In contrast on the right hand side of the same figure, the same cuts are shown for the calibrated data, and it is clear that the individual distributions are being picked out more clearly.

4.4.5 Timing Hodoscope

The BB timing hodoscope will ideally provide a precise start time for events and is a crucial ingredient in measuring the nucleon time of flight (TOF) and related momentum. Various effects must be corrected for in the time recorded by the hodoscope, and further calibrations are required to extract a precise TOF using HCal in coincidence.

The time recorded in a single PMT, t_{PMT}, and the true start time for an event at the interaction vertex, t_{vz}, are related by

$$\begin{aligned} t_{\mathrm{PMT}} - t_{\mathrm{vz}} &= t_{\mathrm{eTOF}} + t_0 - t_{\mathrm{TW}} + t_{\mathrm{prop}} \\ &= t_{\mathrm{eTOF}} + t_0 - p_{\mathrm{TW}} t_{\mathrm{TOT}} + \frac{d}{v_{\mathrm{scint}}}. \end{aligned} \tag{4.43}$$

where t_{eTOF} is the electron TOF from the vertex to the detector and t_0 is an arbitrary timing offset. The correction associated with timewalk effect which is calculated as $t_{\mathrm{TW}} = p_{\mathrm{TW}} t_{\mathrm{TOT}}$ where p_{TW} is a constant calculated from a timewalk calibration procedure and t_{TOT} is the time over threshold (TOT) for the signal. The time taken for the signal to propagate along the bar, t_{prop}, is related simply to d the distance from the hit position to the edge of the bar, and v_{scint} the effective speed of propagation of light in the bar. Though each of the 89 bars are made of the same plastic, small manufacturing defects, radiation exposure and other effects can cause the speed of light in the material to change slightly. In pass 1 the corrected times were constructed as

$$t_{\mathrm{corr}} = t_{\mathrm{PMT}} - t_{\mathrm{TDC,0}} + p_{\mathrm{TW}} t_{\mathrm{TOT}} - t_0 \tag{4.44}$$

where $t_{\text{TDC},0}$ is a TDC channel offset value which aligns the raw signals in a common window at the beginning of the offline reconstruction. In this case a secondary alignment of the times with QE cuts applied and any non zero offset remaining after timewalk calibration are absorbed in t_0.

The raw TDC channel offsets are calculated by fitting the raw leading edge signals for all PMTs with a Gaussian. The mean is taken as the offset. Importantly the value must be converted into TDC units at this stage of reconstruction. The constant of conversion between ns and TDC bins is $c_{\text{TDC}} = 0.0937$ for the v1190 TDC. In the first step of reconstruction the TDC are decoded and the time is formed as

$$t_{\text{PMT}} = (t_{\text{raw,TDC}} - t_{\text{trig,TDC}} - t_{\text{TDC},0})c_{\text{TDC}} \tag{4.45}$$

where $t_{\text{raw,TDC}}$ is the raw TDC signal from the hodoscope PMT and $t_{\text{trig,TDC}}$ is the raw TDC signal from the trigger which is subtracted as a reference.

The next stage in reconstruction is to identify real hits in the bars from noise in the PMTs. This is done by taking the PMT times from Eqn. 4.45 and constructing “bar” level variables. Naturally the first step is identifying which bars had hits in both the left and right hand side PMTs. Any bar in which both sides did not fire is discarded. Next a window cut of ± 30 ns is applied to the left and right leading edge time. This is why the initial raw TDC alignment is important. A cut of $5 < t_{\text{TOT}} < 30$ ns is applied to the time over threshold in each PMT, which removes a lot of low amplitude noise.

At this stage, the bar level variables are corrected for timewalk effects. Timewalk is a shift in the timing of a measured pulse in leading edge discriminators, that occurs due to amplitude variations. A common way to illustrate this is to examine the relationship between the TDC leading edge time and the ADC signal amplitude. However, not all hodoscope channels were read out to ADC in this experiment. As such the TOT out of the TDC can be used as a suitable substitute, since the NINO TOT is defined to be a proxy ADC signal. Fig. 4.15 shows the leading edge time of PMTs which passed the “good bar” cuts described above, plotted against the TOT. A clear linear trend is present. The red line indicates the fit to the mean of each Y-slice. The parameters of this fit can be taken as the timewalk correction parameters for each PMT. The slope is p_{TW} and the offset is absorbed in t_0.

The next step in the reconstruction is clustering. First all good bars are iterated over and considered as possible cluster centres. If a bar has a larger TOT than both its direct neighbours, or one direct neighbour in the case that only one fired, or has no direct neighbours to begin with, it is considered a local maximum. Bars are then aggregated into clusters depending on whether there is another good bar between them and the local maximum. When no more clustering can be performed, clusters are compared to the GEM track in order to match the cluster coming from the scattered electron in the event. The horizontal position

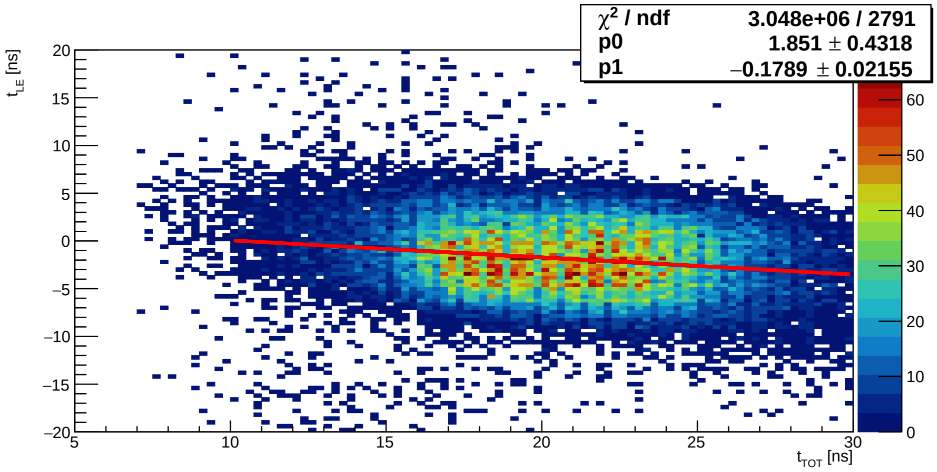

Figure 4.15: The time over threshold vs leading edge for PMT 44L. The linear trend indicates the timewalk effect. GEN2 H_2 dataset.

of a hit in a bar in the timing hodoscope is calculated by

$$y_{\text{bar}} = \frac{-v_{\text{scint}}}{2}(t_{\text{bar,diff}} - t_{0,\text{diff}}) \tag{4.46}$$

where $t_{\text{bar,diff}} = t_{\text{L}} - t_{\text{R}}$ is the left-right time difference in the bar and v_{scint} and t_0 are the calibrated scintillation speed and time difference offset respectively for that bar. The vertical position is simply the x coordinate of the bar. x_{mean}, y_{mean} and t_{mean} are formed for clusters by a TOT weighted average over all bars in a cluster. The projected position of the GEM track onto the hodoscope face is given as

$$\begin{aligned} y_{\text{proj}} &= y_{\text{FP}} + D_{\text{HODO}}\phi_{\text{FP}} \\ x_{\text{proj}} &= x_{\text{FP}} + D_{\text{HODO}}\theta_{\text{FP}} \end{aligned} \tag{4.47}$$

where D_{HODO} is the distance from the front GEM layer to the hodoscope. Fig. 4.16 shows the uncorrected linear relationship between y_{proj} on the x-axis and $\frac{1}{2}t_{\text{bar,diff}}$ on the y axis for a bar. The fit to this directly provides the v_{scint} (gradient) and $t_{0,\text{diff}}$ (intercept) for the bar. One can then perform iterative corrections and checks by constructing the same figure, with a corrected time difference on the y axis given by

$$t_{\text{diff,corr}} = t_{\text{diff}} + \left(\frac{2}{v_{\text{scint}}}(y_{\text{FP}} + D_{\text{HODO}}\phi_{\text{FP}})\right) - t_{0,\text{diff}}. \tag{4.48}$$

The difference between the hodoscope y position and the projected gem position, δy_{FP}, should ideally be a narrow distribution centred on zero, and allows us to directly infer the efficiency of the hodoscope-gem track matching. This is shown for all bars in Fig. 4.17 where the left shows how the difference between the track projection in the non-dispersive plane and the position measured in the hodoscope are heavily misaligned before calibration, and

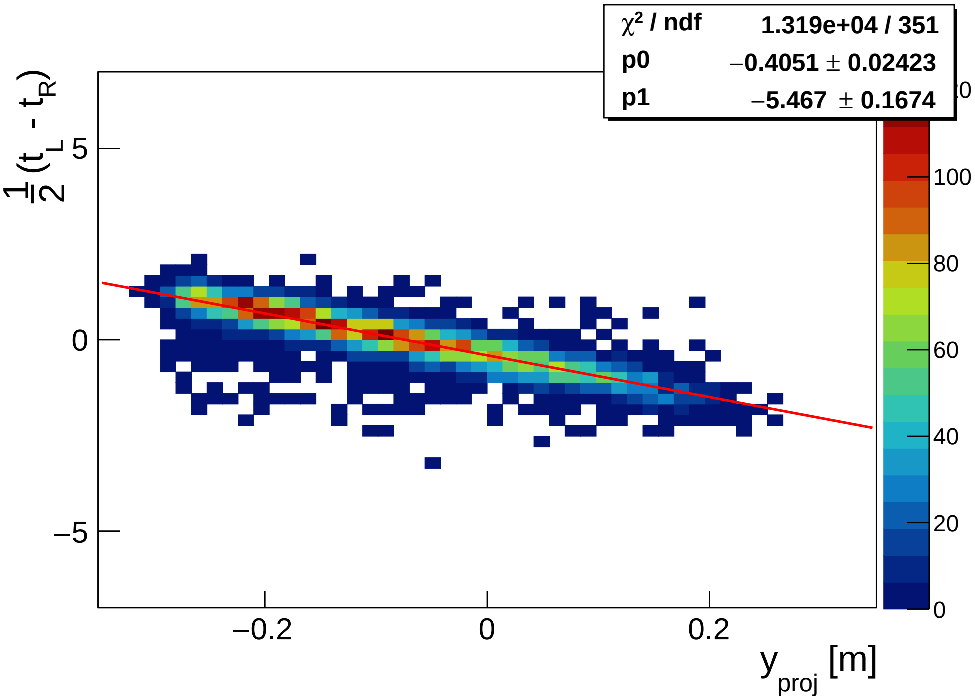

Figure 4.16: The linear relationship between the bar time difference and the y position projection from the GEMs, from which the scintillation speed and offset can be extracted from the linear fit in red.

the right shows that after calibration it is a narrow delta function around zero. This idea can be repeated in the vertical direction for δx(GEM-BBHodo), however there is no direct correction applied in the dispersive region. The position of a cluster in the dispersive plane is calculated as the TOT weighted mean of the x position of constituent bars. The x position of a bar is taken as the centre position of the bar itself.

Finally, clusters can be track matched using the TOT weighted mean positions. Track matching cuts of $|\delta y| < 0.15$ m and $|\delta x| \leq 0.05$ m are applied to all clusters, and if more than 1 pass, the cluster with the smallest δx is taken as the main physics cluster associated with the scattered electron. The resultant efficiency of track matching for all bars after all calibrations is shown in Fig. 4.18. Additionally shown are the resolution in $\delta x, \delta y$ and in t_{mean} and t_{diff}. The averages over all bars for each of the five quantities are given in each image. The hodoscope has been able to maintain a ratio of projected track x position to cluster mean x position (in the dispersive direction) of 0.97, and 700-800 ps intrinsic timing resolution. An analysis of multi-cluster events found that in the vast majority of cases, a negligible number of secondary clusters pass the track match cuts (13 out of 66797 events with at least 1 track). An analysis of multi-bar primary clusters found that 47.5% of clusters which were track matched had only a single bar and therefore 52.5% were multi-bar clusters. Mean time resolutions are calculated specifically from multi-bar clusters where the mean time is taken as $t_{\text{mean}} = t_{\text{mean},j} - t_{\text{mean},(j+1)}$ where j denotes the cluster maximum and $(j+1)$

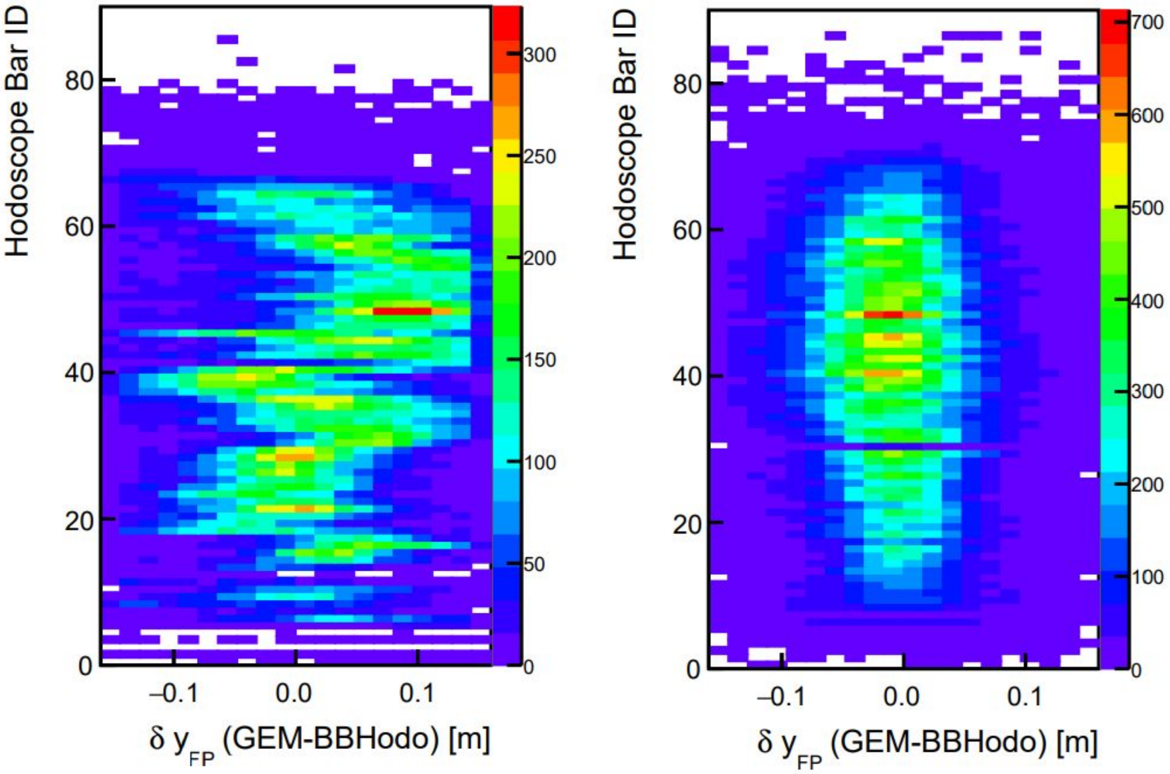

Figure 4.17: GEM to hodoscope track projection in the non-dispersive plane, before (left) and (right) after calibration of the scintillation speed and relative offsets.

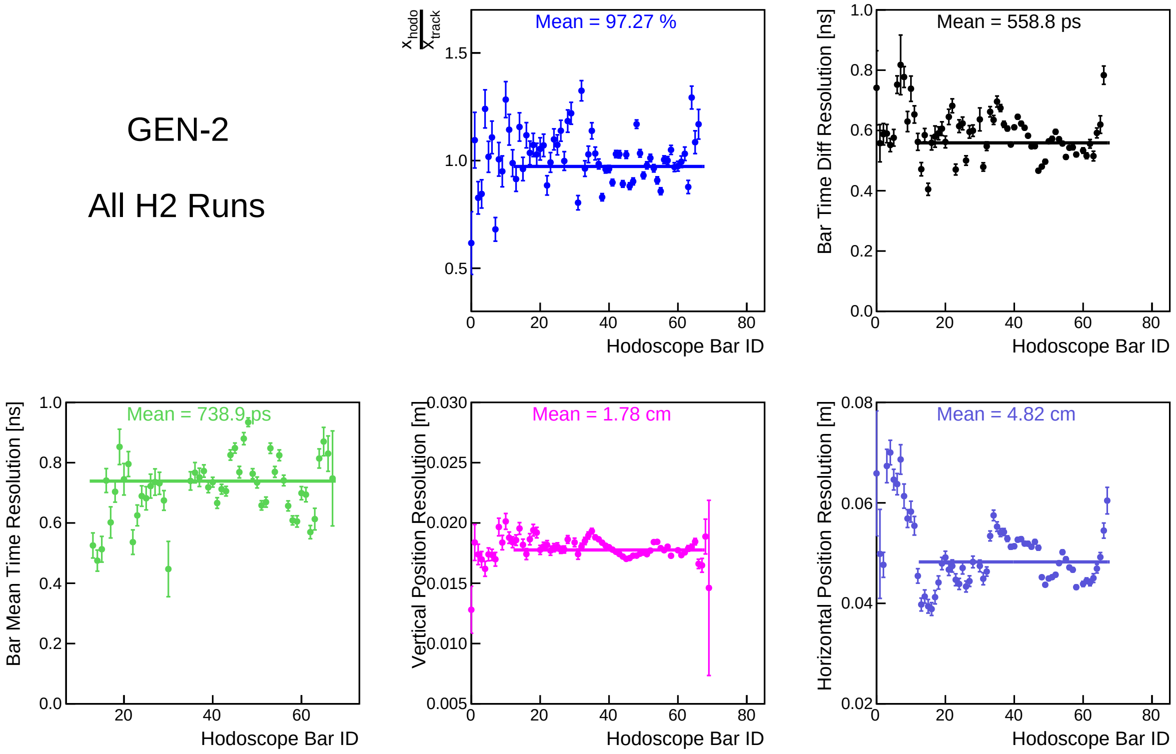

Figure 4.18: Summary of averaged resolutions for various quantities across all bars after calibration on GEN2 H_2 dataset.

is the second largest amplitude bar in the cluster. This quantity is completely free of any resolution bias introduced by the trigger or other external effects, and therefore gives a more direct measure of the effective timing resolution of the system.

4.5 Pass 2 Timing Analysis

4.5.1 Hodoscope

As briefly discussed, the timing resolutions seen in pass 1 data are insufficient in calculating useful nucleon time of flight and momentum. Being able to do this is important as in the end we would like to be able to cut around missing momentum, and missing perpendicular momentum for quasielastic event selection. A method for calibrating the timing hodoscope and hadron calorimeter timing information more rigorously is under exploration. This section will detail the general idea, keeping in mind that the full calibration is still under development.

The calibration formalism follows that of the Hall B TOF systems [227]. The definition of PMT times remains unchanged however now instead of sequential calibration procedures which are susceptible to double counting and hidden variable correlations, a simultaneous

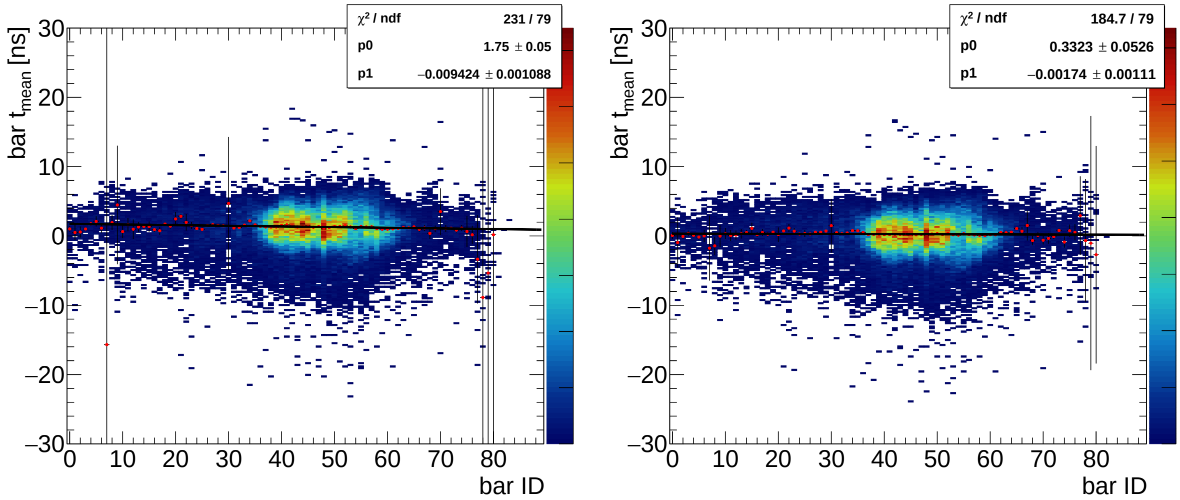

Figure 4.19: The bar mean time across all 89 bars of the timing hodoscope for (left) the pass 1 calibration method and (right) the new simultaneous fitting procedure. The mean of each slice corresponding to 1 bar is shown by the red markers. The fit is a first order polynomial to the means of all bars.

global fit of all parameters is performed. A χ^2 is constructed as

$$\chi^2 = \sum_{i=1}^{N} \sum_{j=i}^{\text{hits}} \left((t_{\text{PMT}} - t_{\text{eTOF}} - t_0 + p_{\text{TW}} t_{\text{TOT}} - \frac{d}{v_{\text{scint}}} \right)^2 , \tag{4.49}$$

where i sums over N events and j sums hits per event. Electron time of flight which was previously unused in the corrected time formation shown in Eqn. 4.44 is now calculated per event using a parameterisation of the track variables at the target. This is modelled from data generated with the elastic generator in the G4SBS simulation, using a 2nd order expansion in $\theta_{\text{tg}}, \phi_{\text{tg}}, y_{\text{tg}}, p$. The exact definition of these variables and their calculation is discussed in Sec. 4.6.

A preliminary attempt at extracting the hodoscope calibration parameters using this method of simultaneous fitting has been shown to be successful [228, 229]. The improvement in bar mean time alignment across all bars is shown in Fig. 4.19. The left plot is after pass 1 calibration and shows that the mean times are fairly well aligned, but an overall offset is still present. For comparison the same plot is shown on the right after the new calibration procedure described here. The new calibration demonstrates an improvement in alignment as seen by the improved χ^2 of the fit, and in the fact that both fit parameters are closer to zero, as would be expected for perfect alignment.

In order to construct the most accurate possible true start time of an event, the timing detectors must be calibrated with respect to the time that the electron bucket from the accelerator interacts at the target vertex. As described in Sec. 3.3.2, electron bunches are delivered to the Hall with a periodicity which depends on the operating frequency of the machine. If the machine is in three Hall running mode then the machine frequency is 499 MHz (2.004 ns bunches), and if all four Halls are active then the frequency is 249.5 MHz (4.008 ns bunches). The time of the RF pulse of the machine is directed into the v1190 and F1 TDCs at 1/40 (4.008 ns) or 1/80 (2.004 ns) of the RF frequency depending on the running mode. For GEN-II this was the latter, therefore the RF pulse time is recorded every 160.32 ns. The time sent to the TDCs is calculated as the time the closest beam bucket reaches $z = 0$ at the target. By subtracting this time from the calibrated detector times we can get the detector time relative to the vertex. In this case we also add back the trigger time which has a worse resolution and washed out the intrinsic resolution of detectors. For the hodoscope this takes the form

$$t_{\mathrm{HODO}}^{\mathrm{vz}} = t_{\mathrm{HODO}}^{\mathrm{mean}} + t_{\mathrm{trig}}^{\mathrm{v1190}} - t_{\mathrm{RF}}^{v1190} - \frac{z_{\mathrm{vz}}}{c} \tag{4.50}$$

where the last term is a correction to the beam bucket time based on the scattering vertex location. This quantity is formed for all bars individually, and can be seen for bar 44 in Fig. 4.20. The low statistics of a single bar can partially obscure the structure, but in general one can see by eye that there are peaks separated by around 2 ns. Before we can look at all bars together, we must find a way to align this to account for relative misalignments between bars.

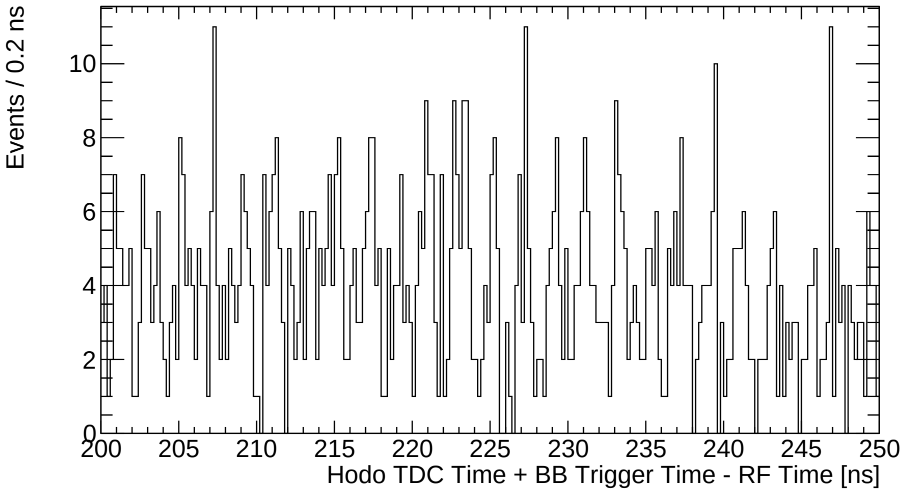

Figure 4.20: The detector time relative to the RF time for bar 44 of the hodoscope.

We can take the modulus of this time with the bunch time of 2.004 ns. This is shown for bar 44 in Fig. 4.21 where the black histogram is before any corrections. A Gaussian is fit around the peak of the uncorrected distribution and the mean of the fit is used as the RF bar correction which we will call $t_{\mathrm{RF}}^{\mathrm{bar}}$. The red histogram shows how the distribution aligns to zero after subtracting this RF bar correction prior to taking the modulus.

By aligning all bars like this we should eliminate any relative internal detector offsets to the RF time. After carrying out this correction, we can re-examine the distribution from

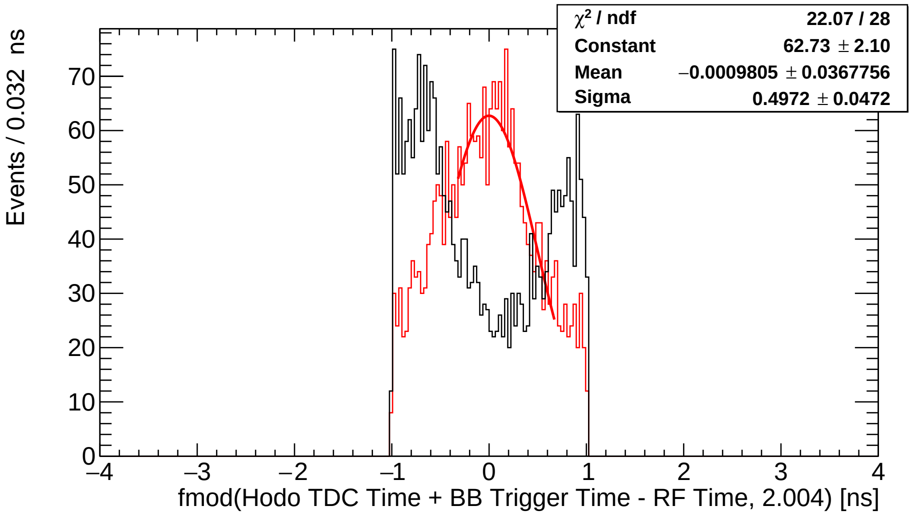

Figure 4.21: The modulus of the detector time relative to the RF to the bunch spacing of 2.004 ns for bar 44 of the hodoscope (Black) before aligning the peak offset and (red) afterwards.

Fig. 4.20 now for all bars. This is shown in Fig. 4.22. The peaks are now clearly visible, spaced ~ 2 ns apart with a resolution of around 500 ps. In order to maintain self consistency, HCal should now be calibrated in the same way to allow direct comparison.

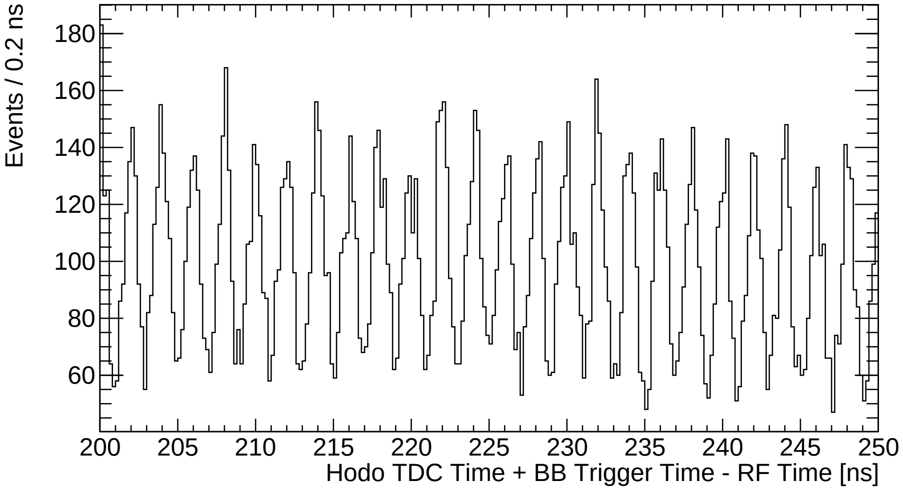

Figure 4.22: The detector time relative to the RF time for all bars in the hodoscope after each bar has been corrected for an RF offset.

4.5.2 HCal

The HCal ADC gain, ADC timing offsets and TDC timing offsets were calibrated for the first pass. However, no timewalk calibration was fully implemented for timing at this point. In the same vein as the new method of calibrating the hodoscope, a minimisation of factors which affect the HCal TDC time is under construction. Neglecting deflection of protons in the SBS magnet for now, the time of the signal from the scattered nucleon at HCal should be

$$t_{\mathrm{PMT}} = t_{\mathrm{NTOF}} + t_0 - t_{\mathrm{walk,HCAL}} \tag{4.51}$$

where t_{NTOF} is the time of flight of the nucleon from the vertex to HCal, $t_{\mathrm{walk,HCAL}}$ is the time associated with timewalk effects, expected to be a non linear function of the deposited energy; and t_0 is an arbitrary offset. Again a χ^2 can be formed,

$$\chi^2 = \sum_i^N \sum_j^{\mathrm{hits}} \left(t_{\mathrm{PMT}} - \left(t_{\mathrm{NTOF}} + t_0 + w_0 E + \frac{w_1}{\sqrt{E}} \right) \right)^2 , \tag{4.52}$$

where we have assumed a form for the timewalk as a function of the energy E to be $A \exp BE + C/\sqrt{E}$, and expanded the exponential in a power series to first order. The zeroth term of the power expansion is simply an offset and can be absorbed in t_0. The corrected time for hits is then constructed as

$$t_{\mathrm{PMT,corr}} = t_{\mathrm{PMT}} - \left((t_{\mathrm{NTOF}} - t_{\mathrm{NTOF0}}) + t_0 + w_0 E + \frac{w_1}{\sqrt{E}} \right) \tag{4.53}$$

where t_{NTOF0} is the central time of flight defined as the time of particles which hit the detector with a path length of exactly 17 m.

The nucleon time of flight is a more difficult quantity to parameterise. This is because since there is no tracking on the hadron arm (the SBS gems were not fully operational at all times during GEN), a power expansion in the track variables performed with simulation data in the same way as for the electron TOF, cannot be directly implemented in real data. As such for now we calculate the nucleon time of flight as an approximation using elastic kinematics and applying elastic cuts to the data. The path length is determined directly as the magnitude of the vector from the vertex to the HCal cluster mean position. $L_{\mathrm{N}} = \sqrt{|\vec{r}_{\mathrm{HCal}} - \vec{r}_{\mathrm{vz}}|^2}$. Elastic kinematics are used to predict the momentum of the final nucleon, which along with the nucleon mass can be converted to a beta factor $\beta = \frac{p}{\sqrt{p^2+M_p^2}}$. The TOF is then simply calculated as $t_{\mathrm{NTOF}} = \frac{L_{\mathrm{N}}}{\beta c}$ and the central TOF is calculated as $t_{\mathrm{NTOF0}} = \frac{D_{\mathrm{HCal}}}{\beta c}$ where as a reminder $D_{\mathrm{HCal}} = 17$ m. The difference $t_{\mathrm{NTOF}} - t_{\mathrm{NTOF0}}$ is then the corrective factor to account for spreads in TOF across the detector.

Equipped with a model of the nucleon TOF for now, we can solve the minimisation of the constructed χ^2. The leading edge times are shown against deposited energy for block

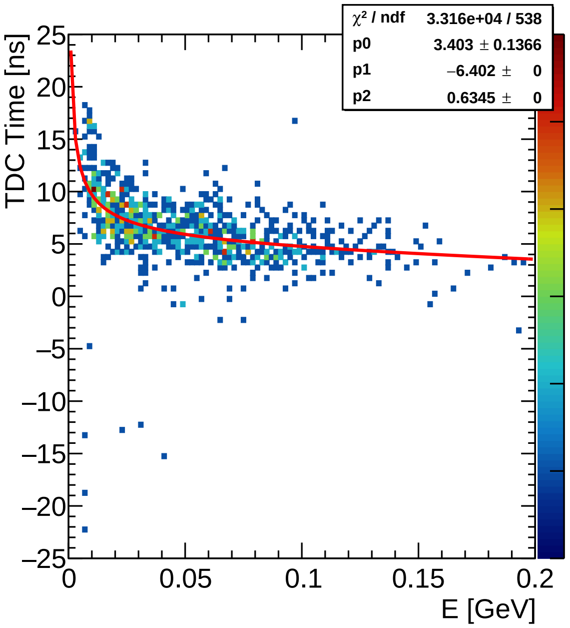

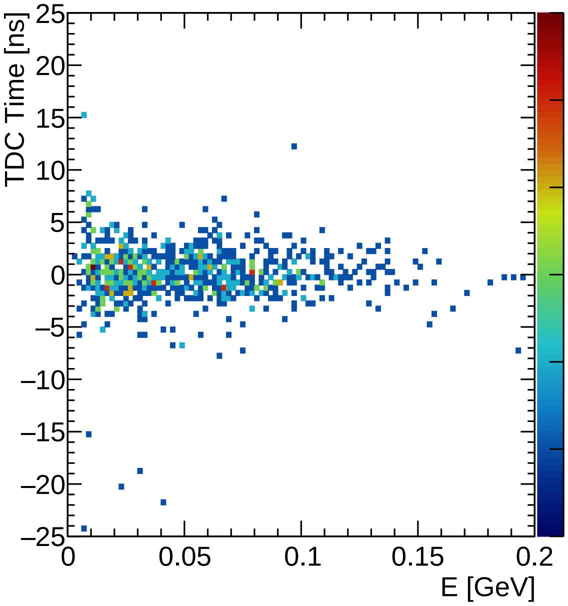

Figure 4.23: HCal TDC leading edge time vs deposited energy for block three (left) before calibration and (right) afterwards. The fit is a power series detailed in the text.

three in Fig. 4.23 in which the effect of timewalk can be clearly seen in the dependence. The red fit uses values fixed from the minimisation and demonstrates that this method correctly measures the timewalk.

As with the hodoscope we can observe how the mean time of the cluster changes across the detector using this calibration method. Fig. 4.24 shows the mean time of clusters in HCal against the primary block ID. The pass 1 calibration data is on the left, and it can immediately be seen that with these calibrations the mean times across the detector were misaligned. The fit across all blocks also indicates a noticeable linear dependence. In comparison the results of this new method are shown on the right. Now the times are much more aligned at zero, and the linear dependence has been reduced by a factor ~ 60 and is effectively negligible.

Efforts to extend this calibration of HCal to include RF corrections as was shown in the hodoscope case are ongoing. There are non-trivial difficulties in repeating this. Firstly the individual statistics available are small to begin with. After cuts these are even smaller, and once they are split between 288 channels in the detector, the number of events in a given RF distribution is so small that currently no offset can be extracted. Additionally the F1 TDCs which readout the HCal are missing RF information in a non-negligible number of events. This is under intensive investigation. Finally it is possible that the intrinsic resolution of the detector is not sufficient to resolve the RF structure in the same way as the hodoscope has demonstrated all together. However all possibilities must be fully explored before this can be confirmed. Nonetheless the improvement to the mean time alignments by correcting

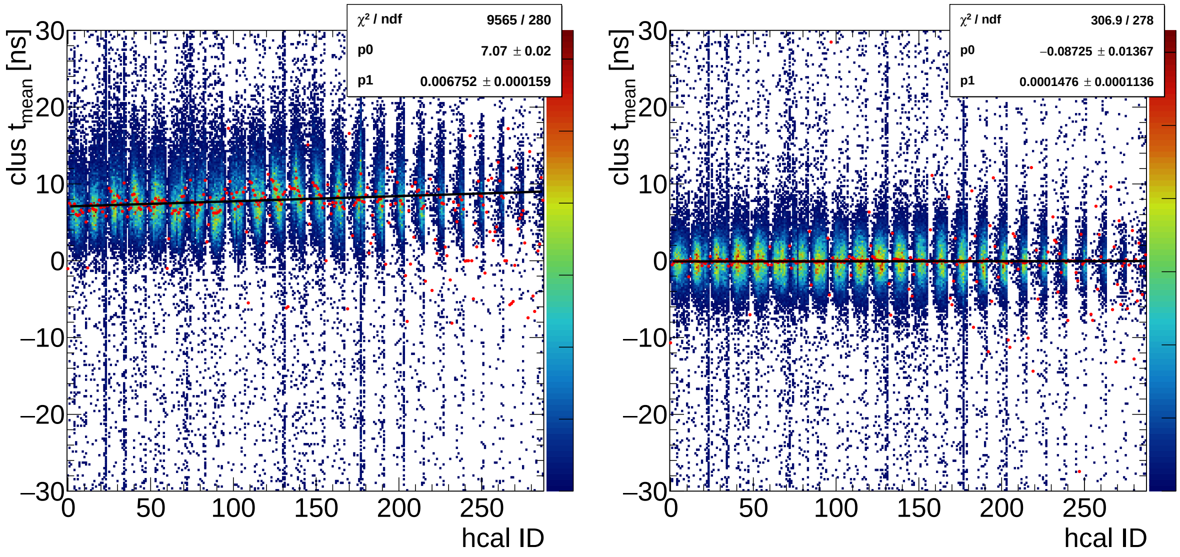

Figure 4.24: The cluster mean time in HCal vs primary block ID for (left) the pass 1 calibration method and (right) the new simultaneous fitting procedure. The mean of each slice corresponding to a block is shown by the red markers. The fit is a first order polynomials to the means of all blocks.

the timewalk, offset and nucleon TOF using this exploratory simultaneous fitting procedure have demonstrated that large improvements in the HCal timing resolution are possible.

4.5.3 Coincidence

Ultimately the goal of timing analysis is to reach the best possible coincidence timing resolution, in order to minimise the accidental background in the final event sample for physics analysis, and construct accurate momentum for the final state nucleons. This will involve taking the minimisation approaches which have been discussed for the hodoscope and HCal and constructing a single global fit for the complete coincidence time. Since this timing analysis is still in it's infancy, this step has not been performed yet. Nonetheless the individually calibrated times can still be used to construct a coincidence time, and the comparison before and after pass 2 analysis can be made. Fig. 4.25 shows the coincidence time taken as the HCal cluster TDC time - hodoscope cluster TDC time, before and after these efforts. A clear improvement in the resolution is present, demonstrated by the narrowing peak which is also aligned at zero. The resolution is taken as the width of a Gaussian fit. For the black distribution which represents the coincidence time from the old calibration procedure this is 1.9 ns. As visible in the figure, the resolution of the new distribution is 1.3 ns.

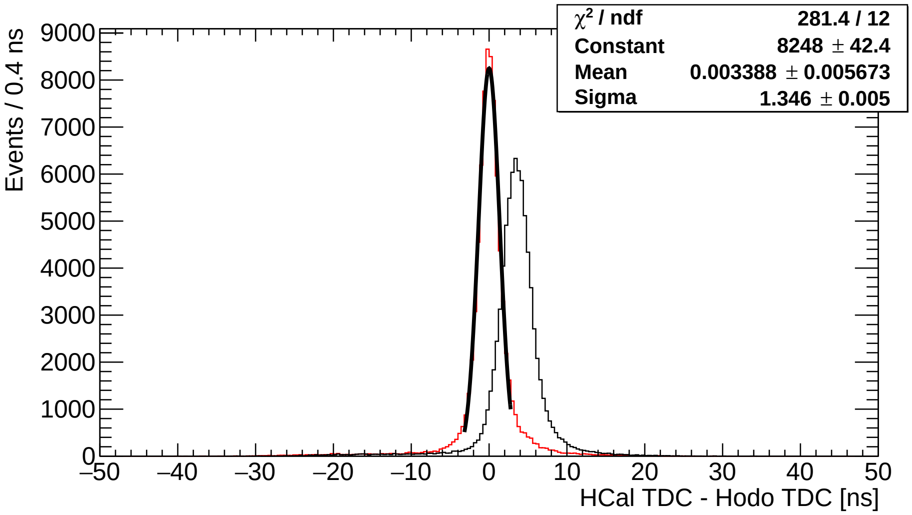

Figure 4.25: Coincidence time between HCal and the timing hodoscope before (red) and after (black) exploratory pass 2 timing analysis, for the H_2 dataset at kinematic setting 2.

4.6 Optics Reconstruction and Calibration

Bigbite measures the electron track's position and trajectory at the focal plane which has z_{fp} position roughly at the $\hat{z}$ position of the centre of the hodoscope. The quantities measured by the GEMs which describe the track in the focal plane are two position $(x_{\mathrm{FP}}, y_{\mathrm{FP}})$ and two angular $(\theta_{\mathrm{FP}}, \phi_{\mathrm{FP}})$ variables where each takes the definition within the transport coordinate system defined in Sec. 3.5. The variables in the target plane that we then reconstruct through the optics are the position of the interaction vertex y_{tg}; the in-plane and out-of-plane scattering angles $(\phi_{\mathrm{tg}}, \theta_{\mathrm{tg}})$ respectively; and the particle momentum relative to the central momentum of the spectrometer $\delta_{\mathrm{tg}} = (p_{\mathrm{tg}} - p_{\mathrm{c}})/p_{\mathrm{c}}$. In a traditional small angular acceptance spectrometer, the central momentum is the momentum for which a particle traversing the central axis of the magnet at $\theta_{\mathrm{tg}} = 0$ will be bent to be perpendicular with the central ray of the spectrometer. For Bigbite with a 750 A current yielding a field integral of 0.93 Tm^{-1} this corresponds to a central momentum of 1.94 GeV and bend angle of 10°. In reality, given the large acceptance of the SBS experimental setup, δ_{FP} corresponds to small deviations from the first-order model for the momentum reconstruction.

Additionally $\vec{v} = [x_{\mathrm{vz}}, y_{\mathrm{vz}}, z_{\mathrm{vz}}]$ defines the interaction vertex in the Lab frame. The position at the vertex in the dispersive plane x_{tg} is also a crucial part of the optics reconstruction, and is calculable iteratively from the vertex information. Therefore the target and vertex variables are related trigonometrically by

$$\begin{aligned} x_{vz} &= -y_{\text{beam}} - z_{\text{vz}}\cos(\theta_{\text{BB}})\tan(\theta_{\text{tg}}) = -x_{\text{tg}} \\ y_{vz} &= x_{\text{beam}} + z_{\text{vz}}\cos(\theta_{\text{BB}})\tan(\phi_{\text{tg}}) \\ z_{vz} &= \frac{-y_{\text{tg}}}{\sin(\theta_{\text{BB}}) + \cos(\theta_{\text{BB}})\tan(\phi_{\text{tg}})} \end{aligned} \tag{4.54}$$

For completion, but less useful, the projection of z_{vz} in the spectrometer coordinates is simply

$$z_{tg} = \frac{z_{vz}}{\cos(\theta_{\text{BB}})} \tag{4.55}$$

which completes the definitions and relationships between the (x, y, z) coordinates of the focal plane, target plane and interaction vertex.

Calibration of a spectrometer typically involves three core parts. First, relative alignment of the trackers and the magnet including position and angular offsets with a Single-Foil carbon target. Next the angle and vertex reconstruction are performed using a Multi-Foil carbon target to extract the coefficients of the optics expansion for the target variables. Finally the momentum can be calibrated using elastic H_2 data.

4.6.1 Alignment

A crucial first step in optics is understanding how the first chamber is aligned relative to the target. This is followed by relative alignment of subsequent chambers including the angular offsets. This procedure includes working out where the magnet is relative to the first tracker. A Single-Foil carbon run (or "carbon optics") run with no current to the spectrometer provides data on a single known vertex from which every track can be projected back towards mm precision. The method of extracting angular and position offsets is detailed in Sec. 4.4.1.

4.6.2 Angle and Vertex Reconstruction

The optics of the Bigbite magnet is a well studied topic [230] and a well understood and successful reconstruction method is an N^{th} order matrix element expansion [231, 232]

$$\Omega_{\text{tg}} = \sum_{i=0}^{i=N} \sum_{j=0}^{j=N-i} \sum_{k=0}^{k=N-i-j} \sum_{l=0}^{l=N-i-j-k} \sum_{m=0}^{m=N-i-j-l-k} C^{\Omega}_{ijkl} x^m_{\text{fp}} y^l_{\text{fp}} \theta^k_{\text{fp}} \phi^j_{\text{fp}} x^i_{\text{tg}} \tag{4.56}$$

where $\Omega \ni \{\delta_{tg}, y_{tg}, \phi_{tg}, \theta_{tg}\}$ and C^{Ω}_{ijkl} are the elements of the "optics matrix" - a set of coefficients corresponding to each target variable in a polynomial expansion of the target plane variables.

Calibration of the optics involves solving for the coefficients C^{Ω} for a given experimental

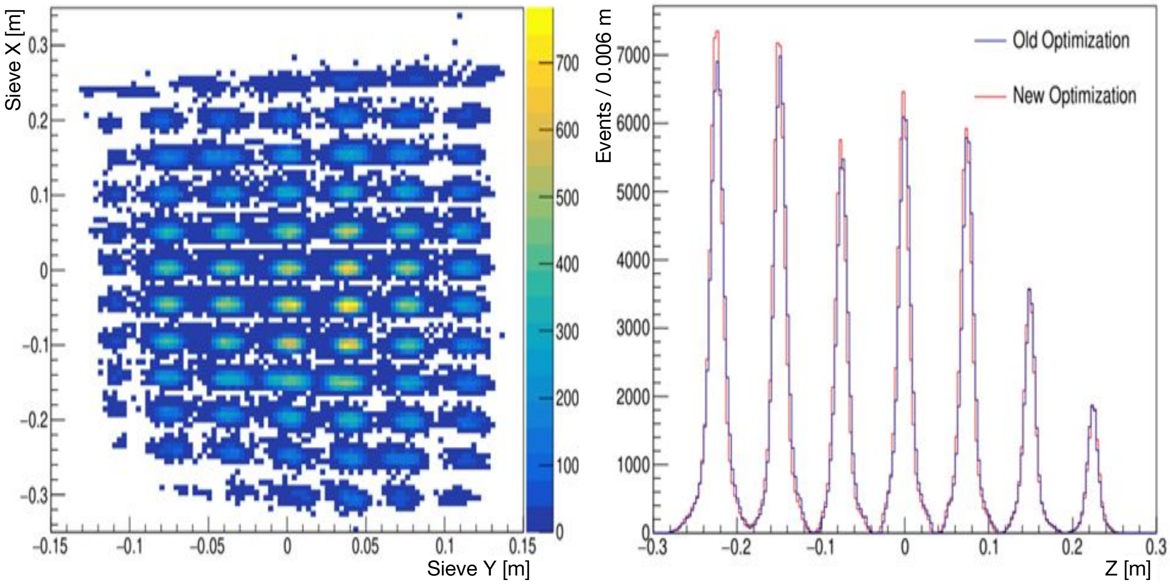

Figure 4.26: (Left) Reconstructed (x,y) position at the sieve plate using the optics expansion and (right) vertex z position of seven out of the eight total carbon foil positions, for kinematic setting 3. Figures from [195].

setup. As introduced in Sec. 3.8 data is taken on the carbon foil target, with a sieve plate placed in front of Bigbite. Since the sieve plate and target are surveyed, the true positions for the scattering vertex are known. The measured quantities using the expansion in Eqn. 4.56 can be calculated and compared to the known variables,

$$\begin{aligned}\Delta y_{\text{tg}} &= y_{\text{tg,meas}} - y_{\text{tg,exp}}\\ \Delta\phi_{\text{tg}} &= \phi_{\text{tg,meas}} - \phi_{\text{tg,exp}}\\ \Delta\theta_{\text{tg}} &= \theta_{\text{tg,meas}} - \theta_{\text{tg,exp}}\\ \Delta\delta_{\text{tg}} &= \delta_{\text{tg,meas}} - \delta_{\text{tg,exp}}\end{aligned} \tag{4.57}$$

A χ^2 can be formed over the $\Delta\Omega_{\text{tg}}$ variables, and the minimisation over the event sample yields new coefficients for the optics matrix. Fig. 4.26 shows the 2D (x,y) reconstructed position using the expansion, and the 1D z vertex position at the target which clearly highlights the seven of the eight individual foils. The eighth foil, which is not visible in this spectrum, is positioned furthest downstream of the beam at $z = 0.3$ m. Events arising from this foil are fully blocked by a downstream tungsten collimator. The old expansion overlaid with the new expansion indicates that the calibration method has produced more well resolved peaks.

Keeping in mind that $x_{\text{tg}}, y_{\text{tg}}$ and z_{vz} are related non linearly, this calibration method is best performed iteratively from some starting point to converge on appropriately accurate x_{tg} and optics coefficients. For kinematic settings 3 and 4 the starting point was optics coefficients obtained from the simulation. However for kinematic setting 2, since no carbon optics data was taken the simulation coefficients are used without further optimisation. This is assumed to be appropriate since kinematic setting 2 has the least background and will be the least sensitive to calibration issues.

4.6.3 Momentum Calibration

The momentum can be calibrated from elastic scattering on H_2 data. H_2 is free of the nuclear effect of Fermi smearing which broadens kinematic variable distributions. As such we can precisely calculate the expected momentum due to elastic scattering, using the elastic scattering formula

$$p_{\text{elastic}} = \frac{E_{\text{beam}}}{1 + \frac{E_{\text{beam}}}{M_p}(1 - \cos\theta_e)} \tag{4.58}$$

where θ_e is the scattering angle of the electron equal to $\theta_e = -\phi_{\text{tg}} + \theta_{\text{BB}}$ which is known to high precision due to the mrad level angular resolution of Bigbite. The reconstructed momentum can then be directly compared with the predicted and we can form the variable $\delta p = p/p_{\text{elastic}} - 1$ which measures how far away from prediction the reconstructed momentum for pure elastic scattering is. Naturally for sufficiently clean elastic selection, a narrow peak around zero indicates good reconstruction.

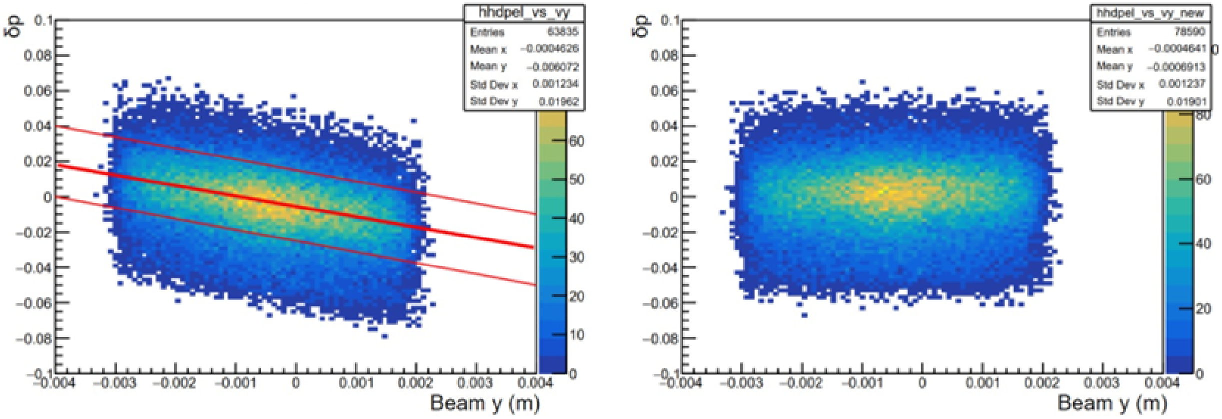

Figure 4.27: Elastic scattering from H_2 in Bigbite, showing the correlation between δ_p and y position of the beam. Figure from [218].

Using Eqn. 3.17 and 4.58, δp is formed and is shown against the beam y position in Fig. 4.27. Clearly before correction there is a negative linear correlation. Typically the momentum can be directly reconstructed to first order by

$$p = \frac{\delta_{\text{fp}}}{\theta_{\text{bend}}} \tag{4.59}$$

where δ_{fp} is extracted from the optics expansion as previously described and the bend angle is calculated for an event by

$$\theta_{\text{bend}} = \arccos(\hat{p}_{\text{fp,r}} \cdot \hat{p}_{\text{tg,fit}}) \tag{4.60}$$

where $\hat{p}_{\text{fp,r}}$ and $\hat{p}_{\text{tg,fit}}$ are the unit vectors of the track in the focal plane and target plane respectively given as

$$\begin{aligned} \hat{p}_{\text{fp,r}} &= \left[x_{\text{fp}}, y_{\text{fp}}, 1.0\right] \\ \hat{p}_{\text{tg,fit}} &= \left[x_{\text{tg}}, y_{\text{tg}}, 1.0\right]. \end{aligned} \tag{4.61}$$

However as shown in Sec. 3.8 δ is linearly correlated with θ_{tg}, and a linear fit to extract constants A, B was shown in Eqn. 3.17. The first order momentum is then given by

$$p' = A\frac{1 + (B + C\,d_{\text{Mag}})x_{\text{tg}}}{\theta_{\text{bend}}} \tag{4.62}$$

where C is a known parameter which encapsulates the offset caused by the distance from the target to the centre of the dipole magnet, d_{Mag}. The corrected momentum can then be calculated as

$$p = p'(1 + \delta) - (A_{\text{vy}} + B_{\text{vy}} y_{\text{beam}}) \tag{4.63}$$

where A_{vy} and B_{vy} are extracted from the fit in Fig. 4.27 and y_{beam} is the y-position of the beam which is derived in Sec. 4.3.2. We can define momentum components in the spectrometer frame as

$$\begin{aligned} p'_z =& p\sqrt{\frac{1}{x_{\text{tg}}^2 + y_{\text{tg}}^2 + 1}} \\ p'_x =& x_{\text{tg}} p'_z \\ p'_y =& y_{\text{tg}} p'_z. \end{aligned} \tag{4.64}$$

These can be rotated into the Hall coordinate frame accordingly, which provides the final calculated momentum components of the recoil electron in the Hall Coordinate System (HCS)

$$\begin{aligned} p_x =& p'_z \sin(\theta_{\text{BB}}) + p'_y \cos(\theta_{\text{BB}}) \\ p_y =& -p'_x \\ p_z =& p'_z \cos(\theta_{\text{BB}}) - p'_y \sin(\theta_{\text{BB}}). \end{aligned} \tag{4.65}$$

Chapter 5

Data Analysis

The goal of the E12-09-16 experiment is to extract the value of G_E^n at three new values of momentum transfer Q^2. This will be achieved at each kinematic setting by first measuring the form factor ratio G_E^n/G_M^n and then extracting G_E^n using existing world data fits for G_M^n. The form factor ratio will be extracted from a direct measurement of the transverse asymmetry in the double polarised elastic scattering of electrons and neutrons, using a fixed helium-3 (^{3}He) target.

The experiment ran at four kinematic settings. The first was a commissioning setting where no production data was taken. This chapter will present the preliminary analysis of the second kinematic setting, GEN2, corresponding to $Q^2 = 2.92$ GeV^2. At this current time the data has undergone one pass of calibrations, and it is known that further calibration work is required. As such physics results described here are purely preliminary with eventual final results due in the future. Where applicable remarks on future work will be made.

5.1 Analysis Flow

An outline of the complete analysis flow is shown by the flowchart of Fig. 5.1. As described in Sec. 3.9, raw data is written from the DAQ to binary encoded EVIO files. The Hall A analyzer is a CERN ROOT [201] based software which is used to decode the raw data files for experiments. Specific to SBS experiments the SBS-offline Root/C++ software was written by the SBS collaboration, which is an extension to the analyzer software. SBS-offline allows the decoded data to be reconstructed at a detector level into hits and clusters. A small number of events (typically around 50k) per run are replayed using the analyzer during the experiment, to produce rootfiles which are used for online monitoring.

Afterwards, the full statistics are reconstructed, and these rootfiles can be used for calibration of each kinematic setting. The new calibration parameters are put into the SBS-replay database, which is directly accessed by the SBS-offline software during the replay stage. Full calibration rounds are called “passes” where each pass of event reconstruction

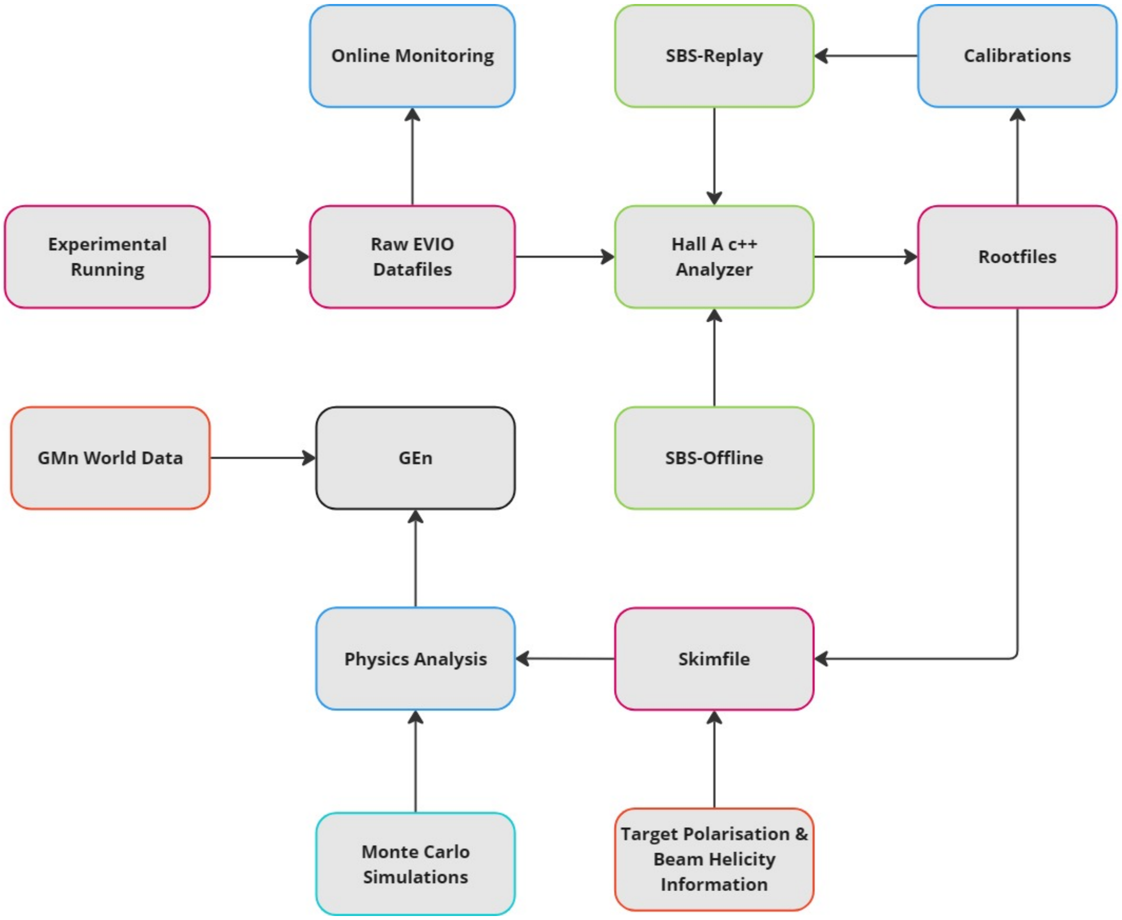

Figure 5.1: Flowchart of the complete analysis process of E12-09-016

corresponds to a complete replay of the production dataset for a kinematic setting through the analyzer software described in Sec. 3.10. While this data has not yet undergone a complete second pass of calibrations and replay, this analysis will explore the methods of cut optimisation, background analysis and final physics extraction using the first pass data, with the preliminary new timing calibrations implemented.

After sufficient calibration, data reduction cuts are used to “skim” the large volume of output production root files into a single more manageable file. At this stage all necessary kinematic variables and physics quantities are calculated and in the case that they are already present in the original rootfiles they are recalculated and checked for numerical validity. The skim also takes in target polarisation and beam helicity information in the form of time stamps at this stage. This file is now used for physics analysis, which includes event selection, cut optimisation, Monte Carlo (MC) simulation fitting and matching, and final physics quantity extraction.

5.1.1 Data Reduction Cuts

Software Cuts

The cut definition file for the initial replay usually contains basic pre-cuts designed to get rid of noise and channels which may have had data written as default values such as 0.0 or -1000 due to no hits. A finer reconstruction process then performs some basic physics reconstruction for kinematic variables from the primary track and clusters from the detectors. At this stage single arm track cuts on Bigbite are made. At least one track is required in Bigbite given by $N_{\text{track}} > 0$.

A minimum preshower amplitude is required by $E_{PS} > 20$ MeV. Originally this was in place to remove a large peak at very low energy corresponding to hits in the preshower which caused a trigger but often did not result in a reconstructed track. This was initially used as part of data reduction in more raw level calibration data replays, which didn't necessarily require a track in Bigbite. However it is almost redundant by the inclusion of at least one track, but nevertheless it is still present in the data.

Coincidence with HCal is then assured by requiring at least one good cluster reconstructed in the calorimeter, $N_{\text{clus}}^{\text{HCAL}} > 0$. Due to the high rates in HCal, this cut typically has little effect on the data size since the bottleneck on good events at this stage is typically reconstructing a track in Bigbite. A further cut is placed on the trigger bits variable which is a binary variable corresponding to the physical number of a given trigger. The coincidence trigger, detailed in Sec. 3.9.1 was the third trigger, labelled "ps3". The corresponding trigger bit (trigbits) value is therefore $2^{3-1} = 4$. Cutting on trigbits = 4 ensures an event triggered by the coincidence trigger, since for some runs the single arm Bigbite trigger was prescaled in to varying amounts for calibration purposes.

Post Analyzer Cuts

After the replay level cuts, further data reduction cuts can be applied to the skimmed data to further reduce the large backgrounds, and begin to isolate events from quasielastic (QE) electron scattering. All reconstructed tracks require by definition a minimum of at least three out of the five layers to contain good 2D hit combinations within the search region. This is naturally because forming a track between only two points leaves too many degrees of freedom, and a huge number of possible combinations. A "good gem track" cut in Bigbite can be applied to increase the likelyhood of the track being a real electron candidate. This takes the form $N_{\text{tr,hit}} > 3$, 4 or 5, as these are the physically possible values. For kinematic setting 2, this value is kept at 3, since the "real" electron signal is already fairly cleanly visible in other variables.

Recall that the track variables are reconstructed via magnetic optics detailed in Sec. 4.6. One variable of particular interest is z_{vz}, the $\hat{z}$ coordinate of the reconstructed vertex posi-

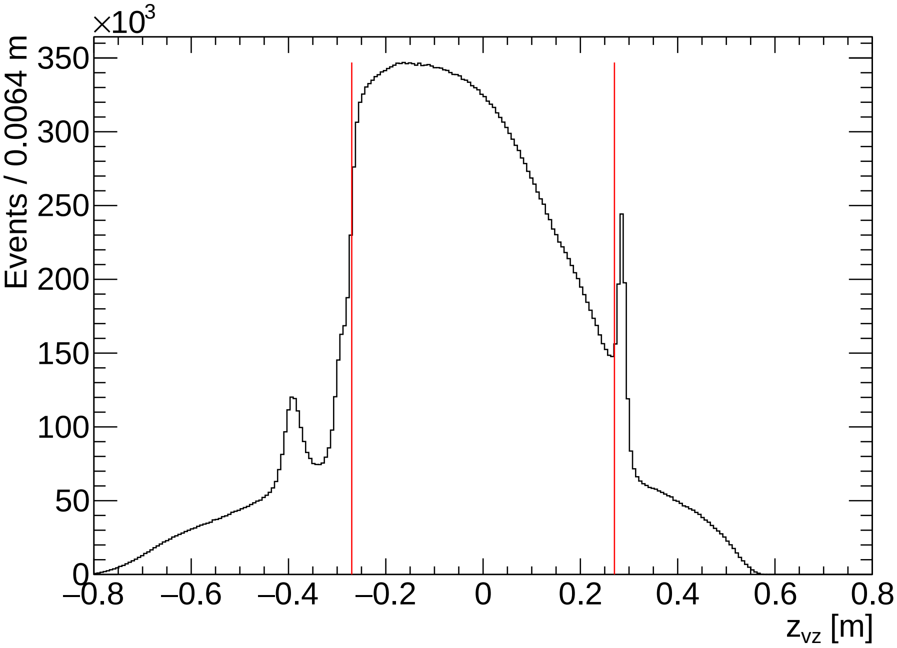

Figure 5.2: z coordinate of the reconstructed scattering vertex before any cuts.

tion in the target. Cutting on this is known as a "target z-vertez cut". z_{vz} is shown in Fig. 5.2 before further event selection, showing the acceptance of events across the full length of the target. The red lines indicate the cut which is applied $|z_{\mathrm{vz}}| < 0.27$ m. This eliminates scattering from the collimators within the windows of the 60 cm glass cell, which produce a large pion background. This is indicated clearly by the peak at +0.3 m in Fig. 5.2, corresponding to scattering off the downstream window. Scattering from the upstream window is less well pronounced in the distribution around -0.3 m, but it is assumed that the cut should be symmetrical about the centre of the target at $z = 0$ m. The additional peak which is visible around -0.4 m comes from scattering off the beryllium window which seals the end of the beampipe. Naturally this is also removed along with everything below -0.27 m.

Next further electron selection cuts on Bigbite can be made by looking at the energy distribution in the preshower calorimeter. At the momentum scale being considered, pions with a mass much greater than the electron produce a different energy distribution in the preshower than electrons. This is illustrated in Fig. 5.3 where a clear low energy pion peak can be seen around 100 MeV, distinguishable from the rest of the high energy distribution which corresponds mainly to electrons. The dashed red histogram is the preshower energy after the target z-vertex cut, which has approximately halved the pion peak while not reducing the yield at higher preshower energies by as much. The solid red line indicates a cut of $E_{\mathrm{PS}} > 200$ MeV, which removes much of the remaining pion background.

The energy measured in the shower calorimeter after cuts on the preshower and target vertex is shown in Fig. 5.4. This is less useful than the preshower distribution on its own, however as alluded to in earlier chapters the combination of the shower and preshower

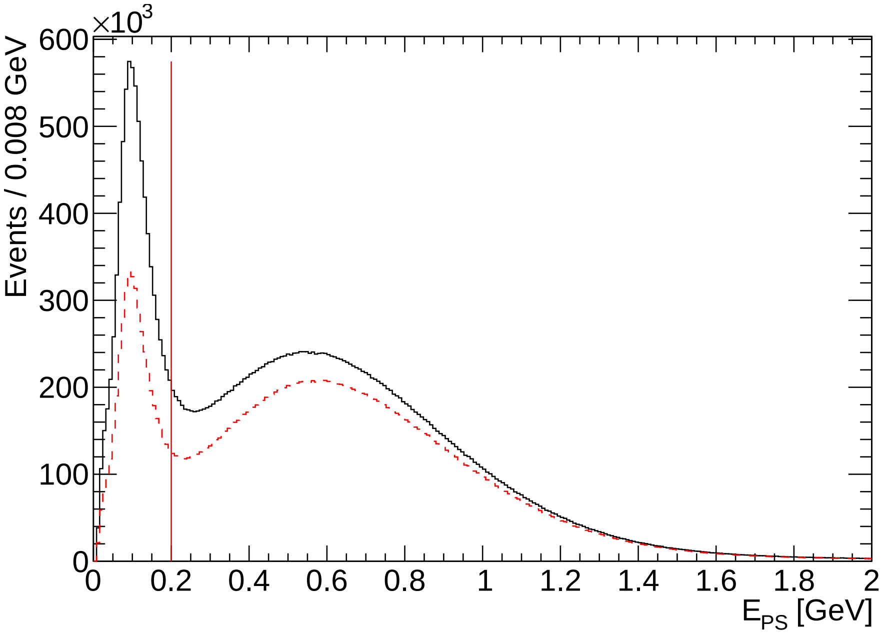

Figure 5.3: Preshower cluster energy distribution (black) before any cuts and (dashed red) after target z-vertex cut.

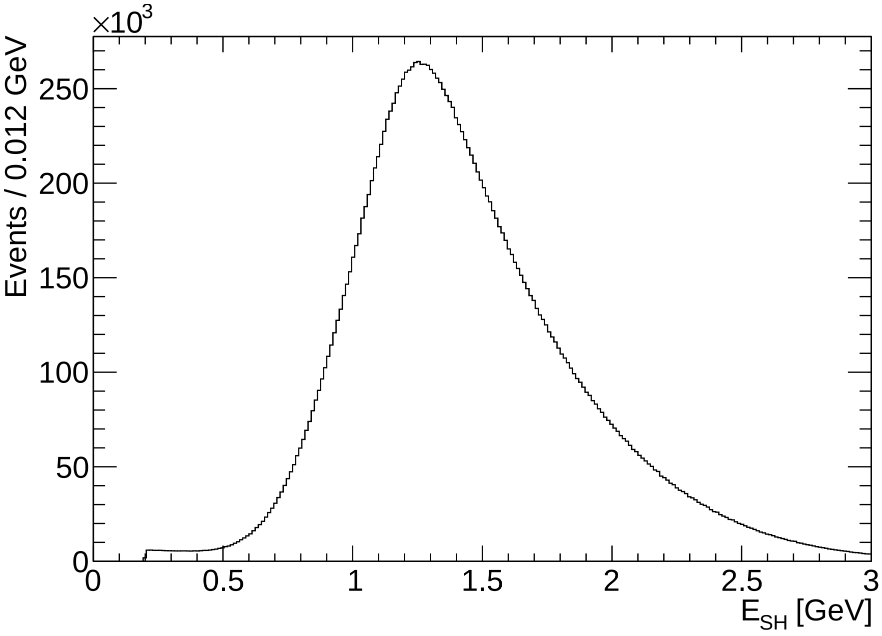

Figure 5.4: Shower energy distribution after preshower energy and target z-vertex cuts.

energies, i.e. the total energy measured by BBCal, can be compared to the track momentum as a tool for selecting electrons. Due to the tiny mass compared to pions, we expect the distribution of E/p to be close to unity. This is shown in Fig. 5.5 after cuts on the preshower energy and target vertex. The peak is fitted with a Gaussian which yields a mean of 1.10, suggesting that the calibration of the calorimeter energy reconstruction could possibly be improved for this data. Nevertheless a cut can be made based on the Gaussian width, which is indicated by the solid red lines at $\pm 3\sigma$.

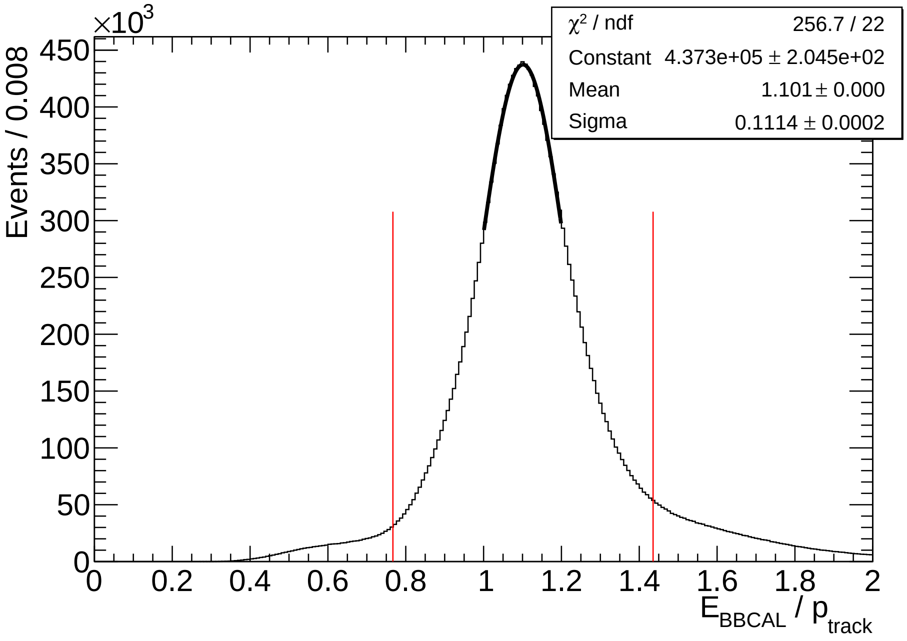

Figure 5.5: BBCal total reconstructed energy divided by track momentum after preshower energy and target z-vertex cuts. The red lines indicate a 3σ cut around the Gaussian peak.

After selecting on electron signals in Bigbite, we can begin to look at identifying nucleons in the hadron calorimeter. The first step is applying a cut on the minimum cluster energy in HCal. Fig. 5.6 shows the total sampled energy for clusters in HCal. A clear low energy peak is visible which mainly corresponds to out of time background noise. This was explored in Sec. 4.4.3, where it was shown that selecting on the timing peak suppressed this out of time background in hydrogen (H_2) data where elastic cuts had been made. Fig. 5.6 shows raw ^{3}He data after electron cuts in Bigbite in comparison, and the red line indicates an energy cut of $E_{\mathrm{HCal}} > 50$ MeV. This suppresses low energy background in HCal enough at first to allow further analysis. At a squared four-momentum of $Q^2 \sim 3.0$ GeV^2 the energy transferred by the virtual photon is around $\nu \sim 1.6$ GeV. This is the kinetic energy acquired by the struck nucleon, which is sampled by HCal. Assuming an average 11% sampling fraction based on the estimates from H_2 calibrations in Sec 4.4.3, this would result in an HCal cluster energy of around 170 MeV which is indicated by the dashed black line in Fig. 5.6. However, the relatively large ~ 30% energy resolution of HCal means that there are no practically useful physics based cuts which can be applied to the energy.

Further data reduction can be done by selecting on the track variables θ_{tg}, ϕ_{tg}, y_{tg}, p which are detailed in Sec. 4.6. However at this point these distributions have been cleaned up by prior cuts such that few events that appear to come from outside of the spectrometer acceptance are included. The four variables are shown after the discussed data reduction cuts in black, in Fig. 5.7. The distributions after complete QE cuts (discussed later) are

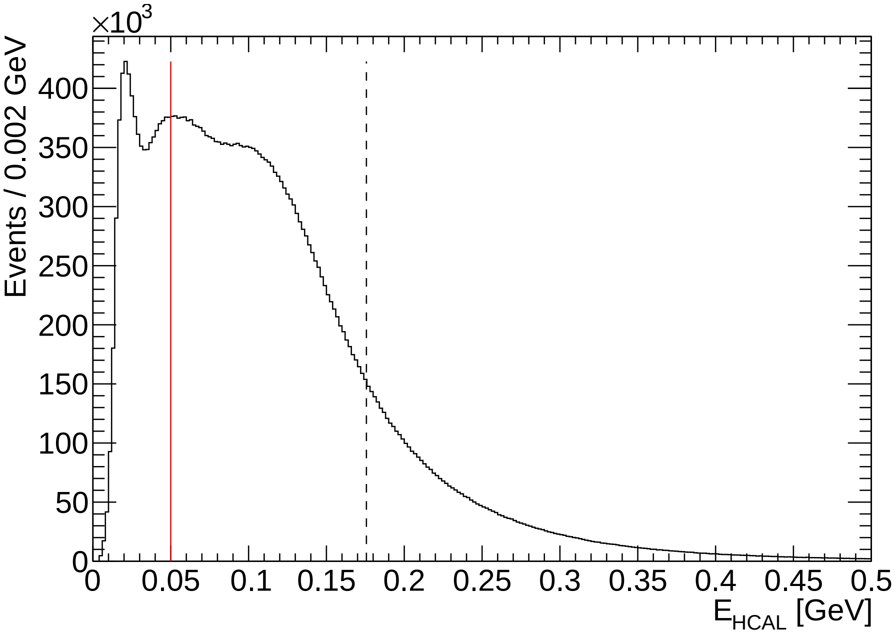

Figure 5.6: Energy sampled by the primary HCal cluster before any cuts. Red line indicates the HCal energy cut and the black dashed line indicates the average expected value of sampled QE nucleon energy.

shown in dashed red. We have jumped ahead here to indicate that the full QE cuts naturally select out the ranges of interest in these variables such that no direct cuts are necessary. This is particularly highlighted in the momentum distribution on the bottom right of Fig. 5.7, wherein after complete QE selection a Gaussian distribution around 2.7 GeV is visible, with most of the lower momentum inelastic events removed. The peak above zero in the θ distribution corresponds to the acceptance region of Bigbite only populated by neutron events in HCal. This extra acceptance comes as a result of the fact that protons at the same angles are deflected above HCal by the SBS magnet. In contrast the in plane angle barely changes between ± 0.1 rad. y_{tg} is highly correlated with z_{vz} as explored in Sec. 4.6. As such the previous z-vertex cut causes this distribution to already have sharply defined edges. After sufficiently reducing the data size to a manageable level, we are in a position to begin considering the kinematic reconstruction of all production runs and the physics analysis. However first we must identify all those runs which are of an acceptable quality.

5.2 Run Selection

Keeping track of run details is a large and important task, particularly in an experiment such as E12-09-016 which runs for months to years in total duration. The ideal "good" production run was one hour long, with relatively steady beam current, stable target polarisation, accurate and stable beam helicity information and stable detectors. The most common issues

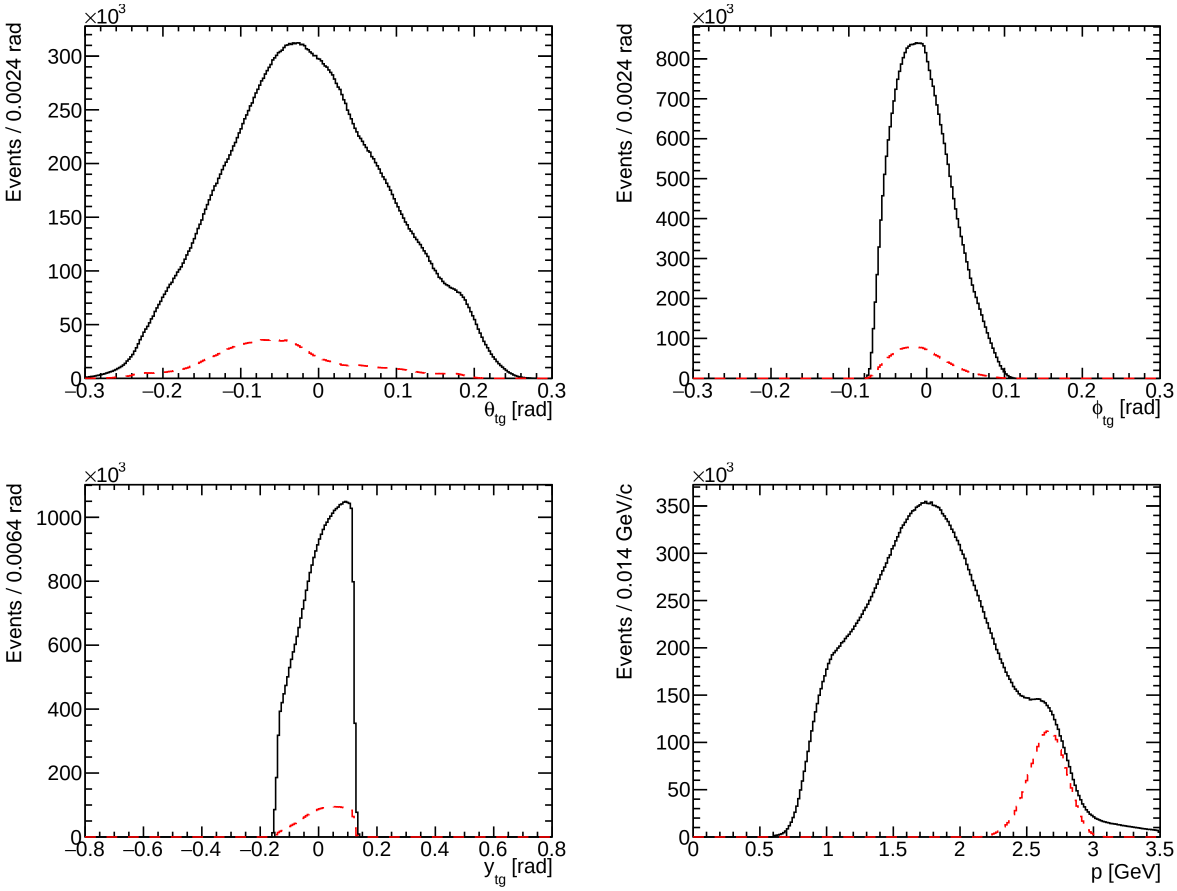

Figure 5.7: The distribution of (top left) $\theta_{\rm tg}$ (top right) $\phi_{\rm tg}$ (bottom left) $y_{\rm tg}$ (bottom right) p for (black) events after preshower energy, z-vertex and HCal energy cuts and (red dashed) further QE selection cuts. The relative scaling is arbitrary for the purposes of comparing the distribution shapes.

which could cause a run to be rejected are DAQ issues which result in a restart, or detector problems which could not be quickly corrected with a high voltage reset.

The first task in run selection is validating the complete run list for a kinematic setting. Runs are kept track of in an online spreadsheet by shift workers during the running of the experiment. While this is typically accurate, it is of course prone to human error and misjudgment of a "bad" run. Therefore all runs have been tested for a set of criteria to verify whether they are good or bad. First, all runs with the zeroth data segment missing, corrupted, or below a certain file size can immediately be rejected. Next the target being used at the time is checked against EPICs monitoring data and the automatic online Hall A electronic log book. Runs which were not production ^{3}He runs are categorised accordingly into Carbon Optics, Carbon Hole, Carbon Foil, Hydrogen Reference Cell, No Target, or Unknown/Bad in the case that the available information is unclear.

Good runs taken on the Helium-3 target are then checked for accumulated charge, target polarisation status and beam helicity status. Fig. 5.8 shows the average beam current

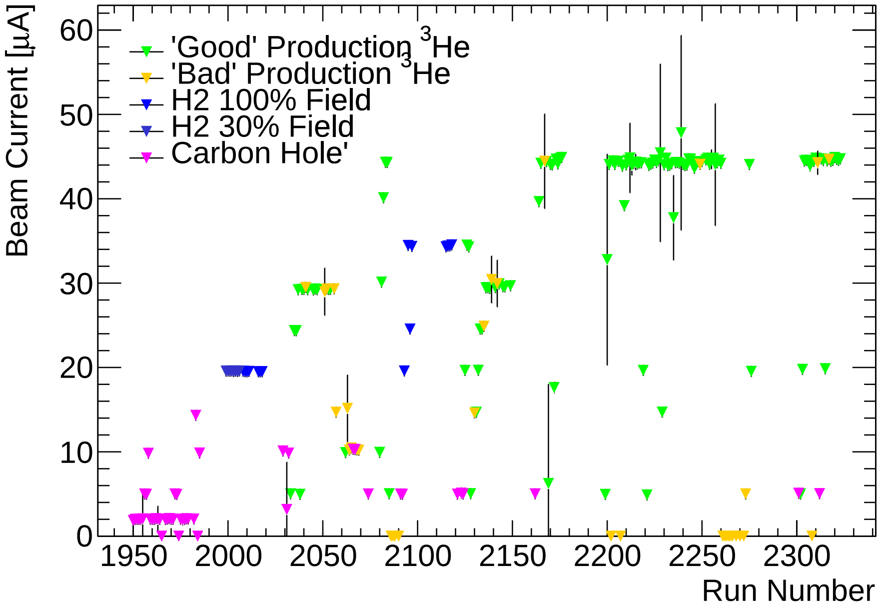

Figure 5.8: Average beam current for all runs in kinematic setting 2. Runs are colour coded by target type in the legend.

measured through EPICs for all runs (which were not immediately labelled as bad runs) in kinematic setting 2, separated by target type. It can be seen that most of the production runs that had been deemed "bad" were in fact so, as they have effectively zero beam current meaning no accumulated charge. However for a number of runs this was not the case and they were then checked for other criteria.

5.2.1 Target Polarisation

As kinematic setting 2 was the first production setting on the polarised ^{3}He target, there were a number of teething problems. Firstly the target polarisation at the beginning of the experiment was particularly low, and the losses due to NMR-EPR calibration were large, relating to a slow NMR sweep speed. As time passed the parameters relating to the polarisation spin-up of the target were fine tuned. Additionally, NMR data between 17-10-22 and 21-10-22 suffered from technical issues at a software and hardware level. One of the multi-channel lock-ins of the NMR software was producing no signal, and for a time an RF amplifier in the EPR coils was missing. This has the effect of rendering the calibration of this time period exceptionally more difficult. It is believed this may yet be corrected for in the future, but for now no polarisation data is available for these runs. This corresponds to all ^{3}He runs within the range 2033-2149. Note that not all runs in this range are production ^{3}He runs however. Other than this known issue, no runs are scrapped purely on the basis of low target polarisation. This is because the impact of event reduction on the statistical error in the final measurement is deemed to be larger than the impact of lower total polarisation on the systematic error.

The polarised target is introduced in Sec. 3.4.1 and the method of polarising it through Spin Exchange Optical Pumping is described in the same section. The calibrations for the NMR measurments in order to extract polarisation values are detailed in Sec. 4.2.3. The final values taken for the polarisation are achieved from time stamping events to a minute level interpolation of the NMR data. The unweighted acceptance averaged polarisation for events in the final QE sample is 37.9 ± 1.9%.

5.2.2 Beam Helicity and Polarisation

The beam helicity is unknown for the first 1000 events of every run (around 0.1% of the total in a 1M event run), while the helicity sequence is determined. After this the helicity is known for all events, except for a small number due to an undefined helicity state in the Pockels cell's transition period. These events with an unknown helicity are allocated a helicity value of 0. Recall that ±1 corresponds to ± helicity of the electron, as measured in the parity DAQ. However, it was found early on that a large portion of runs had a disproportionate number of events with unknown helicity, which ultimately revealed a larger issue in the helicity recording at the time. Runs found to have over 2% of events (after the first 1000) with an unknown helicity state are discarded. In some positive sense this also occurred between 17-10-22 and 21-10-22, meaning most of the affected runs are already unusable due to the aforementioned target polarimetery issues. So less overall production runs were lost. Fig. 5.9 shows the percentage of all events after the first 1000 which had unknown beam helicity (as indicated by a helicity state zero in the data stream), for all production runs which weren't immediately labelled as bad runs. The red dashed line indicates the 2% limit with any run above this being rejected. The method of measuring the beam polarisation is described in Sec. 3.3.3. The results of these measurements are shown in Sec. 4.3.1. The final result out of the single measurement at this setting will be quoted and used for the entire of kinematic setting 2. The beam polarisation is 84.1 ± 0.2%.

5.3 Kinematic Reconstruction

This section will detail the calculation of event kinematics, taking detector quantities reconstructed in SBS-offline and creating physics quantities to be used in analysis. The kinematic reconstruction of an event begins with the electron track in Bigbite. The momentum components and trajectory of the track allow the momentum transfer to the nucleus to be calculated, since the beam four-vector is well known. The momentum transfer to the nucleon with the assumption that it is at rest allows for the invariant mass of the final state to be calculated. The projection of the predicted final state nucleon four vector towards HCal

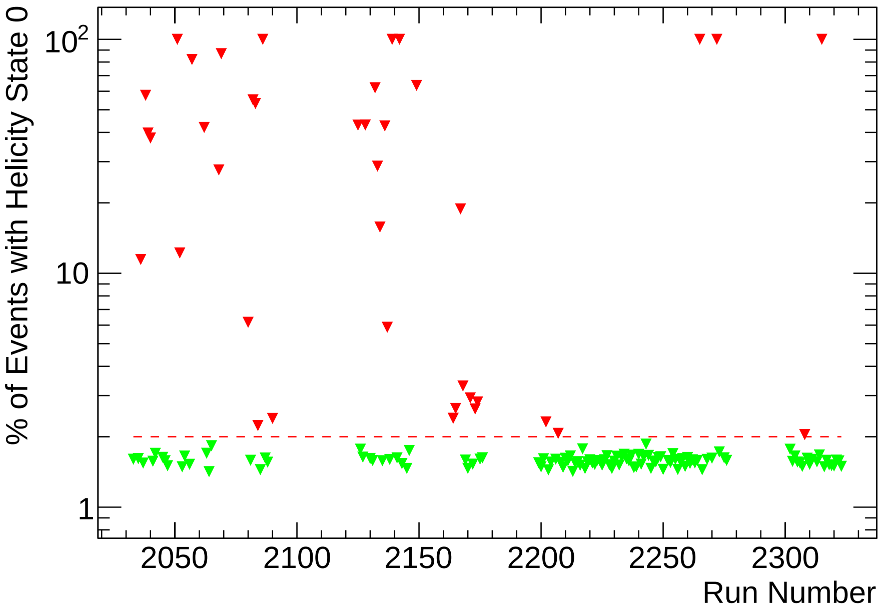

Figure 5.9: Fraction of events with unknown helicity state after the first 1000 for all production ^{3}He runs in kinematic setting 2.

allows us to create delta position variables in x and y, from the difference in the predicted position on the face of HCal to the measured position.

5.3.1 Squared Four-Momentum Transfer

We begin with the definition of squared four-momentum transfer between the incident beam electron and the target nucleon,

$$Q^2 = -q^2 = -(k-k')^2 = 2E_iE_f(1-\cos\theta_e), \tag{5.1}$$

where θ_e is the scattering angle of the electron, $E_{i(f)}$ is the energy of the incident (scattered) electron, $k = (0,0,E_i,E_i)$ is the beam electron four vector and k' is the reconstructed scattered electron four vector $k' = (p_x, p_y, p_z, p)$. The momentum components are those calculated from the tracking reconstruction discussed in Sec. 4.6. The energy of the scattered electron is directly calculable, neglecting electron mass m_e, as

$$E_f = \frac{E_i}{1+\frac{E_i}{M}(1-\cos\theta_e)} \tag{5.2}$$

where M is the mass of the nucleon. Substituting Eqn. 5.2 into Eqn 5.1 provides an alternative expression for momentum transfer which is purely in terms of the initial beam energy and target particle mass

$$Q^2 = \frac{2ME_i^2(1-\cos\theta_e)}{M+E_i(1-\cos\theta_e)}. \tag{5.3}$$

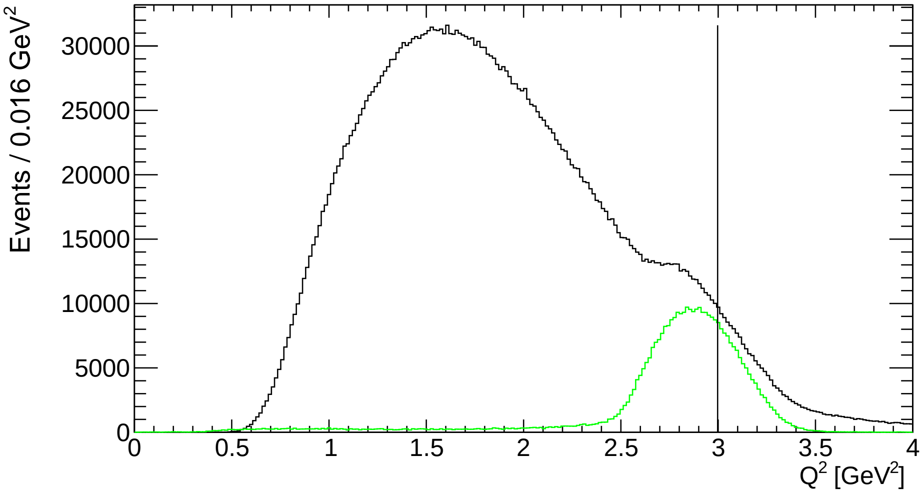

Figure 5.10: Momentum transfer squared from H₂ data before cuts (black) and MC simulation (green). The black solid line indicates the position of the central Q^2 of the kinematic setting.

The reconstructed momentum transfer is shown before any cuts in Fig. 5.10. The black line indicates the "central" value of Q^2 for kinematic setting 2. This is the value of momentum transfer at which the electron with energy E_{beam} would be scattered at exactly the angle θ_{BB}, given by Eqn. 5.3. In practice the distribution shown is not a perfect delta distribution on this value, as a result of the large acceptance of the spectrometers and detector effects. No cuts are made on Q^2. Instead QE cuts on the data naturally select events in a wide range of Q^2 as a result of the large acceptance of the experimental setup.

5.3.2 Nucleon Momentum and Invariant Mass

The true invariant mass W of the final state requires knowledge of the initial target particle momentum components, or the momentum components of the recoil nucleon. The momentum of the final state nucleon can be calculated from the sampled kinetic energy in HCal with proper calibration and knowledge of the sampling fractions in the blocks. However as discussed the energy resolution of HCal does not allow for a practically useful reconstruction, and so W must be calculated using the former method. For data taken on the H₂ target this is fairly trivial as there is no Fermi motion in the nucleus, and so the assumption that the target particle is at rest is a good one. This is not so true in the case of ^{3}He in which the struck nucleon does exhibit Fermi motion. However since we cannot directly observe the momentum of individual target particles, we must still make the assumption that the

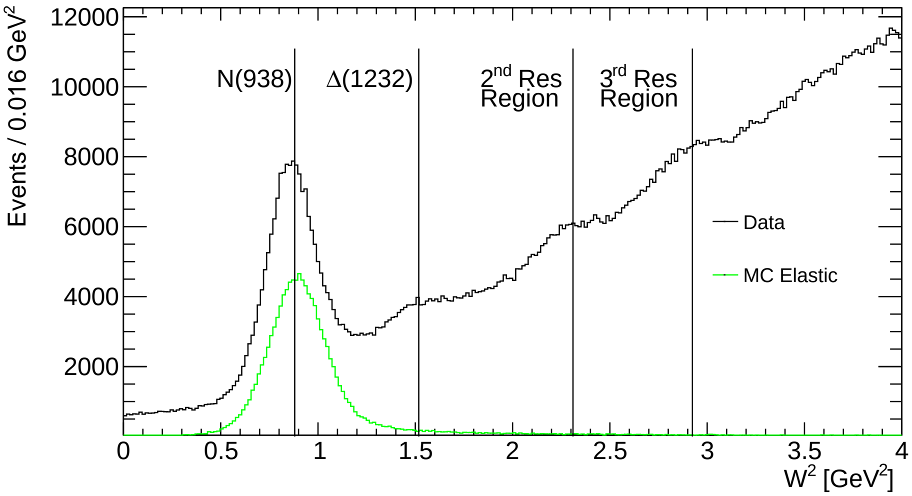

Figure 5.11: Invariant mass squared from H_2 data before cuts (black) and MC simulation (green). Black solid lines indicate the 1st, 2nd and 3^{3rd} resonance regions respectively, which correspond to the peaks in the distribution.

particle is at rest. However now the quantity calculated is technically a “quasi” invariant mass. Nevertheless we will continue calling W (W^2) the invariant mass (squared), for both H_2 and ^{3}He data, while keeping in mind the nuclear effects in the latter case.

The projected nucleon four-vector is calculated assuming single nucleon scattering at rest, as the sum of the rest nucleon (T^μ) and virtual photon (q^μ) states,

$$P^\mu = q^\mu + T^\mu, \tag{5.4}$$

where we have assumed a stationary target nucleon with a corresponding four-vector

$$T^\mu = (0,0,0,M). \tag{5.5}$$

The invariant mass squared is then able to be calculated as

$$W^2 = P^\mu P_\mu = (q+T)^2. \tag{5.6}$$

Additionally, the energy transfer via the virtual photon is defined as

$$\nu = E_i - E_f. \tag{5.7}$$

From this we can also calculate the predicted nucleon momentum,

$$p_N = \sqrt{E_N^2 - M_N^2} = \sqrt{(\nu + M_N)^2 - M_N^2} = \sqrt{\nu^2 + 2M_N\nu}. \tag{5.8}$$

The width of the reconstructed invariant mass distribution W^2 typically increases as a function of the momentum transfer Q^2, due to a combination of Fermi motion in the nucleus and general kinematic broadening at high values of Q^2. This is true for the same resolution of measured electron kinematics. Even if measuring elastic scattering from H_2 with no nuclear effects, there is large broadening of the W^2 distribution due to the kinematic magnification of the factors which determine W^2. This is clearly evident in Fig. 5.11 which shows the W^2 distribution for H_2 data in black, and MC simulation data for an H_2 target in green. The true value of the MC events is a delta function at the proton mass of 0.938 GeV, but after digitisation and reconstruction there is broadening of the distribution which is a near match to the data. The peaks above the nucleon mass in Fig. 5.11 indicate what are known as the 1^{st}, 2nd and 3^{3rd} resonance regions respectively. These correspond to known baryon resonances. The 1^{st} resonance region in particular, is dominated by the $\Delta(1232)$ resonance, which produces the majority of the irreducible backgrounds for this experiment.

5.3.3 Quasielastic Nucleon Position

The recoil nucleon is detected as a cluster in HCal. The energy weighted mean x and y position of the cluster provides the hit position of the nucleon, limited by the position resolution of HCal. Quasielastic kinematics can constrain the trajectory of the recoil nucleon assuming it is initially at rest and we can use the quantities already reconstructed to predict the trajectory,

$$\begin{aligned} \theta_N =& \arccos\left(\frac{z}{r}\right) = \arccos\left(\frac{E_i - E_f\cos\theta_e}{p_N}\right) \\ \phi_N =& \phi_e + \pi, \end{aligned} \tag{5.9}$$

where $\theta_{\mathrm{N}}, \phi_{\mathrm{N}}$ are the polar and azimuthal angles of the struck nucleon four-vector respectively, defined in the hall coordinates. The trajectory can then be projected towards HCal which provides expected positions on the face of the calorimeter

$$\begin{aligned} x_{\mathrm{expect}} &= D_{\mathrm{HCAL}}\tan(\phi_{\mathrm{N}}) \\ y_{\mathrm{expect}} &= D_{\mathrm{HCAL}}\tan(\theta_{\mathrm{N}}). \end{aligned} \tag{5.10}$$

where D_{HCAL} is the distance from the target to HCal which was 17 m for all of E12-09-016. By knowing both the measured and expected position of the nucleon at HCal, the difference between the two can be taken. This forms two variables which are paramount to this analysis,

$$\begin{aligned} \Delta x &= x_{\mathrm{HCAL}} - x_{\mathrm{expect}} \\ \Delta y &= y_{\mathrm{HCAL}} - y_{\mathrm{expect}}. \end{aligned} \tag{5.11}$$

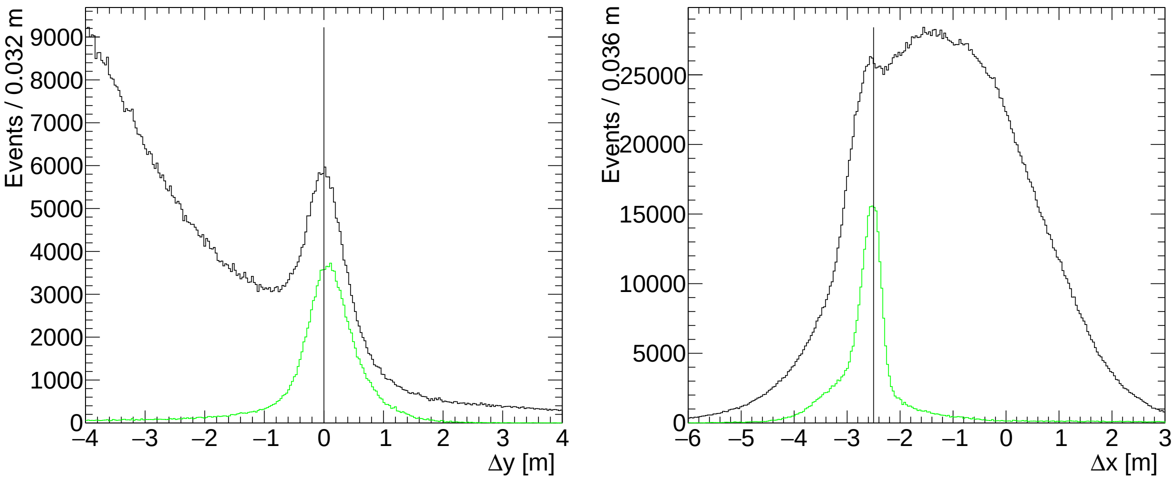

Figure 5.12: (Left) Δy and (right) Δx from H_2 data before cuts (black) and MC simulation (green). The black line indicates the QE peak in both distributions.

These variables are a measure of how far a particle deviates from the expected position in HCal if the scattering were purely (quasi) elastic, and as such can be used directly as a way to select out QE (^{3}He) and elastic (H_2) events. Both variables are shown reconstructed in H_2 data in Fig. 5.12. A Monte Carlo simulation is shown with arbitrary normalisation in order to compare the shape of the distributions. Δy shown on the left is a Gaussian-like peak centred on zero, with a large exponential background before any elastic cuts. Since this is a measure of the position deviation in the non-dispersive plane of the SBS magnet, the signal is expected to be centred on zero like this. Δx is illustrated similarly on the right hand side. This time the peak is offset by around 2.5 m, due to this being a measure of the position deviation in the dispersive plane of the SBS magnet. This means protons are bent upwards towards the top of HCal. Naturally then, the neutron peak reconstructed in ^{3}He production data will be centred on zero. This provides a method of separating QE protons and neutrons. Together the Δ position variables from HCal are crucial ingredients in the final physics analysis of the ^{3}He data.

5.4 Quasielastic Event Selection

Now that we have aptly reduced the data size, ascertained a list of acceptable production runs, and reconstructed the necessary kinematic quantities; physics based cuts can be used to select the desired final QE events sample. The cuts applied to the final sample for analysis of the asymmetries are listed in Tab. 5.1. This section will demonstrate that a relatively few number of cuts are required to select out the QE signal. Namely cutting on just W^2, Δy and Δx can be enough to have a fairly clean selection of QE events. This is particularly true at this kinematic setting, which is the lowest Q^2 value of the experiment, and as such experiences the lowest background rates relative to higher Q^2 kinematic points.

Table 5.1: Final cut values for quantities in QE event selection, after systematic analysis of the final result.

Description	Cut Value
Target z vertex	$\lvert z_{vz}\rvert < 0.27$ m
Preshower energy	$E_{PS} > 0.2$ GeV
HCal energy	$E_{HCAL} > 0.05$ GeV
GRINCH pion rejection	$\mathrm{Clus}^{\mathrm{size}}_{\mathrm{GRINCH}}$ >3 and Track Matched
Invariant Mass Squared	$\lvert W^2 - 0.88\rvert < 0.7$ GeV^2
HCal delta y	$\lvert\Delta y\rvert < 2.0$ m
HCal delta x	$\lvert\Delta x\rvert < 1.0$ m
Coincidence Time Peak	$\lvert t_{\mathrm{coin}} + 1.12\rvert < 6.19$ ns

All cuts in Tab 5.1 are fairly static with the exception of W^2, Δy and Δx. The vertex cut, preshower energy cut, HCal energy cut and GRINCH pion rejection cuts can all clearly separate distinct features in each corresponding distribution. However, for the former three variables, remaining backgrounds lay directly underneath the signal. This makes choosing the cuts less trivial. Additionally, W^2 and Δy are heavily correlated due to their inherent dependence on θ_e.

Fig. 5.13 shows the 2D correlations between each of these variables for production ^{3}He data. The top left in particular highlights the aforementioned correlation. The bottom plot shows the proton and neutron peaks aligned on Δy around zero, and separated in Δx as a result of the SBS magnet deflecting the protons but not the neutrons. The top right plot paints a similar picture, this time in W^2 instead of Δy. The red lines indicate QE cuts which have been found to suppress the inelastic backgrounds for W^2 and Δy while optimising the raw yield and resulting statistical uncertainty.

Since W^2 and Δy are strongly correlated, cutting on one of these variables significantly affects the other as a result. This is shown in Fig. 5.14, which shows each variable after a cut has been applied on the other. The exponential backgrounds in both distributions can be seen to have been largely removed by a single cut on the other variable, with respect to the uncut versions shown in Figs. 5.11 and 5.12 respectively.

We can inspect the distribution of Δy after these cuts, and see from Fig. 5.14 that the remaining signal is approximately a Gaussian peak around 0. This is expected since Δy is a measure of expected deviation in the non dispersive direction. The SBS magnet deflects protons upwards (in the lab frame), and so the Δy should be close to zero for QE recoil nucleons. This is a result of, and constrained purely by, elastic kinematics. The remaining cut on Δy indicated by the red lines removes a small part of the tails of the distributions, however the systematic analysis of these cuts found that a wider Δy and narrower W^2 cut ultimately yielded the best signal to background ratio and statistical uncertainty.

A similar story is told when looking at the resultant W^2 distribution, where we see that

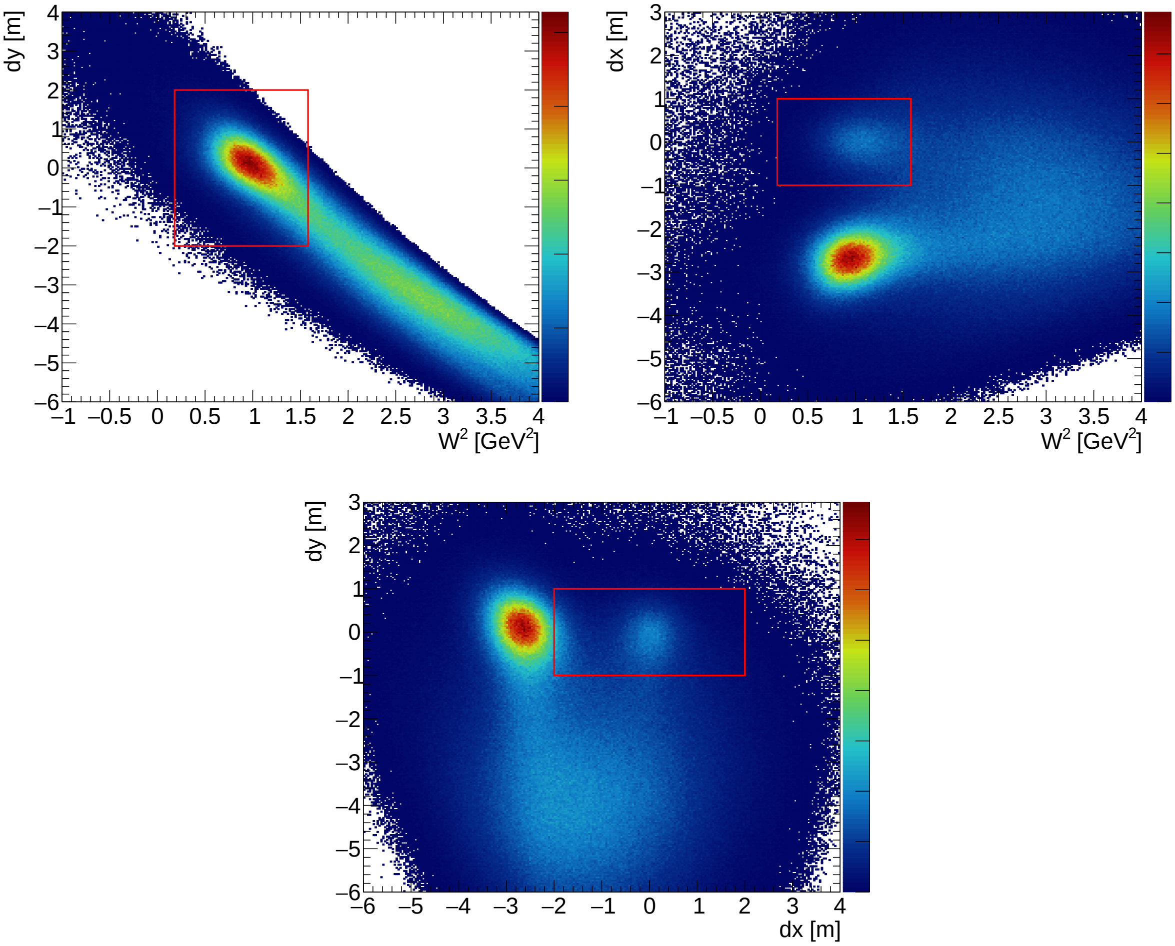

Figure 5.13: 2D correlations between Δy, Δx and W^2. Red lines indicate cuts listed in Tab. 5.1.

much of the inelastic and DIS background has been removed. The remaining signal is an approximately Gaussian peak around the nucleon mass squared with a residual shoulder of background. In reality the peak is slightly higher than 0.88 GeV^2 as a result of Fermi motion and general kinematic smearing. The remaining cut on W^2 indicated by the red lines will remove a large part of this background shoulder. Ultimately this combination of W^2 and Δy cuts were found to produce the smallest final uncertainty on the form factor ratio.

At this point two peaks can begin to be resolved in the Δx distribution as seen in the bottom plot of Fig. 5.15, which was previously completely dominated by background. The shape of the Δy is largely unchanged by the Δx cut, since as already discussed, the deviation of quasielastic nucleons in the non-dispersive direction of SBS is independent of charge and so selecting on the neutron peak of Δx simply reduces the overall yield of the Δy distribution. In contrast the shape of W^2 appears to change quite a bit. The height of the peak around the nucleon mass squared drops as expected, but now the shoulder which was visible appears to smear out the full distribution. This is because the proton peak which has now been removed was dominating the statistics, making the neutron mass peak more

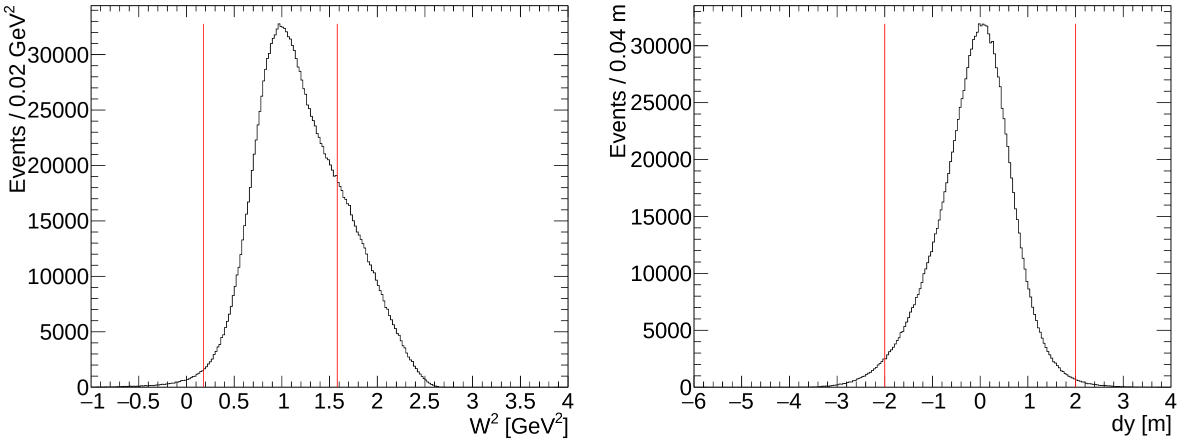

Figure 5.14: (Left) W^2 after Δy cut and (right) Δy after W^2 cut. Red lines indicate the remaining cut on each variable, listed in Tab. 5.1.

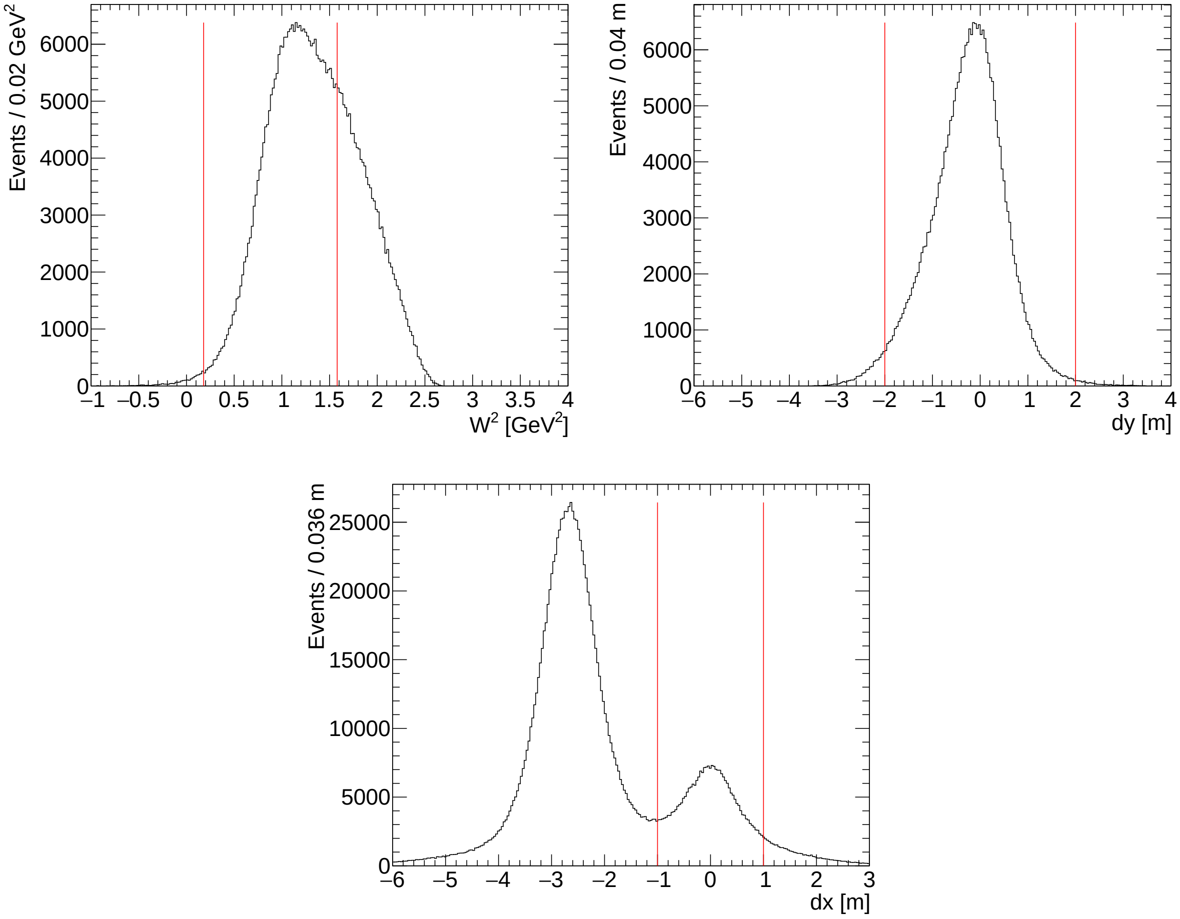

Figure 5.15: (Top Left) W^2 after Δy and Δx cuts and (Top Right) Δy after W^2 and Δx cut. (Bottom) Δx after W^2 and Δy cuts. Red lines indicate the remaining cut on each variable, listed in Tab. 5.1.

visible. Now the remaining neutron mass peak has a similar height with the large residual

$W^2 > 1.6$ GeV^2 background which is present inside the $|\Delta y| < 2.0$ m cut. However this is not a problem, because ultimately the narrow final cut around the nucleon mass squared removes the majority of this background, and the QE Δx distribution is cleanly visible.

Since the scattered electron and recoil neutron are measured in coincidence, then up to small deviations in time of flight the coincidence time between each spectrometer should be a fairly narrow distribution. We can select on this peak to further suppress background events from out of time accidental hits. The coincidence time after all of the discussed QE cuts is shown in Fig. 5.16, where the red lines indicate a 3σ cut around the Gaussian peak. The coincidence time is studied further in Sec. 5.6.

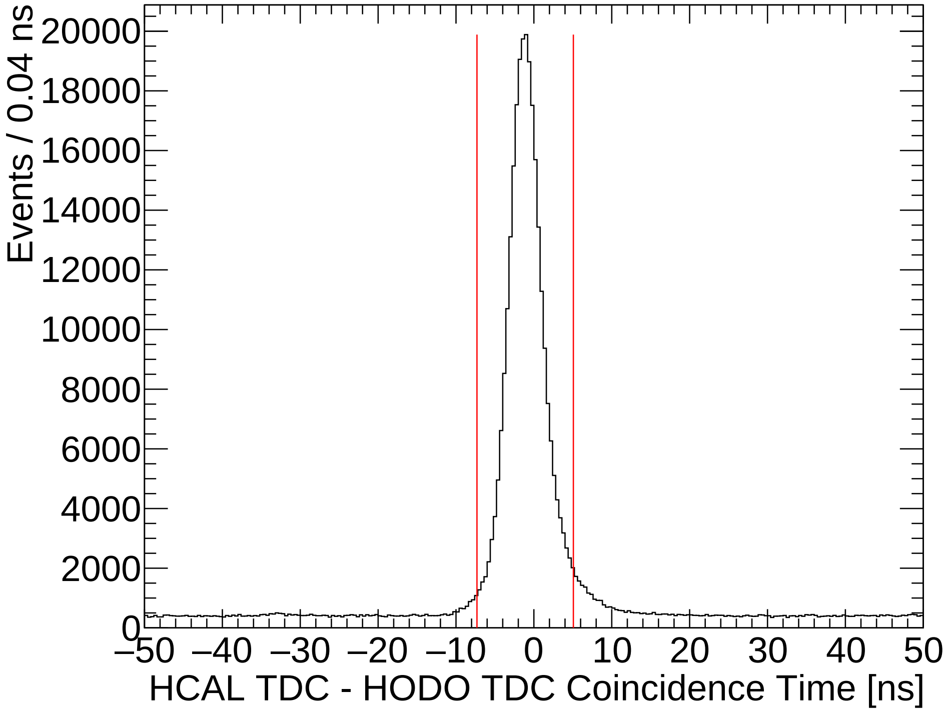

Figure 5.16: Coincidence time spectrum from HCal TDC - Hodo TDC after QE cuts.

The coincidence time, momentum transfer, invariant mass and nucleon position delta distributions are all shown in Fig. 5.17, for progressive event selection cuts, showing how each distribution changes for each cut.

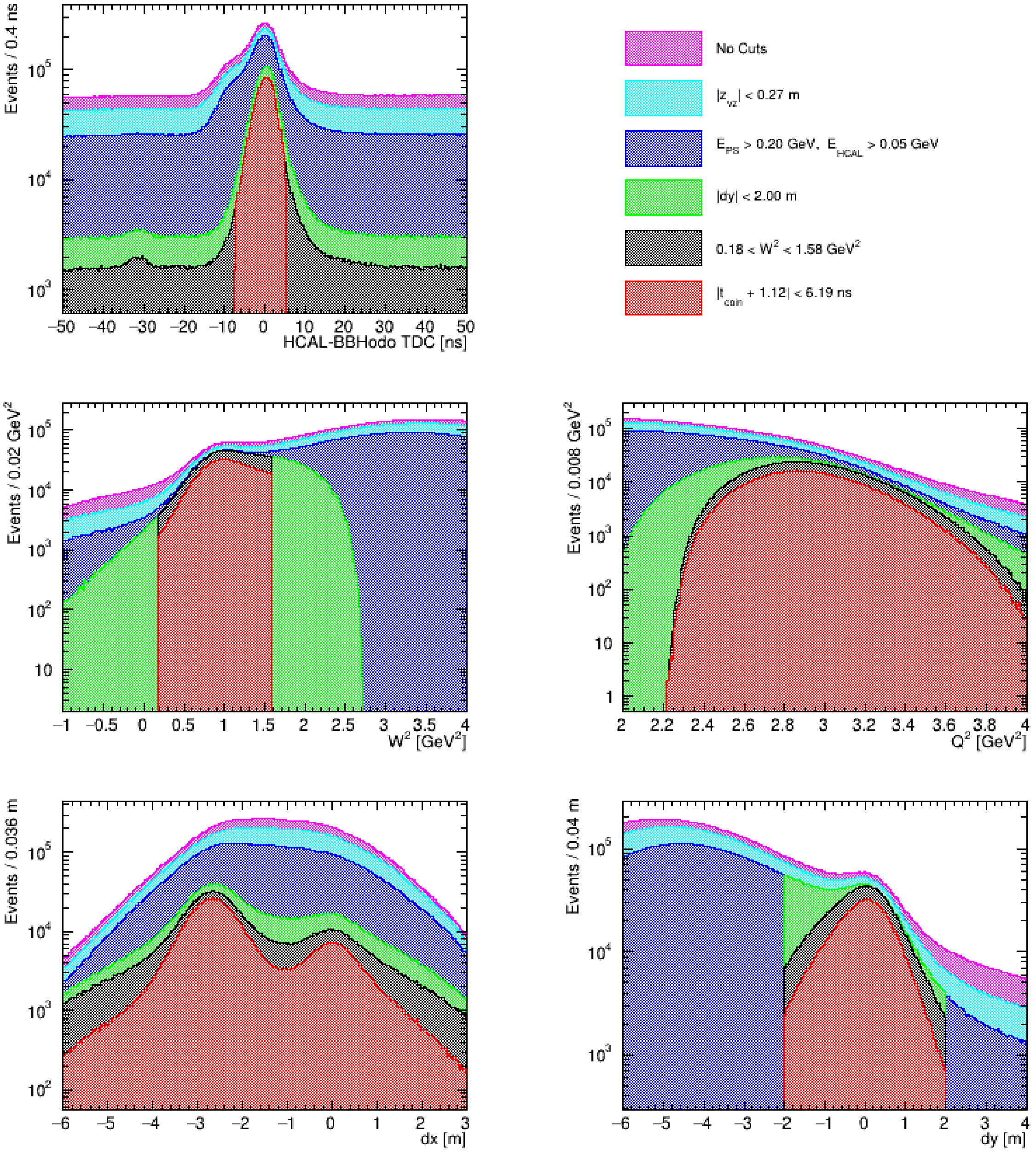

Figure 5.17: Kinematic distributions at various stages of the quasielastic cut selection. The final cut on Δx within which the signal and background fractions and asymmetries are calculated is left open. The gradual resolution of the double peak in Δx is illustrated in the bottom left plot.

5.5 Asymmetry Formalism and Dilutions

After we have selected our final QE event sample, we can begin to measure the raw counting asymmetry. This must then be corrected for backgrounds which remain after all cuts, and the various polarisations involved in the measurement. The raw asymmetry that we measure is defined as

$$A_{\text{raw}} = \frac{N^{+}_{\text{QE}} - N^{-}_{\text{QE}}}{N^{+}_{\text{QE}} + N^{-}_{\text{QE}}} \tag{5.12}$$

where $N^{+(-)}_{\text{QE}}$ are the number of events for +(-) helicity states in our final QE event sample defined by the cuts in Tab. 5.1.

Consider now a background source χ which contaminates our final event sample with a fraction f_χ. The asymmetry associated purely with this channel is

$$A_\chi = \frac{N'_{\chi_+} - N'_{\chi_-}}{N'_{\chi_+} + N'_{\chi_-}} = \frac{N_{\chi_+} - N_{\chi_-}}{N_{\chi_+} + N_{\chi_-}} \tag{5.13}$$

where $N'_{\chi_{+(-)}}$ are the +(-) helicity counts in an arbitrary "pure" background region of phase space, and $N_{\chi_{+(-)}}$ are the +(-) helicity counts for the background fraction f_χ, within the final QE signal cut region. These latter counts are not immediately separable from our desired signal, $N_{s_{+(-)}}$, the +(-) helicity count for the pure quasielastic neutron events. The sum of these is the total number of counts in the sample which pass all final QE cuts

$$N_{+(-)} = N_{s_{+(-)}} + N_{\chi_{+(-)}}. \tag{5.14}$$

If a set of cuts can be made such that this pure background can be isolated, then the associated asymmetry can be measured directly. In order to estimate the fraction of total events caused due to backgrounds, various techniques are employed, which are discussed throughout the remainder of this chapter. In particular numerous backgrounds have been simulated using the G4SBS MC software, alongside a simulation of the quasielastic channel, on the ^{3}He target. Fitting procedures were developed using the background and signal MC simulations in order to match the shapes of distributions (for example preshower energy and Δx) to experimentally observed spectra. The integral of a fitted background distribution within the final cut window provides a measure of the normalised counts in that background, N_χ.

The dilution fraction associated with a given background is then simply $f_\chi = \frac{N_\chi}{N_{\text{QE}}}$. This gives rise to the following asymmetry formalism

$$A_{\text{raw}} = PA_{\text{phys}}(1 - f_\chi) + f_\chi A_\chi \tag{5.15}$$

where A_{phys} is the asymmetry associated with the QE neutron signal of interest, and P encapsulates the polarisation product of the target, beam and neutron. By rearranging for the desired quantity we arrive at

$$A_{\text{phys}} = \frac{A_{\text{raw}} - \Sigma_\chi f_\chi A_\chi}{P_{\text{He}^3} P_{\text{n}} P_{\text{beam}} (1 - \Sigma_\chi f_\chi)} = \frac{A_{\text{raw}} - \Sigma_\chi f_\chi A_\chi}{P f_{\text{n}}} \tag{5.16}$$

where $\sum_\chi$ is the sum over all backgrounds χ with distinguishable A_χ, and $f_n = 1 - \sum_\chi f_\chi$ is the calculated QE neutron yield as a fraction of the raw yield.

5.6 Accidental Background and Prompt Random Subtraction

The majority of background events from all sources will manifest as "out-of-time" events in the coincidence timing spectrum. These random accidentals hits will sit underneath the main coincidence time peak. This can be seen clearly in Fig. 5.18, where the coincidence time between the HCal cluster TDC time and hodoscope cluster TDC time is a peak centred on -1.12 ns with a Gaussian width of 2.06 ns and a low lying approximately flat background extends out towards the positive and negative directions.

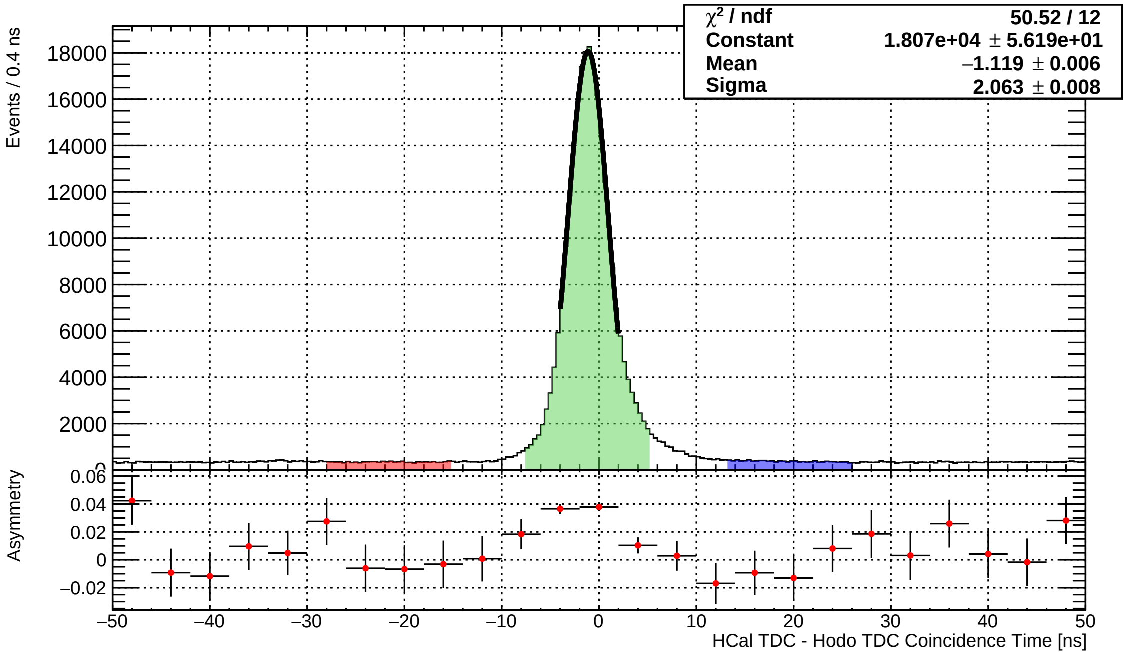

Figure 5.18: Coincidence time between the HCal cluster time from the F1 TDC and the Hodo cluster time from the v1190 TDC. 3σ cut on the signal region is indicated in green. 3σ width side bands around $\pm$ 10σ are shown in red and blue.

When a background is flat in this way, the total number of events in a given cut window is the same no matter where the cut is placed. Additionally assuming that random accidental events are fairly isotropic in every other variable means that the "background shape" of a given variable can be attained from looking at a side band of the coincidence timing spectrum. This is illustrated in Fig. 5.18 where the red (blue) shaded regions indicate a 3σ cut centred at -(+)10σ and the green shaded region is a 3σ cut around the coincidence peak. By forming a histogram of any other variable for the peak and one of these side bands, the former can be subtracted from the latter which leaves a background-subtracted signal for a chosen distribution. This is a process known as prompt-random subtraction, and will be referred back to as such when studied variables involved in other background estimations.

Fig. 5.18 also shows the measured raw asymmetry binned in the coincidence time spectrum along the bottom region of the plot. Due to the small number of events outside of the coincidence peak, the statistical error on any asymmetry bin is fairly large. However to within these errors there is little fluctuation. It is assumed to be appropriate to calculate the asymmetry associated with the accidentals background using more than just the events within a 3σ side band. We elect to take the asymmetry by counting all events outside of 5σ of the coincidence peak. The dilution and asymmetry associated with timing accidentals are $f_{\text{acci}} = 0.0441 \pm 0.0004$ and $A_{\text{acci}} = 0.0061 \pm 0.0032$ respectively.

5.7 Physics Backgrounds and the Δx Fit

The primary source of contamination in our data after prompt random subtraction comes from irreducible physics backgrounds. These are from production mechanisms which produce final states that can appear like quasielastic events, and make their way into the final event sample. The two main mechanisms of interest are photoproduction and electroproduction. Photoproduction occurs prevalently due to the production of Bremsstrahlung, quasi-real and real photons within the target cell, which then interact with protons and neutrons within the target. Electroproduction is the exchange of a virtual photon between the incident electron and target particle which we have already been considering.

Both of these mechanisms contribute to the overall exponential background which can be seen in the raw W^2 distribution shown in Fig. 5.11, through a plethora of channels. An example of channels which contribute to the background are the production of pions from $\Delta(1232)$ resonance decays,

$$\begin{aligned}
&\gamma^{(*)} n \to \Delta^0 \to \pi^0 n \\
&\gamma^{(*)} n \to \Delta^0 \to \pi^- p \\
&\gamma^{(*)} p \to \Delta^+ \to \pi^0 p \\
&\gamma^{(*)} p \to \Delta^+ \to \pi^+ n,
\end{aligned} \tag{5.17}$$

through electro- and photo-production. However since the complete final state of *any* multiparticle final state is not directly measured in HCal then there is no way to say what an event truly was. With this said, the exclusivity of trying to measure an electron in Bigbite, and a neutron in HCal through $\Delta x, y$ cuts provides an acceptable suppression on much of these events at this kinematic setting.

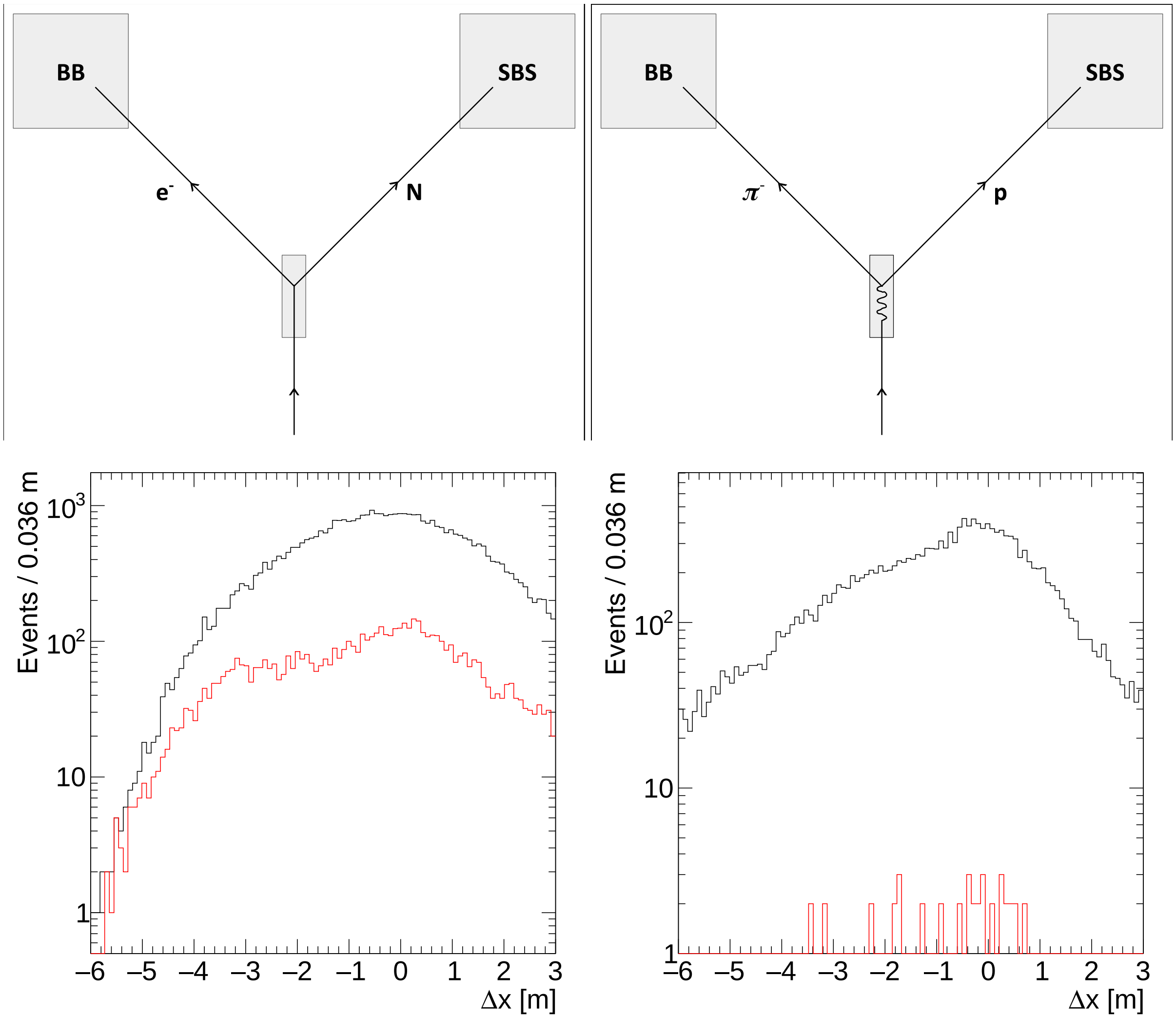

Figure 5.19: (Top) Illustrations of the dominant physics backgrounds which contaminate the final event sample and (bottom) Δx distribution for each background (black) before and (red) after QE cuts. (Left) Semi-inclusive electroproduction which results in an electron in Bigbite and (right) photoproduction which results in a pion in Bigbite.

While both electro- and photo-production mechanisms may result in the same intermediate and final states, the kinematics of each are different. Negatively charged pions which mimic electrons in Bigbite via photoproduction must result in a proton in the final state. If this is detected in HCal then Δx and Δy which would otherwise be clean elastic peaks, are now smeared by the inclusion of the pion and Δ masses in the kinematic calculations. In semi-inclusive electroproduction events wherein an electron is measured in Bigbite, the detected hit in HCal might have arisen from any sort of particle out of a plethora of processes including but not limited to Δ resonances. Again, the position residuals are smeared by the inclusion of intermediate state masses in the kinematics. The difference in Δx for each case respectively is shown in the bottom of Fig. 5.19.

Furthermore contamination due to neutral pions which travel towards Bigbite is considered negligible, since the photons out of the π^0 decay would not leave the required track in the GEM trackers. Positively charged pions might produce a neutron in the correct area of HCal, but will produce downwards bending tracks in which the up bending biased tracking algorithm will produce a non physical target vertex position for the scattering event, thus acting as a quasi-veto of sorts. An analysis of down bending tracks has been performed in the analysis of the E12-09-019 (GMn) dataset, and that work has not been replicated as yet for E12-09-016, but we will consider these events negligible due to the aforementioned reasons as well as coincidence quasielastic considerations. That leaves only π^- as possible candidates for misidentification as electrons in Bigbite. Therefore we focus on two distinct possibilities:

1 Events in which an electron is correctly measured in Bigbite, and some particle is detected in HCal, which passes all QE cuts, and lies directly under the signal Δx peak. We will approximate this full background as semi-inclusive inelastic electro-production.

2 Events in which a pion is misidentified in Bigbite, and a neutron candidate is detected in HCal, which passes all QE cuts. We will assume these are pion photo-production events.

5.7.1 Inelastically Scattered Electrons in Bigbite

Since the final helicity yields of the asymmetry are determined from the neutron Δx peak, it is sensible to approximate the inelastic background under the Δx distribution. Two methods have been identified to attain the shape of this background distribution. A fitting procedure is performed using simulation QE proton and neutron events, and the chosen background shape, to realise the correct normalisation of the background.

The first method which will be called the “anti-cut” method, involves performing “anti” cuts on W^2 and Δy while maintaining all other cuts the same, and looking at the resultant distribution in Δx. In principle by actively selecting events directly in the anti-cut Δy - “QE” W^2 region, this should give a Δx shape for purely inelastic events which leak into the QE sample, provided Δx is isotropic within the $W^2 - \Delta y$ kinematic space. In reality since the signal for this kinematic setting is fairly clean, and W^2 and Δy are correlated, the available statistics within the W^2 cut and Δy anti-cut ends up being very small. This complicates the eventual background fit. However, this idea is revisited later in the section in order to estimate the pure asymmetry in the inelastic region.

The second method is using simulation, wherein the background shape is taken directly from the G4SBS simulation using the “inelastic” generator, which was introduced in Sec. 3.11. This provides a sample of background events generated out of the Bosted-Christy inclusive electro-production model. The elastic generator is used to simulate a sample of purely QE events, and MC truth information allows us to explicitly separate the Δx peak from the elastic simulation into protons and neutrons measured in HCal. The Δx data distribution has undergone prompt-random subtraction detailed in Sec. 5.6 in order to avoid double counting backgrounds. The Δx distribution for all three MC simulations are weighted by cross section, and along with the data distribution undergo the full QE cuts. A chi-squared minimisation fitting procedure is developed in order to match the combination of the MC proton, neutron and background to the data, with the form

$$C_{\mathrm{sim},i} = N(C_{\mathrm{QE,p},i} + RC_{\mathrm{QE,n},i} + N_{\mathrm{bg}}C_{\mathrm{bg},i}) \tag{5.18}$$

where C are the counts in each bin for the respective Δx histograms (QE proton, QE neutron and background), and N, R and N_{bg} are the fit parameters. R controls the relative scale of the neutron peak, N_{bg} controls the relative scale of the background distribution and N is a global normalisation for the full fit. The results of this fit to the data Δx distribution after QE event selection and prompt random subtraction is shown in Fig. 5.20. The blue distribution is simulation protons, green is simulation neutrons, magenta is the inelastic background simulation and red is the complete fit to the data in black. The complete fit noticeably fails to

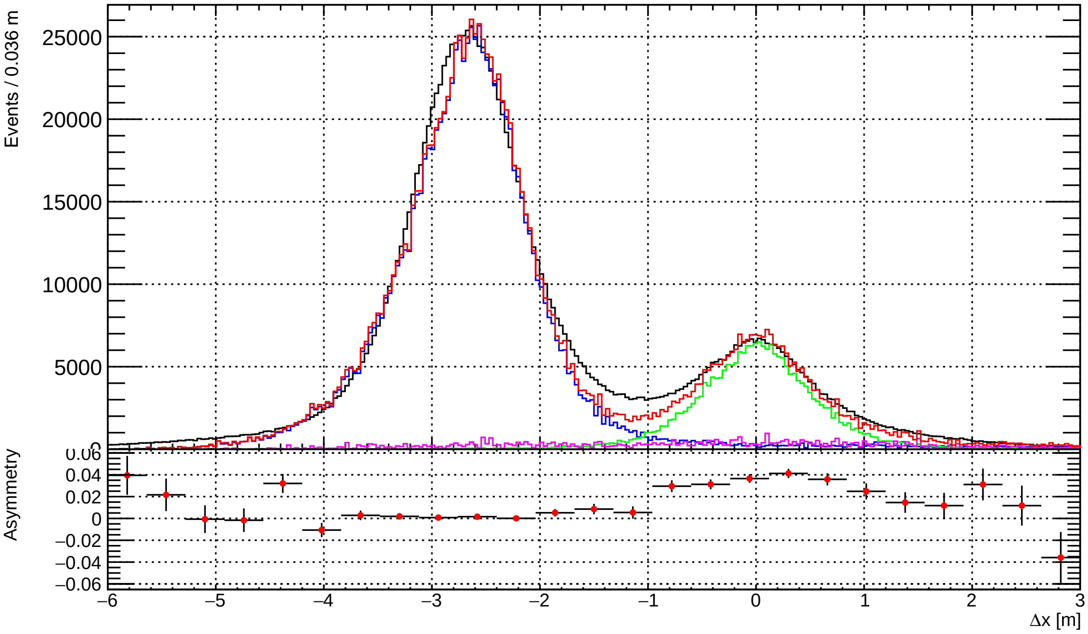

Figure 5.20: Δx after prompt random subtraction and all other QE cuts for (black) data, (blue) QE proton simulation, (green) QE neutron simulation, (magenta) inelastic background simulation and (red) the combined fit.

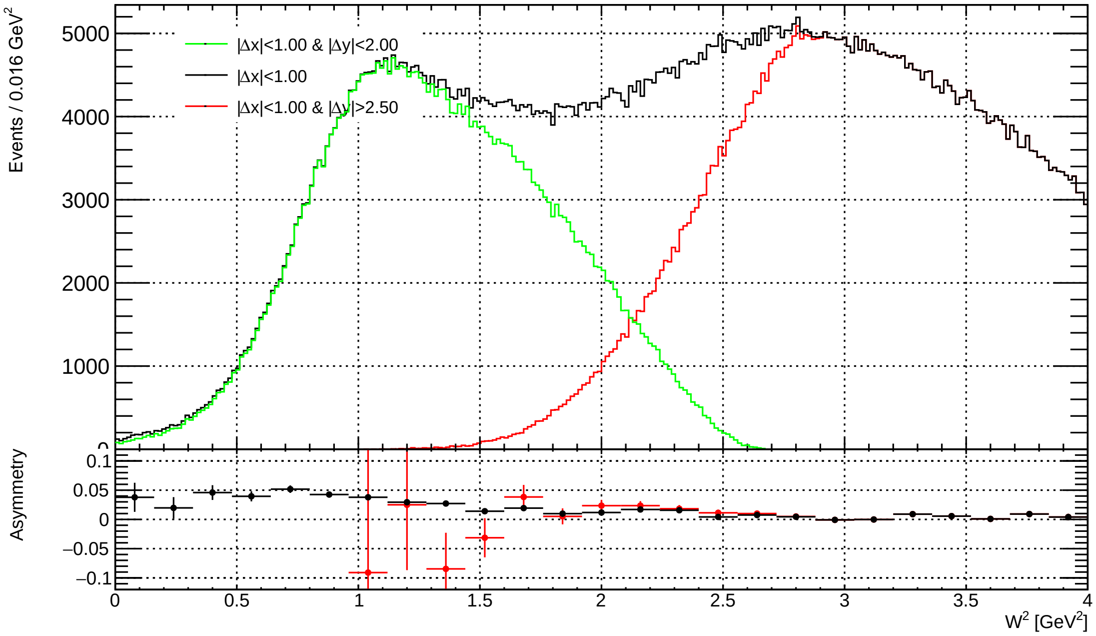

Figure 5.21: (Top)Invariant mass squared W^2 for various cuts detailed in the legend, (bottom) and the asymmetry binned in W^2 for each distribution.

fully model the data distribution, particularly in the valley between the proton and neutron peak around $\Delta x = -1$ m. It is hoped to investigate potential reasons for this and improve the accuracy of the fit in future work. The background fit after prompt random subtraction of the Δx distribution yields $f_{\text{BG}} = 0.0882$ from which we subtract f_π, f_{N2} and f_{fsi} (discussed in subsequent sections) to avoid double counting these contributions within the overall background shape.

To ascertain the asymmetry in the pure inelastic regime we revisit the idea of an anti-cut on Δy. The invariant mass squared W^2 is shown in Fig. 5.21 for a series of cuts. In Black are all events in the Δx cut window corresponding to both QE recoil neutrons as well as semi-inclusive background. In addition green has the missing QE cut on Δy, and red contains an anti cut on Δy. As expected then the green signal distribution sits lower towards the nucleon mass, and the red anti-cut background distribution is maximal at large W^2, eventually equalling the black. The asymmetry of the red (anti-cut background) and black (all neutrons) are plotted below. Clearly at large invariant mass squared the asymmetry is distinctly smaller than asymmetry measured in the QE neutron region. We can treat these as explicitly different, and take the semi-inclusive inelastic asymmetry from the high W^2 region. The final dilution and asymmetry associated with semi-inclusive electroproduction backgrounds are $f_{\text{inelas}} = 0.0701 \pm 0.0019$ and $A_{\text{inelas}} = 0.0040 \pm 0.0007$ respectively.

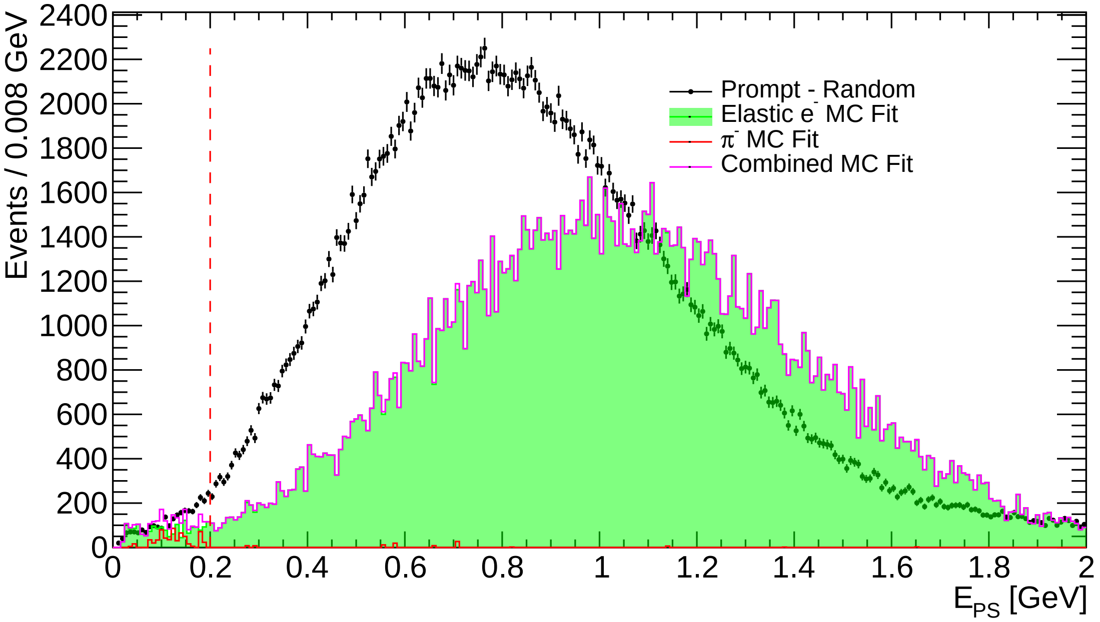

Figure 5.22: Preshower energy distribution for data after prompt random subtraction and QE cuts, before E_{PS} cut. Simulation elastic electron and pion background distribution fits are shown, detailed in the legend.

5.7.2 Pions in Bigbite

The contamination due to pions in Bigbite is expected to be able to be measured separately from the semi-inclusive inelastic electroproduction background. Pion contamination in Bigbite is a function of the relative rate of pion and electron production at a given momentum and scattering angle, and quasi-real / real photon production in the target. Additionally, for a coincidence measurement, the probability of producing a charged pion in coincidence with another particle which is detected in HCal, and that passes all event cuts, factors into the contamination. The result is that these events which appear as misidentified pions in Bigbite will contribute a fairly small amount to the overall background, particularly at the lowest Q^2 value of kinematic setting 2. Nevertheless it is necessary to estimate the π^- contamination in the final quasielastic (e,e'n) sample. In GEN-I, pion contamination was considered to be negligible for all four Q² points. For low-Q² kinematic points, this can be estimated by comparing simulated preshower energy distributions to data, for some given set of cuts.

The Preshower energy distribution is compared to simulation in Fig. 5.22. The signal from electrons and pions are simulated using the elastic and photo-pion (WAPP) generators respectively. The preshower energy is then fitted to the two distributions after all QE cuts with the exception of the E_{PS} cut itself. The red dashed line indicates where this cut would normally be. The data distribution has undergone prompt-random subtraction detailed in Sec. 5.6 in order to avoid double counting backgrounds. The resultant fit at this kinematic

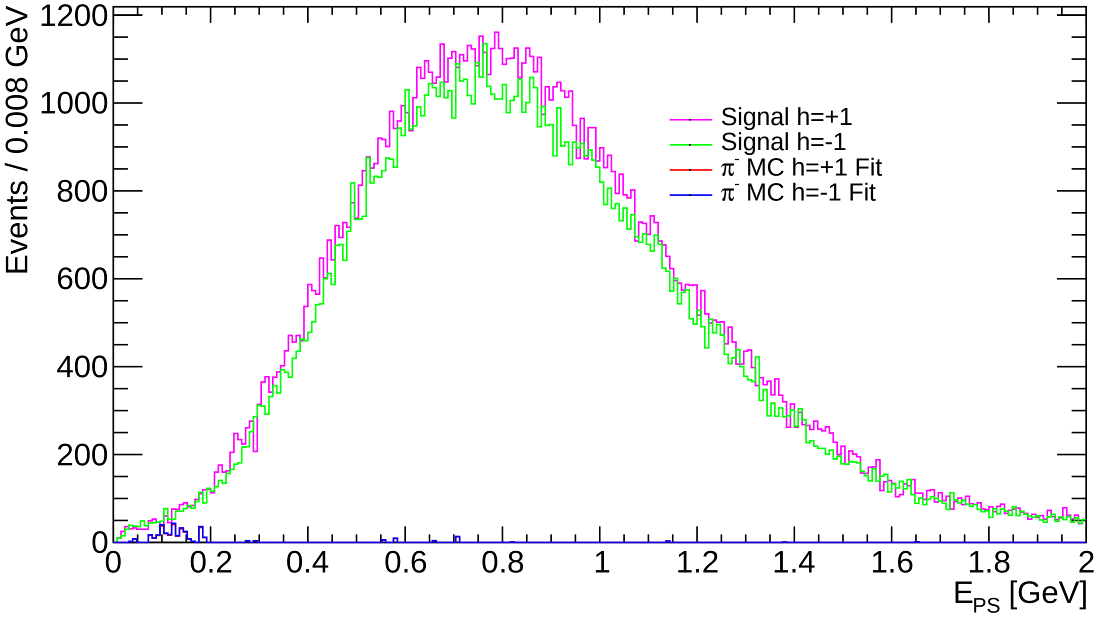

Figure 5.23: Preshower energy distribution for plus and minus helicity contributions of data and the simulation fit.

setting effectively yields a scale of zero for the pion signal, as somewhat expected owing to the aforementioned reasons. The complete shape of the simulation and data energy spectrum are in fairly poor agreement, as a result of issues with the calorimeter geometry, density and reconstruction in the simulation, which are known but not yet fully understood. The asymmetry associated with this contamination can also be estimated using a similar method. Fig. 5.23 shows the same energy distribution separated into helicity components. This time the positive and negative distributions are fitted separately to the pion simulation. This yields an asymmetry of $A_\pi = -0.08 \pm 0.09$ with a relatively large uncertainty owing to the small statistics involved.

A second method is utilised to try and measure the asymmetry more cleanly. Fig. 5.24 shows the preshower energy distribution this time with “anti-cuts” on electrons. The GRINCH is now explicitly not track matched, and we look for small clusters which are typically more likely to be pions, as well as dropping the QE cuts on W^2, Δy and Δx from before. The idea is to almost completely isolate events which really had a pion in Bigbite, and directly measure the asymmetry in the region which is shaded in red. This method yields over an order of magnitude smaller statistical uncertainty in the measured asymmetry for pions. The dilution and asymmetry associated with misidentified pions in Bigbite are $f_\pi = 0.0004 \pm 0.0001$ and $A_\pi = 0.0029 \pm 0.0017$ respectively.

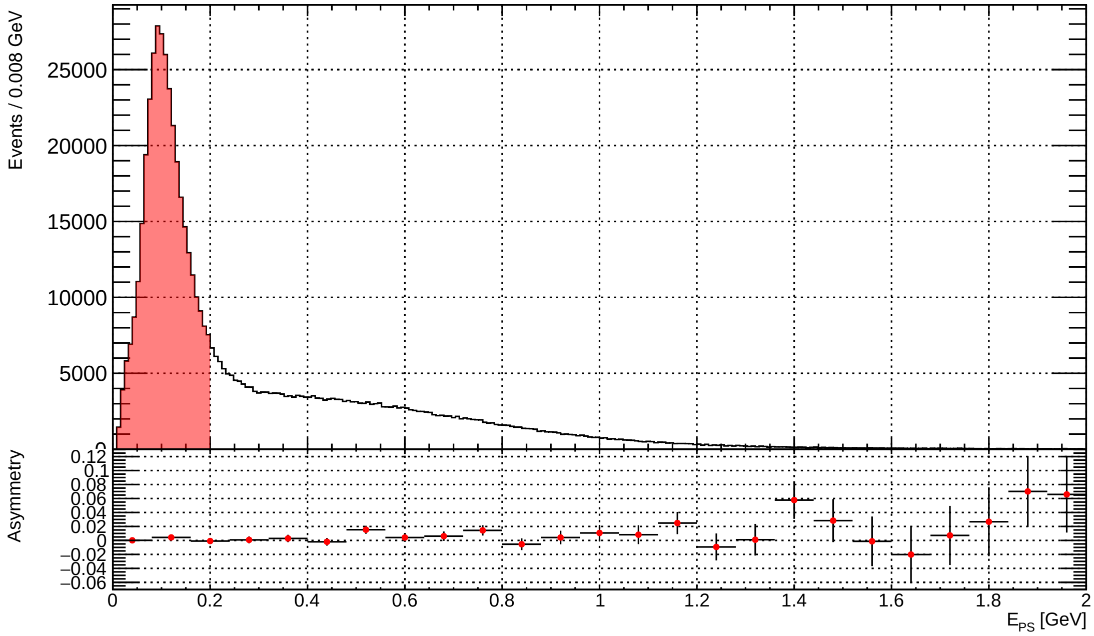

Figure 5.24: Preshower energy distribution for GRINCH clusters with "anti-electron cuts" i.e. which were not track matched and had a cluster size less than two. The red shaded region indicates the region below the nominal analysis cut which is integrated over helicity states to get a "pure" pion asymmetry.

5.8 QE Proton Contamination

Naturally in addition to the QE scattering of neutrons of interest, QE scattering of protons will occur too. This can be simulated and counted separately from any other protons produced in inelastic scattering events, which are misidentified as neutrons. The SBS magnet sweeps protons upwards and out of the acceptance of HCal, however a large number of QE ep events which pass QE cuts can survive. This is evident in Fig. 5.20, in which the blue plot is the QE proton simulation scaled from the fitting procedure described in Sec 5.7.1. It is clear that the tail of the proton distribution lies under the neutron distribution shown in green. As such we can measure the fraction of total events attributed to QE protons which pass our final Δx cut, $f_{\mathrm{p,QE}}$ directly from the integral of the proton tail within the cut region.

The asymmetry associated with this dilution fraction $A_{\mathrm{p,QE}}$ can be estimated using existing world data for the proton form factors. The global fit by Ye et al. discussed in Sec. 2.8.4 describes the proton form factors very well, particularly in the region of Q^2 of interest. The Ye model is applied directly to events in the final sample after QE cuts to calculate the proton form factors at the momentum transfer for a given event. The pure proton asymmetry is calculated as

$$A_{\mathrm{p,QE}} = A_{\mathrm{p,phys}} P_{\mathrm{p}} P_{\mathrm{beam}} P_{\mathrm{He3}} \tag{5.19}$$

where P_{p} is the proton polarisation in ^{3}He assumed to be ~ -0.03 and the physical asymmetry is

$$A_{\mathrm{p,phys}} = -r_p \frac{\sqrt{\frac{2\epsilon(1-\epsilon)}{\tau}} \sin\theta^* \cos\phi^* - \sqrt{1-\epsilon^2}\cos\theta^*}{1+\frac{\epsilon}{\tau} r_p^2} \tag{5.20}$$

where $r_p = G_E^p / G_M^p$. The dilution factor and asymmetry associated with misidentified QE protons are $f_{\mathrm{p,QE}} = 0.0745 \pm 0.0006$ and $A_{\mathrm{p,QE}} = 0.0024 \pm 0.0001$ respectively.

5.9 Target Nitrogen Dilution

Nitrogen (N_2) exists in the cell at an approximate 2% of the partial pressure to produce quenching of the excited nuclei and prevent radiative de-excitation. Quasielastic scattering off nitrogen accounts for a small amount of events in the final sample. Since the nitrogen is unpolarised, the asymmetry associated with this is negligibly small and it is appropriate to take it as zero. The dilution fraction due to scattering off nitrogen can be estimated and taken into account. The calculation of the necessary corrections due to nitrogen was performed by Sean Jeffas (University of Virginia) for the third and fourth kinematics. The calculation was not performed for kinematic 2 due to a lack of necessary carbon optics data. The complete summary of the work done is available here [233], and a brief summary will be given in this subsection.

The carbon optics data can be used to estimate contamination due to scattering from N_2, with the following method

$$f_{N_2} = \frac{Q(He3)}{Q(C)} \frac{m_{N2}(He3)}{m_C(C)} \frac{N_{\mathrm{C}} - N_{\mathrm{acc,C}}}{N_{^3\mathrm{He}} - N_{\mathrm{acc,^3He}}} \tag{5.21}$$

where Q is the total charge accumulated on each target, m is the thickness of the target, N are the counts passing all quasielastic selection cuts for each dataset and (^{3}He, C) denotes the ^{3}He or Carbon (C) target, and the subscript “acc” denotes the number of counts due to timing accidentals for each yield.

The carbon optics produces 7 peaks reconstructed along the z-vertex as shown in Fig. 5.25. Cuts are made around each peak with a 3σ width of the vertex resolution, corresponding to a cut of 2.1 cm. The foils themselves are 0.0254 cm thick, so ± 2.0873 cm of air needs to be accounted for. The same cuts on the vertex are applied to the ^{3}He dataset to match the resulting acceptance. Similarly, the carbon optics data is taken with a sieve plate in place which produces a second acceptance correction for the ^{3}He dataset. Fig. 5.26 shows the x-y position reconstruction at the face of the magnet where the sieve sits, for the optics and ^{3}He datasets. The sieve holes are indicated by a pattern of red ovals. Cuts are made inside all of these regions for both datasets.

The masses of the (air and carbon) target particles involved in scattering inside the cut regions for the optics data, and of the (nitrogen) particles for ^{3}He, can be calculated from

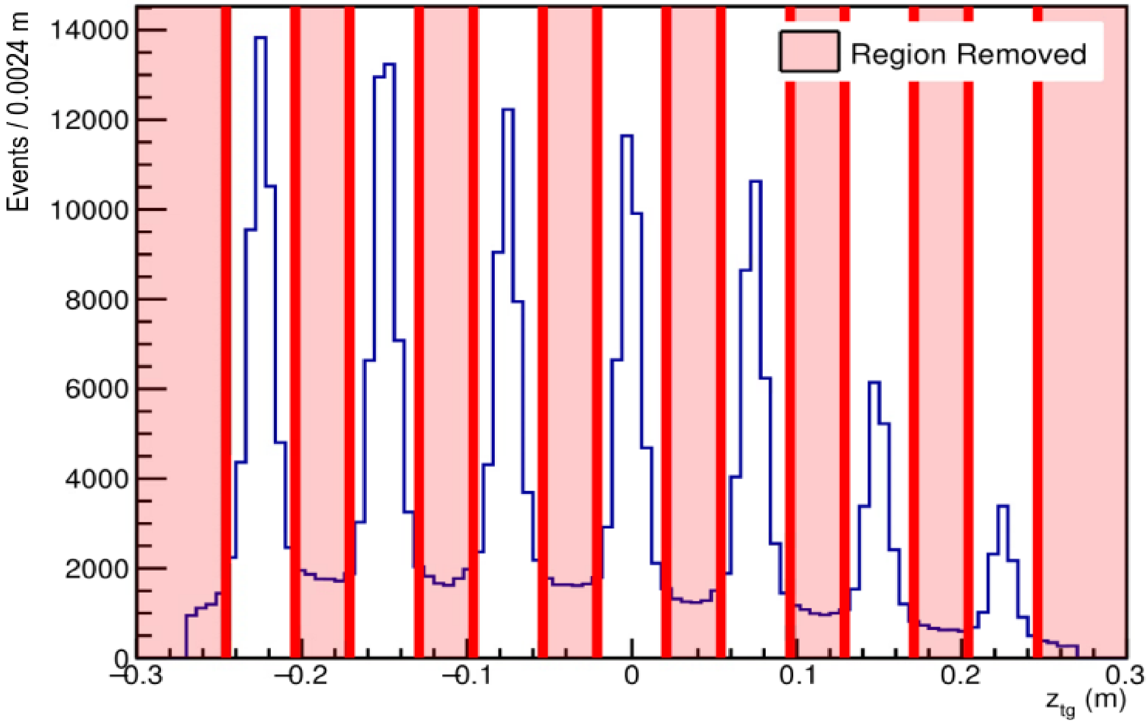

Figure 5.25: The reconstructed track z position of the scattering vertex at the target. The seven peaks account for scattering off each of the 7 carbon foils present at the optics position. The red bands denote where cuts have been made to remove scattering from air. Figure from [195].

the effective target lengths and normal densities at standard room temperature and atmospheric pressure,

$$\begin{aligned} m_C(C) &= \rho_C l_C + \rho_{air} l_{air} \\ m_{N2}(He3) &= \rho_{N2} l_{N2} \end{aligned} \tag{5.22}$$

Where ρ_C = 2.2 g cm^{-3} is the density of carbon, ρ_{air} = 1.225 g cm^{-3} is the density of air and ρ_{N2} = 0.0013 is the density of nitrogen, and $l_{C,air,N2}$ are calculable from the sizes of the vertex cuts and the knowledge that the carbon foils are 0.0254cm thick.

This method results in dilution fractions of nitrogen f_{N_2} of 0.0178 ± 0.0018 and 0.0151 ± 0.0041 for GEN3 and GEN4 respectively. There was no optics data taken during GEN2, due to the fact that the GEN1 data could be used for optics calibration. However, due to the different Q^2 the scattering kinematics which would influence dilution corrections such as this correction for nitrogen would have inaccuracies. As such, given the small nature of the correction, and the empirical similarity between the results for GEN3 and GEN4, we elect to use the GEN3 value for GEN2.

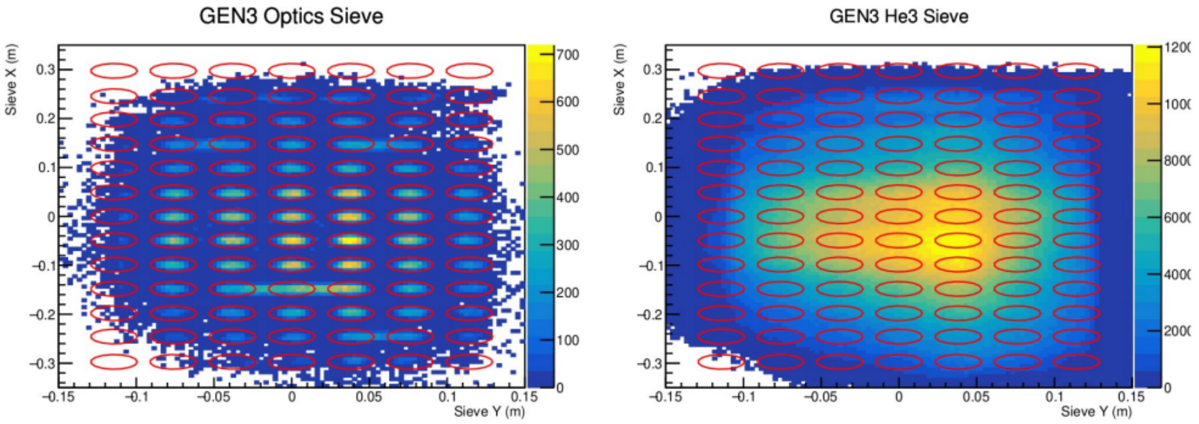

Figure 5.26: Reconstructed x-y position of tracks at the face of the magnet where the sieve plate sits for (left) the GEN3 carbon optics data and (right) the GEN3 ^{3}He production data. Acceptance matching within the sieve plate acceptance indicated by the array of red ovals. Figure from [233].

5.10 Nuclear Corrections

As introduced in chapter 2, early unpolarised G_n^E extractions established the importance of nuclear corrections necessary as the recoil neutron exists as part of the bound nucleus state. Recall that the scattering is parameterised in the plane wave impulse approximation (PWIA). Nuclear effects arise from several processes; rescattering between the struck nucleon and a spectator, final state interactions (FSI); coupling between the virtual photon and a virtual meson exchanged between two nucleons, meson exchange currents (MEC); coupling between the virtual photon to an excited state of the nucleon, isobar configuration (IC); and relativistic distortion of the wavefunction. Additionally, the neutron polarisation within ^{3}He, nominally taken to be 86%, is effectively increased by the selection of the lower transverse momentum parts of the wavefunction in quasielastic kinematics. However, the choice of QE cuts used are fairly wide, which means that more neutrons on average are closer to the Fermi surface and so it is not straightforward what the effect on the neutron polarisation will be.

For large momentum transfer ~ $|q| > 1$ GeV, the relative contribution of MEC and IC compared to PWIA and FSI decreases [45]. In light of this, focus is put on studying the effect of FSI in the final event sample wherein the experimental acceptance is ~ $2 < Q^2 < 3$ GeV^2. In particular, charge exchange wherein a struck neutron re-scatters and becomes a proton which is deflected by the SBS magnet and lost, are the leading mechanism through which the asymmetry is reduced by these FSI effects.

Nuclear corrections are handled with the generalised eikonal approximation (GEA) [234], which is an extension to the Glauber approximation [235]. Where the Glauber approximation requires the struck nucleon be a stationary scatterer, this theoretical framework allows a treatment of the non-zero momentum of the initial nucleon in the bound system, which directly addresses the Fermi motion of the nucleus. A Monte Carlo simulation was developed by Misak M. Sargsian (Florida International University) which calculates the scattering amplitudes for PWIA and FSI using spin-dependent NN scattering data, and the AV18 NN potential for a ^{3}He wavefunction. This framework was originally used in the GEN-I analysis for a complete nuclear correction. Applying it similarly in this analysis is still in infancy, and a full software integration is still in progress. As such an effort will be made to develop an approximate dilution factor for the measured physics asymmetry, noting that a more complete analysis will come in the future.

5.10.1 FSI and Effective Neutron polarisation

The simulation computes A, the asymmetry arising from PWIA+FSI of the neutron as part of a bound system, and A_{Free}, the asymmetry that one would measure for a free neutron with 100% polarisation. This allows a direct comparison between the two to yield a nuclear dilution factor D_{FSI}. GEA calculations for GEN-I demonstrated a nuclear dilution factor which indicated an effective neutron polarisation of ~ 96% (Q^2 = 1.46 GeV²) , 97% (Q^2 = 2.5 GeV²) and 99% (Q^2 = 3.5 GeV²) for the three kinematics respectively [112]. Figure 5.27 shows the perpendicular component of the asymmetry A_{perp} as calculated in the GEA. The upper solid line is the free neutron approximation, and the lower solid line includes a correction for the nominal 86% neutron polarisation in ^{3}He. The dashed line comes from the PWIA calculation and the dotted and dot-dashed lines are from distorted wave impulse approximation (DWIA) and DWIA + charge exchange effects. Each of the GEA curves have also been scaled down by 86% in this figure.The ratio of DWIA + charge exchange effects to the free neutron (corrected for 86% polarisation) provides a measure of the nuclear dilution.

A preliminary test of the simulation code was run using simulated data from G4SBS at kinematic setting 2 for this analysis. The simulated events had the same QE cuts applied as the data discussed in Sec. 5.4. The scattered electron energy and angle, and recoil nucleon momentum, angle and azimuthal angle are integrated over the experimental acceptance. These five parameters are folded into the simulation code to generate the free neutron asymmetry and PWIA+FSI. The output results were seen to be sensitive to choice of cuts which changes the final input values. A complete integration of the GEA simulation with existing analysis machinery is required. The preliminary test yielded the values A = 0.181, A_{Free} = 0.186. This is an approximate dilution of 3% which is numerically similar to the results of GEN-I. The average dilution and asymmetry across the Q^2 = 2.5 GeV² and Q^2 = 3.5 GeV² kinematics of GEN-I were $f_{\mathrm{FSI}} = 0.0287 \pm 0.0026$ and $A_{\mathrm{FSI}} = 0.0003 \pm 0.0005$ respectively [64]. We choose to use these values as an estimation of nuclear effects, since these kinematic settings were at a Q^2 which this measurement falls between. Since no dedicated calculation is currently available to calculate the effective neutron polarisation for the given choice of QE

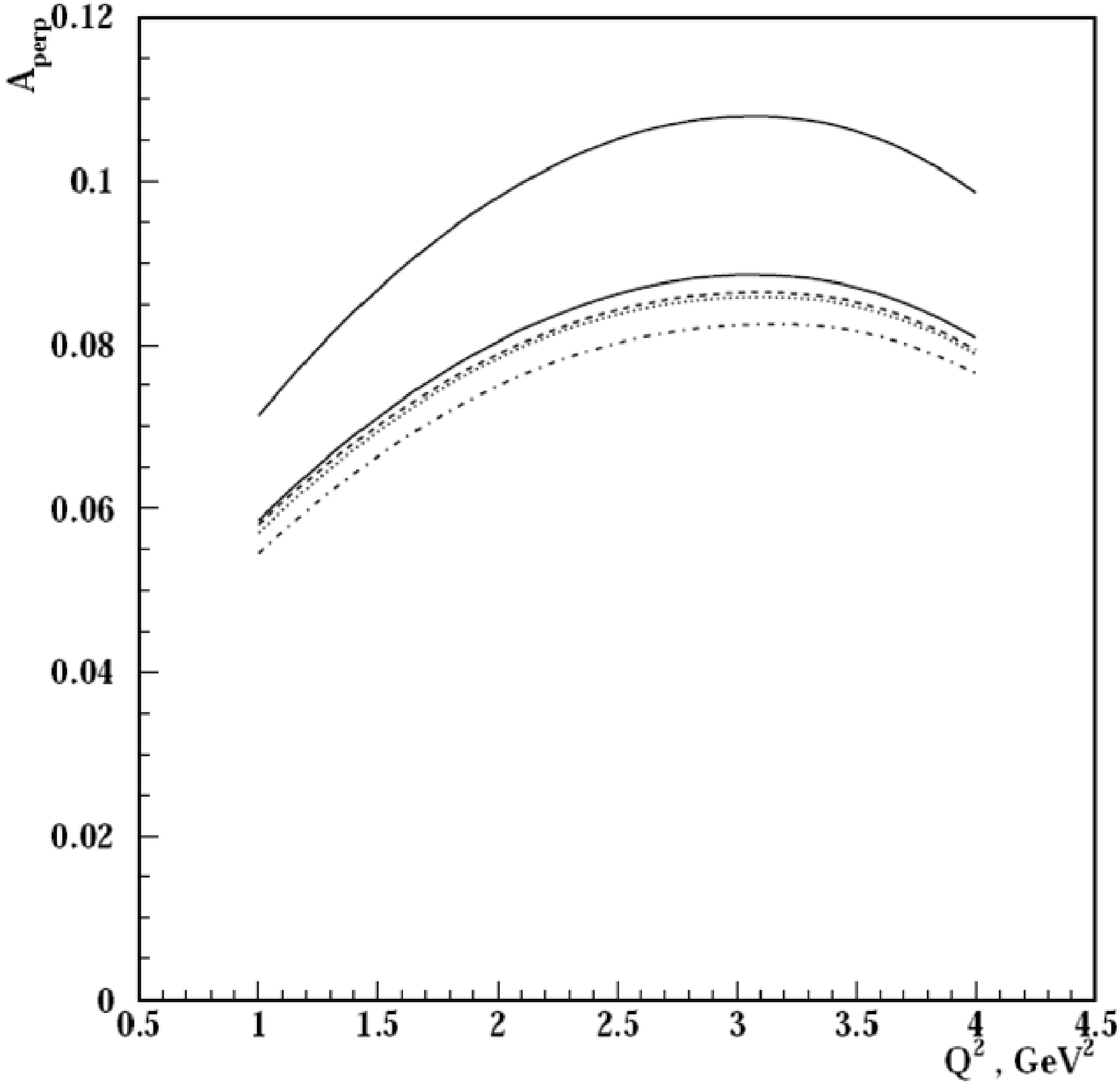

Figure 5.27: The perpendicular asymmetry A_{perp} calculated by M. M. Sargsian [112] in the GEA, for various models which are detailed in the text.

cuts, we take the neutron polarisation to be $P_n = 0.91 \pm 0.05$. When more accurate and final calculations are available they will be implemented into this analysis.

5.11 Physical Asymmetry Measurement

The calculation of A_{phys} is given in Eqn 5.16. However since some quantities can change over time during the data taking for a kinematic setting, it is necessary to treat them as constant only over the duration of a run where possible. Due to statistical limitations with this approach the contamination fractions and their associated asymmetries are taken to be constant. Likewise the beam polarisation is measured infrequently and for kinematic 2 there is only a single data point, so this is taken as constant. The proton asymmetry can be determined for the entire sample due to the precision of the proton form factors in the global fit to world data, with the assumption that the acceptance weighted Q^2 of events in the final sample can be considered the same for proton and neutron events. The raw asymmetry measured between helicity states can be formed for an individual run, and since the target polarisation and uncertainties have been interpolated, these can be matched to events and form run by run or event by event values. As such a run by run physics asymmetry can be formed, $A_{\text{phys},i}$ and the weighted mean of this provides the final asymmetry. This idea is also extended to an event by event weighted asymmetry extraction.

5.11.1 Run by Run Formalism

For an individual run i the physical asymmetry has the same form as Eqn. 5.16,

$$A_{\text{phys},i} = \frac{A_{\text{raw},i} - \sum_\chi f_\chi A_\chi}{P_i f_n}, \tag{5.23}$$

where $A_{\text{raw},i}$ is the raw asymmetry measured over that run and P_i is the product of the polarisation terms $P = P_{^3\text{He},i} P_{\text{beam}} P_n$ in which only the target polarisation changes.To then combine all of the measurements of $A_{\text{phys},i}$, with statistical uncertainty σ_i for N runs, we employ the standard weighted average given by

$$A_{\text{phys}} = \frac{\sum_i \frac{A_{\text{phys},i}}{\sigma_i^2}}{\sum_i \frac{1}{\sigma_i^2}} \tag{5.24}$$

where the summation is over N number of runs. The uncertainty on the final weighted average is given by

$$\sigma_{A_{\text{phys}}} = \sqrt{\frac{1}{\sum \sigma_i^{-2}}}. \tag{5.25}$$

5.11.2 Event by Event Formalism

The technique of extracting the physical asymmetry from the weighted mean of run by run measurements is appropriate for kinematic setting 2 since runs typically have enough statistics after QE cuts that the necessary assumptions of Gaussian statistics apply. However, for higher Q^2 kinematic settings, particularly GEN4, this is not the case. The number of raw events which pass QE cuts in a run can be on the order of one, and the resultant run by run errors are no longer Gaussian and cannot be summed in a straightforward or meaningful way. While kinematic setting 3 and 4 are not the focus of this work, a formalism was developed in order to extract the physical asymmetry from these conditions in a statistically sound manner. This was found to have close numerical and statistical agreement with the original run by run formalism of Sec. 5.11.1 for kinematic setting 2, as a consistency check and proof of concept. Therefore in the interest of having a consistent codebase and analysis between all kinematic settings this has become the adopted formalism in the final analysis of this work.

Consider again Eqn. 5.16. We will expand this in to a form of the parameters which are measured per event

$$A_i = \frac{1}{f_n}\left(\frac{h_i - D_{\chi,i}}{P_i}\right) \tag{5.26}$$

where h_i is the helicity of an event $(h = \pm 1)$, $D_{\chi,i} = \sum_\chi f_\chi A_{\chi,i}$ where the proton asymmetry is being measured each event and $P = P_{^3\mathrm{He},i} P_{\mathrm{beam}}$ where the time stamped polarisation of the target is being taken per event. The weighted asymmetry is then calculated over the sum of events as

$$A_{\mathrm{phys}} = \frac{\sum_i \frac{A_i}{\sigma_i^2}}{\sum_i \frac{1}{\sigma_i^2}} \tag{5.27}$$

where the event by event Poisson uncertainty arising from the raw yield, and weighted by the polarisation, is

$$\sigma_i = \frac{\sigma_{h_i}}{P_i f_n}, \tag{5.28}$$

for $\sigma_{h_i} = 1$ the uncertainty on the electron helicity per event. The full uncertainty on the physical asymmetry is calculated by propagating the errors on each term through the expression for the statistical sources in Sec. 6.1 and the systematic sources in Sec. 6.2.

5.12 G_E^n Extraction

The final step is to extract the form factor ratio from the physical asymmetry, and use G_M^n world data to directly measure G_E^n. Recall that the physics asymmetry associated with elastic scattering off the nucleon is given by

$$A_{\text{phys}} = A_\perp \sin\theta^* \cos\phi^* + A_\parallel \cos\theta^* \tag{5.29}$$

where $A_\perp$ and $A_\parallel$ are the perpendicular and parallel components of polarised scattering respectively, given by

$$\begin{aligned} A_\perp &= -\sqrt{\frac{2\epsilon(1-\epsilon)}{\tau}}\frac{r}{1+\frac{\epsilon}{\tau}r^2} \\ A_\parallel &= -\frac{\sqrt{1-\epsilon^2}}{1+\frac{\epsilon}{\tau}r^2}, \end{aligned} \tag{5.30}$$

and $r = G_E^n/G_M^n$. The angles θ^* and ϕ^* are the azimuthal and polar angles between the direction of the target polarisation (taken to be the calculated direction of the total field inside the Helmholtz coils) and the direction of momentum transfer for an event. The polarisation direction and its variation across the target are known from compass measurement and TOSCA based OPERA simulations detailed in section 4.2.4. The direction of the momentum transfer is known from the q four-vector, purely from electron kinematics given in Eqn 5.1.

By creating new variables A, B, C of the form

$$\begin{aligned} A &= \frac{\epsilon A_{\text{phys}}}{\tau} \\ B &= \sqrt{\frac{2\epsilon(1-\epsilon)}{\tau}}\sin\theta^* \cos\phi^* \\ C &= A_{\text{phys}} + \sqrt{1-\epsilon^2}\cos\theta^* \end{aligned} \tag{5.31}$$

Eqn 5.29 can be rearranged into a quadratic equation in r

$$Ar^2 + Br + C = 0 \tag{5.32}$$

where A_{phys} is the physics asymmetry treated for dilutions as detailed in chapter 5, and each of the kinematic terms in A, B, C can be averaged over the final quasielastic neutron event sample. Solving this allows a direct extraction of the ratio of interest without having to apply corrections for the r^2 term which exists in the denominator of A_{phys}.

Finally, G_E^n can be extracted from the ratio for a given value of G_M^n. The fit to world data by Ye has been discussed several times already, and is known to match data well in this region of Q^2. As such it is appropriate to directly take $G_M^n \equiv G_M^n(Q^2_{\text{meas}})\big|_{\text{Ye}}$. The electric form factor is then simply

$$G_E^n = r * G_M^n\big|_{\text{Ye}} \tag{5.33}$$

Chapter 6

Results and Outlook

In this chapter we present the results of this analysis over kinematic 2 for E12-09-016. The sources of uncertainties in the measured physics asymmetry and the propagation of these uncertainties to a final statistical and systematic uncertainty on the form factor G_E^n will be detailed. The final results will be compared to existing world data and nucleon models. Finally the experiment will be summarised and the results discussed, with an outlook on future work given.

6.1 Sources of Uncertainty on Extracted Asymmetry

There are two main sources of uncertainty on the extracted asymmetry, which are both statistical in nature, and completely dominate the uncertainty on the final result at this kinematic setting. These are the Poisson uncertainty arising from the raw yield, and the combined polarisation uncertainties on the three polarisation terms (beam, target, bound neutron). Much of this analysis deals with counting discrete numbers of positive and negative helicity events. As such we will rely heavily on Poisson statistics in which the uncertainty on a count N is given by $\sigma_N = \sqrt{N}$, and that the uncertainty on a quantity can be propagated as

$$\sigma^2_{y(x_i)} = \sum \left(\frac{\partial y}{\partial x_i} \right)^2 \sigma^2_{x_i}. \tag{6.1}$$

6.1.1 Poisson Uncertainty on the Yield

The uncertainty on the raw yield produces the statistical uncertainty on the raw asymmetry, $\sigma_{A_{\text{raw}}}$. The raw asymmetry is defined as

$$A_{\text{raw}} = \frac{N^+ - N^-}{N^+ + N^-} = \frac{\Delta}{N}. \tag{6.2}$$

The raw yield of quasielastic (QE) neutron events is $N = 248326$, with $N^+ = 128388$, $N^- = 119938$, $\Delta = 8450$. The resultant raw asymmetry is $A_{\text{raw}} = 0.0340$. Since N^+ and N^- are measured in the same experiment they are correlated and we can define the probability q such that $q = N^+/N$. This means that the probability for a given event to have negative helicity is then (1-q). As such the asymmetry is simply $A = q-(1-q) = 2q-1$ and therefore

$$\sigma_{A^2} = 4\sigma_q. \tag{6.3}$$

Then the uncertainty associated with q is

$$\sigma_q^2 = \frac{\sigma_{N^+}^2}{N^2} \tag{6.4}$$

For correlated N^+, N^-, the distribution of each is binomial: an event can only either be N^+ with a probability of q, or not, with a probability $1-q$. The variance in this case is given by

$$\sigma_{N^+}^2 = Nq(1-q) \tag{6.5}$$

and so by inserting Eqns. 6.5 and 6.4 into Eqn. 6.3, we arrive at the uncertainty in a correlated measured asymmetry

$$\sigma_A^2 = \frac{4q(1-q)}{N} = \frac{4N^+N^-}{N^3}. \tag{6.6}$$

Since we are dealing with a relatively small asymmetry (that is, $N^+ \sim N^- \sim N/2$, it is worth noting that Eqn. 6.6 approximates to $\sigma \sim 1/\sqrt{N}$. Inserting the measured plus and minus yields gives a value of $\sigma_{A_{\text{raw}}} = 0.0020$. The relative uncertainty on the raw asymmetry is then $\sigma_{A_{\text{raw}}}/A_{\text{raw}} = 0.0020/0.0340 = 5.89\%$. In reality the uncertainty in the raw asymmetry enters the uncertainty on the physical asymmetry as $\sigma_{A_{\text{raw}}}/(Pf_n)$ which might change this relative value. Additionally, recall from Secs. 5.11.1 and 5.11.2 that we can measure the physical asymmetry as a weighted average over runs or even events. Since we opt to measure this over events, the Poisson uncertainty associated with the yield is also weighted, and this changes the overall value. The form of the weighted uncertainty is explicitly

$$\sigma_{\text{stat,Poisson}} = \sqrt{\sum \frac{1}{\left(\frac{\sigma_{h_i}}{P_i f_n}\right)^2}}, \tag{6.7}$$

where $\sigma_{h_i}^2 = 1$ is the uncertainty on a helicity count ($h = \pm 1$), P_i is the product of the target, beam and neutron polarisation for an event given by $P_i = P_{^3\text{He},i} P_{\text{beam}} P_n$, and f_n is the fraction of the yield measured to be QE neutrons after accounting for backgrounds. The treatment of the polarisation uncertainties is discussed in the next section, and the treatment of f_n is discussed in Sec. 6.2.1. We find the statistical uncertainty associated with the yield from this method to be $\sigma_{\text{stat,Poisson}} = 6.09\%$.

6.1.2 Uncertainty from Polarisations

Recall from Sec. 4.2.3 that the uncertainty on a given EPR calibration is taken as the standard deviation divided by the square root of the sample size of number of NMR sweeps. This is a statistical uncertainty and is the main factor in the final uncertainty on the target polarisation. The target polarisation for an event is attained from the minute-to-minute interpolation of the calibrated NMR data, and the final uncertainty on the target polarisation is an unweighted mean of the errors. The uncertainty on the beam polarisation and neutron polarisation are fixed for the kinematic setting. They are taken as $P_{\text{beam}} = 0.841 \pm 0.002$ and $P_n = 0.91 \pm 0.05$ respectively. The target polarisation, beam polarisation and neutron polarisation are completely uncorrelated quantities. As such the uncertainty of the combined polarisation terms can be added in quadrature

$$\sigma_P^2 = P^2 \left[\left(\frac{\sigma_{P_{^3\text{He}}}}{P_{^3\text{He}}} \right)^2 + \left(\frac{\sigma_{P_{\text{beam}}}}{P_{\text{beam}}} \right)^2 + \left(\frac{\sigma_{P_n}}{P_n} \right)^2 \right]. \tag{6.8}$$

The polarisation values and their uncertainties are summarised in Tab. 6.1. Recall that the polarisation enters the event by event weighting of the physical asymmetry due to the interpolation of the NMR data to a minute-level discretisation. However calculating the event by event weighted polarisation would assume that P_i and its uncertainty σ_{P_i} are uncorrelated and perfectly localized, but in this case these values are interpolated from broader, time-averaged measurements. This means that to correctly calculate the statistical uncertainty associated with the polarisation, it must be done outside of the A_{phys} summation. We choose to calculate the unweighted mean of the polarisation and its uncertainty, and use these values to extract σ_P. The unweighted target polarisation is measured as 0.379 ± 0.019. The combined polarisation and uncertainty from Eqn 6.8 is then 0.290 ± 0.022. This yields a relative uncertainty on the physical asymmetry of $\sigma_{\text{stat,pol}} = \sigma_P/P = 7.43\%$.

Table 6.1: Polarisation values and their uncertainties. The target polarisation is taken as an unweighted mean over the final event sample.

Parameter	Kin. 2 Result		
$P_{^3\text{He}}$	0.379	±	0.019
P_{beam}	0.841	±	0.002
P_n	0.91	±	0.050
P	0.290	±	0.022

6.1.3 Statistical Uncertainty on Physical Asymmetry

The statistical uncertainties arising from the yield and polarisation are completely uncorrelated, and can be combined in quadrature to provide the final statistical uncertainty on the physical asymmetry,

$$\sigma^2_{\text{stat}} = \sigma^2_{\text{stat,Poisson}} + \sigma^2_{\text{stat,pol}}. \tag{6.9}$$

The combined relative uncertainty is then $\sigma_{\text{stat}} = 9.57\%$. The result of this propagation of these statistical uncertainties on the physical asymmetry yields $A_{\text{phys}} = 0.148 \pm 0.014$ (stat).

6.2 Effect of Background Dilutions

There are various backgrounds which dilute the measured asymmetry. These are introduced in Sec. 5.5 and an analysis of the dilution fraction and asymmetry of each background is presented throughout chapter 5. Each of these terms (denoted as f_χ and A_χ for a background χ) has an associated uncertainty, which can be propagated onto the final physics asymmetry. These are taken to be systematic in nature, and are generally very small in comparison to the statistical uncertainties presented in the preceding section. Nevertheless each is propagated fully to the final physical asymmetry, however ultimately the final uncertainty is completely dominated by statistics.

6.2.1 Dilution Fraction and Asymmetry Uncertainties

Most asymmetry values for backgrounds are measured and follow the statistics of Eqn. 6.6, with the exception of the QE proton background asymmetry. This is simply because the proton asymmetry value is calculated using the Ye global fit proton form factor data, and so the uncertainty on this comes directly from the error bands of the fit combined with the uncertainty on the polarisation terms.

The fractional background contributions also follow a common formula

$$f_\chi = \frac{N_\chi}{N}, \tag{6.10}$$

where N_χ is the number of counts for the associated background, and N is the total number of events. Since N_χ and N must be correlated, the uncertainties on these terms are given by

$$\sigma^2_{f_\chi} = f^2_\chi \left[\frac{1}{N_\chi} + \frac{1}{N} - \frac{2\sigma_{N_\chi N}}{N_\chi N} \right], \tag{6.11}$$

where $\sigma_{N_\chi N} = \rho_{N_\chi N} \sigma_{N_\chi} \sigma_N$ and $\rho_{N_\chi N}$ describes the correlation between N_χ and N. However, no calculation of the necessary covariance matrix exists, we elect to treat these as uncorrelated and neglect the final term in square brackets for now. As will be seen the uncertainties due to f_χ terms are negligible with respect to the statistical uncertainty, so we expect this approach to be appropriate. The results for each background and its asymmetry value are discussed in subsequent sections, and the calculations are detailed.

QE Proton Background

The contamination due to QE recoil protons which leak into the neutron Δx peak is measured to be the largest background fraction. The size of this background is directly related to how large the lower bound of the Δx cut is. This cut is applied symmetrically, and was chosen to be $|\Delta x| < 1$ m, in order to optimise the statistical uncertainty coming from the yield without allowing in an overly large level of background. In principle this could be further optimised with an anti-symmetric Δx cut, increasing the upper bound to include more QE neutrons. A future analysis may do so.

The analysis of the QE proton fraction and its asymmetry are detailed in Sec. 5.8. The yield $N_{\mathrm{p,QE}}$ is measured from the integral of the fitted proton Δx peak within the chosen Δx cut, and the fraction is calculated from Eqn. 6.10. The uncertainty follows the statistics of Eqn. 6.11. The asymmetry for these misidentified QE protons is directly attained from the global fit to world form factor data. As such the uncertainties do not follow the generic form of Eqn. 6.6. Recall from Sec. 5.8 that the asymmetry is calculated as

$$A_{\mathrm{p,QE}} = A_{\mathrm{p,phys}} P_{\mathrm{p}} P_{\mathrm{beam}} P_{\mathrm{He3}} \tag{6.12}$$

where $A_{\mathrm{p,phys}}$ is the physical asymmetry given by Eqn. 5.20 which is measured over events, P_{p} is the polarisation of the proton within ^{3}He, taken as a widely accepted value of -0.03 and assumed to have negligible uncertainty. The uncertainty on the final proton QE asymmetry is then

$$\sigma^2_{A_{\mathrm{p,QE}}} = A^2_{\mathrm{p,QE}} \left[\left(\frac{\sigma_{A_{\mathrm{p,phys}}}}{A_{\mathrm{p,phys}}} \right)^2 + \left(\frac{\sigma_{P_{\mathrm{beam}}}}{P_{\mathrm{beam}}} \right)^2 + \left(\frac{\sigma_{P_{\mathrm{He3}}}}{P_{\mathrm{He3}}} \right)^2 \right]. \tag{6.13}$$

The uncertainties on the kinematic variables used to calculate $A_{\mathrm{p,phys}}$ are assumed to be negligible, and so the uncertainty is assumed to be purely dependent on the uncertainty of the form factor ratio from the global fit,

$$\sigma^2_{A_{\mathrm{p,phys}}} = A^2_{\mathrm{p,phys}} \left(\frac{\sigma_{r_p}}{r_p} \right)^2. \tag{6.14}$$

where $r_p = G_E^p / G_M^p |_{\mathrm{Ye}}$. The uncertainties on G_E^p and G_M^p are also taken from the Ye fit, and propagated to r_p as

$$\sigma^2_{r_p} = r_p^2 \left[\left(\frac{\sigma_{G_E}}{G_E} \right)^2 + \left(\frac{\sigma_{G_M}}{G_M} \right)^2 \right]. \tag{6.15}$$

Bringing together Eqns. 6.15, 6.14 and 6.13 provides the uncertainty on the proton asymmetry. The dilution factor and asymmetry associated with misidentified QE protons are $f_{\mathrm{p,QE}} = 0.0745 \pm 0.0006$ and $A_{\mathrm{p,QE}} = 0.0024 \pm 0.0001$ respectively.

Inelastic Background

Events in which an electron is detected in Bigbite, and something is detected in HCal which appears like a QE recoil nucleon which passes all QE cuts are modelled as a semi-inclusive inelastic background. This is measured to be the second largest contamination at this kinematic setting, with the chosen cut values. Since this is a measure of the inelastic background, it is particularly sensitive to the choice of cuts which can suppress inelastic events. Specifically, the cuts on Δy and W^2 largely control the signal to background ratio of inelastic to elastic events in the final sample. The cut on Δx will also affect this, but the scale of the underlying inelastic background in the Δx distribution is smaller than the former two, in which it grows exponentially in the positive direction for W^2, and negative direction for Δy.

The inelastic fraction was calculated from the background fraction of the Δx fit and is discussed in Sec. 5.7.1, f_{BG}. The fraction due to nitrogen, pions in Bigbite and nuclear effects were subtracted to avoid double counting,

$$f_{\text{inelas}} = f_{\text{BG}} - f_{\text{N2}} - f_{\pi} - f_{\text{fsi}}. \tag{6.16}$$

The uncertainties can therefore be added in quadrature

$$\sigma^2_{f_{\text{inelas}}} = \sigma^2_{f_{\text{BG}}} + \sigma^2_{f_{\text{N2}}} + \sigma^2_{f_{\pi}} + \sigma^2_{f_{\text{fsi}}}. \tag{6.17}$$

The background fraction from timing accidentals need not be subtracted, since the Δx distribution has been subtracted for random accidentals prior to fitting, and the background fraction from QE recoil protons is simultaneously fitted. The uncertainty on the background fit is found using Eqn. 6.11, taking background yield N_{BG} to be the integral of the background fit of the inelastic Δx distribution, within the Δx cut region. This analysis is detailed in Sec. 5.7.1. The inelastic asymmetry is calculated in the same section, by selecting events in an "anti-cut" region of squared invariant mass W^2 and Δy which is expected to correspond to pure inelastic events. The asymmetry is calculated as

$$A_{\text{inelas}} = \frac{N^+_{\text{inelas}} - N^+_{\text{inelas}}}{N^+_{\text{inelas}} + N^+_{\text{inelas}}} \tag{6.18}$$

where $N^{+(-)}_{\text{inelas}}$ are the positive (negative) helicity counts for events which pass the inelastic cuts. The fraction and asymmetry are measured as $f_{\text{inelas}} = 0.0701 \pm 0.0019$ and $A_{\text{inelas}} = 0.0040 \pm 0.0007$ respectively.

Timing Accidentals Background

Random timing accidentals sit underneath the coincidence timing peak. This background can be directly measured from side bands of the peak and is found to be the third largest contamination. This background is directly related to the resolution of the coincidence time, and improvements to timing calibrations have been found to directly decrease the fraction of accidentals which lay under the coincidence peak. Timing accidentals can be subtracted from distributions of other variables in a technique known as prompt-random subtraction, which is detailed in Sec. 5.6. In the same section the yield is calculated from the integral of a 3σ width sideband, and the asymmetry is measured outside of $\pm 5\sigma$ of the coincidence peak. The uncertainty on both the fraction and asymmetry follow simply from the statistics of Eqns. 6.11 and 6.6 respectively. The dilution and asymmetry associated with timing accidentals are $f_{\text{acci}} = 0.0441 \pm 0.0004$ and $A_{\text{acci}} = 0.0061 \pm 0.0032$ respectively.

FSI Background

Charge exchange from final state interactions is assumed to be the most dominant nuclear effect which contaminates the final event sample and reduces the measured asymmetry. The values for the dilution fraction and asymmetry have been estimated based on the average results for the kinematic settings of the GEN-I experiment. Their values are set with no direct calculation as $f_{\text{fsi}} = 0.0287 \pm 0.0026$ and $A_{\text{fsi}} = 0.0003 \pm 0.0005$ [64].

Nitrogen Background

Recall that nitrogen (N_2) exists in the target ^{3}He cell at $\sim 2\%$ partial pressure in order to enhance the polarisation through quenching the de-excitation of the polarised alkali vapour. This N_2 can undergo QE scattering and cause events which pass all cuts. The fraction of events attributable to a background from this N_2 scattering is calculated for kinematic setting 3 and 4 by Sean Jeffas, as discussed in Sec. 5.9. As also mentioned in the same section, the values for kinematic setting 3 are taken for kinematic setting 2 as a result of there being no necessary carbon optics data to perform the analysis at this setting. The uncertainty on f_{N_2} comes directly from the thesis of Sean Jeffas [195]. It is assumed that the accumulated charges in the ^{3}He and C datasets, Q and the mass densities, m have negligible uncertainties. The uncertainty on f_{N2} is measured on the counts within each yield,

$$\sigma^2_{f_{N2}} = \left(\frac{Q(^3\text{He})}{Q(\text{C})}\frac{m_{\text{N2}}(^3\text{He})}{m_{\text{C}}(\text{C})}\right)\left[\frac{\Sigma(\text{C}) + \Sigma_{\text{acc}}(\text{C})}{(\Sigma(^3\text{He}) - \Sigma_{\text{acc}}(^3\text{He}))^2} + \frac{(\Sigma(\text{C}) - \Sigma_{\text{acc}}(\text{C}))^2(\Sigma(^3\text{He}) + \Sigma_{\text{acc}}(^3\text{He}))}{(\Sigma(^3\text{He}) - \Sigma_{\text{acc}}(^3\text{He}))^4}\right] \tag{6.19}$$

where Σ represents a given target yield and the subscript "acc" denotes the number of counts attributed to timing accidentals, which are subtracted in the analysis to avoid double counting backgrounds. The final value is taken as $f_{N_2} = 0.0178 \pm 0.0018$. The asymmetry is taken to be zero as nitrogen is unpolarised.

Pion Background

Pions misidentified as electrons in Bigbite produce a measurable background. This is discussed in Sec. 5.7.2 where signals from a pion in Bigbite and a particle in HCal which pass QE cuts are estimated from a Monte Carlo simulation using a pion photoproduction generator. This is measured to be the smallest background in the experiment. This is due in part to good particle identification (PID) between electrons and pions using both the preshower calorimeter and GRINCH Cherenkov detector. Furthermore as discussed in the same section, residual events in which pions which are misidentified as electrons are likely to be removed by the full QE cuts as a result of the kinematics of producing a pion in the acceptance of Bigbite and something which appears as a QE recoil neutron within the final cut acceptance of HCal. The yield of pion background events is calculated from the integral of the background fit, and the associated asymmetry is measured through anti-cuts on an expected pure pion signal. The uncertainty on each of these quantities follows the statistics of Eqns. 6.11 and 6.6 respectively. The dilution and asymmetry associated with misidentified pions in Bigbite are $f_\pi = 0.0004 \pm 0.0001$ and $A_\pi = 0.0029 \pm 0.0017$ respectively.

Neutron Fraction

The neutron fraction f_n is not a background contamination, but rather the subtraction of all the background fractions which measures the remaining fraction of events which come from QE neutrons of interest. It is given simply by

$$f_n = 1 - f_{\mathrm{p,QE}} - f_{\mathrm{inelas}} - f_{\mathrm{acci}} - f_{\mathrm{fsi}} - f_{\mathrm{N}_2} - f_\pi = 1 - \sum_\chi f_\chi \tag{6.20}$$

where each background fraction f_χ has previously been discussed. The uncertainties are simply added in quadrature, and the final value is found to be $f_n = 0.7645 \pm 0.0038$.

6.2.2 Systematic Uncertainty on Physical Asymmetry

The results for each background fraction and asymmetry have been discussed in the preceding section, and are summarised in Tab. 6.2. The uncertainties on these values are combined to form a single systematic uncertainty for the physical asymmetry. The propagation of these to the full asymmetry has the form

$$\sigma_{\text{sys}}^2 = \frac{\sum \sigma_{f_\chi}^2 A_\chi^2}{P^2 f_n^2} + \frac{\sum \sigma_{A_\chi}^2 f_\chi^2}{P^2 f_n^2} + A_{\text{phys}}^2 \left(\frac{\sigma_{f_n}}{f_n} \right). \tag{6.21}$$

The result of the propagation of these systematic uncertainties on the physical asymmetry yields $A_{\text{phys}} = 0.148 \pm 0.014\,(\text{stat}) \pm 0.001\,(\text{syst})$. As expected, the impact of the background dilution terms on the physical asymmetry and its systematic uncertainty are negligibly small in comparison with the statistical uncertainty.

Table 6.2: Results of background dilution fractions and asymmetries and their uncertainties.

Parameter	Kin. 2 Result		
$f_{\text{P,QE}}$	0.0745	±	0.0006
$f_{\text{inelastic}}$	0.0701	±	0.0019
f_{acci}	0.0441	±	0.0004
f_{FSI}	0.0287	±	0.0026
f_π	0.0004	±	0.0001
f_{N_2}	0.0178	±	0.0018
f_{BG}	0.0882	±	0.0006
f_n	0.7645	±	0.0038
$A_{\text{P,QE}}$	0.0024	±	0.0001
$A_{\text{inelastic}}$	0.0040	±	0.0007
A_{acci}	0.0061	±	0.0032
A_{FSI}	0.0003	±	0.0005
A_π	0.0029	±	0.0017

6.3 Final Preliminary Results

6.3.1 Asymmetry Result

The physical asymmetry is calculated as

$$A_{\text{phys}} = \frac{A_{\text{raw}} - \Sigma_\chi f_\chi A_\chi}{P_{\text{He}^3} P_{\text{n}} P_{\text{beam}} (1 - \Sigma_\chi f_\chi)} = \frac{A_{\text{raw}} - \Sigma_\chi f_\chi A_\chi}{P f_{\text{n}}}. \tag{6.22}$$

The results of calculating the physical asymmetry A_{phys} and propagating the statistical and systematic uncertainties are summarised in Tab. 6.3. The physical asymmetry is measured as $A_{\text{phys}} = 0.148 \pm 0.014\,(\text{stat}) \pm 0.001\,(\text{syst})$. As discussed previously the statistical uncertainty dominates in the combined uncertainty on A_{phys}. As such the propagation of the full uncertainty through to the form factor ratio and G_E^n is not split into statistical and systematic parts.

Table 6.3: Results of calculations of A_{phys} and statistical and systematic uncertainties.

Parameter	Kin. 2 Result
N_{QE}	248326
A_{raw}	0.0340
$\sigma_{A_{\text{raw}}}$	0.0020
$\sigma_{A_{\text{raw}}}/A_{\text{raw}}$	5.89%
$\sigma_{\text{stat,Poisson}}$	6.09%
$\sigma_{\text{stat,pol}}$	7.43%
A_{phys}	0.148
$\sigma_{A_{\text{phys}}}$	0.014
σ_{stat}	0.014
$\sigma_{\text{stat}}/A_{\text{phys}}$	9.57%
σ_{syst}	0.001
$\sigma_{\text{syst}}/A_{\text{phys}}$	0.67%

6.3.2 Form Factor Results

The method of extracting the form factor ratio is detailed in Sec. 5.12. From Eqn. 5.29, the physical asymmetry can be written as

$$A_{\text{phys}} = -\sqrt{\frac{2\epsilon(1-\epsilon)}{\tau}}\frac{r}{1+\frac{\epsilon}{\tau}r^2}\hat{P}_x - \frac{\sqrt{1-\epsilon^2}}{1+\frac{\epsilon}{\tau}r^2}\hat{P}_z \tag{6.23}$$

where $\hat{P}_x = \sin\theta^* \cos\phi^*$, $\hat{P}_z = \cos\theta^*$, τ and ϵ are measured quantities discussed in the aforementioned section. These are averaged over the final event sample, and new variables A, B, C are formed,

$$\begin{aligned} A &= \frac{\epsilon A_{\text{phys}}}{\tau} \\ B &= \sqrt{\frac{2\epsilon(1-\epsilon)}{\tau}}\hat{P}_x \\ C &= A_{\text{phys}} + \sqrt{1-\epsilon^2}\hat{P}_z \end{aligned} \tag{6.24}$$

and Eqn. 6.23 can be rearranged into a polynomial in r^2 which is solved for the form factor ratio $r = G_E^n/G_M^n$. The uncertainty on the averaged kinematic variables is assumed to be negligible, since the angular track reconstruction resolution of Bigbite is much smaller than the kinematic broadening on these terms which arises from nuclear effects. The uncertainty from the measured physical asymmetry is then propagated by variation. Recall that the final extraction of G_E^n from the measured form factor ratio r is simply $G_E^n = r_{\text{meas}} * G_M^n|_{\text{Ye}}$. The uncertainty is propagated straightforwardly as

$$\sigma^2_{G^n_E} = (G^n_E)^2 \left[\left(\frac{\sigma_{G^n_M}}{G^n_M} \right)^2 + \left(\frac{\sigma_r}{r} \right)^2 \right]. \tag{6.25}$$

The magnetic form factor G^n_M and the corresponding uncertainty $\sigma_{G^n_M}$ are again taken from the global fit to world data and the uncertainty band respectively. Taking the result for A_{phys} given in Tab. 6.3 and summing over the kinematic variables involved in Eqn. 5.29, we can form the required A, B, C for our polynomial in $r = G^n_E/G^n_M$. The values obtained for these as well as the final calculation of the form factor ratio are given in Tab. 6.4. The form factor ratio is extracted as $G^n_E/G^n_M = -0.1735^{+0.0255}_{-0.0263}$.

Table 6.4: Averaged values of kinematic variables which are used in the extraction of the form factor ratio in the quadratic method, with the form factor results.

Parameter	Kinematic 2 Result
Q^2	2.92 GeV^2
τ	0.824
ϵ	0.799
P_x	0.986
P_z	-0.075
A	0.142
B	0.615
C	0.101
G^n_E/G^n_M	$-0.1735^{+0.0255}_{-0.0263}$
G^n_M	-0.0742 ± 0.0007
G^n_E	0.0129 $^{+0.0019}_{-0.0020}$

The magnetic form factor of the neutron is taken from the global fit to world data by Ye, and at $Q^2 = 2.92$ GeV² is extracted as $G^n_M = -0.0742 \pm 0.0007$. The final result for the electric form factor of the neutron is measured as $G^n_E = 0.0129^{+0.0019}_{-0.0020}$. The results are shown in Fig. 6.1 for (top) the form factor ratio and (bottom) for G^n_E, against world data and nucleon models. The result appears to be in agreement with the world fit within 1.6σ error with $G^n_E(Q^2 = 2.92)|_{\text{Ye}} = 0.0169 \pm 0.0017$, and notably falls between the CSM and RCQM models that overlap with world data, and the more recent DSE based calculations which predict a lower form factor ratio. Future work which might improve the precision of this result has a chance to discern between models, and this is discussed in Sec. 6.4.

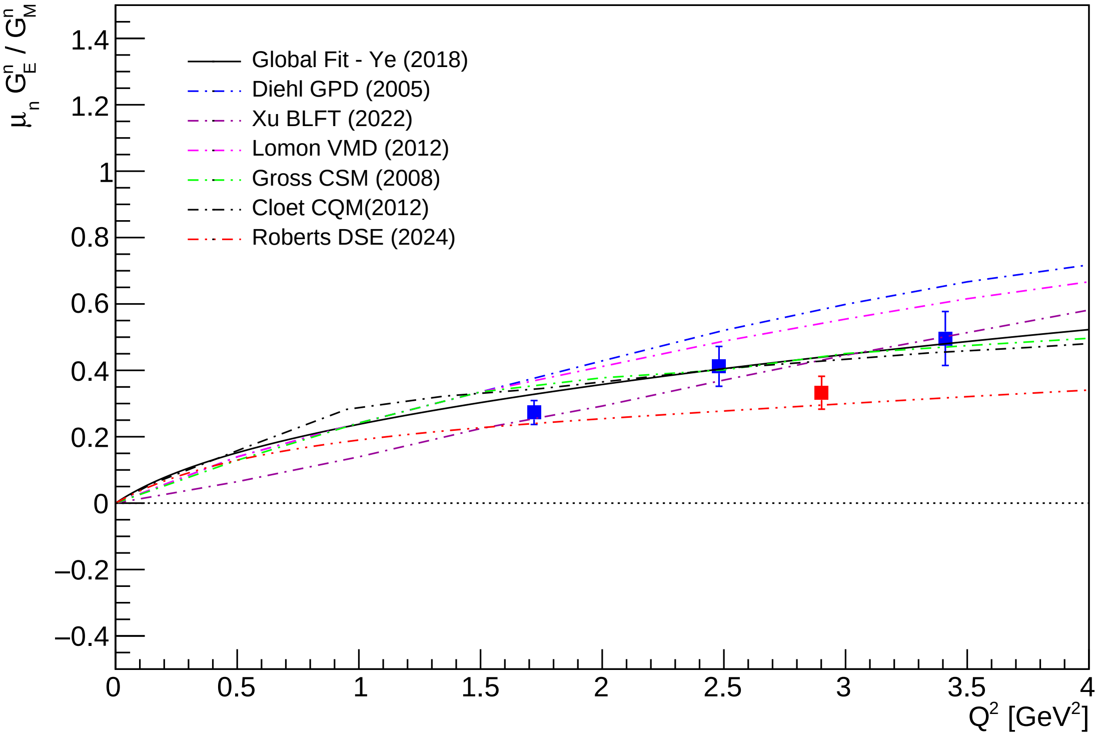

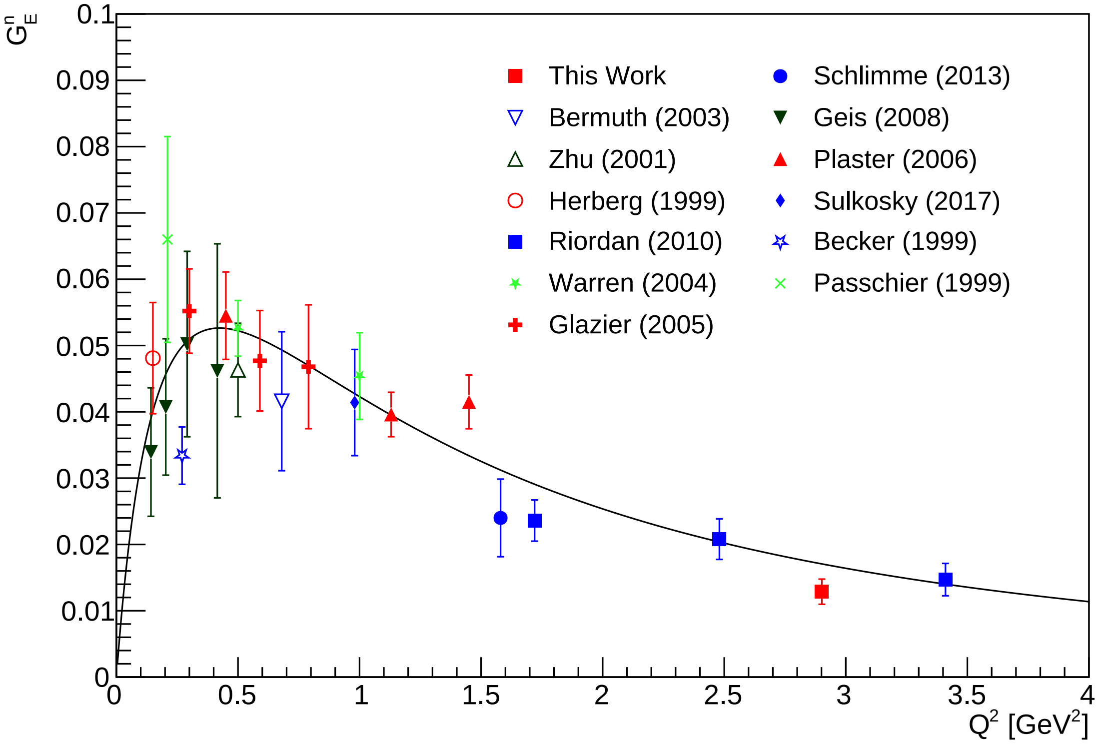

Figure 6.1: Final results from this work. (Top) The measured form factor ratio multiplied by $\mu_n = -1.91$ and (Bottom) the extracted electric form factor of the neutron from world data of the magnetic form factor. Error bars correspond to 1σ uncertainty in all data points.

6.4 Conclusion and Outlook

The E12-09-016 (GEN-II) experiment undertaken within Hall A of Jefferson Lab has measured the electric form factor of the neutron G_E^n at three kinematic settings corresponding to new values of squared four-momentum transfer Q^2. This thesis has presented a preliminary analysis of the first production setting, kinematic setting 2 (GEN2 or KIN2), corresponding to an acceptance weighted $Q^2 = 2.92$ GeV². Chapter 1 provided a short pedagogical introduction to modern hadron physics and the nucleon. In chapter 2 the theoretical foundations of electron scattering and nucleon structure were discussed, and an overview of past nucleon form factor measurements and current world data was given. The experimental setup for this measurement was detailed in chapter 3 and the calibration of detector and target subsystems was shown in chapter 4. The physics analysis of the QE signal selection, background estimations and asymmetry formalism was presented in chapter 5, and this chapter has presented the final results and uncertainty calculations for kinematic setting 2.

The complete analysis of kinematic settings 3 and 4, which will triple the current Q^2 range of the world data are expected to be completed in the future. The results of this analysis stand to test existing world data and provide a consistency check on the analysis technique. The results of this analysis are slightly lower than one might expect from the current global fit to world data, which at this Q^2 is constrained by the measurements by Riordan et al. at $Q^2 = 2.5$ and 3.5 GeV² [112]. However the result is still within 1.6σ of the world data fit. Additionally, this is also in close agreement with a recent exploratory thesis result by Sean Jeffas of this kinematic point [195].

This result does not suggest stronger agreement one way or the other between the recent DSE theoretical calculations by Roberts et al, and the VMD, CSM and RCQM models which overlap with the global fit at this Q^2. It appears to fall in between models, with the upper bound agreeing with RCQM and CSM within errors, and the lower bound agreeing with the new DSE model within errors. To gain more precise agreement with a model for this kinematic setting therefore requires a more precise result. The uncertainty is dominated by three sources, the Poisson error on the raw yield, the uncertainty on the target polarisation and the uncertainty on the neutron polarisation. The former is likely to change with improved detector calibrations, as these may increase the overall yield of QE events for the same set of cuts which would reduce the corresponding statistical uncertainty. The uncertainties on the target polarisation are expected to improve with further polarimetry. In particular, if the early polarimetery data taken while the NMR lock-in channel was missing can be recovered and calibrated, then not only might the polarisation uncertainty improve, but the yield will also increase by the inclusion of those currently excluded runs. The neutron polarisation was assigned a conservatively large uncertainty to account for the fact that no full dedicated calculation of nuclear effects has been performed for this analysis yet. While it is assumed that the dilution due to charge exchange in final state interactions will be a similar level to the GEN-I experiment, this should be verified with a dedicated calculation within the GEA framework. Likewise it is expected that selecting QE events picks out a part of the ^{3}He wavefunction corresponding to lower transverse momentum of the neutron, effectively increasing the polarisation above the nominal 86% value. This must also be verified for the choice of cuts in the analysis using the GEA code discussed in Sec. 5.10.

Further improvements to the calibrations for all detector systems offer the best hope for improving the precision of this measurement not only at kinematic setting 2, but for all three settings. In particular the analysis and calibration of the coincidence timing, which was presented in Sec. 4.5, presents a unique opportunity to greatly improve the accuracy of the experiment when completed. The preliminary calibration of performing a global fit to each spectrometer-arm's timing parameters has already yielded a measurable improvement in the resolution of the coincidence timing, which reduces the accidental timing background under the coincidence peak, and if sufficiently calibrated might offer a method of calculating the recoil neutron momentum through precision time of flight calculations. It is hoped to improve this calibration by first absorbing the separate fits for the timing hodoscope and hadron calorimeter TDC information into one fully self consistent global fit, and then to use the accelerator RF signal to align events to the nearest beam bunch - ultimately removing dilution to the timing signals which arise from a relatively slow trigger.

Additionally, the choice of QE cuts in this analysis could be revisited in closer detail. Relatively large Δx and Δy cuts have been chosen because the statistical uncertainty (which appears to be the dominant contribution) is minimised with these wider cuts. The inelastic background is sufficiently suppressed even with this large Δy cut given the $0.18 < W^2 < 1.58$ GeV^2 cut. However the effect of changing these, particularly with asymmetric upper and lower bounds, should be studied in detail. Additionally, if coupled with a dedicated GEA calculation this will allow a full comparison of how the uncertainty arising from the effective neutron polarisation within a given set of cuts evolves.

Kinematic setting 2 was the first production setting which ran, and therefore the first time this target was used. There were many initial technical difficulties which arose and were overcome in this analysis. The target polarimetery was not well understood at first, and the polarisation was considered to be fairly low for a significant period of the kinematic setting. Great effort was made to optimise the target running conditions in order to achieve a suitable polarisation, which ultimately made this measurement possible. However the early polarimetry changes ultimately may introduce systematic uncertainties to the data which is not fully encapsulated in this preliminary analysis.

This is a first analysis of data which was recently acquired, which has seen only one full pass of detector calibrations. It was performed during the stage of data taking and immediate subsequent data checking, and as such the collaboration still has to work together to progress the calibration techniques and fully understand the subsystems and their responses during this experiment. It is well known that further calibrations are required on all systems, and it is expected that the confidence, and interpretable knowledge of the measurement (at all kinematic settings) will improve with these. While the backgrounds estimated are already fairly small for the presented kinematic point, this is not the case at higher Q^2, and improved calibrations are expected to reduce the large inelastic background which ultimately contributes the largest systematic uncertainty for those kinematic settings.

This is a completely new experimental set up with a totally new target system and a new experimental analysis in a first of a kind measurement. This analysis has measured the electric form factor of the neutron, within challenging kinematics, at a new value of Q^2 with more precision than any measurement to date. This result precedes a more complete analysis, and validates an analysis method which can be applied to the higher Q^2 kinematics.

Appendix A

Trigger Logic Diagrams

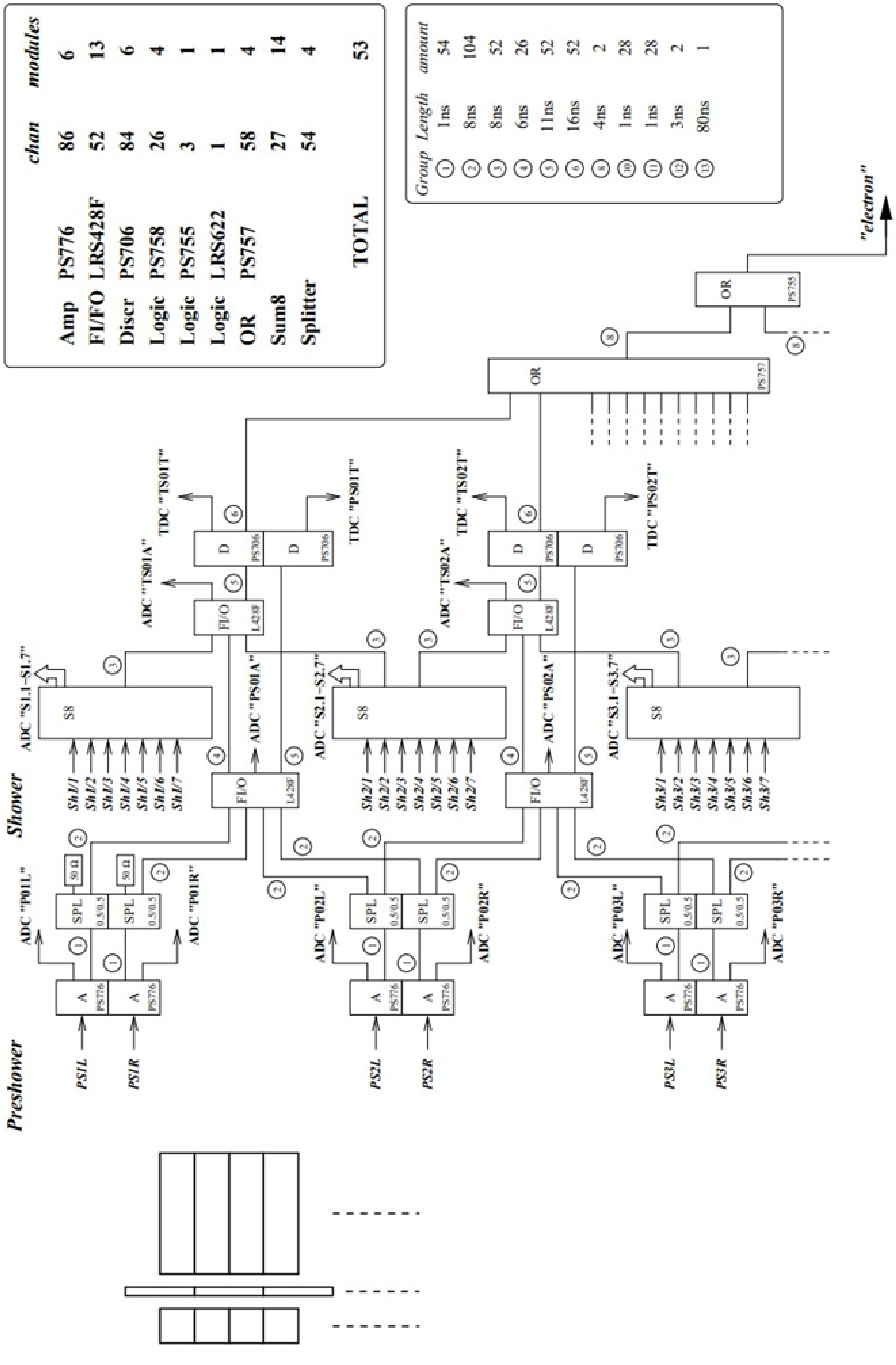

		chan	modules
Amp	PS776	86	6
FI/FO	LRS428F	52	13
Discr	PS706	84	6
Logic	PS758	26	4
Logic	PS755	3	1
Logic	LRS622	1	1
OR	PS757	58	4
Sum8		27	14
Splitter		54	4
TOTAL			53

Group	Length	amount
①	1ns	54
②	8ns	104
③	8ns	52
④	6ns	26
⑤	11ns	52
⑥	16ns	52
⑧	4ns	2
⑩	1ns	28
⑪	1ns	28
⑫	3ns	2
⑬	80ns	1

Figure A.1: Schematic of BBCal trigger.

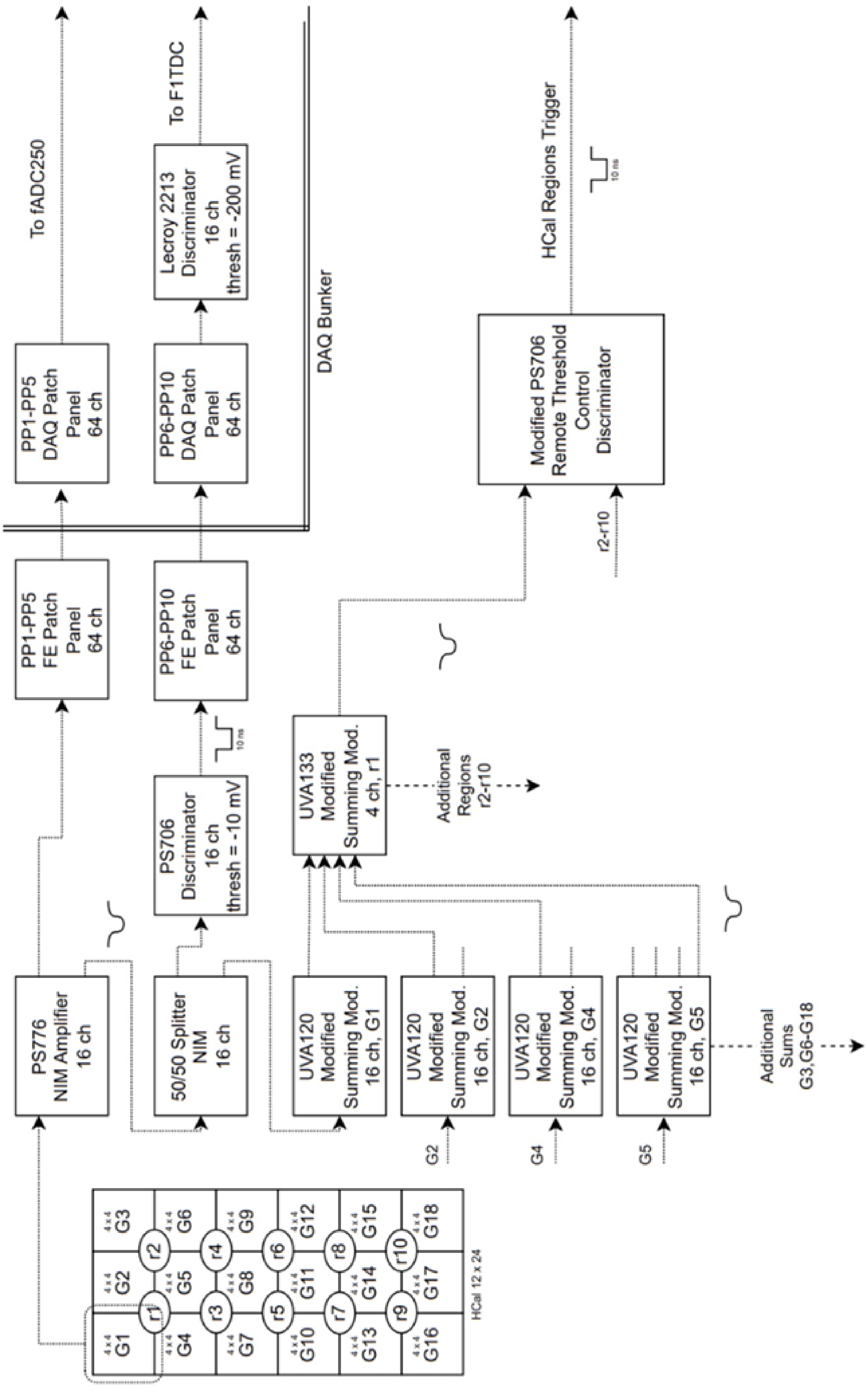

Figure A.2: Schematic of HCal trigger.

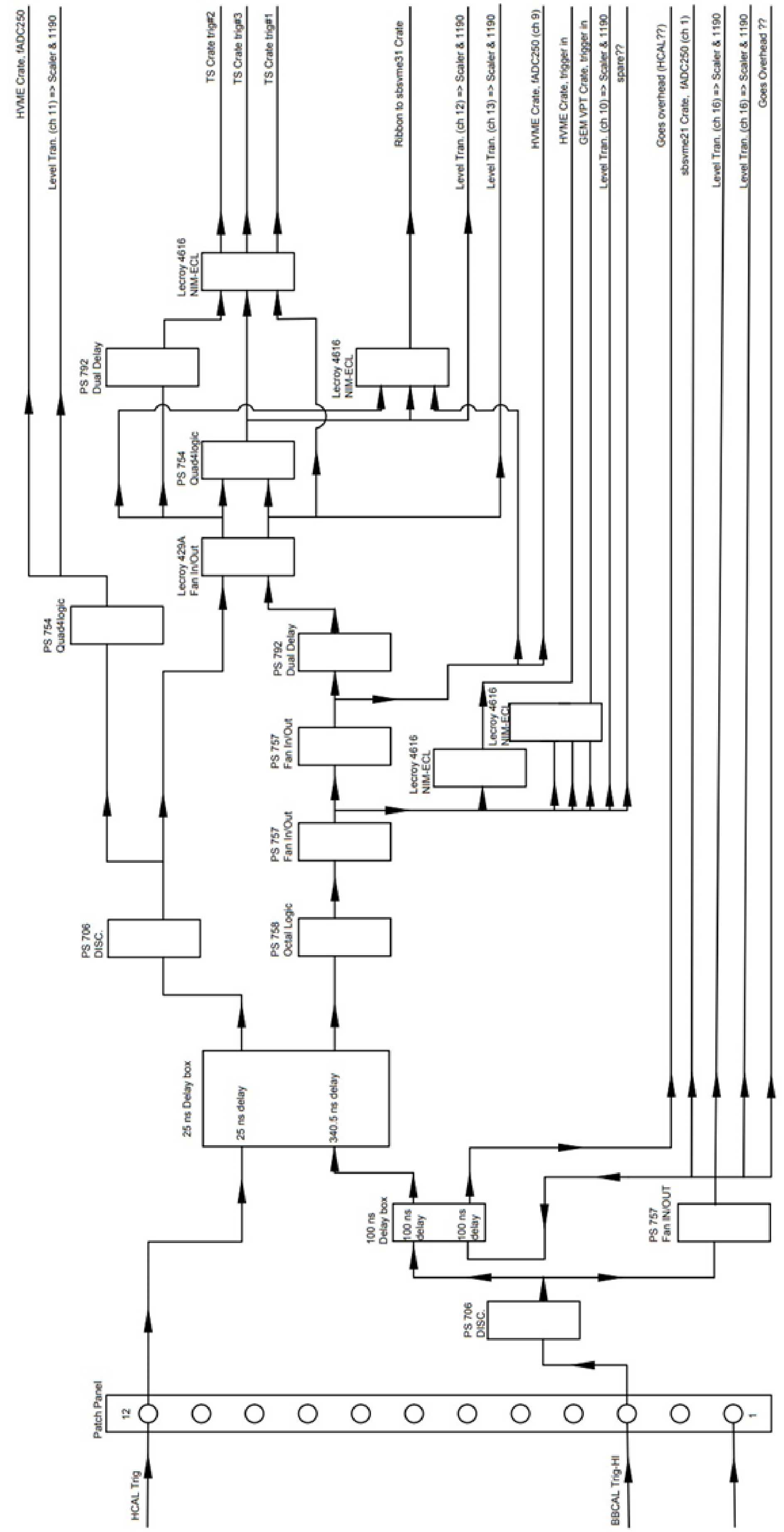

Figure A.3: Schematic of coincidence trigger.

References

[1] Yuri L. Dokshitzer. “Quantum chromodynamics and hadron dynamics”. In: *Philosophical Transactions of the Royal Society of London. Series A: Mathematical, Physical and Engineering Sciences* 359.1779 (Feb. 2001). Ed. by I. Butterworth, J. Ellis, and E. Gabathuler, pp. 309–324. ISSN: 1471-2962. DOI: `10.1098/rsta.2000.0728`. URL: `http://dx.doi.org/10.1098/rsta.2000.0728`.

[2] Professor E. Rutherford F.R.S. “LXXIX. The scattering of α and β particles by matter and the structure of the atom”. In: *The London, Edinburgh, and Dublin Philosophical Magazine and Journal of Science* 21.125 (1911), pp. 669–688. DOI: `10.1080/14786440508637080`. eprint: `https://doi.org/10.1080/14786440508637080`. URL: `https://doi.org/10.1080/14786440508637080`.

[3] E. Rutherford. “Collision of α particles with light atoms. IV. An anomalous effect in nitrogen”. In: *Philosophical Magazine* 90.sup1 (2010), pp. 31–37. DOI: `10.1080/14786431003659230`. eprint: `https://doi.org/10.1080/14786431003659230`. URL: `https://doi.org/10.1080/14786431003659230`.

[4] James Chadwick. “The existence of a neutron”. In: *Proceedings of the Royal Society of London. Series A, Containing Papers of a Mathematical and Physical Character* 136.830 (1932), pp. 692–708. DOI: `10.1098/rspa.1932.0112`. eprint: `https://royalsocietypublishing.org/doi/pdf/10.1098/rspa.1932.0112`. URL: `https://royalsocietypublishing.org/doi/abs/10.1098/rspa.1932.0112`.

[5] I. ESTERMANN and O. STERN. “Magnetic Moment of the Deuton”. In: *Nature* 133.3372 (June 1934), pp. 911–911. ISSN: 1476-4687. DOI: `10.1038/133911a0`. URL: `https://doi.org/10.1038/133911a0`.

[6] Hideki YUKAWA. “On the Interaction of Elementary Particles. I”. In: *Proceedings of the Physico-Mathematical Society of Japan. 3rd Series* 17 (1935), pp. 48–57. DOI: `10.11429/ppmsj1919.17.0_48`.

[7] Luis W. Alvarez and F. Bloch. “A Quantitative Determination of the Neutron Moment in Absolute Nuclear Magnetons”. In: *Phys. Rev.* 57 (2 Jan. 1940), pp. 111–122. DOI: `10.1103/PhysRev.57.111`. URL: `https://link.aps.org/doi/10.1103/PhysRev.57.111`.

[8] Paul Adrien Maurice Dirac and Niels Henrik David Bohr. “The quantum theory of the emission and absorption of radiation”. In: *Proceedings of the Royal Society of London. Series A, Containing Papers of a Mathematical and Physical Character* 114.767 (1927), pp. 243–265. DOI: 10.1098/rspa.1927.0039. eprint: https://royalsocietypublis org/doi/pdf/10.1098/rspa.1927.0039. URL: https://royalsocietypublishing.org/doi/abs/10.1098/rspa.1927.0039.

[9] H. A. Bethe. “The Electromagnetic Shift of Energy Levels”. In: *Phys. Rev.* 72 (4 Aug. 1947), pp. 339–341. DOI: 10.1103/PhysRev.72.339. URL: https://link.aps.org/doi/10.1103/PhysRev.72.339.

[10] R. Hofstadter, H. R. Fechter, and J. A. McIntyre. “Scattering of High-Energy Electrons and the Method of Nuclear Recoil”. In: *Phys. Rev.* 91 (2 July 1953), pp. 422–423. DOI: 10.1103/PhysRev.91.422. URL: https://link.aps.org/doi/10.1103/PhysRev.91.422.

[11] R. Hofstadter and R. W. McAllister. “Electron Scattering From the Proton”. In: *Phys. Rev.* 98 (1955), pp. 217–218. DOI: 10.1103/PhysRev.98.217.

[12] Robert Hofstadter. “Electron Scattering and Nuclear Structure”. In: *Rev. Mod. Phys.* 28 (3 July 1956), pp. 214–254. DOI: 10.1103/RevModPhys.28.214. URL: https://link.aps.org/doi/10.1103/RevModPhys.28.214.

[13] M. N. Rosenbluth. “High Energy Elastic Scattering of Electrons on Protons”. In: *Phys. Rev.* 79 (4 Aug. 1950), pp. 615–619. DOI: 10.1103/PhysRev.79.615. URL: https://link.aps.org/doi/10.1103/PhysRev.79.615.

[14] M. Gell-Mann. “A schematic model of baryons and mesons”. In: *Physics Letters* 8.3 (1964), pp. 214–215. ISSN: 0031-9163. DOI: https://doi.org/10.1016/S0031-9163(64)92001-3. URL: https://www.sciencedirect.com/science/article/pii/S0031916364920013.

[15] E. D. Bloom et al. “High-Energy Inelastic $e-p$ Scattering at 6° and 10°”. In: *Phys. Rev. Lett.* 23 (16 Oct. 1969), pp. 930–934. DOI: 10.1103/PhysRevLett.23.930. URL: https://link.aps.org/doi/10.1103/PhysRevLett.23.930.

[16] F. Abe et al. “Observation of Top Quark Production in $\overline{p}p$ Collisions with the Collider Detector at Fermilab”. In: *Phys. Rev. Lett.* 74 (14 Apr. 1995), pp. 2626–2631. DOI: 10.1103/PhysRevLett.74.2626. URL: https://link.aps.org/doi/10.1103/PhysRevLett.74.2626.

[17] S. Abachi et al. “Observation of the Top Quark”. In: *Phys. Rev. Lett.* 74 (14 Apr. 1995), pp. 2632–2637. DOI: 10.1103/PhysRevLett.74.2632. URL: https://link.aps.org/doi/10.1103/PhysRevLett.74.2632.

[18] Steven Weinberg. "A Model of Leptons". In: *Phys. Rev. Lett.* 19 (21 Nov. 1967), pp. 1264–1266. DOI: `10.1103/PhysRevLett.19.1264`. URL: `https://link.aps.org/doi/10.1103/PhysRevLett.19.1264`.

[19] Abdus Salam and J. C. Ward. "Weak and electromagnetic interactions". In: *Il Nuovo Cimento (1955-1965)* 11.4 (Feb. 1959), pp. 568–577. ISSN: 1827-6121. DOI: `10.1007/BF02726525`. URL: `https://doi.org/10.1007/BF02726525`.

[20] Peter W. Higgs. "Broken Symmetries and the Masses of Gauge Bosons". In: *Phys. Rev. Lett.* 13 (16 Oct. 1964), pp. 508–509. DOI: `10.1103/PhysRevLett.13.508`. URL: `https://link.aps.org/doi/10.1103/PhysRevLett.13.508`.

[21] J Iliopoulos. "Progress in gauge theories". In: *High energy physics. Proceedings, 17th International Conference, ICHEP*. 1974, pp. 89–116.

[22] G. Aad et al. "Observation of a new particle in the search for the Standard Model Higgs boson with the ATLAS detector at the LHC". In: *Physics Letters B* 716.1 (Sept. 2012), pp. 1–29. ISSN: 0370-2693. DOI: `10.1016/j.physletb.2012.08.020`. URL: `http://dx.doi.org/10.1016/j.physletb.2012.08.020`.

[23] F. Halzen and Alan D. Martin. *QUARKS AND LEPTONS: AN INTRODUCTORY COURSE IN MODERN PARTICLE PHYSICS*. Wiley, 1984. ISBN: 978-0-471-88741-6.

[24] D.H. Perkins. *Introduction to High Energy Physics*. Cambridge University Press, 2000. ISBN: 9780521621960. URL: `https://books.google.co.uk/books?id=e63cNigcmOUC`.

[25] M. R. A. Newman. *Rutherford Scattering*. 2024. URL: `https://prefetch.eu/know/concept/rutherford-scattering/`.

[26] John McArthur Reid. *The atomic nucleus*. Manchester University Press, 1984.

[27] Herbert Goldstein. *Classical mechanics*. Pearson Education India, 2011.

[28] L. D. Landau, A. Abrikosov, and L. Halatnikov. "On the Quantum theory of fields". In: *Nuovo Cim. Suppl.* 3 (1956), pp. 80–104. DOI: `10.1007/BF02745513`.

[29] Alison Wright. "QED". In: *Nature Materials* 9.1 (May 2010), S9–S9. ISSN: 1476-4660. DOI: `10.1038/nmat2643`. URL: `https://doi.org/10.1038/nmat2643`.

[30] T. van Ritbergen, J.A.M. Vermaseren, and S.A. Larin. "The four-loop β-function in quantum chromodynamics". In: *Physics Letters B* 400.3–4 (May 1997), pp. 379–384. ISSN: 0370-2693. DOI: `10.1016/s0370-2693(97)00370-5`. URL: `http://dx.doi.org/10.1016/S0370-2693(97)00370-5`.

[31] CMS Collaboration. *Search for a heavy resonance decaying to a top quark and a W boson at $\sqrt{s} = 13$ TeV in the fully hadronic final state*. 2021. arXiv: `2104.12853 [hep-ex]`.

[32] Owe Philipsen and Jonas Scheunert. *QCD in the heavy dense regime: Large N_c and quarkyonic matter.* 2020. arXiv: `2011.00504 [hep-lat]`.

[33] KLF Collaboration, Moskov Amaryan, and et al. *Strange Hadron Spectroscopy with Secondary KL Beam in Hall D.* 2021. arXiv: `2008.08215 [nucl-ex]`.

[34] B. A. Lippmann and Julian Schwinger. "Variational Principles for Scattering Processes. I". In: *Phys. Rev.* 79 (3 Aug. 1950), pp. 469–480. DOI: `10.1103/PhysRev.79.469`. URL: `https://link.aps.org/doi/10.1103/PhysRev.79.469`.

[35] Pierre A. M. Guichon and M. Vanderhaeghen. "How to reconcile the Rosenbluth and the polarization transfer method in the measurement of the proton form-factors". In: *Phys. Rev. Lett.* 91 (2003), p. 142303. DOI: `10.1103/PhysRevLett.91.142303`. arXiv: `hep-ph/0306007`.

[36] A. Afanasev et al. "Two-photon exchange in elastic electron–proton scattering". In: *Progress in Particle and Nuclear Physics* 95 (2017), pp. 245–278. ISSN: 0146-6410. DOI: `https://doi.org/10.1016/j.ppnp.2017.03.004`. URL: `https://www.sciencedirect.com/science/article/pii/S0146641017300352`.

[37] R. Hofstadter, C. de Vries, and Robert Herman. "Dirac and Pauli Form Factors of the Neutron". English. In: *Physical review letters* 6.6 (1961), pp. 290–293.

[38] F. J. Ernst, R. G. Sachs, and K. C. Wali. "Electromagnetic Form Factors of the Nucleon". In: *Phys. Rev.* 119 (3 Aug. 1960), pp. 1105–1114. DOI: `10.1103/PhysRev.119.1105`. URL: `https://link.aps.org/doi/10.1103/PhysRev.119.1105`.

[39] L. Andivahis et al. "Measurements of the electric and magnetic form factors of the proton from Q^2=1.75 to 8.83 (GeV/c)^2". In: *Phys. Rev. D* 50 (9 Nov. 1994), pp. 5491–5517. DOI: `10.1103/PhysRevD.50.5491`. URL: `https://link.aps.org/doi/10.1103/PhysRevD.50.5491`.

[40] L. W. MO and Y. S. TSAI. "Radiative Corrections to Elastic and Inelastic ep and up Scattering". In: *Rev. Mod. Phys.* 41 (1 Jan. 1969), pp. 205–235. DOI: `10.1103/RevModPhys.41.205`. URL: `https://link.aps.org/doi/10.1103/RevModPhys.41.205`.

[41] L. C. Maximon and J. A. Tjon. "Radiative corrections to electron-proton scattering". In: *Phys. Rev. C* 62 (5 2000), p. 054320. DOI: `10.1103/PhysRevC.62.054320`. URL: `https://link.aps.org/doi/10.1103/PhysRevC.62.054320`.

[42] V. Punjabi et al. *The Structure of the Nucleon: Elastic Electromagnetic Form Factors.* 2015. arXiv: `1503.01452 [nucl-ex]`. URL: `https://arxiv.org/abs/1503.01452`.

[43] C. Perdrisat and V. Punjabi. "Nucleon Form factors". In: *Scholarpedia* 5.8 (2010). revision #143981, p. 10204. DOI: `10.4249/scholarpedia.10204`.

[44] S. Platchkov et al. “The deuteron A(Q2) structure function and the neutron electric form factor”. In: *Nuclear Physics A* 510.4 (1990), pp. 740–758. ISSN: 0375-9474. DOI: https://doi.org/10.1016/0375-9474(90)90358-S. URL: https://www.sciencedirect.com/science/article/pii/037594749090358S.

[45] MISAK M. SARGSIAN. “SELECTED TOPICS IN HIGH ENERGY SEMI-EXCLUSIVE ELECTRO-NUCLEAR REACTIONS”. In: *International Journal of Modern Physics E* 10.06 (Dec. 2001), pp. 405–457. ISSN: 1793-6608. DOI: 10.1142/s0218301301000617. URL: http://dx.doi.org/10.1142/S0218301301000617.

[46] AI Akhiezer and MP Rekalo. “Polarization phenomena in electron scattering by protons in the high-energy region”. In: *Soviet Physics Doklady*. Vol. 13. 1968, p. 572.

[47] T.W Donnelly and A.S Raskin. “Considerations of polarization in inclusive electron scattering from nuclei”. In: *Annals of Physics* 169.2 (1986), pp. 247–351. ISSN: 0003-4916. DOI: https://doi.org/10.1016/0003-4916(86)90173-9. URL: https://www.sciencedirect.com/science/article/pii/0003491686901739.

[48] A. Camsonne et al. “Measurement of the Neutron electromagnetic Form Factor Ratio G_E^n/G_M^n at High Q^2”. (A New Proposal to Jefferson Lab PAC34).

[49] M. R. Yearian and Robert Hofstadter. “Magnetic Form Factor of the Neutron”. In: *Phys. Rev.* 110 (2 Apr. 1958), pp. 552–564. DOI: 10.1103/PhysRev.110.552. URL: https://link.aps.org/doi/10.1103/PhysRev.110.552.

[50] M. K. Jones et al. “GEp/GMpRatio by Polarization Transfer ine→p→ep→”. In: *Physical Review Letters* 84.7 (Feb. 2000), pp. 1398–1402. ISSN: 1079-7114. DOI: 10.1103/physrevlett.84.1398. URL: http://dx.doi.org/10.1103/PhysRevLett.84.1398.

[51] V. et al. Punjabi. “Proton elastic form factor ratios to $Q^2 = 3.5$ GeV^2 by polarization transfer”. In: *Phys. Rev. C* 71 (5 May 2005), p. 055202. DOI: 10.1103/PhysRevC.71.055202. URL: https://link.aps.org/doi/10.1103/PhysRevC.71.055202.

[52] L. N. Hand, D. G. Miller, and Richard Wilson. “Electric and Magnetic Form Factors of the Nucleon”. In: *Rev. Mod. Phys.* 35 (2 Apr. 1963), pp. 335–349. DOI: 10.1103/RevModPhys.35.335. URL: https://link.aps.org/doi/10.1103/RevModPhys.35.335.

[53] T. Janssens et al. “Proton Form Factors from Elastic Electron-Proton Scattering”. In: *Phys. Rev.* 142 (4 Feb. 1966), pp. 922–931. DOI: 10.1103/PhysRev.142.922. URL: https://link.aps.org/doi/10.1103/PhysRev.142.922.

[54] D. H. Coward et al. “Electron-Proton Elastic Scattering at High Momentum Transfers”. In: *Phys. Rev. Lett.* 20 (6 Feb. 1968), pp. 292–295. DOI: 10.1103/PhysRevLett.20.292. URL: https://link.aps.org/doi/10.1103/PhysRevLett.20.292.

[55] L. E. Price et al. "Backward-Angle Electron-Proton Elastic Scattering and Proton Electromagnetic Form Factors". In: *Phys. Rev. D* 4 (1 July 1971), pp. 45–53. DOI: 10.1103/PhysRevD.4.45. URL: https://link.aps.org/doi/10.1103/PhysRevD.4.45.

[56] Ch. Berger et al. "Electromagnetic form factors of the proton at squared four-momentum transfers between 10 and 50 fm–2". In: *Physics Letters B* 35.1 (1971), pp. 87–89. ISSN: 0370-2693. DOI: https://doi.org/10.1016/0370-2693(71)90448-5. URL: https://www.sciencedirect.com/science/article/pii/0370269371904485.

[57] W. Bartel et al. "Measurement of proton and neutron electromagnetic form factors at squared four-momentum transfers up to 3 (GeV/c)2". In: *Nuclear Physics B* 58.2 (1973), pp. 429–475. ISSN: 0550-3213. DOI: https://doi.org/10.1016/0550-3213(73)90594-4. URL: https://www.sciencedirect.com/science/article/pii/0550321373905944.

[58] F. Borkowski et al. "Electromagnetic form factors of the peoton at low four-momentum transfer (II)". In: *Nuclear Physics B* 93.3 (1975), pp. 461–478. ISSN: 0550-3213. DOI: https://doi.org/10.1016/0550-3213(75)90514-3. URL: https://www.sciencedirect.com/science/article/pii/0550321375905143.

[59] G.G. Simon et al. "Absolute electron-proton cross sections at low momentum transfer measured with a high pressure gas target system". In: *Nuclear Physics A* 333.3 (1980), pp. 381–391. ISSN: 0375-9474. DOI: https://doi.org/10.1016/0375-9474(80)90104-9. URL: https://www.sciencedirect.com/science/article/pii/0375947480901049.

[60] A. F. Sill et al. "Measurements of elastic electron-proton scattering at large momentum transfer". In: *Phys. Rev. D* 48 (1 July 1993), pp. 29–55. DOI: 10.1103/PhysRevD.48.29. URL: https://link.aps.org/doi/10.1103/PhysRevD.48.29.

[61] R. C. Walker et al. "Measurements of the proton elastic form factors for $1 \leq Q^2 \leq 3$ $(\mathrm{GeV}/c)^2$ at SLAC". In: *Phys. Rev. D* 49 (11 June 1994), pp. 5671–5689. DOI: 10.1103/PhysRevD.49.5671. URL: https://link.aps.org/doi/10.1103/PhysRevD.49.5671.

[62] M. E. Christy et al. "Measurements of electron-proton elastic cross sections for $0.4 < Q^2 < 5.5(\mathrm{GeV}/c)^2$". In: *Phys. Rev. C* 70 (1 July 2004), p. 015206. DOI: 10.1103/PhysRevC.70.015206. URL: https://link.aps.org/doi/10.1103/PhysRevC.70.015206.

[63] I. A. Qattan et al. "Precision Rosenbluth Measurement of the Proton Elastic Form Factors". In: *Phys. Rev. Lett.* 94 (14 Apr. 2005), p. 142301. DOI: 10.1103/PhysRevLett.94.142301. URL: https://link.aps.org/doi/10.1103/PhysRevLett.94.142301.

[64] Richard Frederick Obrecht Jr. "Electric form factor of the neutron from asymmetry measurements". PhD thesis. University of Connecticut, 2019.

[65] C. W. Akerlof et al. "Neutron Form Factors from Inelastic Electron-Deuteron Scattering". In: *Phys. Rev.* 135 (3B Aug. 1964), B810–B815. DOI: 10.1103/PhysRev.135.B810. URL: https://link.aps.org/doi/10.1103/PhysRev.135.B810.

[66] J. R. Dunning et al. "Electromagnetic Structure of the Neutron and Proton". In: *Phys. Rev. Lett.* 13 (21 Nov. 1964), pp. 631–635. DOI: 10.1103/PhysRevLett.13.631. URL: https://link.aps.org/doi/10.1103/PhysRevLett.13.631.

[67] E. B. Hughes et al. "Neutron Form Factors from Inelastic Electron-Deuteron Scattering". In: *Phys. Rev.* 139 (2B July 1965), B458–B471. DOI: 10.1103/PhysRev.139.B458. URL: https://link.aps.org/doi/10.1103/PhysRev.139.B458.

[68] E. B. Hughes et al. "Neutron Form Factors from a Study of Inelastic Electron Spectra in the Electrodisintegration of Deuterium". In: *Phys. Rev.* 146 (4 June 1966), pp. 973–979. DOI: 10.1103/PhysRev.146.973. URL: https://link.aps.org/doi/10.1103/PhysRev.146.973.

[69] B. Grossetête, S. Jullian, and P. Lehmann. "Electrodisintegration of the Deuteron Around $q^2 = 3.5\ \mathrm{F}^{-2}$". In: *Phys. Rev.* 141 (4 Jan. 1966), pp. 1435–1440. DOI: 10.1103/PhysRev.141.1435. URL: https://link.aps.org/doi/10.1103/PhysRev.141.1435.

[70] R. J. Budnitz et al. "Neutron Form Factors from Quasi-Elastic Electron-Deuteron Scattering". In: *Phys. Rev.* 173 (5 Sept. 1968), pp. 1357–1390. DOI: 10.1103/PhysRev.173.1357. URL: https://link.aps.org/doi/10.1103/PhysRev.173.1357.

[71] B. Grossetete, D. Drickey, and P. Lehmann. "Elastic Electron-Deuteron Scattering". In: *Phys. Rev.* 141 (4 Jan. 1966), pp. 1425–1434. DOI: 10.1103/PhysRev.141.1425. URL: https://link.aps.org/doi/10.1103/PhysRev.141.1425.

[72] S. Galster et al. "Elastic electron-deuteron scattering and the electric neutron form factor at four-momentum transfers 5 fm–2 < q2 < 14 fm–2". In: *Nuclear Physics B* 32.1 (1971), pp. 221–237. ISSN: 0550-3213. DOI: https://doi.org/10.1016/0550-3213(71)90068-X. URL: https://www.sciencedirect.com/science/article/pii/055032137190068X.

[73] G.G. Simon, Ch. Schmitt, and V.H. Walther. "Elastic electric and magnetic e-d scattering at low momentum transfer". In: *Nuclear Physics A* 364.2 (1981), pp. 285–296. ISSN: 0375-9474. DOI: https://doi.org/10.1016/0375-9474(81)90572-8. URL: https://www.sciencedirect.com/science/article/pii/0375947481905728.

[74] R. Schiavilla and I. Sick. "Neutron charge form factor at large q^2". In: *Physical Review C* 64.4 (Sept. 2001). ISSN: 1089-490X. DOI: 10.1103/physrevc.64.041002. URL: http://dx.doi.org/10.1103/PhysRevC.64.041002.

[75] M. Gourdin. “Deuteron electromagnetic form factors — II”. In: *Il Nuovo Cimento (1955-1965)* 35.4 (Feb. 1965), pp. 1105–1113. ISSN: 1827-6121. DOI: 10.1007/BF02735528. URL: https://doi.org/10.1007/BF02735528.

[76] T. Hamada and I.D. Johnston. “A potential model representation of two-nucleon data below 315 MeV”. In: *Nuclear Physics* 34.2 (1962), pp. 382–403. ISSN: 0029-5582. DOI: https://doi.org/10.1016/0029-5582(62)90228-6. URL: https://www.sciencedirect.com/science/article/pii/0029558262902286.

[77] E. LOMON and H. FESHBACH. “A Nucleon-Nucleon Interaction Consistent with Theory and Experiment”. In: *Rev. Mod. Phys.* 39 (3 July 1967), pp. 611–621. DOI: 10.1103/RevModPhys.39.611. URL: https://link.aps.org/doi/10.1103/RevModPhys.39.611.

[78] K. M. Hanson et al. “Large-Angle Quasielastic Electron-Deuteron Scattering”. In: *Phys. Rev. D* 8 (3 Aug. 1973), pp. 753–778. DOI: 10.1103/PhysRevD.8.753. URL: https://link.aps.org/doi/10.1103/PhysRevD.8.753.

[79] D. Benaksas, D. Drickey, and D. Frerejacque. “Electromagnetic form Factors of the Deuteron”. In: *Phys. Rev. Lett.* 13 (10 Sept. 1964), pp. 353–355. DOI: 10.1103/PhysRevLett.13.353. URL: https://link.aps.org/doi/10.1103/PhysRevLett.13.353.

[80] D. Benaksas, D. Drickey, and D. Frèrejacque. “Deuteron Electromagnetic Form Factors for $3F^{-2} < q^2 < 6F^{-2}$”. In: *Phys. Rev.* 148 (4 Aug. 1966), pp. 1327–1331. DOI: 10.1103/PhysRev.148.1327. URL: https://link.aps.org/doi/10.1103/PhysRev.148.1327.

[81] J. R. Dunning et al. “Quasi-Elastic Electron-Deuteron Scattering and Neutron Form Factors”. In: *Phys. Rev.* 141 (4 Jan. 1966), pp. 1286–1297. DOI: 10.1103/PhysRev.141.1286. URL: https://link.aps.org/doi/10.1103/PhysRev.141.1286.

[82] Loyal Durand. “Inelastic Electron-Deuteron Scattering Cross Sections at High Energies”. In: *Phys. Rev.* 115 (4 Aug. 1959), pp. 1020–1038. DOI: 10.1103/PhysRev.115.1020. URL: https://link.aps.org/doi/10.1103/PhysRev.115.1020.

[83] J. Lachniet et al. “Precise Measurement of the Neutron Magnetic Form Factor G_M^n in the Few-GeV^2 Region”. In: *Phys. Rev. Lett.* 102 (19 May 2009), p. 192001. DOI: 10.1103/PhysRevLett.102.192001. URL: https://link.aps.org/doi/10.1103/PhysRevLett.102.192001.

[84] B. Quinn et al. “Precision Measurement of the Neutron Magnetic Form Factor up to Q^2=13.5 (GeV/c)^2 by the Ratio Method”. URL: https://www.jlab.org/exp_prog/proposals/proposal_updates/PR12-09-019_pac35.pdf.

[85] P. Stein et al. "Measurements of Neutron Form Factors". In: *Phys. Rev. Lett.* 16 (13 Mar. 1966), pp. 592–594. DOI: 10.1103/PhysRevLett.16.592. URL: https://link.aps.org/doi/10.1103/PhysRevLett.16.592.

[86] S. Rock et al. "Measurement of Elastic Electron-Neutron Cross Sections up to $Q^2 = 10\ (\mathrm{GeV}/c)^2$". In: *Phys. Rev. Lett.* 49 (16 Oct. 1982), pp. 1139–1142. DOI: 10.1103/PhysRevLett.49.1139. URL: https://link.aps.org/doi/10.1103/PhysRevLett.49.1139.

[87] Esaulov A. S. et al. "Measurement of the neutron magnetic form factor in the reaction d(e,e')np in the interval 048 GeV2 � Q2 � 083 GeV2". In: *Soviet Journal of Nuclear Physics* 45.2 (1987), pp. 258–262. ISSN: 0038-5506. URL: http://inis.iaea.org/search/search.aspx?orig_q=RN:18084352.

[88] R. G. Arnold et al. "Measurements of Transverse Quasielastic Electron Scattering from the Deuteron at High Momentum Transfers". In: *Phys. Rev. Lett.* 61 (7 Aug. 1988), pp. 806–809. DOI: 10.1103/PhysRevLett.61.806. URL: https://link.aps.org/doi/10.1103/PhysRevLett.61.806.

[89] A. Lung et al. "Measurements of the electric and magnetic form factors of the neutron from Q^2=1.75 to 4.00 $(\mathrm{GeV/c})^2$". In: *Phys. Rev. Lett.* 70 (6 Feb. 1993), pp. 718–721. DOI: 10.1103/PhysRevLett.70.718. URL: https://link.aps.org/doi/10.1103/PhysRevLett.70.718.

[90] P. Markowitz et al. "Measurement of the magnetic form factor of the neutron". In: *Phys. Rev. C* 48 (1 July 1993), R5–R9. DOI: 10.1103/PhysRevC.48.R5. URL: https://link.aps.org/doi/10.1103/PhysRevC.48.R5.

[91] H. Anklin et al. "Precision measurement of the neutron magnetic form factor". In: *Physics Letters B* 336.3 (1994), pp. 313–318. ISSN: 0370-2693. DOI: https://doi.org/10.1016/0370-2693(94)90538-X. URL: https://www.sciencedirect.com/science/article/pii/037026939490538X.

[92] E. E. W. Bruins et al. "Measurement of the Neutron Magnetic Form Factor". In: *Phys. Rev. Lett.* 75 (1 July 1995), pp. 21–24. DOI: 10.1103/PhysRevLett.75.21. URL: https://link.aps.org/doi/10.1103/PhysRevLett.75.21.

[93] G Kubon et al. "Precise neutron magnetic form factors". In: *Physics Letters B* 524.1 (2002), pp. 26–32. ISSN: 0370-2693. DOI: https://doi.org/10.1016/S0370-2693(01)01386-7. URL: https://www.sciencedirect.com/science/article/pii/S0370269301013867.

[94] A. Puckett. ""SBS Results"". 2024 Summer Hall A/C Collaboration Meeting. URL: https://indico.jlab.org/event/843/contributions/14563/attachments/11476/17756/PuckettHallAC_2024.pdf.

[95] O. Gayou et al. “Measurement ofGEp/GMpine→p→ep→toQ2=5.6GeV2”. In: *Physical Review Letters* 88.9 (Feb. 2002). ISSN: 1079-7114. DOI: `10.1103/physrevlett.88.092301`. URL: `http://dx.doi.org/10.1103/PhysRevLett.88.092301`.

[96] A. J. R. Puckett et al. “Final analysis of proton form factor ratio data atQ2=4.0, 4.8, and 5.6 GeV2”. In: *Physical Review C* 85.4 (Apr. 2012). ISSN: 1089-490X. DOI: `10.1103/physrevc.85.045203`. URL: `http://dx.doi.org/10.1103/PhysRevC.85.045203`.

[97] A. J. R. Puckett et al. “Recoil Polarization Measurements of the Proton Electromagnetic Form Factor Ratio toQ2=8.5 GeV2”. In: *Physical Review Letters* 104.24 (June 2010). ISSN: 1079-7114. DOI: `10.1103/physrevlett.104.242301`. URL: `http://dx.doi.org/10.1103/PhysRevLett.104.242301`.

[98] C. Perdrisat et al. “Large Acceptance Proton Form Factor Ratio Measurements at 13 and 15 (GeV/c)^2 Using Recoil Polarization Method”. URL: `https://www.jlab.org/exp_prog/proposals/07/PR12-07-109.pdf`.

[99] C. E. Jones-Woodward et al. “Determination of the neutron electric form factor in quasielastic scattering of polarized electrons from polarized ^{3}He”. In: *Phys. Rev. C* 44 (2 Aug. 1991), R571–R574. DOI: `10.1103/PhysRevC.44.R571`. URL: `https://link.aps.org/doi/10.1103/PhysRevC.44.R571`.

[100] A. K. Thompson et al. “Quasielastic Scattering of Polarized Electrons from Polarized He^3 and Measurement of the Neutron’s Form Factors”. In: *Phys. Rev. Lett.* 68 (19 May 1992), pp. 2901–2904. DOI: `10.1103/PhysRevLett.68.2901`. URL: `https://link.aps.org/doi/10.1103/PhysRevLett.68.2901`.

[101] M. Meyerhoff et al. “First measurement of the electric formfactor of the neutron in the exclusive quasielastic scattering of polarized electrons from polarized 3He”. In: *Physics Letters B* 327.3 (1994), pp. 201–207. ISSN: 0370-2693. DOI: `https://doi.org/10.1016/0370-2693(94)90718-8`. URL: `https://www.sciencedirect.com/science/article/pii/0370269394907188`.

[102] T. Eden et al. “Electric form factor of the neutron from the ^{2}H(e→,e'n→)^{1}H reaction at Q^2=0.255 (GeV/c)^2”. In: *Phys. Rev. C* 50 (4 Oct. 1994), R1749–R1753. DOI: `10.1103/PhysRevC.50.R1749`. URL: `https://link.aps.org/doi/10.1103/PhysRevC.50.R1749`.

[103] J. Becker et al. “Determination of the neutron electric form factor from the reaction 3He(e,e’n) at medium momentum transfer”. In: *The European Physical Journal A - Hadrons and Nuclei* 6.3 (Nov. 1999), pp. 329–344. ISSN: 1434-601X. DOI: `10.1007/s100500050351`. URL: `https://doi.org/10.1007/s100500050351`.

[104] C. Herberg et al. “Determination of the neutron electric form factor in the D(e,e’n)p reaction and the influence of nuclear binding”. In: *The European Physical Journal A - Hadrons and Nuclei* 5.2 (June 1999), pp. 131–135. ISSN: 1434-601X. DOI: 10.1007/s100500050268. URL: https://doi.org/10.1007/s100500050268.

[105] I. Passchier et al. “Charge Form Factor of the Neutron from the Reaction $^{2}\vec{H}(\vec{e}, e' n)p$”. In: *Phys. Rev. Lett.* 82 (25 June 1999), pp. 4988–4991. DOI: 10.1103/PhysRevLett.82.4988. URL: https://link.aps.org/doi/10.1103/PhysRevLett.82.4988.

[106] H. Zhu et al. “Measurement of the Electric Form Factor of the Neutron through $\vec{d}(\vec{e}, e' n)p$ at $Q^2 = 0.5(\mathrm{GeV}/c)^2$”. In: *Phys. Rev. Lett.* 87 (8 Aug. 2001), p. 081801. DOI: 10.1103/PhysRevLett.87.081801. URL: https://link.aps.org/doi/10.1103/PhysRevLett.87.081801.

[107] J. Bermuth and et al. “The neutron charge form factor and target analyzing powers from 3He(e→,e′n) scattering”. In: *Physics Letters B* 564.3 (2003), pp. 199–204. ISSN: 0370-2693. DOI: https://doi.org/10.1016/S0370-2693(03)00725-1. URL: https://www.sciencedirect.com/science/article/pii/S0370269303007251.

[108] G. Warren et al. “Measurement of the Electric Form Factor of the Neutron at $Q^2 = 0.5$ and 1.0 GeV^2/c^2”. In: *Phys. Rev. Lett.* 92 (4 Jan. 2004), p. 042301. DOI: 10.1103/PhysRevLett.92.042301. URL: https://link.aps.org/doi/10.1103/PhysRevLett.92.042301.

[109] D. I. Glazier et al. “Measurement of the electric form factor of the neutron at Q2 = 0.3-0.8 (GeV/ c) 2 ⊠”. In: *The European Physical Journal A - Hadrons and Nuclei* 24.1 (Apr. 2005), pp. 101–109. ISSN: 1434-601X. DOI: 10.1140/epja/i2004-10115-8. URL: https://doi.org/10.1140/epja/i2004-10115-8.

[110] B. Plaster et al. “Measurements of the neutron electric to magnetic form factor ratio G_{En}/G_{Mn} via the $^2\mathrm{H}(\vec{e}, e' \vec{n})^1\mathrm{H}$ reaction to $Q^2 = 1.45\,(\mathrm{GeV}/c)^2$”. In: *Phys. Rev. C* 73 (2 Feb. 2006), p. 025205. DOI: 10.1103/PhysRevC.73.025205. URL: https://link.aps.org/doi/10.1103/PhysRevC.73.025205.

[111] E. Geis et al. “Charge Form Factor of the Neutron at Low Momentum Transfer from the $^2\vec{\mathrm{H}}(\vec{e}, e' n)^1\mathrm{H}$ Reaction”. In: *Phys. Rev. Lett.* 101 (4 July 2008), p. 042501. DOI: 10.1103/PhysRevLett.101.042501. URL: https://link.aps.org/doi/10.1103/PhysRevLett.101.042501.

[112] S. Riordan and et al. “Measurements of the Electric Form Factor of the Neutron up to $Q^2 = 3.4\mathrm{GeV}^2$ Using the Reaction $^3\vec{\mathrm{He}}(\vec{e}, e'' n)pp$”. In: *Physical Review Letters* 105.26 (Dec. 2010). ISSN: 1079-7114. DOI: 10.1103/physrevlett.105.262302. URL: http://dx.doi.org/10.1103/PhysRevLett.105.262302.

[113] B. S. Schlimme et al. "Measurement of the Neutron Electric to Magnetic Form Factor Ratio at Q^2=1.58 GeV^2 Using the Reaction $^3\vec{\mathrm{He}}(\vec{e},e'n)pp$". In: *Phys. Rev. Lett.* 111 (13 Sept. 2013), p. 132504. DOI: 10.1103/PhysRevLett.111.132504. URL: https://link.aps.org/doi/10.1103/PhysRevLett.111.132504.

[114] V. Sulkosky et al. "Extraction of the neutron electric form factor from measurements of inclusive double spin asymmetries". In: *Phys. Rev. C* 96 (6 Dec. 2017), p. 065206. DOI: 10.1103/PhysRevC.96.065206. URL: https://link.aps.org/doi/10.1103/PhysRevC.96.065206.

[115] J. J. Kelly. "Simple parametrization of nucleon form factors". In: *Phys. Rev. C* 70 (6 Dec. 2004), p. 068202. DOI: 10.1103/PhysRevC.70.068202. URL: https://link.aps.org/doi/10.1103/PhysRevC.70.068202.

[116] Zhihong Ye et al. "Proton and neutron electromagnetic form factors and uncertainties". In: *Physics Letters B* 777 (Feb. 2018), pp. 8–15. ISSN: 0370-2693. DOI: 10.1016/j.physletb.2017.11.023. URL: http://dx.doi.org/10.1016/j.physletb.2017.11.023.

[117] A. V. Belitsky, Xiangdong Ji, and Feng Yuan. "Perturbative QCD Analysis of the Nucleon's Pauli Form Factor $F_2(Q^2)$". In: *Physical Review Letters* 91.9 (Aug. 2003). ISSN: 1079-7114. DOI: 10.1103/physrevlett.91.092003. URL: http://dx.doi.org/10.1103/PhysRevLett.91.092003.

[118] G. D. Cates et al. "Flavor Decomposition of the Elastic Nucleon Electromagnetic Form Factors". In: *Phys. Rev. Lett.* 106 (25 June 2011), p. 252003. DOI: 10.1103/PhysRevLett.106.252003. URL: https://link.aps.org/doi/10.1103/PhysRevLett.106.252003.

[119] Xiangdong Ji. "Gauge-Invariant Decomposition of Nucleon Spin". In: *Phys. Rev. Lett.* 78 (4 Jan. 1997), pp. 610–613. DOI: 10.1103/PhysRevLett.78.610. URL: https://link.aps.org/doi/10.1103/PhysRevLett.78.610.

[120] M. Diehl et al. "Generalized parton distributions from nucleon form factor data". In: *The European Physical Journal C* 39.1 (Jan. 2005), pp. 1–39. ISSN: 1434-6052. DOI: 10.1140/epjc/s2004-02063-4. URL: http://dx.doi.org/10.1140/epjc/s2004-02063-4.

[121] Jorge Segovia et al. "Nucleon and Δ Elastic and Transition Form Factors". In: *Few-Body Systems* 55.12 (Oct. 2014), pp. 1185–1222. ISSN: 1432-5411. DOI: 10.1007/s00601-014-0907-2. URL: http://dx.doi.org/10.1007/s00601-014-0907-2.

[122] Zhao-Qian Yao et al. "Nucleon charge and magnetisation distributions: flavour separation and zeroes". In: (Mar. 2024). arXiv: 2403.08088 [hep-ph].

[123] Earle L. Lomon and Simone Pacetti. "Timelike and spacelike electromagnetic form factors of nucleons, a unified description". In: *Phys. Rev. D* 85 (11 June 2012), p. 113004. DOI: 10.1103/PhysRevD.85.113004. URL: https://link.aps.org/doi/10.1103/PhysRevD.85.113004.

[124] Yong-Hui Lin, Hans-Werner Hammer, and Ulf-G. Meißner. "Dispersion-theoretical analysis of the electromagnetic form factors of the nucleon: Past, present and future". In: *The European Physical Journal A* 57.8 (Aug. 2021), p. 255. ISSN: 1434-601X. DOI: 10.1140/epja/s10050-021-00562-0. URL: https://doi.org/10.1140/epja/s10050-021-00562-0.

[125] J J Sakurai. "THEORY OF STRONG INTERACTIONS". In: *Annals of Physics (New York) (U.S.)* Vol: 11 (Sept. 1960). DOI: 10.1016/0003-4916(60)90126-3. URL: https://www.osti.gov/biblio/4134581.

[126] Earle L. Lomon. "Effect of recent R_p and R_n measurements on extended Gari-Krümpelmann model fits to nucleon electromagnetic form factors". In: *Physical Review C* 66.4 (Oct. 2002). ISSN: 1089-490X. DOI: 10.1103/physrevc.66.045501. URL: http://dx.doi.org/10.1103/PhysRevC.66.045501.

[127] Franz Gross, G. Ramalho, and M. T. Peña. "Pure *S*-wave covariant model for the nucleon". In: *Physical Review C* 77.1 (Jan. 2008). ISSN: 1089-490X. DOI: 10.1103/physrevc.77.015202. URL: http://dx.doi.org/10.1103/PhysRevC.77.015202.

[128] Ian C. Cloët and Gerald A. Miller. "Nucleon form factors and spin content in a quark-diquark model with a pion cloud". In: *Phys. Rev. C* 86 (1 July 2012), p. 015208. DOI: 10.1103/PhysRevC.86.015208. URL: https://link.aps.org/doi/10.1103/PhysRevC.86.015208.

[129] J. P. Vary et al. "Hamiltonian light-front field theory in a basis function approach". In: *Phys. Rev. C* 81 (3 Mar. 2010), p. 035205. DOI: 10.1103/PhysRevC.81.035205. URL: https://link.aps.org/doi/10.1103/PhysRevC.81.035205.

[130] Siqi Xu et al. "Nucleon structure from basis light-front quantization". In: *Phys. Rev. D* 104 (9 Nov. 2021), p. 094036. DOI: 10.1103/PhysRevD.104.094036. URL: https://link.aps.org/doi/10.1103/PhysRevD.104.094036.

[131] 1879-1955 Einstein Albert. *The collected papers of Albert Einstein.* "English translation"–Cover.;Intended for use in conjunction with the documentary ed. of the same title.;Vols. 3-5: Don Howard, consultant.;Vol. 6-7: Alfred Engel, translator ; Engelbert Schucking, consultant.;Vol. 8: Ann M. Hentschel, translator ; Klaus Hentschel, consultant. Princeton, N.J. : Princeton University Press, c1987-, c1987. URL: https://search.library.wisc.edu/catalog/999588086102121.

[132] Carlos Hernandez-Garcia, Patrick O'Shea, and Marcy Stutzman. "Electron sources for accelerators". In: *Physics Today - PHYS TODAY* 61 (Feb. 2008). DOI: 10.1063/1.2883909.

[133] D. Jones. "Determining the sign of the asymmetry for GEN". Unpublished internal document. Oct. 2024. URL: https://sbs.jlab.org/cgi-bin/DocDB/private/ShowDocument?docid=583.

[134] Christoph Leemann, David Douglas, and Geoffrey Krafft. "The Continuous Electron Beam Accelerator Facility: CEBAF at the Jefferson Laboratory". In: *Annu. Rev. Nucl. Part. Sci* 51 (Dec. 2001), pp. 413–50. DOI: 10.1146/annurev.nucl.51.101701.132327.

[135] R D McKeown. "The Jefferson Lab 12 GeV Upgrade". In: *Journal of Physics: Conference Series* 312.3 (Sept. 2011), p. 032014. DOI: 10.1088/1742-6596/312/3/032014. URL: https://dx.doi.org/10.1088/1742-6596/312/3/032014.

[136] M Spata. "Continuous Electron Beam Accerlator Facility Overview". unpublished. Jan. 2015. URL: https://indico.jlab.org/event/98/contributions/7445/attachments/6315/8363/18T_-_CEBAF_USPAS_SRF.pdf.

[137] John Thomas Austin Williamson. "APEX (A? Experiment): The search for a dark photon at Jefferson Lab". PhD. PhD thesis. University of Glasgow, 2022. URL: https://theses.gla.ac.uk/83215/.

[138] Pengjia Zhu et al. "Beam position reconstruction for the g2p experiment in Hall A at Jefferson lab". In: *Nuclear Instruments and Methods in Physics Research Section A: Accelerators, Spectrometers, Detectors and Associated Equipment* 808 (Feb. 2016), pp. 1–10. ISSN: 0168-9002. DOI: 10.1016/j.nima.2015.10.086. URL: http://dx.doi.org/10.1016/j.nima.2015.10.086.

[139] J. Alcorn et al. "Basic instrumentation for Hall A at Jefferson Lab". In: *Nuclear Instruments and Methods in Physics Research Section A: Accelerators, Spectrometers, Detectors and Associated Equipment* 522.3 (2004), pp. 294–346. ISSN: 0168-9002. DOI: https://doi.org/10.1016/j.nima.2003.11.415. URL: https://www.sciencedirect.com/science/article/pii/S0168900203033977.

[140] W. Barry, J. Heefner, and J. Perry. "Electronics systems for beam position monitors at CEBAF". In: *AIP Conference Proceedings* 229.1 (June 1991), pp. 48–74. ISSN: 0094-243X. DOI: 10.1063/1.40758. eprint: https://pubs.aip.org/aip/acp/article-pdf/229/1/48/11998875/48_1_online.pdf. URL: https://doi.org/10.1063/1.40758.

[141] K. B. Unser. “The parametric current transformer, a beam current monitor developed for LEP”. In: *AIP Conference Proceedings* 252.1 (Apr. 1992), pp. 266–275. ISSN: 0094-243X. DOI: 10.1063/1.42124. eprint: https://pubs.aip.org/aip/acp/article-pdf/252/1/266/11666911/266_1_online.pdf. URL: https://doi.org/10.1063/1.42124.

[142] J. Denard, A. Saha, and G. Lavessiere. “High Accuracy Beam Current Monitor System for CEBAF’s Experimental Hall A”. In: *Conf. Proc. C* 0106181 (2001). Ed. by Peter W. Lucas and Sara Webber, pp. 2326–2328.

[143] Reza Kazimi et al. “CEBAF injector achieved world’s best beam quality for three simultaneous beam with a wide range of bunch charges”. In: July 2004. URL: https://www.osti.gov/biblio/827516.

[144] P.A. Adderley et al. “An overview of how parity-violating electron scattering experiments are performed at CEBAF”. In: *Nuclear Instruments and Methods in Physics Research Section A: Accelerators, Spectrometers, Detectors and Associated Equipment* 1046 (2023), p. 167710. ISSN: 0168-9002. DOI: https://doi.org/10.1016/j.nima.2022.167710. URL: https://www.sciencedirect.com/science/article/pii/S0168900222010026.

[145] J. Berthot and P. Vernin. “Beam Energy Measurement in Hall-A of CEBAF”. In: *Nuclear Physics News* 9.4 (1999), pp. 12–16. DOI: 10.1080/10506899909411146. eprint: https://doi.org/10.1080/10506899909411146. URL: https://doi.org/10.1080/10506899909411146.

[146] S. N. Santiesteban et al. *Precise Beam Energy Determination for Hall A after the CEBAF 12 GeV Upgrade*. 2021. arXiv: 2110.06281 [physics.acc-ph].

[147] A. Minten. “Electron Scattering, Form Factors, Vector Mesons”. Lectures given in the Academic Training Programme of CERN 1968-1969. URL: https://cds.cern.ch/record/275318/files/CERN-69-22.pdf.

[148] D. Jones. “GEn Moller Polarimetery Plan”. Unpublished internal document. Oct. 2022.

[149] F.M. Gonzalez et al. “Improved Neutron Lifetime Measurement with UCNτ”. In: *Physical Review Letters* 127.16 (Aug. 2021). ISSN: 1079-7114. DOI: 10.1103/physrevlett.127.162501. URL: http://dx.doi.org/10.1103/PhysRevLett.127.162501.

[150] B. Blankleider and R. M. Woloshyn. “Quasi-elastic scattering of polarized electrons on polarized ^{3}He”. In: *Phys. Rev. C* 29 (2 Feb. 1984), pp. 538–552. DOI: 10.1103/PhysRevC.29.538. URL: https://link.aps.org/doi/10.1103/PhysRevC.29.538.

[151] R.-W. Schulze and P. U. Sauer. “Inelastic electron scattering from the three-nucleon bound states with polarization”. In: *Phys. Rev. C* 48 (1 July 1993), pp. 38–63. DOI: `10.1103/PhysRevC.48.38`. URL: `https://link.aps.org/doi/10.1103/PhysRevC.48.38`.

[152] J.M. Laget. “On the measurement of the neutron electric form factor”. In: *Physics Letters B* 273.4 (1991), pp. 367–370. ISSN: 0370-2693. DOI: `https://doi.org/10.1016/0370-2693(91)90284-W`. URL: `https://www.sciencedirect.com/science/article/pii/037026939190284W`.

[153] C. Ciofi degli Atti, E. Pace, and G. Salmè. “Investigation of the neutron form factors by inclusive quasielastic scattering of polarized electrons off polarized ^{3}He: A theoretical overview”. In: *Phys. Rev. C* 51 (3 Mar. 1995), pp. 1108–1119. DOI: `10.1103/PhysRevC.51.1108`. URL: `https://link.aps.org/doi/10.1103/PhysRevC.51.1108`.

[154] J. Golak et al. “Sensitivity studies for extraction of G_E^n from inclusive and semi-inclusive electron scattering on polarized ^{3}He”. In: *Phys. Rev. C* 65 (4 Mar. 2002), p. 044002. DOI: `10.1103/PhysRevC.65.044002`. URL: `https://link.aps.org/doi/10.1103/PhysRevC.65.044002`.

[155] C. Ciofi degli Atti and L.P. Kaptari. “Ground-state correlations and final-state interactions in exclusive lepton scattering off few-nucleon systems”. In: *Nuclear Physics A* 699.1–2 (Feb. 2002), pp. 49–56. ISSN: 0375-9474. DOI: `10.1016/s0375-9474(01)01469-5`. URL: `http://dx.doi.org/10.1016/S0375-9474(01)01469-5`.

[156] R. J. Eden. “Mathematical Aspects of the Three-body Problem in Quantum Scattering Theory. By L. D. Fadeev. Pp. 110. (Israel Program for Scientific Translations, Jerusalem)”. In: *The Mathematical Gazette* 50.374 (1966), pp. 443–443. DOI: `10.1017/S0025557200244136`.

[157] C. Ciofi degli Atti and S. Scopetta. “On the extraction of the neutron spin structure functions and the Gerasimov-Drell-Hearn integral from the process in the resonance region”. In: *Physics Letters B* 404.3–4 (July 1997), pp. 223–229. ISSN: 0370-2693. DOI: `10.1016/s0370-2693(97)00576-5`. URL: `http://dx.doi.org/10.1016/S0370-2693(97)00576-5`.

[158] C. Ciofi degli Atti et al. “Nuclear effects in deep inelastic scattering of polarized electrons off polarized 3He and the neutron spin structure functions”. In: *Physical Review C* 48.3 (Sept. 1993), R968–R972. ISSN: 1089-490X. DOI: `10.1103/physrevc.48.r968`. URL: `http://dx.doi.org/10.1103/PhysRevC.48.R968`.

[159] R.-W. Schulze and P. U. Sauer. “Polarized deep-inelastic lepton scattering from the polarized two- and three-nucleon bound states”. In: *Phys. Rev. C* 56 (4 Oct. 1997), pp. 2293–2315. DOI: `10.1103/PhysRevC.56.2293`. URL: `https://link.aps.org/doi/10.1103/PhysRevC.56.2293`.

[160] F. Bissey, A. W. Thomas, and I. R. Afnan. “Structure functions for the three-nucleon system”. In: *Phys. Rev. C* 64 (2 July 2001), p. 024004. DOI: `10.1103/PhysRevC.64.024004`. URL: `https://link.aps.org/doi/10.1103/PhysRevC.64.024004`.

[161] R.M. Woloshyn. “Polarized lepton deep-inelastic scattering from few-nucleon targets”. In: *Nuclear Physics A* 496.4 (1989), pp. 749–769. ISSN: 0375-9474. DOI: `https://doi.org/10.1016/0375-9474(89)90122-X`. URL: `https://www.sciencedirect.com/science/article/pii/037594748990122X`.

[162] J. L. Friar et al. “Neutron polarization in polarized ^{3}He targets”. In: *Phys. Rev. C* 42 (6 Dec. 1990), pp. 2310–2314. DOI: `10.1103/PhysRevC.42.2310`. URL: `https://link.aps.org/doi/10.1103/PhysRevC.42.2310`.

[163] Thad G. Walker and William Happer. “Spin-exchange optical pumping of noble-gas nuclei”. In: *Rev. Mod. Phys.* 69 (2 Apr. 1997), pp. 629–642. DOI: `10.1103/RevModPhys.69.629`. URL: `https://link.aps.org/doi/10.1103/RevModPhys.69.629`.

[164] Matthew D. Rotondaro and Glen P. Perram. “Collision-induced transitions between the Zeeman-split (J, m) levels of Rb$(5^2P_{1/2}, 5^2P_{3/2})$”. In: *Phys. Rev. A* 58 (3 Sept. 1998), pp. 2023–2029. DOI: `10.1103/PhysRevA.58.2023`. URL: `https://link.aps.org/doi/10.1103/PhysRevA.58.2023`.

[165] M. V. Romalis, E. Miron, and G. D. Cates. “Pressure broadening of Rb D_1 and D_2 lines by ^{3}He, ^{4}He, N_2, and Xe: Line cores and near wings”. In: *Phys. Rev. A* 56 (6 Dec. 1997), pp. 4569–4578. DOI: `10.1103/PhysRevA.56.4569`. URL: `https://link.aps.org/doi/10.1103/PhysRevA.56.4569`.

[166] J. Jackson. “Private Communications”. Slack Conversation.

[167] B. Lancor and T. G. Walker. “Effects of nitrogen quenching gas on spin-exchange optical pumping of ^{3}He”. In: *Phys. Rev. A* 82 (4 Oct. 2010), p. 043417. DOI: `10.1103/PhysRevA.82.043417`. URL: `https://link.aps.org/doi/10.1103/PhysRevA.82.043417`.

[168] Emily P Wang and Kelley Rivoire. “Optical Pumping of Rubidium Vapor”. In: ().

[169] J. Singh. “Alkali-Hybrid Spin-Exchange Optically-Pumped Polarized ^3He Targets Used for Studying Neutron Structure”. PhD thesis. University of Virginia, 2010.

[170] E. Babcock et al. “Limits to the Polarization for Spin-Exchange Optical Pumping of ^{3}He”. In: *Phys. Rev. Lett.* 96 (8 Mar. 2006), p. 083003. DOI: `10.1103/PhysRevLett.96.083003`. URL: `https://link.aps.org/doi/10.1103/PhysRevLett.96.083003`.

[171] A. Tadepalli. “A polarized ^{3}He target for the GEn-II experiment in Hall A at Jefferson Lab”. In: 25th International Spin Symposium (SPIN 2023). Sept. 2023. URL: https://indico.jlab.org/event/663/contributions/13253/.

[172] D.J.J.de Lange et al. “The optical properties of the BigBite spectrometer at NIKHEF”. In: *Nuclear Instruments and Methods in Physics Research Section A: Accelerators, Spectrometers, Detectors and Associated Equipment* 412.2 (1998), pp. 254–264. ISSN: 0168-9002. DOI: https://doi.org/10.1016/S0168-9002(98)00476-8. URL: https://www.sciencedirect.com/science/article/pii/S0168900298004768.

[173] D.J.J de Lange et al. “A large acceptance spectrometer for the internal target facility at NIKHEF”. In: *Nuclear Instruments and Methods in Physics Research Section A: Accelerators, Spectrometers, Detectors and Associated Equipment* 406.2 (1998), pp. 182–194. ISSN: 0168-9002. DOI: https://doi.org/10.1016/S0168-9002(98)91981-7. URL: https://www.sciencedirect.com/science/article/pii/S0168900298919817.

[174] Serge Duarte Pinto and Jens Spanggaard. “Gas Electron Multipliers versus Multiwire Proportional Chambers”. In: *2nd International Beam Instrumentation Conference*. 2013, TUCL3. arXiv: 1309.2908 [physics.ins-det].

[175] Fabio Sauli. “The gas electron multiplier (GEM): Operating principles and applications”. In: *Nuclear Instruments and Methods in Physics Research Section A: Accelerators, Spectrometers, Detectors and Associated Equipment* 805 (2016). Special Issue in memory of Glenn F. Knoll, pp. 2–24. ISSN: 0168-9002. DOI: https://doi.org/10.1016/j.nima.2015.07.060. URL: https://www.sciencedirect.com/science/article/pii/S0168900215008980.

[176] John Boyd. “Measurements of the Neutron Magnetic Form Factor and the Two-Photon Exchange Contribution to the Electron-Neutron Elastic Scattering Cross Section”. PhD thesis. Physics - Graduate School of Arts and Sciences, University of Virginia, 2024. DOI: 10.18130/pk2s-b031.

[177] Dmitriy Baranov and Oleg Rogachevsky. “Simulation of the GEM detector for BM@N experiment”. In: *EPJ Web Conf.* 138 (2017). Ed. by S. Bondarenko, V. Burov, and A. Malakhov, p. 11004. DOI: 10.1051/epjconf/201713811004.

[178] Leila Jones et al. “The APV25 deep submicron readout chip for CMS detectors”. In: (Jan. 1999). DOI: 10.5170/CERN-1999-009.162.

[179] Paolo Musico. *MPD Specifications*. Oct. 18. URL: https://coda.jlab.org/drupal/system/files/pdfs/HardwareManual/MPD/MPD4_UserManual_r2.5.pdf.

[180] Scott Kaneta et al. “The Global Trigger Processor: A VXS Switch Module for Triggering Large Scale Data Acquisition Systems”. In: (Oct. 2011). URL: https://www.osti.gov/biblio/1995784.

[181] M. Satnik. “The Gas Ring Cherenkov Detector (GRINCH) for Jefferson Lab, Hall A”. Hall A Winter Collaboration Meeting. 2023. URL: https://sbs.jlab.org/DocDB/0003/000360/001/Satnik%20HallA%20Winter%202023.pdf.

[182] T. Averett. “Update on the BigBite Gas Ring Imaging Cherenkov (GRINCH) Detector for SBS”. Unpublished internal document. 2018.

[183] F. Anghinolfi et al. “NINO: an ultra-fast and low-power front-end amplifier/discriminator ASIC designed for the multigap resistive plate chamber”. In: *Nuclear Instruments and Methods in Physics Research Section A: Accelerators, Spectrometers, Detectors and Associated Equipment* 533.1 (2004). Proceedings of the Seventh International Workshop on Resistive Plate Chambers and Related Detectors, pp. 183–187. ISSN: 0168-9002. DOI: https://doi.org/10.1016/j.nima.2004.07.024. URL: https://www.sciencedirect.com/science/article/pii/S0168900204014299.

[184] CAEN. *Mod. V1190-VX1190 A/B, 128/64 Ch Multihit TDC.* Aug. 2011. URL: https://coda.jlab.org/drupal/system/files/pdfs/HardwareManual/CAEN/V1190_REV10.pdf.

[185] M.Y. Balatz et al. “The lead-glass electromagnetic calorimeter for the SELEX experiment”. In: *Nuclear Instruments and Methods in Physics Research Section A: Accelerators, Spectrometers, Detectors and Associated Equipment* 545.1 (2005), pp. 114–138. ISSN: 0168-9002. DOI: https://doi.org/10.1016/j.nima.2005.01.328. URL: https://www.sciencedirect.com/science/article/pii/S0168900205005310.

[186] A. Tadepalli. “Bigbite Calorimeter Status”. Unpublished internal document. 2021. URL: https://indico.jlab.org/event/430/contributions/7812/attachments/6473/8673/sbs_collaboration_meeting_feb17.pdf.

[187] Jefferson Lab. *FADC250 User’s Manual.* URL: https://www.jlab.org/Hall-B/ftof/manuals/FADC250UsersManual.pdf.

[188] P. Datta. “Precision Measurements of the Neutron Magnetic Form Factor to High Momentum Transfer using Durand’s Method”. PhD thesis. University of Connecticut, 2024.

[189] M. Satnik. “Remade BBCal Illustration”. 2024. URL: https://sbs.jlab.org/cgi-bin/DocDB/private/ShowDocument?docid=651.

[190] Christian Wolfgang Fabjan and F Gianotti. “Calorimetry for Particle Physics”. In: *Rev. Mod. Phys.* 75 (2003), pp. 1243–1286. DOI: 10.1103/RevModPhys.75.1243. URL: https://cds.cern.ch/record/692252.

[191] D. Hamilton and R. Montgomery. “BigBite Timing Hodoscope Performance Update”. SBS DAQ Meeting. 2023. URL: https://sbs.jlab.org/DocDB/0003/000399/001/BB-TH-PerformanceUpdate-v1.pdf.

[192] C. Petta. "HCAL-J: Hadron Calorimeter for the study of nucleon Form Factors at Jefferson Lab". In: *CHERNE 2018 - 14th Workshop on European Collaboration in Higher Education on Radiological and Nuclear Engineering and Radiation Protection*. 2018. URL: https://indico.cern.ch/event/696724/contributions/2994185/attachments/1859127/3054775/05_Petta_CHERNE18_Petta.pdf.

[193] Jefferson Lab. *F1TDC: A High-Resolution, Multi-Hit, VME64x Time-to-Digital Converter User's Manual V1.1*. Apr. 2004. URL: https://halldweb.jlab.org/DocDB/0010/001021/001/F1TDC%20-%20User%20Manual%20V1.1.pdf.

[194] Sebastian Seeds. "The Two-Photon Exchange Contribution to Electron- Neutron Elastic Scattering (nTPE) and Extraction of G_M^n at $Q^2 = 4.5\,(\text{GeV/c})^2$ in Hall A at Jefferson National Lab". PhD thesis. Connecticut U., 2024.

[195] S. Jeffas. "Measurement of the Neutron Electromagnetic Form Factor Ratio at High Momentum Transfer". PhD thesis. Graduate School of Arts and Sciences, University of Virginia, 2024.

[196] CODA Homepage. URL: https://coda.jlab.org/.

[197] EPICS Homepage. URL: https://epics.anl.gov/.

[198] P. Datta. "Performance of the BigBite Calorimeter during $SBS - G_m^n$ Experiment". In: *2022 Frontiers and Careers in Nuclear and Hadronic Physics*. 2022. URL: https://indico.jlab.org/event/529/contributions/10270/attachments/8180/11693/F%26C_MIT_gmn%26bbcal_2022.pdf.

[199] J. Poudel. "SBS coincidence trigger set-up during GEn." Unpublished internal document. 2021. URL: https://sbs.jlab.org/DocDB/0005/000500/001/GEn_analysis_meeting_trigger_022024.pdf.

[200] Analyzer Homepage. URL: https://redmine.jlab.org/projects/podd/wiki.

[201] ROOT Homepage. URL: https://root.cern/.

[202] SBS-offline github. URL: https://github.com/JeffersonLab/SBS-offline.

[203] SBS-replay github. URL: https://github.com/JeffersonLab/SBS-replay.

[204] G. Penman. "GEN Analysis Github". URL: https://github.com/garypenman/SBS-Analysis.

[205] G4SBS Homepage. URL: https://hallaweb.jlab.org/wiki/index.php/Documentation_of_g4sbs.

[206] S. Agostinelli et al. “Geant4—a simulation toolkit”. In: *Nuclear Instruments and Methods in Physics Research Section A: Accelerators, Spectrometers, Detectors and Associated Equipment* 506.3 (2003), pp. 250–303. ISSN: 0168-9002. DOI: https://doi.org/10.1016/S0168-9002(03)01368-8. URL: https://www.sciencedirect.com/science/article/pii/S0168900203013688.

[207] S. Riordan et al. “Comparison between Wiser π^- rates calculation and data from transversity and PVDIS experiments”. Unpublished internal document.

[208] David Earl Wiser. *INCLUSIVE PHOTOPRODUCTION OF PROTONS, KAONS, AND PIONS AT SLAC ENERGIES*. The University of Wisconsin-Madison, 1977.

[209] P. E. Bosted and M. E. Christy. “Empirical fit to inelastic electron-deuteron and electron-neutron resonance region transverse cross sections”. In: *Physical Review C* 77.6 (June 2008). ISSN: 1089-490X. DOI: 10.1103/physrevc.77.065206. URL: http://dx.doi.org/10.1103/PhysRevC.77.065206.

[210] M. E. Christy and P. E. Bosted. “Empirical fit to precision inclusive electron-proton cross sections in the resonance region”. In: *Physical Review C* 81.5 (May 2010). ISSN: 1089-490X. DOI: 10.1103/physrevc.81.055213. URL: http://dx.doi.org/10.1103/PhysRevC.81.055213.

[211] libsbsdig github. URL: https://github.com/JeffersonLab/libsbsdig.

[212] Anatole Abragam. *The principles of nuclear magnetism*. 32. Oxford university press, 1961.

[213] M. V. Romalis and G. D. Cates. “Accurate ^{3}He polarimetry using the Rb Zeeman frequency shift due to the Rb$-^3$He spin-exchange collisions”. In: *Phys. Rev. A* 58 (4 Oct. 1998), pp. 3004–3011. DOI: 10.1103/PhysRevA.58.3004. URL: https://link.aps.org/doi/10.1103/PhysRevA.58.3004.

[214] H. Presley. Private communication.

[215] F. Chahili. “GEn-II Moller Polarimetry”. unpublished internal document.

[216] B. Zihlmann. “The absolute Helicity sign in the Hall C Möller Polarimeter.” Unpublished internal document. 1997.

[217] S. Jeffas. *Beam Position Reconstruction in GEN-II*. Unpublished internal document. URL: https://sbs.jlab.org/cgi-bin/DocDB/private/ShowDocument?docid=402.

[218] S. Jeffas. *GEN All Optics for Pass 1*. Unpublished internal document. URL: https://sbs.jlab.org/cgi-bin/DocDB/private/ShowDocument?docid=416.

[219] S. Jeffas. *GEN GEM calibratino for Pass1*. Unpublished internal document. URL: https://sbs.jlab.org/cgi-bin/DocDB/private/ShowDocument?docid=440.

[220] K. T. Evans. *BBCal H2 Energy Calibrations for GEN2 and GEN3*. Unpublished internal document. URL: https://sbs.jlab.org/cgi-bin/DocDB/private/ShowDocument?docid=436.

[221] H. Presley. *HCal Calibration GEn pass0*. Unpublished internal document. URL: https://sbs.jlab.org/cgi-bin/DocDB/private/ShowDocument?docid=437.

[222] J. Jacksdon. *GRINCH timing calibrations for GEN-II pass 2*. Private communication (slack).

[223] G. Penman. *GEN Hodoscope for Pass 0*. Unpublished internal document. URL: https://sbs.jlab.org/cgi-bin/DocDB/private/ShowDocument?docid=430.

[224] D. Di. "High Momentum Transfer Nucleon Elastic Electromagnetic Form Factor Measurements Using Super BigBite Spectrometer at Jefferson Lab". PhD thesis. Graduate School of Arts and Sciences, University of Virginia, 2019.

[225] *Procedure Wise How-to for BBCAL*. Unpublished internal document. URL: https://sbs.jlab.org/cgi-bin/DocDB/private/ShowDocument?docid=313.

[226] *BBCAL ADC Time Calibration Results for GMn/nTPE Pass2 Readiness*. Unpublished internal document. URL: https://sbs.jlab.org/cgi-bin/DocDB/public/ShowDocument?docid=406.

[227] D.S. Carman et al. "Description of the Calibration Algorithms for the CLAS12 Forward Time-Of-Flight System". June 2022. URL: https://www.jlab.org/Hall-B/ftof/notes/ftof_calib.pdf.

[228] A.J.R. Puckett. "SBS Timing Analysis Update". Unpublished internal document. Mar. 2024. URL: https://sbs.jlab.org/cgi-bin/DocDB/private/ShowDocument?docid=540.

[229] G. Penman. "GEN Analysis Meeting: SBS Timing Update 14/11/24". Unpublished internal document. 2024. URL: https://sbs.jlab.org/cgi-bin/DocDB/private/ShowDocument?docid=649.

[230] M. Mihovilovic et al. "Methods for optical calibration of the BigBite hadron spectrometer". In: *Nuclear Instruments and Methods in Physics Research Section A: Accelerators, Spectrometers, Detectors and Associated Equipment* 686 (2012), pp. 20–30. ISSN: 0168-9002. DOI: https://doi.org/10.1016/j.nima.2012.04.085. URL: https://www.sciencedirect.com/science/article/pii/S0168900212004901.

[231] W. Bertozzi et al. "High resolution spectrometers for electron scattering". In: *Nuclear Instruments and Methods* 162.1 (1979), pp. 211–238. ISSN: 0029-554X. DOI: https://doi.org/10.1016/0029-554X(79)90714-6. URL: https://www.sciencedirect.com/science/article/pii/0029554X79907146.

[232] N. Liyanage. “Optics Calibration of the Hall a High Resolution Spectrometers Using the C Optimizer”. JLab Technical Note JLAB-TN-02-012. 2002.

[233] S. Jeffas. “GEN Nitrogen Correction”. unpublished internal document. 2024. URL: `https://sbs.jlab.org/DocDB/0005/000556/002/GEN_Nitrogen_Correction.pdf`.

[234] M. M. Sargsian et al. “Exclusive electrodisintegration of ^{3}He at high Q^2. I. Generalized eikonal approximation”. In: *Phys. Rev. C* 71 (4 Apr. 2005), p. 044614. DOI: `10.1103/PhysRevC.71.044614`. URL: `https://link.aps.org/doi/10.1103/PhysRevC.71.044614`.

[235] R. J. Glauber. “Cross Sections in Deuterium at High Energies”. In: *Phys. Rev.* 100 (1 Oct. 1955), pp. 242–248. DOI: `10.1103/PhysRev.100.242`. URL: `https://link.aps.org/doi/10.1103/PhysRev.100.242`.